



# Corrosion behavior of a silicon enriched austenitic stainless steel in hot and concentrated nitric acid media

Barbara Laurent

## ► To cite this version:

Barbara Laurent. Corrosion behavior of a silicon enriched austenitic stainless steel in hot and concentrated nitric acid media. Analytical chemistry. Université Paris sciences et lettres, 2017. English. NNT : 2017PSLEC003 . tel-01793175

**HAL Id: tel-01793175**

**<https://pastel.hal.science/tel-01793175>**

Submitted on 16 May 2018

**HAL** is a multi-disciplinary open access archive for the deposit and dissemination of scientific research documents, whether they are published or not. The documents may come from teaching and research institutions in France or abroad, or from public or private research centers.

L'archive ouverte pluridisciplinaire **HAL**, est destinée au dépôt et à la diffusion de documents scientifiques de niveau recherche, publiés ou non, émanant des établissements d'enseignement et de recherche français ou étrangers, des laboratoires publics ou privés.

# THÈSE DE DOCTORAT

De l'Université de recherche Paris Sciences et Lettres

PSL Research University

Préparée à *Chimie ParisTech*

## Compréhension du comportement en corrosion d'un acier austénitique inoxydable enrichi en silicium en milieu acide nitrique chaud et concentré

Ecole doctorale n°388

Chimie Physique et Chimie Analytique de Paris-Centre

**Spécialité** Chimie Analytique

**Soutenue par Barbara LAURENT**  
**le 19 Octobre 2017**

Dirigée par **Kevin OGLE**

### JURY

#### Présidente

Mme. TURMINE Mireille  
Université Pierre et Marie Curie,  
Examineur

Mme. DAVENPORT Alison  
University of Birmingham,  
Rapporteur

M. BAROUX Bernard  
Grenoble INP,  
Examineur

M. KEDDAM Michel  
Université Pierre et Marie Curie,  
Examineur

M. OGLE Kevin  
Paris Sciences et Lettres,  
Directeur de thèse

M. VUILLEMIN Bruno  
Université de Bourgogne,  
Rapporteur







## ***Remerciements***

*J'adresse mes premiers remerciements aux membres de mon jury,  
Dont chacune des présences revêt un sens qui m'est singulier,  
Je n'éprouve pas seulement du respect pour l'importance de leur travail scientifique,  
Je leur suis redevable également pour leurs qualités humaines,  
Le chemin qu'ils ont su tracer pour que nous puissions les rejoindre un jour.*



*Pour leur soutien technique comme humain,  
Merci à Karine Rousseau, Christian Bataillon, Renaud Cornut, Olivier Genève,  
Kevin Ginestar, Frédéric Miserque et Michel Tabarant.  
La rigueur et la justesse de leur expertise m'ont permis de grandir en tant que scientifique.*



*Au partenaire industriel, Areva,  
pour le financement de la thèse,  
les jours passés, et les aventures à venir.*



*A Jérôme et Fred,  
avec qui j'ai réalisé à quel point j'aimais ce métier.*

*Someday I shall rise and leave my friends  
And seek you again through the world's far ends,  
You whom I found so fair  
My only god in the days that were.  
My eager feet shall find you again,  
Though the sullen years and the mark of pain  
Have changed you wholly; for I shall know  
How could I forget having loved you so?*

**Rupert Brooke**

*A mon directeur de thèse, Kevin Ogle.*

Merci d'avoir été cette voix unique, patiente et entière, guidée par la fascination d'une Science exigeante et sincère. Merci d'avoir ouvert les portes, abattu les cloisons, et soufflé dans les cabanes que je pensais des maisons.

*A Time to Talk – Robert Frost*



*A mon encadrante, Nathalie.*

Le temps que je réalise à quel point ces trois années m'avaient bouleversée et nous étions au bout de la jetée. J'étais là, j'avais grandi, sous le regard bienveillant que tu as toujours su m'accorder. Un voilier m'attendait.

*La fleur qui fait le printemps – Théophile Gautier*



*A mon encadrant, Benoit.*

De deux routes nous avons rarement choisi la même, mais à travers ta patience et ta gentillesse, je savais que les ponts à bâtir pour les relier feraient les plus belles constructions de cette incroyable aventure.

*J'arrive où je suis étranger – Louis Aragon*

*A mes Chefs de Service et de Laboratoire, Fabrice et Raphaël.*

C'est l'exercice le plus difficile au monde que d'emmener, suggérer, diriger. Et de traduire en quelques secondes le meilleur d'une personnalité. Comprendre ce qui suscite l'impulsion, jongler avec un millier de raisons, je crois avoir appris de vous bien plus que vous n'en avez eu l'impression.

*L'indulgence* – René-François Sully Prudhomme



*A tous ceux qui étaient là pour moi, les équipes du SCCME et de l'I2E.*

Des milliers de sourires que vous m'avez adressés, pas un seul ne s'est évanoui, chacun d'eux m'a servi, comme une terre que l'on sème, à cultiver une meilleure version de moi-même.

*J'ai plus de souvenirs que si j'avais mille ans* – Charles Baudelaire



*A des collègues, qui sont devenus des amis, qui sont devenus des proches.*

Je n'ai presque aucun mot, vous avez tout su de moi, à la minute où nos trajectoires se sont interceptées.

*A mon ami Alfred T* – Alfred de Musset



*A mes amis.*

Qu'ils soient au bout de la rue, ou au bout du monde, que l'on se retrouve chaque jour, chaque an, chaque mois, je danse, je pense, chaque fois que je les vois. Et ces trois années n'auraient eu aucun sens en leur absence.

*J'ai cueilli cette fleur pour toi sur la colline* – Victor Hugo

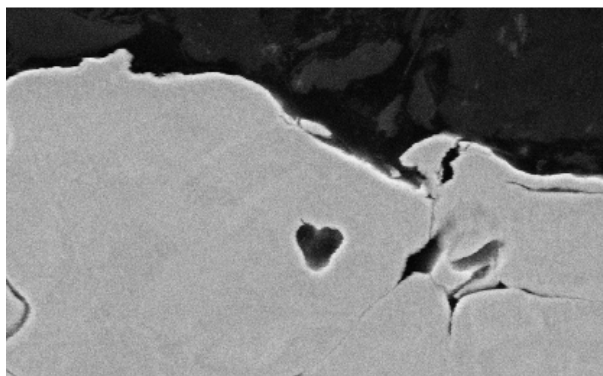
*A ma famille.*

J'ai voulu devenir docteur, comme ma mère. Elle qui pensait que je ne devais ça qu'à mon père.

*Avec le même amour* – Emile Verhaeren



*Et à ceux qui ont mis pied sur le pont mon bateau,  
Qui m'ont donné la force de traverser ces eaux,  
A la vitesse d'un cheval au galop.*



*En 1095 jours, et autant de doutes.*









# T

## ABLE OF CONTENTS

1.	Introduction (English and French)		1
2.	State of the art		8
	2.1.	Industrial context, history of development, fabrication and metallurgy of the Uranus S1N SS	8
	2.1.1.	Context – Electrolyte and materials	8
	2.1.2.	History of the development of the Uranus S1N SS	10
	2.1.3.	Metallurgy – fabrication of how is the Si in the bulk material	12
	2.1.3.1.	Fabrication	12
	2.1.3.2.	Chemical composition	13
	2.2.	The metal-electrolyte interface that pilots the corrosion rate of the material	13
	2.3.	The passive layer and the electrochemical behavior of austenitic stainless steels in acidic media	15
	2.4.	Conclusion	17
3.	Experimentals		19
	3.1.	Materials	19
	3.1.1.	Experimental strategy	19
	3.1.2.	Stainless steels samples	19
	3.2.	Atomic emission spectroelectrochemistry	19
	3.2.1.	Experimental strategy	19
	3.2.2.	Experimental device	20
	3.3.	Combining <i>in situ</i> and <i>ex situ</i> analysis	22
	3.3.1.	200 mL reactor electrochemistry measurements	23
	3.3.2.	Optical microscopy and scanning electron microscopy	23
	3.3.3.	X-ray photoelectron spectroscopy	24
	3.3.4.	Transmission electron microscopy and energy dispersive X-ray spectroscopy	25

4.	Results	26
	4.1. Silicon enrichment of an austenitic stainless steel – impact on electrochemical behavior in concentrated nitric acid with oxidizing ions	26
	4.1.3. Introduction, the flaws in the literature	26
	4.1.4. Experimental strategy	27
	4.1.5. Main results	28
	4.1.6. Conclusion	35
	4.1.7. Publication to be submitted	36
	4.2. A direct measurement of the activation potential of stainless steels in nitric acid	60
	4.2.3. Introduction to the activation potential	60
	4.2.4. Experimental strategy	60
	4.2.5. Main results	63
	4.2.6. Conclusion	64
	4.2.7. Publication	70
	4.3. Dissolution and passivation of a silicon-rich austenitic stainless steel during active-passive cycles in sulfuric and nitric acid	78
	4.3.3. Kinetics parameters determination and stoichiometry identification	78
	4.3.4. Main results	81
	4.3.5. Conclusion	90
	4.3.6. Publication	92
	4.4. The kinetics of transpassive dissolution chemistry of stainless steels in nitric acid: The impact of Si	128
	4.4.3. On the origin of the intergranular attack	128
	4.4.4. In situ study of the transpassive dissolution	128
	4.4.5. Main results	131
	4.4.6. Conclusion	137
	4.4.7. Publication	138
5.	Conclusion (English and French)	182

6.	Symbols	187
7.	References	188
Annexe. Unachieved experiments		
	1. Impact of an argon flow in the electrolyte on the corrosion potential of the 304L and the Uranus S1N SS	
	1.1. Experimentals	
	1.2. Results and discussion	
	1.3. Perspectives	
	2. Ratio of the reduction current density between the two SS in 4 mol dm <sup>-3</sup> HNO <sub>3</sub> at 100°C	
	2.1. Experimentals	
	2.2. Results and discussion	
	2.3. Perspectives	
	3. Electrochemical microscopy: determining the reduction mechanisms and characterization of the passive layer's conductivity	
	3.1. Feedback mode	
	3.2. Generator-collector mode	
	4. Why is the selective dissolution invisible during active-passive cycles in HNO <sub>3</sub> ?	
	4.1. A quick reminder of the results	
	4.2. Is the AESEC technique sensitive enough?	
	4.3. Perspectives	
	5. AESEC transpassive measurements versus SCIANS model	
	5.1. Results	
	5.2. Conclusions	
	6. References of the unachieved experiments section	

# INTRODUCTION

*I shall be telling this with a sigh  
Somewhere ages and ages hence:  
Two roads diverged in a wood, and I,  
I took the one less traveled by,  
And that has made all the difference.*

***Robert Frost***

*Quand j'étais jeune et fier et que j'ouvrais mes ailes,  
Les ailes de mon âme à tous les vents des mers,  
Les voiles emportaient ma pensée avec elles,  
Et mes rêves flottaient sur tous les flots amers.*

***Alphonse de Lamartine***



# I NTRODUCTION (EN)

1. Yves Bréchet [1] used to say that corrosion is the evil conscience of metallurgists,

... a price to pay for this free electron gas ensuring metallic cohesion and attractive properties of materials. Too often metallurgists and corrosionists have been ignoring each other. The first ones see corrosion as a wound asking for a remedy provided *a posteriori* or for an *a priori* foresight. The second ones are convinced that everything is said of an alloy as soon as its composition is known, and everything is said of its corrosion resistance as soon as the environment is identified. The idea that corrosion of a certain material in a given environment couldn't be approached by a single point of view has motivated deeply the present work.

This thesis work investigated the corrosion behavior of the Uranus S1N stainless steel (SS), an austenitic SS that was enriched in silicon (4 wt. %). The Si enrichment has proven to provide a satisfying resistance to corrosion in hot and concentrated nitric acid,  $\text{HNO}_3$ , containing oxidizing species. In this case, these species come from the recycling process of the nuclear spent fuel. This process enables an optimized use of nuclear energy resources, and provides a way to reuse up to 96% of the spent fuel. In France, it results from the recycling process of nuclear fuel an important saving of the natural uranium resources. Furthermore, it enables to extract the ultimate wastes that can be then glazed and stored in a limited volume and controlled radiotoxicity. One of the first steps of the process consists in the immersion of the fuel assembly (preliminarily sheared) in concentrated nearly boiling  $\text{HNO}_3$ . The fuel assembly dissolves, releasing in solution many species such as uranium, plutonium, minor actinides, and fission products. These species enhance the oxidizing character of  $\text{HNO}_3$ , which is already an oxidizing agent, as the nitrogenous species it contains may already reduce at high potentials.

With the Si enrichment, the Uranus S1N SS revealed to be a good candidate for such environment [2]. Firstly, when oxidizing species are added to the environment, its corrosion rate is lower than for the 304L SS, which is a very similar alloy but without Si [3, 4]. Secondly, even when conditions are so oxidizing that the passivity of the steel breaks down and the material enters in its “transpassive domain”, the Uranus S1N SS’s surface remains homogeneously dissolved, while the 304L SS displays a localized attack of the surface at grain boundaries called intergranular corrosion [4-10]. On the other hand, the Uranus S1N SS dissolves at higher rates than the 304L when the environment is less oxidizing, for example in pure  $\text{HNO}_3$  [11-13]. This paradox, among others that will be discussed later, motivated further investigations on the role of Si in the corrosion resistance properties of the Uranus S1N in hot and concentrated  $\text{HNO}_3$  containing oxidizing species.

The dissolution rate of stainless steels is drastically lowered thanks to a particular oxide interface spontaneously created at the surface, called the passive layer. Investigating this interface is therefore a crucial aspect for the material lifetime forecasting. In the case of the Uranus S1N SS, the Si revealed to be present in high concentration in the passive layer [4, 6]. It is therefore natural to examine how Si at the interface between the alloy and the environment impacts its resistance to corrosion. Four main issues arise from it:

1. How can Si preserve the SS passivity, even in very oxidizing conditions? In particular, the impact of Si on the reduction reaction –mechanisms and kinetics- and on the oxidation reaction will be identified.
2. How does Si influence the stability of the passive layer (thermodynamics)? More precisely, how does Si modify the required energy for the formation of the passive layer?
3. Are the kinetics of passive layer formation impacted by the presence of Si?

4. Does Si play a role during the passive-transpassive transition when the potential is elevated (corresponding to very oxidizing conditions)?

To explore these four issues, the comparison with the 304L SS was used, as it presents a similar composition to the Uranus S1N SS but with a low concentration in Si (0.3 wt. %). Electrochemistry tools were mainly used to measure *in situ* the characteristics of the metal-electrolyte interface. Electrochemistry, as an interdisciplinary science that describes chemical transformations involving electronic transfers, was complemented by classical metallurgists' means such as *ex situ* surface analysis. Another particularity of the present work was the use of a chemical analysis of the electrolyte online with the electrochemistry measurement, enabling the simultaneous measurement of both electrical and quantitative chemical analysis.

Four publishing projects were made out of this multiscale and multidisciplinary approach. Therefore, a particular format of dissertation was chosen. Firstly, a state of the art will bring the reader from the industrial context to the interest found in the study of the passive layer. An experimental section will help the reader understanding the four chapters that will follow. Each chapter will be introduced by several paragraphs explaining the flaws in the state of the art and/or the calculations and methods and the experimental strategy the chapter is based on. Results will be synthetized and conclusions given, then the associated publication project containing the exhaustive results will state in its latest version, either published or ready to be submitted. One of the goals of this presentation format was to highlight both the academic dimension of the present work and the industrial interest. Aiming also at this last purpose, unachieved experiments will be discussed in a separate final part, in order to raise further questions and perspectives related to the four main issues of the thesis. Eventually, the reader will eventually find conclusions and general perspectives at the end of this dissertation.



# **I**NTRODUCTION (FR)

**1. « La corrosion est la mauvaise conscience du métallurgiste, le prix à payer pour ce gaz d'électrons libres qui assure la cohésion métallique et les propriétés attractives des métaux. [...] Trop souvent les métallurgistes et les corrosionnistes s'ignorent mutuellement.**

Les uns considèrent la corrosion comme une plaie qui demande certes un remède, mais un remède que l'on apporte *a posteriori* ou une méfiance *a priori*. Les autres sont persuadés que l'on a tout dit d'un alliage quand on a donné sa composition et de sa tenue à la corrosion quand on a spécifié le milieu. », Yves Bréchet [1]. L'idée que l'on ne pouvait appréhender la corrosion d'un matériau dans un milieu donné par un unique point de vue fût un véritable moteur du présent travail de thèse.

Ces travaux se sont intéressés au comportement en corrosion d'un acier austénitique inoxydable enrichi en silicium (3,5 % m.), l'acier Uranus S1N. Cet enrichissement est à l'origine d'une tenue en corrosion satisfaisante de l'acier dans un milieu auquel il est destiné, l'acide nitrique chaud et concentré contenant des espèces oxydantes, que l'on retrouve notamment au cours du procédé de traitement-recyclage du combustible nucléaire usé.

Le traitement-recyclage du combustible nucléaire usé permet de tendre vers une production optimisée (en termes de ressources) de l'énergie nucléaire, et offre la possibilité de récupérer et de réutiliser jusqu'à 96 % du combustible usé. L'ensemble des procédés du traitement-recyclage du combustible nucléaire usé aboutit ainsi, en France, à une économie annuelle importante des ressources naturelles en uranium. Par ailleurs, les déchets ultimes issus de ces procédés sont vitrifiés et stockés dans un volume limité, avec une radiotoxicité maîtrisée. Une des premières étapes de ce traitement-recyclage consiste à plonger les assemblages de combustible cisailés dans une solution d'acide nitrique concentré à une température proche de l'ébullition. Au cours de cette dissolution, de nombreuses espèces

issues du combustible à recycler (uranium, plutonium, actinides mineurs, produits de fission) vont se trouver en solution sous forme ionique. Si l'acide nitrique est à lui seul un oxydant, c'est-à-dire contenant des espèces azotées capables de se réduire à des potentiels élevés, la présence de ces ions métalliques peut encore augmenter son pouvoir oxydant. Or l'enrichissement en Si dont a bénéficié l'acier Uranus S1N fait de lui un candidat satisfaisant pour les installations contenant ce type d'électrolyte [2]. D'une part, en présence d'espèces oxydantes, il présente une vitesse de corrosion plus faible qu'un alliage homologue sans Si tel que l'acier 304L (également utilisé pour les installations de traitement recyclage du combustible usé) [3, 4]. D'autre part, même lorsqu'il est soumis à un électrolyte si oxydant qu'il se trouve porté dans son domaine transpassif, sa corrosion demeure généralisée à l'ensemble de la surface, et l'on observe aucune attaque localisée de type intergranulaire contrairement à l'acier 304L [4-10]. Parallèlement à ces propriétés, l'acier Uranus S1N se dissout plus rapidement que son homologue sans Si dans des conditions moins oxydantes, comme en acide nitrique seul par exemple [11-13]. Ce paradoxe (et d'autres motivations non détaillées ici) a donc conduit à la nécessité d'apporter de nouveaux éléments de compréhension sur le rôle du Si dans les propriétés de tenue en corrosion de l'acier Uranus S1N en milieu acide nitrique chaud et concentré et en présence d'ions oxydants. C'est l'objectif principal de ce travail de thèse.

C'est grâce à une interface d'oxydes particulière spontanément présente à la surface d'un acier inoxydable, la couche passive, que la vitesse de corrosion de ce dernier est ralentie. La connaissance de cette interface est donc d'intérêt pour mieux appréhender la durée de vie du matériau du point de vue de la corrosion. En outre, le Si de l'acier Uranus S1N se trouve être présent dans cette couche passive en grande quantité [4, 6]. On peut donc légitimement s'interroger sur la manière dont ce Si présent dans les oxydes peut ou non impacter le phénomène de passivité. Dans ce travail, cette interrogation a été traitée sous différents angles

au travers de quatre questions majeures qui ont structuré ce travail de thèse. Ces quatre questions ont permis de balayer l'ensemble des composantes de la corrosion pouvant être affectées par la couche passive, de la cinétique de réduction du milieu à l'interface métal-électrolyte au mécanisme de rupture de passivité à haut potentiel (transpassif), en passant par une détermination des caractéristiques thermodynamiques et cinétiques de cette interface :

5. Comment le Si préserve-t-il la passivité de l'acier en conditions oxydantes sévères ?

En effet, comme discuté plus haut, il apparaît important de pouvoir comprendre pourquoi l'acier Uranus S1N reste passif en milieu acide nitrique contenant des ions oxydants, alors que d'autres aciers (comme l'acier 304L) vont perdre cette passivité en étant portés dans leur domaine transpassif (avec une corrosion de type intergranulaire). En particulier, c'est l'influence du Si sur les mécanismes et cinétiques de réduction et d'oxydation qui est analysée à travers ce premier volet.

6. Le Si modifie-t-il la formation de la couche passive sur le plan thermodynamique ?

En étudiant notamment si le Si modifie l'énergie (au travers du potentiel électrochimique) nécessaire à la formation de la couche passive.

7. Le Si impacte-t-il la cinétique de formation-dissolution de cette couche passive ?

8. Le Si joue-t-il un rôle dans le mécanisme de la transition passif-transpassif lorsque l'acier est porté à plus haut potentiel ?

La réponse à ces différentes questions s'est principalement reposée sur la comparaison de l'acier Uranus S1N avec l'acier 304L dont la composition est proche mais qui n'est que très faiblement allié au Si (0,3 %m.) et également plus faiblement allié au nickel (10 % m.). Sur le plan des outils, c'est l'électrochimie qui a été choisie comme outil principal d'étude de l'interface *in situ* entre le matériau et son milieu. Science interdisciplinaire décrivant les transformations chimiques de la matière mettant en jeu des échanges d'énergie électrique, elle a été complétée par d'autres outils plus classiquement utilisés en métallurgie permettant

l'analyse chimique et morphologique des surfaces, la plupart du temps *ex situ*. Au cœur de ces travaux, le couplage de la mesure électrochimique à une technique d'analyse chimique élémentaire en ligne a permis d'acquérir *in situ* des informations originales, à la fois électriques et chimiques, sur le comportement de l'interface métal-électrolyte.

A travers cette approche à la fois multi-échelles et pluridisciplinaire, quatre publications ont été réalisées (publications publiée ou à soumettre). Un format de rédaction particulier s'est articulé autour de ces quatre projets. Le texte s'ouvre sur un état de l'art général visant à expliquer les orientations de recherche choisies pour ce travail. Il est suivi d'une partie expérimentale à part entière. Puis, chacun des quatre chapitres est introduit par un état de l'art dédié à l'expérience proposée, une explication de la stratégie expérimentale adoptée, et un résumé de ses résultats et conclusions principaux. Chacun de ces quatre chapitre ayant donné lieu à une publication (trois publiées et une à soumettre), les textes associés sont joints. Le lecteur trouvera à la suite un recueil d'expériences inachevées pouvant éclairer ou soulever de nouvelles questions et perspectives. Enfin, une conclusion et une proposition générale de perspectives seront apportées. A l'image de cette première introduction, une traduction française sera proposée pour la conclusion et perspectives.



# STATE OF THE ART

*A Man may make a Remark—  
In itself—a quiet thing  
That may furnish the Fuse unto a Spark  
In dormant nature—lain—*

*Let us deport—with skill—  
Let us discourse—with care—  
Powder exists in Charcoal—  
Before it exists in Fire.*

*Emily Dickinson*

*Avant donc que d'écrire, apprenez à penser.  
Selon que notre idée est plus ou moins obscure,  
L'expression la suit, ou moins nette, ou plus pure.  
Ce que l'on conçoit bien s'énonce clairement,  
Et les mots pour le dire arrivent aisément.*

*Nicolas Boileau*



# **S** TATE OF THE ART

## **2. From the industrial context to the interest raised into the study of the passive layer**

### **2.1. Industrial context, history of development, fabrication and metallurgy of the Uranus S1N SS**

#### **2.1.1. Context – Electrolyte and materials**

In the present work, an austenitic stainless steel containing low amount of C and enriched in Si was studied. This SS called Uranus S1N was designed for hot and concentrated nitric acid in presence of oxidizing species. This very aggressive electrolyte is used in the recycling process of the nuclear waste, known as PUREX (Plutonium Uranium Refining by Extraction). This process was performed in 1945 and then first exploited in 1958 in Marcoule until 1997. It requires a first step of dissolution in  $\text{HNO}_3$  of the sheared nuclear waste material which contains mostly U, Pu, other actinides and fission products. Then, following a liquid-liquid extraction process, U and Pu are recycled. Over the whole process, the  $\text{HNO}_3$  temperature and concentration vary and lots of different metallic species might elevate its oxidizing character.



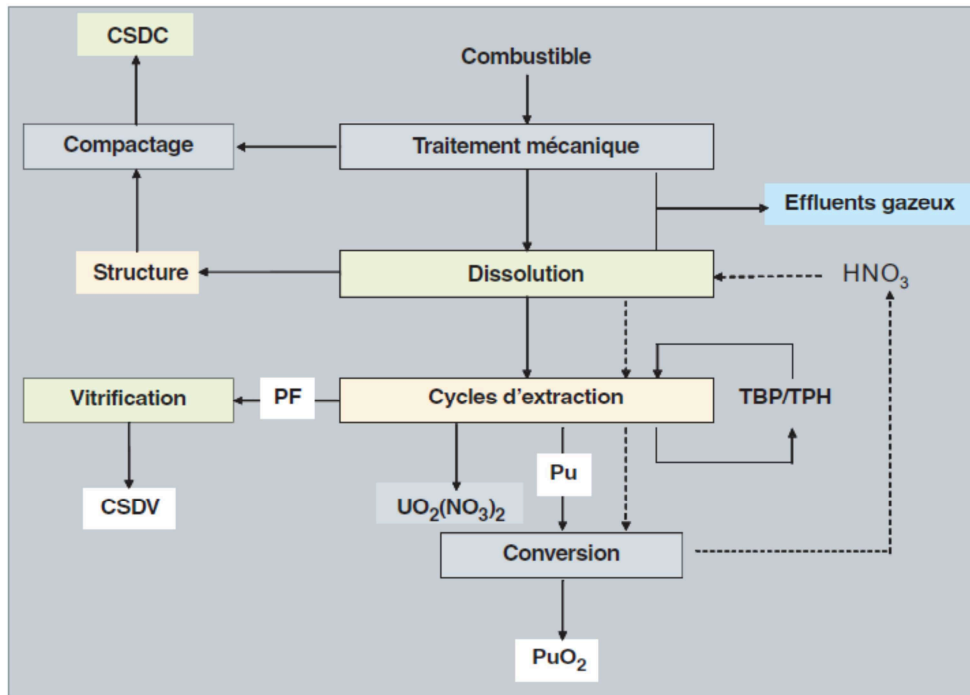


*Fig. 1. PUREX process main steps [14]*

Therefore, different materials can be chosen as good candidates to resist premature ageing of the different parts of the plant regarding their corrosion behavior in the different possible conditions (Fig. 2).

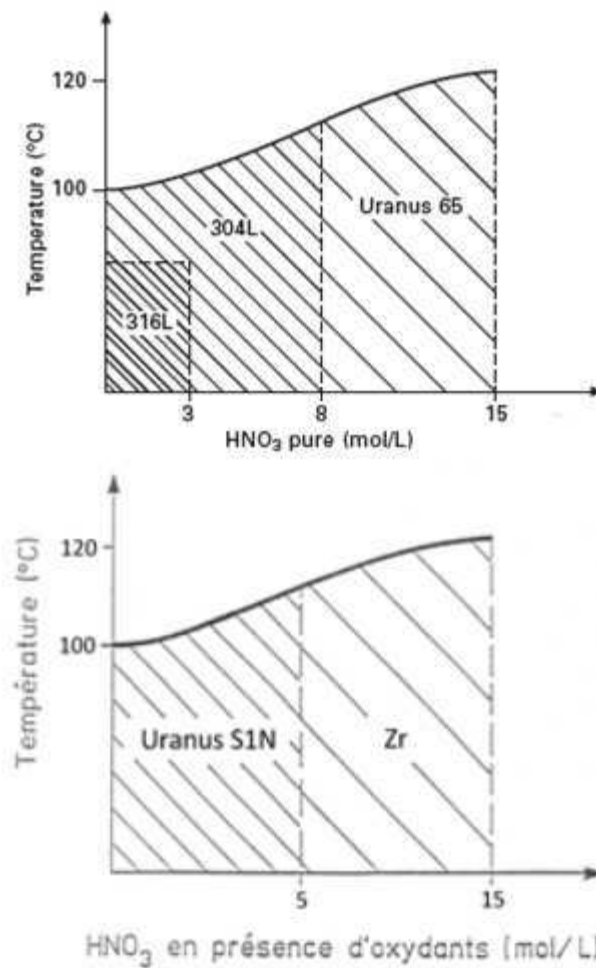


*Fig. 2. Possible materials depending on HNO<sub>3</sub> temperature, concentration, concentration in oxidizing species[2]*

SS containing low C such as AISI 304L, 316L and Uranus 65 are usually chosen for pure HNO<sub>3</sub> containing parts of the the plant, and Uranus S1N SS is especially designed for moderate concentrations in oxidizing species. Zr can also be used for the most aggressive electrolytes under certain circumstances.

### **2.1.2. History of the development of the Uranus S1N SS**

Low C austenitic SS containing Si were developed over the 60s because of the growing concerns about intergranular corrosion phenomenon observed for several materials in certain electrolytes (for example the 304L in the presence of oxidizing species). Numerous studies

can be found on the addition of Si in Fe-Cr-Ni alloys very similar to the 304L or 316L SS. It was shown that for alloys containing more than 16 wt.% in Cr and 14 wt.% in Ni, adding more than 2 wt.% in Si could efficiently prevent from the intergranular attack (IGC) [5, 10, 15]. An important decrease of the mass loss in the presence of Cr(VI) species is also measured as shown in Fig. 3 from Desestret *et al.* [3].

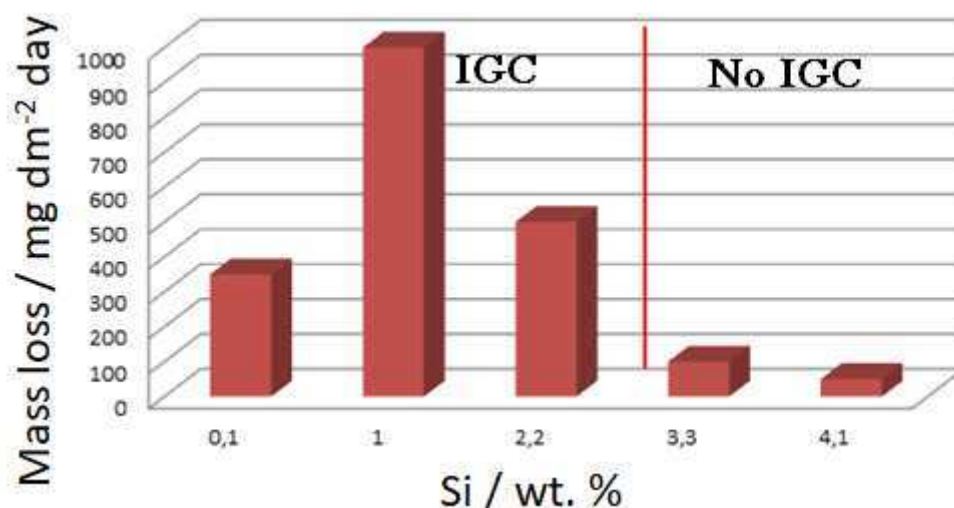
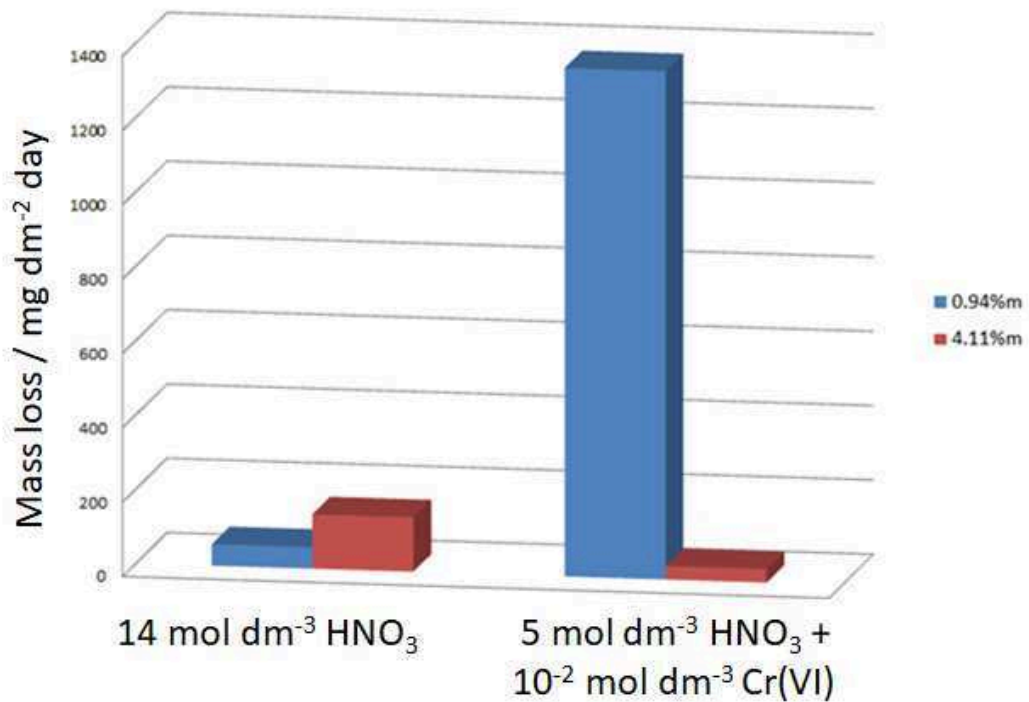


Fig. 3. Influence of the Si content on the mass loss of a 18Cr – 14Ni alloy in boiling  $5 \text{ mol dm}^{-3} \text{ HNO}_3$  containing Cr(VI) ( $2 \cdot 10^{-2} \text{ mol dm}^{-3}$ ) [3]

Similar results were found by Armijo and Holtzer in the 70s [4,16]. Also, Si tends to increase the corrosion rate of the alloy between 0.1 and 1 wt.%. At lower and higher contents, the corrosion rates are found to be very low, especially over 3 wt.%. This tendency could reveal a competition between two contrary effects provided by the Si, one that leads to an increase of the corrosion rate while the other tends to inhibit it.

The relative corrosion rate between two SS that contain respectively 0.94 and 4.11 wt.% varies depending on the presence of oxidizing species. It was shown by Ghiban and Cosmealta [12] that in pure  $\text{HNO}_3$  the Si-rich SS was dissolving at higher rate, as shown in Fig. 4 in  $14 \text{ mol dm}^{-3}$  boiling  $\text{HNO}_3$ . But when Cr(VI) is added, the opposite result is obtained and the low Si SS corrodes faster while displaying a high IGC morphology.



*Fig. 4. Corrosion rates obtained in 14 mol dm<sup>-3</sup> boiling HNO<sub>3</sub> and in 5 mol dm<sup>-3</sup> boiling HNO<sub>3</sub> containing 2.10<sup>-2</sup> mol dm<sup>-3</sup> of Cr(VI) depending on the Si content in an 18Cr-15Ni alloy [12]*

### 2.1.3. Metallurgy – Fabrication and how is the Si in the bulk material

#### 2.1.3.1. Fabrication

The Uranus S1N SS is a vacuum casted material because its composition has to be well controlled especially containing as few C as possible [17]. It is then casted in ingot before annealing and overhardening. It is maintained at a high temperature between 1000 and 1150°C then rapidly cooled to obtain a homogeneous austenitic phase where all the alloying elements, especially C and N, are in solid solution [18]. Carbonitrides are indeed soluble in austenite at high temperatures and this state can be maintained if the cooling is sufficiently rapid. Ferritic phase  $\delta$  can also appear for certain steels at higher temperatures than 1100°C and this phase can be preserved over the cooling, which could be a problem because of  $\sigma$  phase precipitation it would be responsible for. Therefore, an upper limit of temperature was

introduced for the annealing. The duration of heating is about 0.7 to 2.5 minutes per mm. The longer the heating, the lower the residual constraints, and short heating durations limit the growth of the grains [19].

#### **2.1.3.2. Chemical composition**

As Si content was fixed, then the other elements concentrations had to be adjusted. Si is an alpha stabilizing element like Cr. Therefore, the Ni concentration must be elevated in order to promote austenite  $\gamma$ . Ni also facilitates the plastic deformation [20]. Uranus S1N C content is maintained low ( $C < 0,015$  wt. %) and it also contains few Nb. Nb prevents from local carburization or nitrocarburization of Cr, known to promote IGC. In the 70s, few adjustments of the chemical formulation of the Uranus S1N were made, for example, Al was added to stabilize N [21]. Nb could also stabilize N at higher concentration, but the weldability would then have been affected.

### **2.2. The metal-electrolyte interface that pilots the corrosion rate of the material**

In order to understand the phenomena involved in the corrosion of the Uranus S1N SS, and especially to understand the impact of Si, the present work was specifically dedicated to the interface between the metal and the electrolyte. The Uranus S1N SS displays a typical oxide layer called passive layer that spontaneously covers its surface when immersed into an oxidizing electrolyte such as hot and concentrated  $\text{HNO}_3$ .

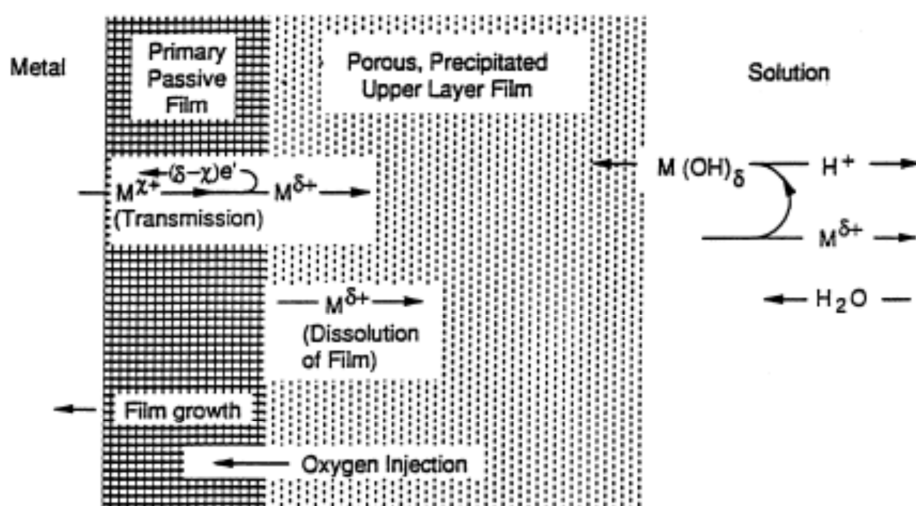


*Fig. 5. Schematic processes involved in the formation of a passive film at a metallic interface [22]*

Usually, passive layers of austenitic SS formed in  $\text{HNO}_3$  are nanometric layers composed by several alloying elements from the bulk material [22-24]. These oxides are organized in several layers as shown in Fig. 5 [22, 25, 26]. They ensure a protection for the SS against dissolution in the acidic medium [27-31]. Their chemical composition can be different from the bulk composition, because a selective dissolution occurs between the alloying elements [32-34]. In particular, for austenitic SS, Cr dissolution happens to be slower than Fe, and therefore a Cr rich oxide layer is established at the surface.

It was also shown that Si occupies an important place in the Uranus S1N oxide layer, as more than 30 at.% can be detected [6]. As indicated previously, this could be the result of a slower dissolution of Si versus Fe. However, this selectivity has never been clearly shown.

If the oxide layer enables to lower the dissolution rate of the material, it also may impact the cathodic reaction occurring simultaneously. This reaction needs indeed as much electron quantity as it is required for the oxidation to occur, and these electrons are provided nearby the metal electrolyte interface. The composition and structure of the passive layer therefore

can play a significant role on the mechanisms and kinetics of the reduction reaction. Based on this assumption, a large amount of studies have tried to elucidate the mechanisms involved in the  $\text{HNO}_3$  electrolyte reduction reactions on inert materials then at passive interfaces [35-40].

As the oxide layer might play such an important role both concerning cathodic anodic reactions, the great amount of Si in the Uranus S1N oxide layer naturally orientated the present work experimental strategy to a comparison with the 304L SS which composition is very similar but contains only 0.3 wt.% in Si. The general corrosion behavior of the 304L has been largely studied over the past decades [4-6, 9, 41-44] and sometimes compared to Si rich similar alloys [6]. One can notice that the Uranus S1N SS contains also more Ni (15 wt.% for the Uranus S1N whereas the 304L contains only around 10 wt.%). However, this element is never detected in the passive layer. According to the literature it is expected to be rapidly oxidized under a soluble form [45]. Moreover, the ratios between each elements are very comparable between the two stainless steels. A hypothesis will be thus made that the Ni will not impact drastically the corrosion behavior of the steel between the two compositions. The measured composition of the materials used in the present work will be detailed in the experimental section.

### **2.3. The passive layer and the electrochemical behavior of austenitic stainless steels in acidic media**

As previously mentioned, the passive layer is responsible for a limitation of the oxidation current density. On the anodic branch of a I-E curve of an austenitic SS in acidic medium, three domains of potential can be characterized, where the oxidation current density varies with the stability of the passive layer. This passive layer is almost inexistant in the active domain at low potentials, then starts to cover the surface and provides its protective property

in the passive domain, and eventually loses its stability when entering the transpassive domain at high potentials (Fig. 6). The electrochemical domain in which the material will remain is determined by equilibrium of electron exchanged between the cathodic and the anodic reactions. The nature of the cathodic process and its oxidizing character (that can be evaluated from its own equilibrium potential) is a determining factor for the passivity of the alloy. The cathodic process happening on the vicinity of the surface (at the surface or close), the passive layer has therefore a direct impact on the cathodic reaction. This reinforces the interlinked relationship between the cathodic and the anodic reaction and highlights the need for a better knowledge of the Si-rich passive layer.

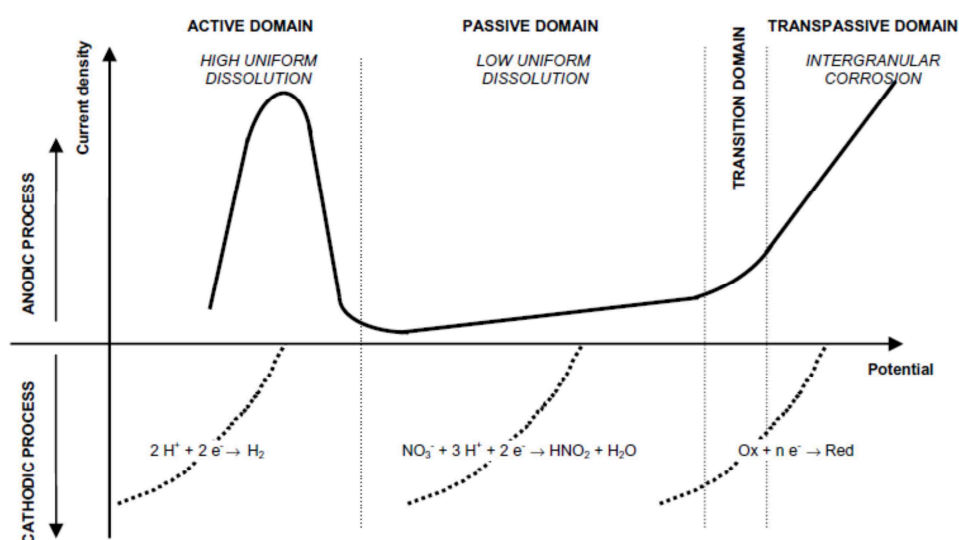


Fig. 6. Typical SS Evans diagram in different acidic electrolytes [2]

Because the cathodic and the anodic reactions are so connected, the present work will open on a general study of the impact of Si on the anodic and cathodic current densities from polarization curves in various  $\text{HNO}_3$  electrolytes, containing or not oxidizing species. This will enable to highlight the impact of the Si on the cathodic reaction (mechanism and kinetics) especially when oxidizing species will be added. It will also show how the passivity is



affected by the Si alloying. Then, to access thermodynamic and kinetic properties of the passive layer, the use of transitions between the three domains of potential will be used. For example, the passive-active transition will enable to access some thermodynamic properties of the oxide, and successive polarizations between these two domains will provide more information on the kinetics of formation of the oxide layer, for the first time *in situ* in  $\text{HNO}_3$ . The transpassive domain will be naturally chosen to study the inhibition of the intergranular corrosion, and the transients between passive and transpassive will help highlighting possible selective dissolution effects.

## **2.4. Conclusion**

The Uranus S1N was initially formulated for a specific use in hot and concentrated  $\text{HNO}_3$  in presence of oxidizing species; however the explanation on the origin of its satisfying behavior has never been clearly and completely elucidated.

The Si alloying indeed increases the dissolution rate of the steel in pure  $\text{HNO}_3$ , but when oxidizing species are added, it plays a more positive role, because the steel corrodes at lower rates than a regular 304L SS would do. The most probably hypothesis to explain this paradox is that the reduction reaction is kinetically lowered at the Si-rich surface, while the oxidation kinetics are on the otherside increased, and therefore the corrosion potential would remain passive even in highly oxidizing electrolytes. However, this was actually never clearly shown. Therefore, the first chapter of the present work will focus on elucidating the impact of Si on the electrochemical behavior of austenitic SS in pure  $\text{HNO}_3$  and containing oxidizing species. Both cathodic and anodic processes will be investigated through the use of polarization curves.

Furthermore, the passive layer of the Uranus S1N has barely been studied. It is only known to be a Si-rich oxide, probably made of mixed oxide silicates whose thickness and exact composition have never been determined. The second and third chapters of the thesis will focus on providing new insights in the properties of this passive layer, giving both thermodynamic and kinetic new information on the properties of the oxide layer.

Eventually, the transpassive dissolution of the Uranus S1N SS will be investigated. The inhibition of the IGC, while frequently observed in the literature, has found no clear explanation and limited number of hypothesis. Therefore, the last chapter of this present work will aim at providing new elements and hypothesis to explain what is observed in this region of potential when the electrolyte becomes sufficiently oxidizing.



# EXPERIMENTALS

*Up in the air and over the wall,  
Till I can see so wide,  
River and trees and cattle and all  
Over the countryside —  
Robert Louis Stevenson*

*Voulez-vous que verté vous dire ?  
Il n'est jouer qu'en maladie,  
Lettre vraie qu'en tragédie,  
Lâche homme que chevalereux,  
Orrible son que mélodie,  
Ne bien conseillé qu'amoureux.  
François Villon*



# EXPERIMENTALS

## 3. From hypothesis to proof

### 3.1. Materials

#### 3.1.1. Experimental strategy

As mentioned earlier, a similar stainless steel as the Uranus S1N but without Si was chosen to compare, the 304L SS. Even if the 304L SS contains less Ni, ratios between each element are really comparable between the two SS. Moreover, the literature about the 304L SS is sufficiently large.

#### 3.1.2. Stainless steels samples

Uranus S1N samples were prepared from a 35mm thick plate (moulding n° 12723) annealed at 1135°C. 304L samples were prepared from a 10mm thick plate (moulding n°372048) annealed between 1000 and 1100°C. Table 1 provides chemical compositions of the two materials used, determined at the beginning of the thesis using glowing discharge optical emission spectroscopy (GD OES).

*Table 1. Mass composition of the Uranus S1N and 304L SS determined using GD-OES between 10 and 40μm depth (wt.%)*

	Fe	Cr	Ni	Si	Mn	Add.
Uranus S1N	59,8	18,8	15,1	3,5	2,0	0,8
304L	70,3	17,8	9,5	0,3	1,5	0,6

## 3.2. Atomic emission spectroelectrochemistry

### 3.2.1. Experimental strategy

The study of the Uranus S1N SS passivity exploited the characterization of the three

domains of potentials that are the active, passive and transpassive states. An interesting method to investigate these three domains was to couple the electrochemical classical measurement to an online elementary analysis such as atomic emission spectroscopy using an induced coupled plasma (ICP-AES). Coupling both techniques was motivated by the following assertions. First, the conventional electrochemical methods only measure currents and potentials from the redox system :

- Anodic and cathodic current densities can't be distinguished nearby the corrosion potential

It is very difficult to distinguish the anodic current that will be involved in the passive layer formation from the part involved in the dissolution of the material

Second, gravimetric measurements of the mass loss occurring over a potentiostatic or galvanostatic measurement could be of interest to separate the anodic from the cathodic contribution, however it is limited to a global mass loss and doesn't give access to any information upon the selectivity of the dissolution that occurs. To solve such problem, one could possibly analyze the solutions and analyze the passive layer formed by surface investigation means, however these informations are both ex situ and punctual, not giving any information on the kinetics for example.

### **3.2.2. Experimental device**

In the early 90s, Ogle et al. developed the Atomic emission spectroelectrochemistry (AESEC) [46]. They achieved coupling an ICP-AES to the electrochemical measurement as shown in Fig. 7 [47].

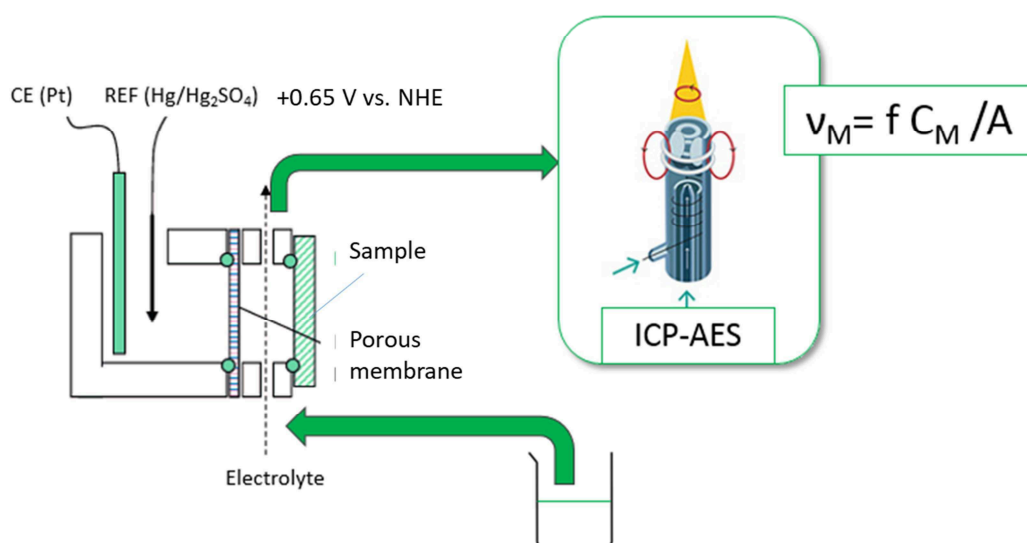


Fig. 7. Experimental AESEC device with  $v_M$ : dissolution rate of  $M$ ,  $f$ : flow rate,  $C_M$ :

concentration in  $M$ ,  $A$ : surface of the sample

The elemental analysis of the dissolved species is real time coupled to the electrochemical measurements that enables to :

- Distinguish anodic from cathodic current contribution,
- Distinguish current contribution to the passive layer formation from contribution to the dissolution
- Determine the possible selectivity of the dissolution

The electrolyte is brought from a reserve to the ICP-AES using a peristaltic pump whose rotation speed and capillaries diameter control the flow rate. The electrolyte in contact with the sample (working electrode) must be carefully controlled in terms of flow rate and volume. Therefore, the WE is in contact with a small volume of electrolyte separated from the rest of the cell by a porous membrane. In the biggest part of the cell can be set the counter and the reference electrodes that are respectively a small Pt grid and a small mercurous sulfate electrode. The smallest compartment has a volume of  $0,2 \text{ cm}^3$  and the surface of the electrode



in contact with the solution is 1 cm<sup>2</sup>. the sealing between the sample and the flow cell is ensured by a pneumatic compression. Toric joint prevents from leakage. The electrolyte is nebulized in a chamber before accessing the plasma where it is analyzed by two optical captors, one that is an adjustable monochromator and the other one which is a polychromator. The nebulizer and the chamber are chosen to minimize the residence time to enable the simultaneous measurements from both electrochemical and elemental analyses.

The data acquisition system is slightly modified from a regular ICP-AES data acquisition system, in order to collect on-line data from the potentiostat, and also get rid as much as possible of the hydrodynamics of the ICP device. However, when necessary, an additional mathematic correction of the hydrodynamics of the device will be performed. Detailed calculation will be explained later on. The whole acquisition system enables to measure on the same time scale the electrochemical measurements and the elemental analysis from the ICP. Each alloying element can be measured independently using the polychromator and the ICP-AES signal, after a classical standard calibration for each element of interest, can be translated into a dissolution rate  $v_M$  knowing the flow rate  $f$ , and surface of the sample. The experiments were realized with the electrochemical flow cell using plane SS samples as working electrodes. Average flow rate was 2.9 mL dm<sup>-3</sup> and was carefully measured after each experiment. The porous membrane was made of cellulose, and the electrolyte and sample could be heated from a water bath and heating copper block pressed on the sample but electrically isolated.

### 3.3. Combining *in situ* and *ex situ* analysis

To understand better the *in situ* results obtained with electrochemistry or AESEC, some *ex situ* surface analyses were performed.

### 3.3.1. 200 mL reactor electrochemistry measurements

For basic electrochemistry, a double jacketted reactor of 200 mL was used. In this reactor were put three electrodes. The working electrode was made of a bullet shape sample of the steel to be studied, a Pt grid was used as the counter electrode, and a mercurous sulfate electrode was used as a reference (+0.65 V vs. NHE) (Fig. 8).

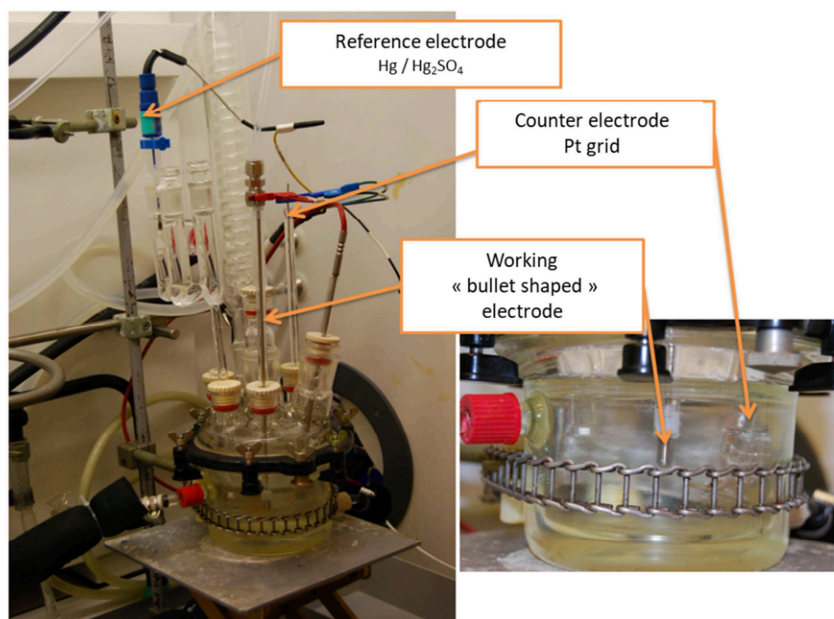


*Fig. 8. Picture of the experimental set-up for electrochemical measurements used in the first chapter*

The double jacketted reactor is heated by a thermostat using oil at 100°C. A VSP Potentiostat (BioLogic®) was dedicated to these experiments.

### 3.3.2. Optical microscopy and scanning electron microscopy

Optical and scanning electron microscopies enabled to observe the corrosion morphology of the samples, especially the intergranular attack that could occur in the transpassive domain of the steels. Observations were performed using a reverse optical microscope (Olympus GX51). Two scanning electron microscopes were used: SEM-Leo (Leo 1450 VP Zeiss) and SEM-FEG (Ultra 55 Zeiss).

### 3.3.3. X-ray photoelectron spectroscopy

X-ray photoelectron spectroscopy (XPS) is a well known technique associated to the study of the passive layers. In the present work, it has been largely used to analyze the chemical composition of the oxides in various types of conditions. Moreover, the XPS measurements give precious information about the close environment of the excited atoms. It enabled to confirm that the high content in Si in the oxide layer was or not associated to mixed silicates rather than pure SiO<sub>2</sub> for example [14]. The XPS measurements were performed using a Thermofisher Escalab 250 XI spectroscope, using a monochromatic X-ray source Al-K $\alpha$  (1486.6 eV). The instrument was calibrated in energy with the Ag Fermi level (0 eV) and the 3d<sup>5/2</sup> core level of metallic silver (368.3 eV). The C-1s signal was used to correct a possible charge effect: the CC/ CH contribution of C-1s spectra was fixed at 285.0 eV. The analysis zone consisted of a 900  $\mu$ m diameter spot. The data processing was performed using the commercially available *Avantage*<sup>TM</sup> software. For the fitting procedure, a Shirley background has been used and Lorentzian-Gaussian (L/G) ratio was fixed at 30 %. Main parameters used to decompose XPS spectra are presented in Table 2.

*Table 2. Parameters used for the deconvolution of XPS spectra (Avantage<sup>TM</sup> software)*

*Binding energies and full width at half maximum (FWHM)*

	[ Fe Ox ] / at. %		[ Cr Ox ] / at. %			[ Si Ox ] / at. %	
	Fe - 2p <sub>3/2</sub>	Fe - 2p <sub>3/2</sub>	Cr - 2p <sub>3/2</sub>	Cr - 2p <sub>3/2</sub>	Cr - 2p <sub>3/2</sub>	Si - 2p	Si - 2p
Binding energy / eV	709.69	712.07	576.26	577.32	578.99	102.05	102.65
FWHM / eV	2.36	2.93	1.08	1.92	1.71	1.36	1.32

### 3.3.4. Transmission electron microscopy and energy dispersive X-ray spectroscopy

Cross-sections of materials were analyzed using transmission electron microscopy (TEM) in high resolution imaging mode. In order to identify zones of interest on each sample, electron backscattered diffraction (EBSD) was performed at the surface of the materials prior to sample cross-section elaboration, using a scanning electron microscope field emission gun ZEISS Gemini 500 scanning electron microscope (SEM), a *Hikari Super* charge coupled device (CCD) camera, and OIM<sup>TM</sup> Data collection and OIM<sup>TM</sup> Analysis software for the acquisition and exploitation of the data. Cross-section TEM lamellas were thinned using focused ion beam (FIB) FEI Strata DB400 and analyzed with a FEI Tecnai Osiris TEM using a an accelerating voltage of 200 kV and equipped with ChemiSTEM<sup>TM</sup> and GIF Quantum® detectors X-ray energy dispersive spectroscopy (X-EDS).

One key point of the experimental strategy of the present work was therefore to associate *in situ* and *ex situ* results combined to the comparison between the two stainless steels whose Si content is different, and take advantage of the whole electrochemical anodic branch to investigate the impact of Si on the corrosion behavior of the Uranus S1N SS.

#### Note to the reader

The major parts of the experiments was actually performed by the student. AESEC and classical electrochemistry were directly performed by the student, and XPS and TEM-EDX were respectively performed in narrow collaboration with Frédéric Miserque (CEA/DEN/DANS/ DPC/SCCME/LECA) and Karine Rousseau (*Serma Technologies*). TEM-EDX analyses of the 304L SS in the transpassive domain had been performed by Karine Rousseau during the PhD thesis of Elsa Tcharkhtchi [33].



# RESULTS

*If it is true, what the Prophets write,  
That the heathen gods are all stocks and stones,  
Shall we, for the sake of being polite,  
Feed them with the juice of our marrow-bones?*

**William Blake**

*La lumière, le Temps, l'Espace, l'Énergie  
Furent jadis des dieux de la mythologie :  
La Physique a la sienne et nous les a ravis  
Sous l'autorité de sa Muse rigoureuse.  
Notre vie en est-elle ou moins ou plus heureuse,  
À ton avis?*

**Jacques Réda**



## **4.1. Silicon enrichment of an austenitic stainless steel – impact on electrochemical behavior in concentrated nitric acid with oxidizing ions**

### **4.1.1. Introduction, the flaws in the literature**

As it was shown in the State of the Art chapter, literature counts numerous studies about SS with or without Si alloying in various electrolytes. However, these studies are difficult to compare as the conditions are sometimes very different in temperatures, concentrations, etc. It also reveals some paradoxes. For example, the relationship between the spontaneous corrosion rate and the state of dissolution the steel is actually involved in (passive or transpassive) is not always clear. Armijo *et al.* [4] have shown that a Si-rich austenitic SS in presence of certain oxidizing species could remain passive while the Si-low SS was transpassivated. They formulated the hypothesis that the decrease of the reduction kinetics at the Si-rich interface was responsible for this phenomenon. It was also measured by Robin *et al.* [6] that the passive current density of the Uranus S1N was more intense than for the 304L SS in the same conditions.

Moreover, the most studied oxidizing species in the state of the art was Cr(VI). However, it was shown by Plante that Cr(VI) altered the anodic branch of the Si-rich SS [48], which complicates the interpretation of the results as long as the oxidizing species is not a simple oxidant species. (Fig. 9).



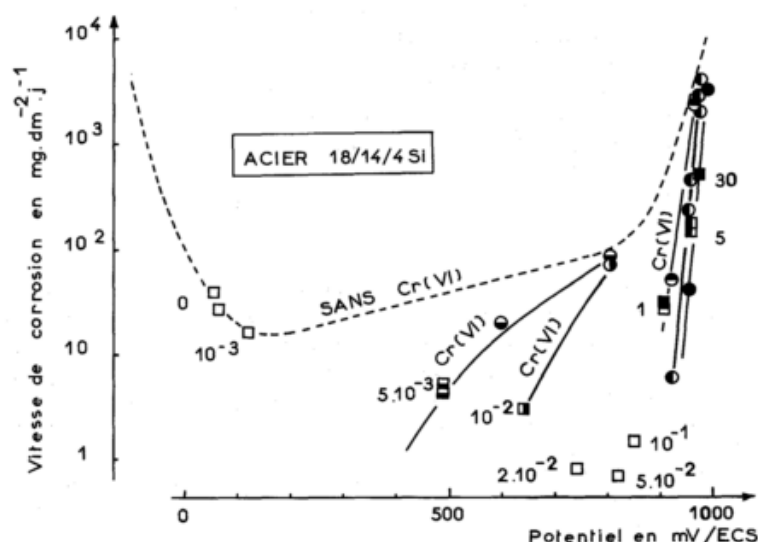


Fig. 9. Corrosion rate of a Si-rich SS as a function of potential in boiling  $5 \text{ mol dm}^{-3}$   $\text{HNO}_3$  with different concentrations in Cr (VI) (Plante [48]).

■ : at equilibrium / ● : potentiostatic measurement / --- : polarization curve without Cr

Because of the decrease that Cr(VI) provokes on the oxidation current of the Si-rich SS, the Si-rich SS even corrodes at a lower rate in the presence of Cr(VI) than in pure  $\text{HNO}_3$  and obviously at a lower rate than the 304L SS. In fact, two phenomena are actually observed: one is the transpassive dissolution of the 304L triggered by the oxidizing character of the Cr(VI) that the Si-rich SS doesn't suffer from because of kinetically lowered reduction reaction, and the second one is the improved passivity of the Si-rich SS because of the Cr(VI).

#### 4.1.2. Experimental strategy

To distinguish these two phenomena, different oxidizing species were chosen. Three different electrolytes were then used: pure  $\text{HNO}_3$ ,  $\text{HNO}_3$  containing V(V),  $\text{HNO}_3$  containing Cr(VI). This first chapter aimed at bringing an overall sight of the impact of Si on the electrochemical behavior of SS in conditions close to the industrial electrolyte.

V(V) was chosen for its stability at 100°C under its fifth oxidation state, and for it can be assimilated to a pure oxidant that doesn't alter the passivity [35]. Historically, V(V) was also used to simulate Np species that can be found in the real conditions but that are more delicate to use because of their radioactivity.

As mentionned previously, the 304L SS is used as the material of comparison. XPS analyses, TEM and EDX measurements enabled to get general informations about the thickness and composition of the passive layers of both materials.

#### **4.1.3. Main results**

Fig. 10 displays the polarization curves obtained at 100°C in the three electrolytes for the Uranus S1N and the 304L SS.

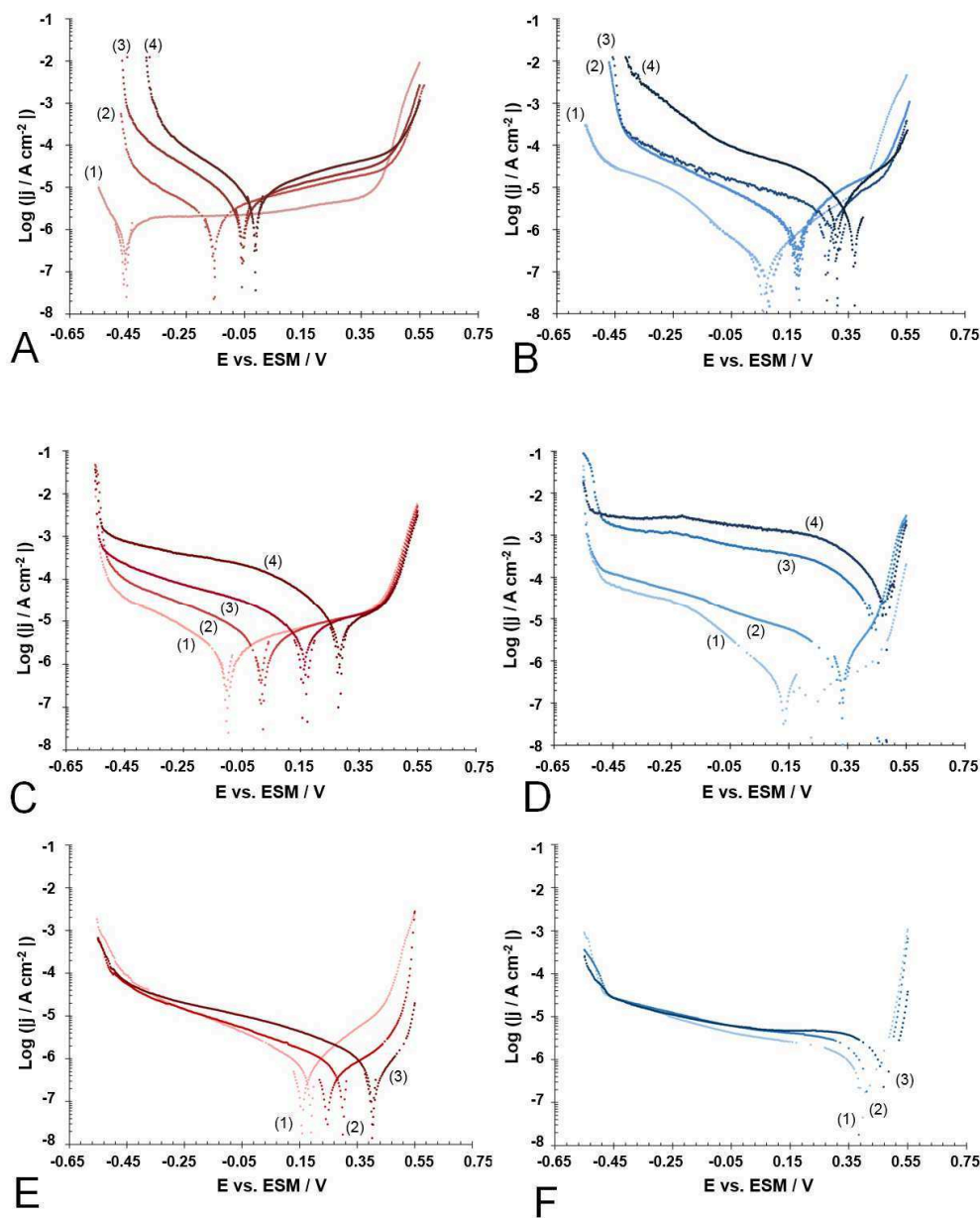


Fig. 10. Linear polarization curves ( $v = 0.2 \text{ mV s}^{-1}$ ) in  $4 \text{ mol dm}^{-3} \text{ HNO}_3$  at  $100^\circ \text{C}$  for the

*Uranus S1N SS (red) and 304L SS (blue)*

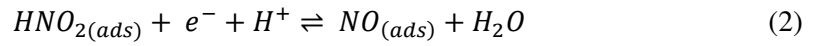
(A/B):  $\text{HNO}_3$  1 (1), 4 (2), 6 (3), 9 (4)  $\text{mol dm}^{-3}$

(C/D) :  $\text{HNO}_3$  4  $\text{mol dm}^{-3}$ ; V(V)  $1.9 \cdot 10^{-4}$  (1),  $1.9 \cdot 10^{-3}$  (2),  $9.8 \cdot 10^{-3}$  (3),

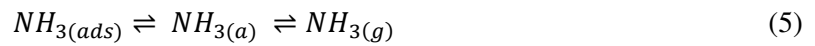
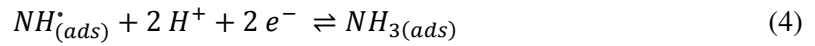
$3.9 \cdot 10^{-2}$  (4)  $\text{mol dm}^{-3}$

(E/F) :  $\text{HNO}_3$  4  $\text{mol dm}^{-3}$ ; Cr(VI)  $9.6 \cdot 10^{-5}$  (1),  $4.8 \cdot 10^{-4}$  (2),  $9.6 \cdot 10^{-4}$  (3)  $\text{mol dm}^{-3}$

Firstly, the mechanism of the reduction reaction was investigated at the Uranus S1N SS surface through the shapes of the cathodic branches observed on the Uranus S1N polarization curves. In pure HNO<sub>3</sub> (between 1 and 9 mol dm<sup>-3</sup>) Uranus S1N cathodic branches (Fig. 10A) display two  $\log (|j|)$  vs.  $E$ . slopes. These slopes could be associated to several reactions described in the literature [35, 40]. The first reaction, occurring between  $E_{\text{corr}}$  and -0.45 V vs. MSE could be the nitrous acid reduction reaction as described by Schmid [50] but without the autocatalytic reaction as shown by Benoit *et al.* [39] :

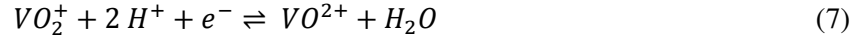


The second reaction, below -0.45 V vs. MSE would be ammoniac formation as described by Razygraev *et al.* [40] :

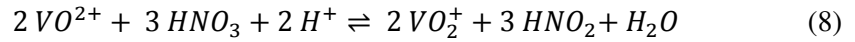


However, this second reaction could also be the first reactions (Eqs. 1 to 3) whose kinetics would be increased by the active domain of the SS. However, the activation potential measurements displayed in the second chapter of this work are closer to -0.64 V vs. MSE for the Uranus S1N in a 4 mol dm<sup>-3</sup> HNO<sub>3</sub> at 80°C, which seems to be much lower than the -0.45 V vs. MSE observed in Fig. 10. Also, at lower potentials than -0.60 V vs. MSE, the proton reduction reaction will be expected.

In the presence of V(V), the Uranus S1N cathodic branch shape (Fig. 10C) doesn't seem to be affected by the concentration in V(V). The reduction reaction of the V(V) species are supposed to be :



In the conditions of the experiments (4 mol dm<sup>-3</sup> HNO<sub>3</sub>, 100 °C), this reaction is immediately followed by a reoxidation of VO<sup>2+</sup> [51]:



Therefore, V(V) can be seen as a catalyzer for the nitric acid reduction reaction. In Fig. 10C it is difficult to conclude if the reduction reaction observed is consequently the nitric medium reduction reactions, the V(V) reduction reaction, or a mixed of both. In Fig. 11 are superimposed polarization curves of the Uranus S1N in 4 mol dm<sup>-3</sup> HNO<sub>3</sub> at 100°C with and without V(V). From the very subtle modification of the slopes, Fig. 11 suggests that a mixed reduction reaction is observed, but that the HNO<sub>3</sub> reduction reactions prevail.

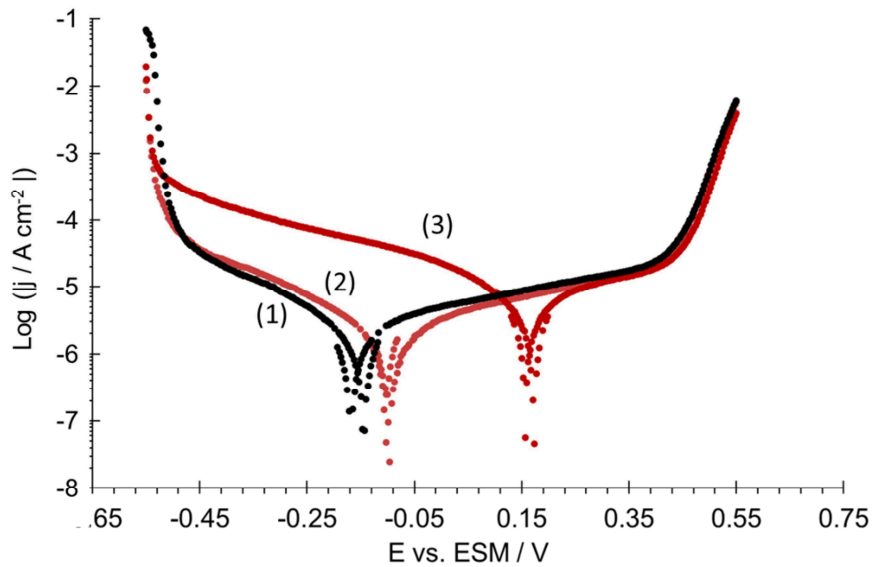
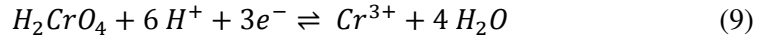


Fig. 11. Linear polarization curves of the Uranus S1N in 4 mol dm<sup>-3</sup> HNO<sub>3</sub> at 100 °C

$$HNO_3 \ 4 \text{ mol dm}^{-3} \ (1)$$

$$HNO_3 \ 4 \text{ mol dm}^{-3} + V(V) \ 1.9 \ 10^{-4} \text{ mol dm}^{-3} \ (2); + V(V) \ 9.8 \ 10^{-3} \text{ mol dm}^{-3} \ (3)$$

In the case of the Cr(VI) species(Fig. 5E), the reduction reaction also seems to be independant from the concentration in terms of mechanism. The reduction reaction of Cr(VI) species are expected to follow Eq. 9:



According to the Pourbaix diagrams, the reduction reaction product,  $Cr^{3+}$ , is stable in the conditions of the experiment unlike for the V(V). Two possible reduction reactions can be then expected in Fig. 10E. First, it could be the reduction reaction of Cr(VI) as described by Eq. 9. The other hypothesis would be once again the reduction reaction of  $HNO_3$  prevailing but kinetically decreased by a local reinforcement of the passivity of the steel because of the reduction reaction of Cr(VI). Benoit *et al.* [36] tended to show that the passivity of a material could affect in this way the intensity of the  $HNO_3$  reduction reactions.

Then, the two materials are compared in the same conditions. Fig. 12 displays several superimpositions of the polarization curves obtained for the two materials in different conditions.

As the general aspect of the reduction reaction does not seem to vary, it can be thought that Si alloying does not affect the species involved in the reduction reaction (Fig. 12). However, it is clear that the Si decreases efficiently the kinetics of the reduction reaction. For each concentration of each electrolyte, the intensity of the reduction reaction is lower for the Uranus S1N.

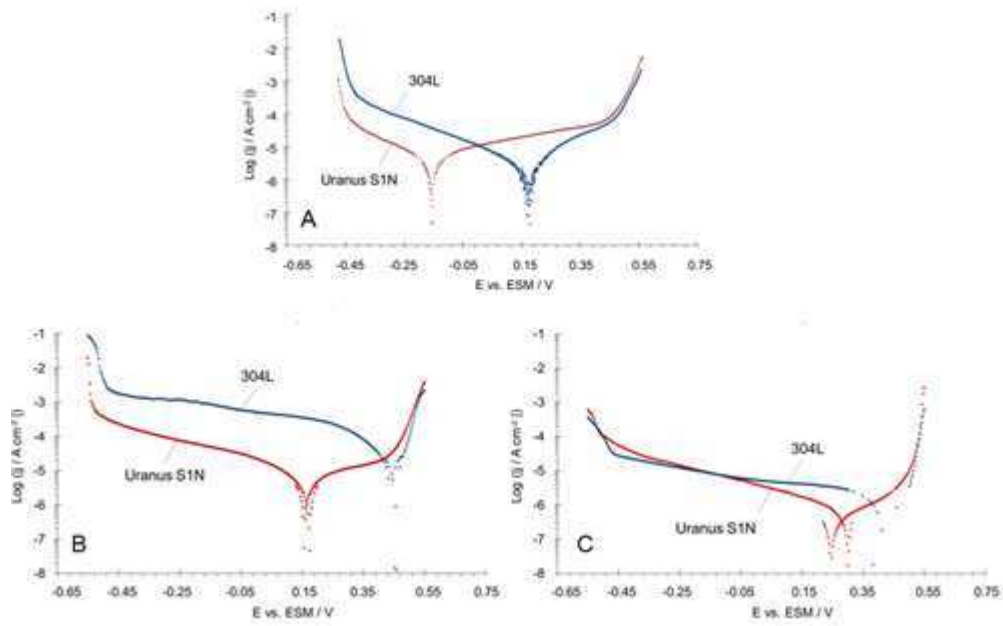


Fig. 12. Linear polarization curves of the Uranus S1N (red) and 304L SS (blue) in  $4 \text{ mol dm}^{-3}$   $\text{HNO}_3$  at  $100^\circ \text{C}$

(A)  $\text{HNO}_3$   $4 \text{ mol dm}^{-3}$

(B)  $\text{HNO}_3$   $4 \text{ mol dm}^{-3}$ ;  $\text{V(V)}$   $9.8 \cdot 10^{-3} \text{ mol dm}^{-3}$

(C)  $\text{HNO}_3$   $4 \text{ mol dm}^{-3}$ ;  $\text{Cr(VI)}$   $4.8 \cdot 10^{-4} \text{ mol dm}^{-3}$

Fig. 13 sums up the different  $E_{\text{corr}}$  and  $j_{\text{corr}}^*$  estimated from the polarization curves.  $j_{\text{corr}}^*$  is a Tafel extrapolation from the cathodic branch of the polarization curves.

Fig. 13 shows clearly that as the reduction reaction kinetics are lowered for the Uranus S1N, while the oxidation current is increased,  $E_{\text{corr}}$  is systematically lowered as compared to the 304L. As the transpassive transition  $E_{\text{tp}}$  is never really affected by the conditions, a mean value is represented in Fig. 13. Consequently, it is shown that as  $E_{\text{corr}}$  is lowered by the presence of Si, the Uranus S1N always remain passive in the present range of conditions, whereas the 304L is shifted to its transpassive domain.

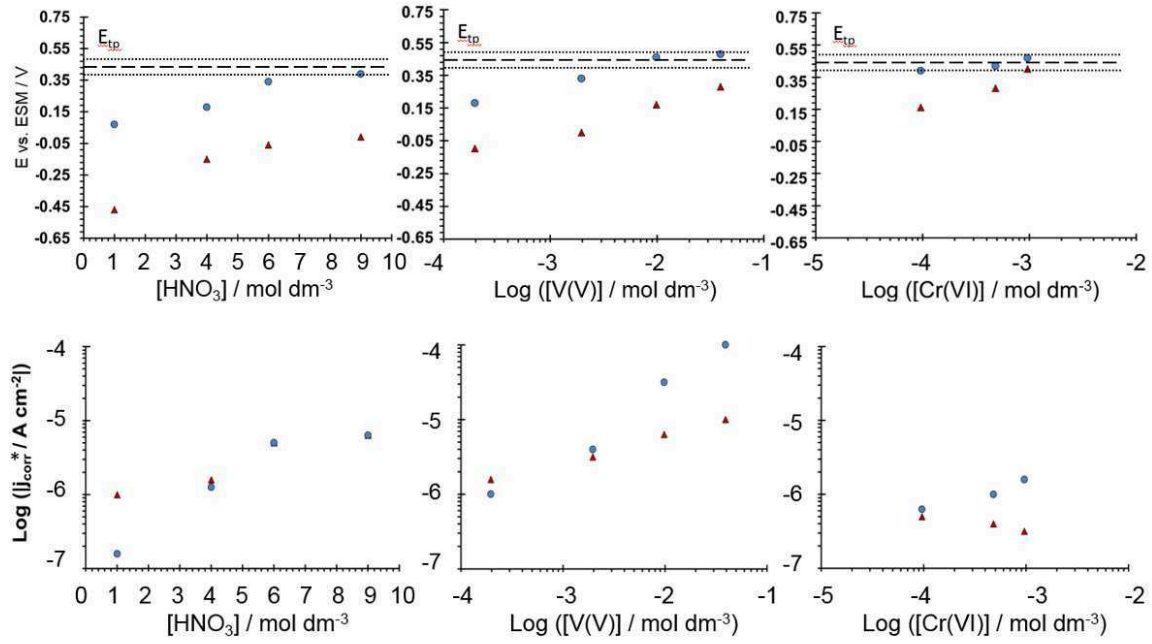


Fig. 13.  $E_{\text{corr}}$  et  $j_{\text{corr}}^*$  for Uranus S1N (red) and 304L (blue)

The direct consequence of this result is that the  $j_{\text{corr}}^*$  value of the 304L SS increases rapidly as soon as the material becomes transpassive, and the inversion between Uranus S1N and 304L corresponds exactly to the limit condition where the 304L will start being transpassive. These results confirm what was found by Armijo *et al.* [4].

In this first chapter, the specific case of the Cr(V) is also investigated. In Fig. 13 is clearly shown the decreasing  $j_{\text{corr}}^*$  for the Uranus S1N that is not observed in the case of the 304L SS. The Uranus S1N displays a very singular interaction with the Cr(VI). However, this phenomenon occurs apparently because the concentration in Cr(VI) are low, because in literature, higher concentrations were investigated using different Cr(VI) isotopes. They were meant to prove that Cr(VI) could reduce at the Uranus S1N surface, but they couldn't conclude [52].



#### 4.1.4. Conclusion

In this first chapter, polarization curves were performed in different electrolytes with both SS. It was shown that Si was capable of preserving the passivity of the Uranus S1N even in very oxidizing conditions. It is directly related to the fact that Si in the passive layer of the SS kinetically limits the reduction reaction while increasing the oxidation current. Therefore, the corrosion potential is largely decreased and the material remains passive even at high concentrations in oxidizing species. It clearly explains why the Si-rich SS corrode at higher rates than the 304L in pure  $\text{HNO}_3$  and at lower rates than the 304L when adding oxidizing species, because the 304L SS starts dissolving in its transpassive state.

The second conclusion involved the particular affinity of the Uranus S1N to Cr(VI) species. For low concentrations (less than  $0.1 \text{ g dm}^{-3}$ ), the passivity of the Uranus S1N improves, which is not the case for the 304L SS. One can think that other oxidizing species could display similar behavior, which highly stresses the importance of working with different oxidizing species.

#### **4.1.5. Publication (to be submitted)**

##### *Abstract*

The present work relies on linear sweep voltammetry to investigate the impact of a 3.5 wt. % addition of Si on the corrosion resistance of an 18Cr-15Ni stainless steel (SS) in 100 °C nitric acid, HNO<sub>3</sub>. The X1CrNiSi18-15-4 SS was compared to the X2CrNi18-10 SS in various types of conditions: pure concentrated HNO<sub>3</sub> with or without oxidizing species (V(V) and Cr(VI)). In pure HNO<sub>3</sub>, both SS are passive and the X1CrNiSi18-15-4 SS dissolves spontaneously faster than the X2CrNi18-10 SS. The addition of oxidizing species V(V) or Cr(VI) in the electrolyte leads to the opposite result: the X1CrNiSi18-15-4 stainless steel remains in the passive state, whereas the 18Cr-10Ni stainless steel is polarized in the transpassive state. As a consequence, the X1CrNiSi18-15-4 SS corrodes slower than the X2CrNi18-10 SS. All these observations are explained by the fact that the presence of Si in the oxide film slightly deteriorates the passivity of the stainless steel but also moderates the reduction processes. It keeps the corrosion potential of the X1CrNiSi18-15-4 SS low enough for the alloy to remain passive. A specific impact of the addition of Cr(VI) is also shown, as Cr(VI) seems to play a role on both cathodic and anodic processes, whereas V(V) mainly impacts the cathodic kinetics.

##### *1. Introduction*

Industrial devices involving nitric acid in their processes, such as in plants for spent nuclear fuel reprocessing, have to face material choice in regards to this constraining environment. Indeed, nitric acid, HNO<sub>3</sub>, acts both as an acid and an oxidizing agent. Some frequently chosen alloys such as several austenitic stainless steels (SS) present a satisfying corrosion resistance in nitric acid, especially when concentrated, because of a dissolution rate that can be lower than a few tens of micrometers per year. Each composition of alloy can be

dedicated to a specific environment in terms of temperature,  $\text{HNO}_3$  concentration and the possible presence of oxidizing species dissolved in the acid [1]. Oxidizing species refer to heavy metallic ions coming from the process itself that reduce at very high potentials. Their presence in the electrolyte ( $\text{HNO}_3$ ) raises the steady state potential of the alloys to values that could cause loss of passivity. Shifted to their transpassive domain of potential, they may undergo severe dissolution. High dissolution may also come along with surface heterogeneity, for example, the corrosion can be more intense at grain boundaries than at grain faces. It results from this phenomenon, called intergranular corrosion, a non-faradaic contribution to mass loss of the material, caused by grains being removed from the surface before they have actually dissolved into the electrolyte [2, 3]. To limit risks associated with such type of corrosion, the chemical composition of some SS was optimized. In particular, by the end of the 60s it was shown that the addition of Si had a major impact on the corrosion behavior of 18Cr-15Ni type SS [1, 4-9]. Very low-Si alloyed materials were performing satisfyingly, alloys containing around 1 wt. % severely degraded in concentrated  $\text{HNO}_3$ , but more than 1 wt.% Si addition revealed benefic in the presence of oxidizing species [10]. An X1CrNiSi18-15-4 SS was then developed to resist these specific conditions. In pure  $\text{HNO}_3$ , the X1CrNiSi18-15-4 SS dissolves more rapidly than the X2CrNi18-10 SS (more commonly referred to as 304L SS), but in presence of various oxidizing species, the X1CrNiSi18-15-4 dissolves much slower than the X2CrNi18-10 SS [10]. It proved to dissolve even slower than it did in pure  $\text{HNO}_3$  in the presence of Cr(VI) in the electrolyte [11]. Moreover, even in transpassive conditions, the X1CrNiSi18-15-4 SS does not undergo intergranular corrosion [4, 5, 7]. An assumption proposed by Camus *et al.* [12] is that Si enrichment over 1 wt. % levelled grain boundaries and grain faces energies at the surface of the material. However, this hypothesis was moderated by Armijo *et al.* [13] because even if low-Si alloys present more active grain boundaries than grain faces, they are not always subject to intergranular

corrosion. Nevertheless it was shown in previous work [13, 14] that the surface of X1CrNiSi18-15-4 SS was covered by an oxide layer containing much more silicon than the bulk material (over 30 at. %) in various conditions. Based on core level energies measured by X-ray photoelectron spectroscopy (XPS), Robin *et al.* [14] formulated the hypothesis that silicon is present in the layer as a Cr-Si oxide. If the exact chemistry and structure of this oxide layer remains unclear, it is nevertheless different from the Cr oxide that is usually analyzed at the X2CrNiN18-10 SS surface, which contains no enrichment in Si. As the passive layer acts as the interface at which corrosion reactions to proceed, such differences in the composition of passive layer between the X1CrNiSi18-15-4 and the X2CrNiN18-10 SS could be responsible for the differences in the corrosion behavior that have been discussed above. But this point seems not to have been discussed by many authors.

A lot of corrosion rate measurements of different SS in HNO<sub>3</sub> in various conditions of concentration and temperature, and with or without addition of oxidizing ions are available in the literature [10, 13-16]. However, only a few authors [13, 14, 17, 18] tried to express precisely the relationships between corrosion (dissolution rate and surface morphology) and electrochemical behavior of the alloys (corrosion potential, limits of passivity, reduction mechanisms and kinetics). The present work aims at measuring and explaining more exhaustively the electrochemical differences involved by with silicon enrichment of the 18Cr-15Ni type SS by comparing the X1CrNiSi18-15-4 SS and the X2CrNiN18-10 SS in various HNO<sub>3</sub> based electrolytes.

The following work will focus on three main types of electrolyte. First, the impact of the Si enrichment will be examined in pure HNO<sub>3</sub>. The concentration will be varied from 1 to 9 mol dm<sup>-3</sup> at a temperature of 100 °C. Then, V(V) and Cr(VI) will be added to a 4 mol dm<sup>-3</sup> HNO<sub>3</sub> electrolyte at 100 °C to increase the electrochemical potential of the electrolyte. Comparisons of corrosion currents and potentials for the two alloys in these three electrolytes

will help the establishment of a clear link between the pre-existing studies and it will be proposed some hypothesis to explain better the role of Si in the corrosion behavior of SS in HNO<sub>3</sub> environments.

## 2. Experimental

The experiments performed at 100°C. To ensure a better stability of this temperature, a system of thermocryostat (*LAUDA*) heating oil and jacketed 200 mL reactor was used.

### 2.1. Samples

Bullet shape samples (2 cm<sup>2</sup>) made out of X1CrNiSi18-15-4 SS and X2CrNiN18-10 SS were used in the present work for electrochemical measurements. Plane samples (20 mm x 20 mm x 1 mm) polished to diamond finish 0.03µm were used for XPS measurements. The elemental analysis of the steel have been performed by glow discharge optical emission spectroscopy (GD-OES) using a GD-Profilier from *Horiba Jobin-Yvon*. The bulk of the sample was clearly reached from 10 to 45 µm depth and the composition of the steel is averaged over two craters on different samples. This analysis is given in Table 1.

*Table 1. Mass composition of X1CrNiSi18-15-4 SS and X2CrNiN18-10 SS determined by GD-OES profiles performed on samples and averaged between 40 µm and 50 µm depth expressed in wt. %*

	Fe	Cr	Ni	Si	Mn	Add.
X1CrNiSi18-15-4 SS	59.76	18.79	15.08	3.54	1.97	0.18
X2CrNiN18-10 SS	70.35	17.78	9.51	0.34	1.46	0.16

The stainless steel samples used for linear polarization curves were cut into 2 cm<sup>2</sup> “bullet shaped” electrodes, ultrasonic cleaned with ethanol and acetone and then left at open circuit potential (OCP) in 4 mol dm<sup>-3</sup> 100°C HNO<sub>3</sub> for 24h prior to any measurement.

## 2.2. Electrolytes

A 18.2 MΩ cm water prepared with a *Millipore*<sup>TM</sup> system and HNO<sub>3</sub> 52.5 % (*VWR Chemicals*) were used for all the electrolytes. pH were measured using a *Mettler-Toledo* DL55 titrator and NaOH (*Sigma Aldrich*) 1 mol dm<sup>-3</sup> reagent. Preliminary study showed that desaerating nitric acid before the experiment had few impact on the X1CrNiSi18-15-4 SS electrochemical behavior. Considering this, the solutions were not desaerated. Nitric acid solutions containing V(V) were prepared with vanadium sulfate pentahydrate VOSO<sub>4</sub>·5H<sub>2</sub>O (*Sigma Aldrich*, 97.0 %) that were heated up to 100°C for 24 hours for V(IV) to be oxidized in V(V) and then controlled by UV-visible spectroscopy (Cary ‘50 scan’ *Varian* spectroscope). For hexavalent chromium solutions, anhydrous potassium dichromate K<sub>2</sub>Cr<sub>2</sub>O<sub>7</sub> (*Sigma Aldrich*, 99.9 %) was weighed and added to the electrolytes.

## 2.3. Electrochemistry measurement

### 2.3.1. Experiments

A three electrodes cell was used. Samples were used as working electrodes (X1CrNiSi18-15-4 SS or X2CrNi18-10 SS), counter electrode was made of a platinum grid, and reference electrode was a mercury-mercurous sulphate electrode (MSE) provided by *Radiometer* (E=+0.65 V vs NHE in sat'd K<sub>2</sub>SO<sub>4</sub>). A *Biologic* VSP potentiostat performed the experiments, functioning in the potentiodynamic linear polarization mode at 0.2 mV s<sup>-1</sup> scan rate and recorded by *EC-Lab* software V10.37. This scan rate was chosen to be as close as possible to quasi-stationary conditions and perform experiments in a reasonable amount of time. Polarization was performed in two distinct measurements. The first measurement was

started 30 mV above OCP and followed a cathodic sweep direction down to -0.45 V vs. MSE. The second measurement was started after 24 h OCP. It was started 30 mV below OCP and followed an anodic sweep up to +0.55 V vs. MSE. During the OCP period between the two measurements, the potential of the sample usually reached almost perfectly its initial value prior to the first scan.

### 2.3.2. *Determination of parameters*

Several parameters were extracted from the electrochemical measurements presented. Firstly, the corrosion potentials, corresponding to a measured current density  $j = 0$ , and called  $E_{\text{corr}}$  will be compared. In most of cases, as said before, the OCP of the sample reached almost perfectly its initial value in the 24 h OCP period, therefore  $E_{\text{corr}}$  measurements displayed a very small uncertainty (inferior to 5 mV) except for few experiments on the X2CrNiN18-10 SS that lead to an uncertainty for  $\pm 40$  mV.

Secondly, during a linear polarization measurement, it is possible under specific conditions [19] to distinguish on a semi-log scale at both side of  $E_{\text{corr}}$  two slopes (usually called Tafel slopes) that would bring to the measurement of  $j_{\text{corr}}$ , corresponding to the instantaneous dissolution rate of the material. However, in the case of passive materials, the anodic Tafel slope is usually inexistent. Moreover, when the reduction reaction involves complex mechanisms, as it will be shown in the case of  $\text{HNO}_3$ , cathodic Tafel slope is also rigorously difficult to establish. Nevertheless, it was proposed in the present work to define a  $j_{\text{corr}}^*$  that provides a qualitative information on the relative dissolution rates of the alloys.  $j_{\text{corr}}^*$  was determined as the intersection between a cathodic slope identified on at least one decade and  $x = E_{\text{corr}}$ .

Eventually, the passivity breakdown at high potentials, usually called transpassive domain transition, was associated to a potential  $E_{\text{tp}}$  identified at the intersection between the passive

domain slope (when measurable) and the transpassive domain slope. The uncertainty associated with  $E_{tp}$  was found to be about  $\pm 40$  mV.

#### 2.4. X-ray photoelectron spectroscopy measurements

XPS analyses were carried out with a *ThermoFisher Escalab 250 XI* spectrometer using a monochromatic X-ray Al K $\alpha$  source. The instrument was calibrated in energy with the Ag Fermi level (0 eV) and the 3d<sup>5/2</sup> core level of metallic silver (368.3 eV). The C-1s signal was used to correct a possible charge effect: the CC/ CH contribution of C-1s spectra was fixed at 285.0 eV. The analysis zone consisted of a 900  $\mu$ m diameter spot. The data processing was performed using the commercially available *Avantage<sup>TM</sup>* software. For the fitting procedure, a Shirley background has been used and Lorentzian-Gaussian (L/G) ratio was fixed at 30 %. Main parameters used to decompose XPS spectra are presented in Table 2.

Table 2. Parameters used for the deconvolution of XPS spectra (*Avantage<sup>TM</sup>* software)

*Binding energies and full width at half maximum (FWHM)*

	[ Fe Ox ] / at. %		[ Cr Ox ] / at. %			[ Si Ox ] / at. %	
	Fe - 2p <sub>3/2</sub>	Fe - 2p <sub>3/2</sub>	Cr - 2p <sub>3/2</sub>	Cr - 2p <sub>3/2</sub>	Cr - 2p <sub>3/2</sub>	Si - 2p	Si - 2p
Binding energy / eV	709.69	712.07	576.26	577.32	578.99	102.05	102.65
FWHM / eV	2.36	2.93	1.08	1.92	1.71	1.36	1.32



### 2.5. Transmission electron microscopy and energy dispersive X-ray spectroscopy

Cross-sections of materials passivated in 4 mol dm<sup>-3</sup> HNO<sub>3</sub> at 100 °C were analyzed using transmission electron microscopy (TEM) in high resolution imaging mode. These studies were performed by *Serma Technologies* (France). In order to identify zones of interest on each sample, electron backscattered diffraction (EBSD) was performed at the surface of the materials prior to sample cross-section elaboration, using a scanning electron microscope field emission gun *ZEISS Gemini 500* scanning electron microscope (SEM), a *Hikari Super* charge coupled device (CCD) camera, and OIM<sup>TM</sup> Data collection and OIM<sup>TM</sup> Analysis software for the acquisition and exploitation of the data. Cross-section TEM lamellas were thinned using focused ion beam (FIB) *FEI Strata DB400* and analyzed with a *FEI Tecnai Osiris* TEM using a an accelerating voltage of 200 kV and equipped with ChemiSTEM<sup>TM</sup> and GIF Quantum® detectors X-ray energy dispersive spectroscopy (X-EDS)

## 3. Results and discussion

### 3.1. Impact of Si on the passive layer of SS

Both SS materials are covered by an oxide film with similar morphology after exposure to 4 mol dm<sup>-3</sup> HNO<sub>3</sub> electrolyte at 100°C for 24 hrs at open circuit. This is seen clearly by comparing the cross sections of the X1CrNiSi18-15-4 SS (Fig. 1A) and the X2CrNiN18-10 SS (Fig. 1B). In both cases, the oxide film is continuous over the surface. Fig. 1 also seems to demonstrate the amorphous character of the passive layer [20]. The X2CrNiN18-10 SS shows localized zones where Cr was found to penetrate about 10-20 nm (white arrow on Fig. 1). No such penetration zones were detected for the X1CrNiSi18-15-4 SS.

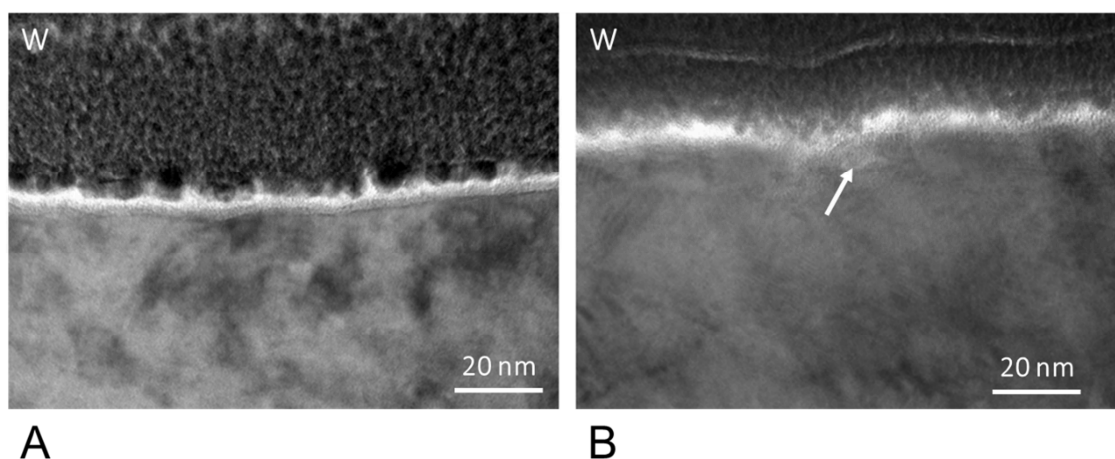


*Fig.1. Cross section of passive layers established on X1CrNiSi18-15-4 (A) and X2CrNiN18-10 (B) SS in 4 mol dm<sup>-3</sup> 100°C HNO<sub>3</sub> for 24 hours and observed using transmission electron microscopy (TEM)*

*Table 3. XPS measurements on passive layers established for 24 hours in 4 mol dm<sup>-3</sup> HNO<sub>3</sub> at 100 °C (averaged over 10 experiments)*

		[ Fe Ox ] / at. %	[ Cr Ox ] / at. %	[ Si Ox ] / at. %
HNO <sub>3</sub> 4 mol dm <sup>-3</sup>	X1CrNiSi18-15-4	26 ± 4	46 ± 4	28 ± 3
	X2CrNiN18-10	41 ± 4	59 ± 5	None

Chemical compositions of the passive layers were obtained using XPS on the same samples (Table 3): the X2CrNiN18-10 SS surface was mainly composed of Cr (59 at. %) while the X1CrNiSi18-15-4 SS, contained mainly Cr (46 at. %) and Si (28 at. %). As mentioned previously, and already found in literature [14, 21], the passive layer formed at a Si enriched alloy's surface is also enriched in Cr but also in Si in higher concentration than the

bulk material. Moreover, a core level energy lower than 104 eV was found for Si-2p at the X1CrNiSi18-15-4 SS's surface. This indicates that Si atoms are not bonded to O under the form of SiO<sub>2</sub>. Robin *et al.* [14] highlighted that this particular structure of the X1CrNiSi18-15-4 SS oxide was probably due to a mixed silicate oxide.

In conclusion, Si seems to impact the chemical composition of the oxide layer, morphological properties being mainly similar. This composition difference may impact the electrical properties provided by the oxide layer, and therefore, the corrosion behavior. Therefore, both anodic and cathodic contributions characteristics will be compared in pure HNO<sub>3</sub> and using oxidizing species for both SS.

### *3.2. Impact of Si in pure HNO<sub>3</sub>*

Typical linear polarization curves obtained in 100 °C pure HNO<sub>3</sub> for X1CrNiSi18-15-4 SS and X2CrNi18-10 SS are displayed on Fig. 2 for concentrations of 1 mol dm<sup>-3</sup> (A), 4 mol dm<sup>-3</sup> (B) and 6 mol dm<sup>-3</sup> HNO<sub>3</sub> (C). Red curves represent X1CrNiSi18-15-4 SS and blue curves are associated to X2CrNi18-10 SS.

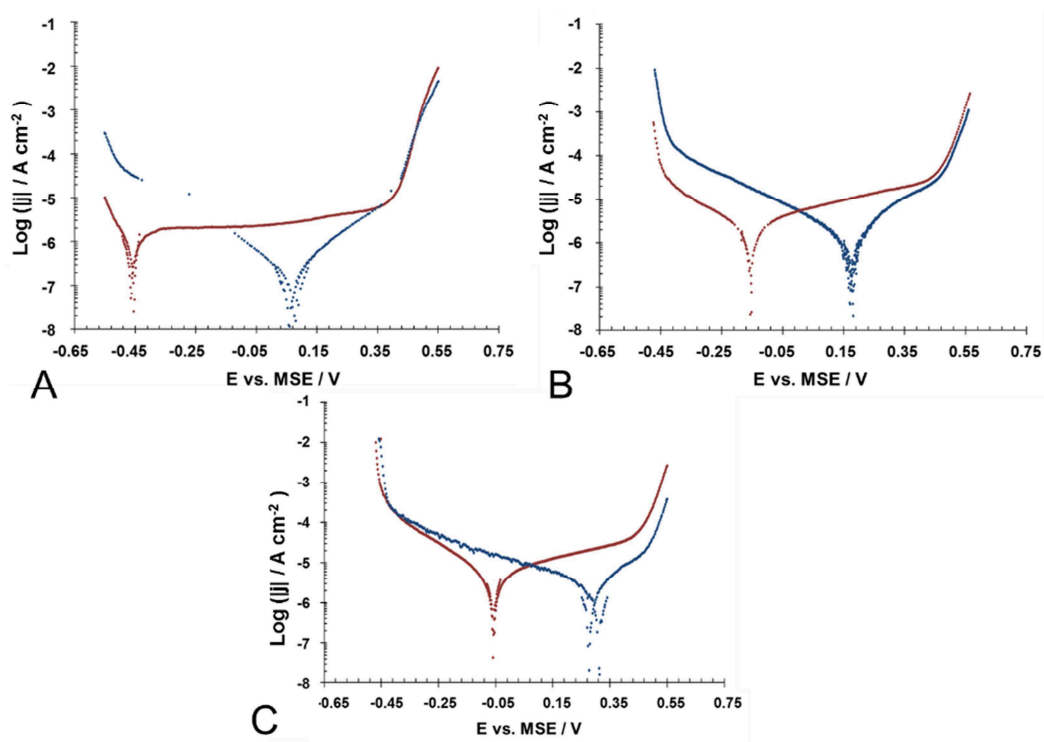
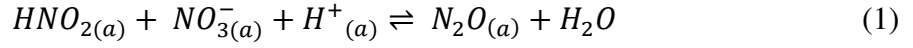
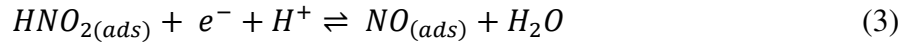


Fig. 2. Linear sweep voltammetry ( $v = 0.2 \text{ mV s}^{-1}$ ) performed at  $T = 100 \text{ }^{\circ}\text{C}$  for X1CrNiSi18-15-4 (red) and X2CrNiN18-10 (blue) SS in  $\text{HNO}_3$  1 (A), 4 (B), 6 (C)  $\text{mol dm}^{-3}$

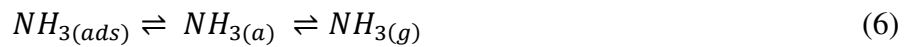
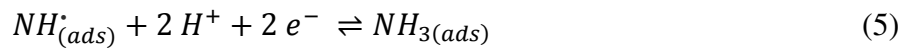
The shape of the cathodic branch and the cathodic Tafel slope does not differ significantly between the two steel samples, suggesting that the cathodic reaction is not significantly affected by the presence of Si (Fig. 2). The cathodic branch for both steel specimens at every  $\text{HNO}_3$  concentration displays two slopes. The first cathodic domain is detected between  $E_{\text{corr}}$  and  $-0.45 \text{ V vs. MSE}$  (almost  $-0.30 \text{ V vs. MSE}$  for the highest concentration) and the second domain starts below  $-0.45 \text{ V vs. MSE}$ . Concentrated  $\text{HNO}_3$  reduction reactions have been extensively investigated on various ranges of materials from platinum to stainless steel [22-27]. In concentrated  $\text{HNO}_3$ , various nitrogenous species were shown to be in equilibrium, as described exhaustively by various authors [22-27]. Briefly, the nitrosonium ion,  $\text{NO}^{3-}$ , being in equilibrium with nitrous acid  $\text{HNO}_2$  according to Eq. 1,  $\text{HNO}_2$  has been shown to be, between  $-0.45$  and  $-0.25 \text{ V vs. MSE}$ , one of the main electroactive species reducing at a SS surface [27].



The reduction reaction of  $HNO_2$  is given by Eqs. 2 to 4. It reduces into N(II) species such as nitrogen monoxide, NO, which after desorbing (Eq. 4) may be reoxidized by  $HNO_3$  close to the interface. In the case these third oxidation state species produced by this reoxidation would reduce again, the overall reduction process becomes autocatalytic (also called Schmid's mechanism), and this autocatalytic behavior depends on the nature of the interface [23, 24]. Benoit *et al.* [26] showed that the autocatalytic behavior was not triggered at the 304L SS surface.



Between -0.60 and -0.45 V vs. MSE, ammonia formation is expected to happen according to Razygraev *et al.* [27] (Eqs. 5 to 7)



$NH^*_{(ads)}$  being itself produced by a number of different equilibria of the  $HNO_3$  electrolyte. At lower potentials than -0.60 V vs. MSE, the proton reduction reaction is expected. In the present work, polarization curves were performed at higher potentials, therefore this reaction is never observed. Fig. 2 seems to reveal previously mentioned mechanisms consistent with

literature in terms of potentials (Eqs 1-3 and 4-6), although further investigations should confirm the nature of reduced species.

The Si alloying is not responsible for any significant modification of the reduction mechanism, however, the reduction current density of the X2CrNi18-10 SS is systematically between 0.5 to 1 decade higher than for the X1CrNiSi18-15-4 SS in Fig. 2 and Table 4. Si contained in the passive layer seems to inhibit  $\text{HNO}_2$  reduction, as described by Armijo *et al.* [13]. The results of Fig. 2 fully support this hypothesis, showing a similar mechanism with a decreased reaction rate.

Table 4. Values of cathodic current 100 mV below  $E_{corr} / \mu A cm^{-2}$ , cathodic Tafel slope / mV dec<sup>-1</sup>,  $E_{tp}$  vs. MSE / V, passive current 100 mV below  $E_{tp} / \mu A cm^{-2}$  and transpassive current 100 mV above  $E_{tp} / mA cm^{-2}$  for both SS in the exhaustive range of conditions tested for the present work at 100 °C

100°	HNO <sub>3</sub> / mol dm <sup>-3</sup>	V(V) / mol dm <sup>-3</sup>	Cr(VI) / mol dm <sup>-3</sup>	$E_{corr}$ vs. MSE / V	Cathodic current 100mV below $E_{corr} / \mu A$ cm <sup>-2</sup>	Cathodic Tafel slope / mV dec <sup>-1</sup>	$E_{tp}$ vs. MSE / V	Passive current 100mV below $E_{tp} / \mu A cm^{-2}$	Transpassive current 100mV above $E_{tp} / mA$ cm <sup>-2</sup>
X1CrNiSi18-15-4	1	-	-	-0.47	8.9	-19.6	0.44	6.0	5.00
	4	-	-	-0.15	4.4	-17.9	0.45	19.0	1.15
	6	-	-	-0.06	13.0	-19.5	0.45	27.0	2.60
	9	-	-	-0.01	21.0	-20.6	0.47	43.4	1.20
	4	$1.96 \cdot 10^{-4}$	-	-0.097	4.1	-17.2	0.44	12.3	2.80
	4	$1.96 \cdot 10^{-3}$	-	0	11.2	-19.4	0.44	12.4	2.80
	4	$0.0098$	-	0.17	14.9	-19.7	0.44	12.4	2.70
	4	0.039	-	0.28	32.0	-21.6	0.44	12.5	2.70
	4	-	$9.6 \cdot 10^{-4}$	0.16	1.7	-16.9	0.44	5.0	0.55
	4	-	0.019	0.28	1.7	-17	0.48	1.1	0.55
	4	-	0.029	0.4	1.7	-17.1	0.51	-	0.02
X2CrNiN18-10	1	-	-	0.07	0.5	-15.6	0.45	4.8	3.75
	4	-	-	0.18	3.8	-17.9	0.47	3.4	0.69
	6	-	-	0.34	5.5	-15.9	0.45	-	0.38
	9	-	-	0.39	20.0	-20.5	0.44	-	0.23
	4	$1.96 \cdot 10^{-4}$	-	0.18	1.1	-16.3	0.46	5.0	2.90
	4	$1.96 \cdot 10^{-3}$	-	0.33	2.9	-17	0.45	-	2.80
	4	$0.0098$	-	0.46	77.0	-23	-	-	2.80
	4	0.039	-	0.48	240.0	-26	-	-	2.70
	4	-	$9.6 \cdot 10^{-4}$	0.39	1.6	-16.9	-	-	0.96
	4	-	0.019	0.42	2.5	-17	-	-	0.96
	4	-	0.029	0.47	3.3	-17	-	-	0.03

The passive current density is also affected by the presence of Si, the mean passive current density of the X1CrNiSi18-15-4 SS being markedly higher than for the X2CrNiN18-10 SS. For example, Table 4 shows that in 4 mol dm<sup>-3</sup> HNO<sub>3</sub> the passive current density value 100mV below  $E_{tp}$  is 5 times higher for the X1CrNiSi18-15-4 SS than for the alloy without Si.

The combined inhibition of the cathodic reaction and activation of the anodic reaction by Si alloying, causes the corrosion potential  $E_{corr}$  of the X1CrNiSi18-15-4 SS to be systematically lower than for X2CrNiN18-10 SS. This applies to the whole range of conditions tested as shown on Fig. 3.

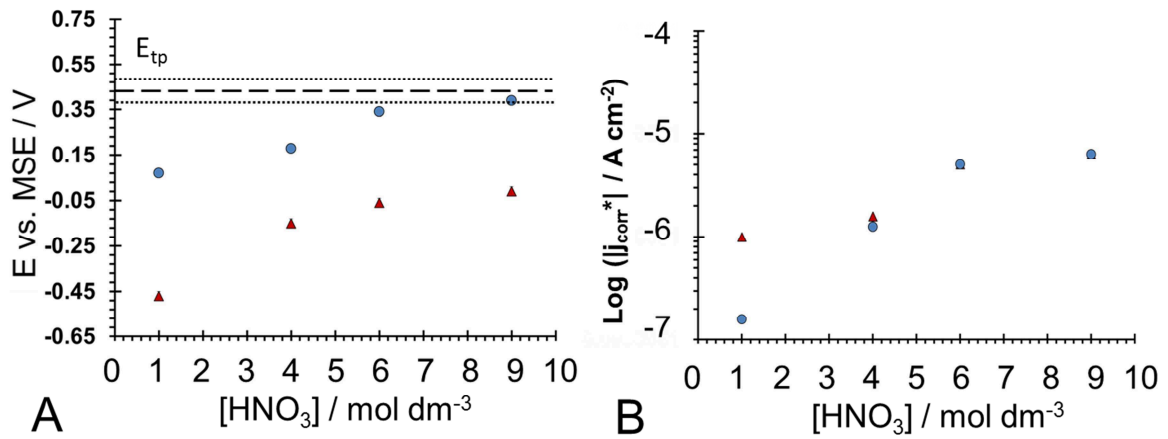


Fig. 3. (A)  $E_{corr}$  measured for X1CrNiSi18-15-4 (triangles) and X2CrNiN18-10 (circles)

SS as a function of HNO<sub>3</sub> concentration at 100°C

(B) Log ( $|j_{corr}^*|$ ) for X1CrNiSi18-15-4 (triangles) and X2CrNiN18-10 (circles) SS as a

function of HNO<sub>3</sub> concentration at 100°C

According to Eqs. 1 to 6, this cathodic inhibition could either result from a modification of the charge transfer properties at the X1CrNiSi18-15-4 SS interface, or from an alteration in the adsorption capability of the X1CrNiSi18-15-4 SS surface.



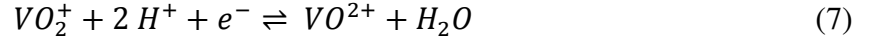
It can be noticed that the measurements of  $j_{\text{corr}}^*$  (Fig. 3) are consistent with dissolution rates ascertained in literature [10, 13]. For example, Desestret *et al.* [10] found a mass loss of  $20 \text{ mg cm}^{-2}$  per day in boiling  $5 \text{ mol dm}^{-3} \text{ HNO}_3$ . Based on the Fe molar mass of  $53.46 \text{ g mol}^{-1}$ , on the density of the X1CrNiSi18-15-4 SS of  $7.81 \text{ g cm}^{-3}$ , and on an averaged value of number of electrons exchanged  $n_e$  of 2.7, the value  $j_{\text{corr}}^* = 1.5 \cdot 10^{-6} \text{ A cm}^{-2}$  found in  $100^\circ\text{C}$   $4 \text{ mol dm}^{-3} \text{ HNO}_3$  leads to a mass loss of  $26 \text{ mg cm}^{-2}$  per day.

$E_{\text{tp}}$  was not influenced by the presence of Si as indicated in Fig. 2. This value is usually associated with the transition of Cr(III) to Cr(VI) in the passive layer. However, it was demonstrated that, on artificial Fe-Cr oxides [28], Fe(III) oxides in acidic electrolyte lowers the Cr(III)/Cr(VI) transition rate [29]. Values for  $E_{\text{tp}}$  were found identical within a small variance of 20 mV ( $0.45 \pm 0.2 \text{ V vs. MSE}$ ) in all concentrations for both steels although a slight difference in the transpassive currents were observed. For example, in  $4 \text{ mol dm}^{-3} \text{ HNO}_3$  at  $0.55 \text{ V vs. MSE}$ , current density recorded for the X1CrNiSi18-15-4 SS 100 mV above  $E_{\text{tp}}$  is  $1.15 \text{ mA cm}^{-2}$  while the X2CrNiN18-10 SS displays a current density of  $0.70 \text{ mA cm}^{-2}$ . The difference was expected to increase slightly with nitric acid concentration and this may be due to pH as demonstrated by Schmuki *et al.* [28], but was found to be almost steady between 0.5 and 2 mA in the whole range of conditions tested (Table 4).

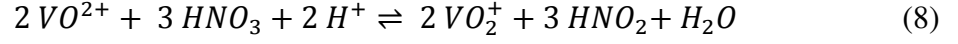
### 3.3. Impact of Si in the presence of oxidizing species

#### 3.3.1. V(V)

Oxidizing species are known to increase the corrosion rate of SS in  $\text{HNO}_3$  [1-3, 5, 11, 15-18]. V(V) has been historically used as an oxidizing agent for simulating redox couple of pentavalent neptunium  $\text{NpO}_2^{2+}/\text{NpO}_2^+$  in nuclear fuel treatment-recycling electrolytes [30]. Pentavalent vanadium is involved in the  $\text{VO}_2^+/\text{VO}^{2+}$  redox couple through the Eq. 7 (31), whose standard equilibrium potential is predicted to be  $1.04 \text{ V vs. SHE}$  [32].



At 100 °C in the conditions of the present work ( $HNO_3$  4 mol  $dm^{-3}$ ) V(V) is expected to be stable [33]. The oxidation of V(IV) was described by Irisawa *et al.* [33] as:



This reaction can directly enhance the reactions described by Eqs. 1 to 3 in which case V(IV) would be considered a catalysis for the reduction of  $HNO_3$ .

In the presence of V(V) in 4 mol  $dm^{-3}$   $HNO_3$  at 100 °C , the X1CrNiSi18-15-4 SS, originally designed for such specific electrolyte ( $HNO_3$  containing oxidizing species), displays typical polarization curves as shown on Fig. 4A for concentrations in V(V) of 0(1),  $1.9 \cdot 10^{-4}$ (2),  $1.9 \cdot 10^{-3}$ (3),  $9.8 \cdot 10^{-3}$ (4) and  $3.9 \cdot 10^{-2}$ (5) mol  $dm^{-3}$ . A comparison with the X2CrNiN18-10 SS is given on Fig. 4B in 4 mol  $dm^{-3}$   $HNO_3$  at 100 °C for a concentration in V(V) of  $1.9 \cdot 10^{-3}$  mol  $dm^{-3}$ .

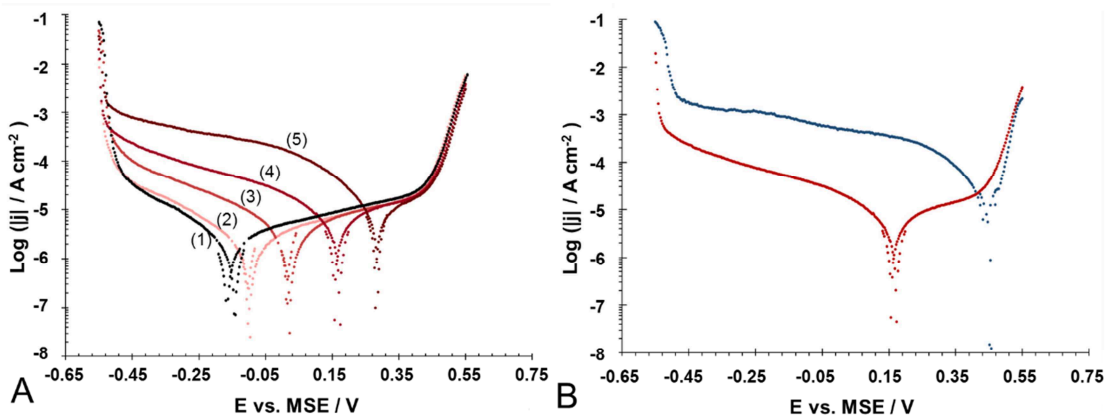


Fig. 4. Linear sweep voltammetry ( $v = 0.2 \text{ mV s}^{-1}$ ) performed in 4 mol  $dm^{-3}$   $HNO_3$  at  $T = 100 \text{ }^{\circ}\text{C}$  for X1CrNiSi18-15-4 (A) with V(V) at 0 (1),  $1.9 \cdot 10^{-4}$ (2),  $1.9 \cdot 10^{-3}$ (3),  $9.8 \cdot 10^{-3}$ (4),  $3.9 \cdot 10^{-2}$ (5) mol  $dm^{-3}$  and for X1CrNiSi18-15-4 and X2CrNiN18-10 (B) SS with V(V) at  $1.9 \cdot 10^{-3}$  mol  $dm^{-3}$

The nature of the cathodic current in Fig. 4 contains contribution from the reduction of V(V) as well as  $HNO_2$  reduction. However, in the case of the X1CrNiSi18-15-4 SS, the shape

of the cathodic curve in presence of V(V) is very similar to pure HNO<sub>3</sub> (Fig 4A) and the cathodic Tafel slopes were found to be of  $18.6 \pm 2.5 \text{ mV dec}^{-1}$  (Table 4) in the whole range of conditions tested.

The shape of the reduction curves and the cathodic Tafel slopes are similar for both SS (Fig. 4B, Table 4) suggesting that the overall reduction mechanism of the electrolyte containing V(V) is comparable between the two alloys and therefore not influenced by the Si alloying. Similar to what was observed in the case of pure HNO<sub>3</sub>, for the same concentrations, cathodic current density is also systematically higher for the X2CrNiN18-10 SS than for the X1CrNiSi18-15-4 SS. This would once again support an inhibiting effect of the Si on the cathodic reactions. The passive current density of the X1CrNiSi18-15-4 SS is once again generally higher than for the X2CrNiN18-10 SS with a similar effect on  $E_{\text{corr}}$  (Fig. 5) as was observed for HNO<sub>3</sub> alone in Fig. 2. At the lowest concentration in V(V),  $1.9 \cdot 10^{-4} \text{ mol dm}^{-3}$ , the passive current 100 mV below  $E_{\text{tp}}$  was found to be 2 times higher for the X1CrNiSi18-15-4 SS than for the X2CrNiN18-10 SS. However, at higher concentrations in V(V), the transpassive transition was too close to determine properly the same difference.

It is clear from Figs. 3 and 5 that when HNO<sub>3</sub> or V(V) concentrations are sufficiently high, or when Cr(VI) species are added, the  $j_{\text{corr}}^*$  is lower for X1CrNiSi18-15-4 SS than for X2CrNiN18-10 SS and that this inversion matches perfectly the threshold of transpassive domain. Therefore, as a direct consequence of the presence of Si, the X1CrNiSi18-15-4 SS remains passive even while the X2CrNiN18-10 SS is shifted into its transpassive domain and starts to dissolve at a much higher rate.

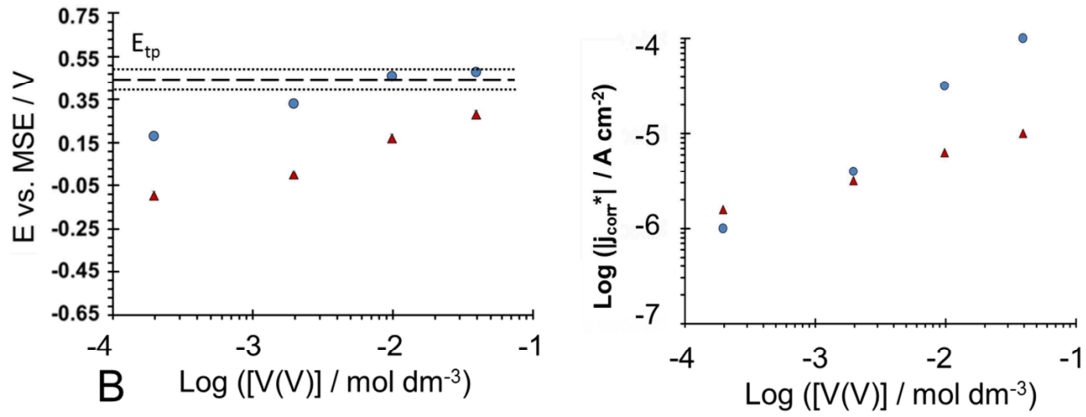


Fig. 5. (A)  $E_{corr}$  measured for X1CrNiSi18-15-4 (triangles) and X2CrNi18-10 (circles) SS as a function of V(V) concentration in 4 mol dm<sup>-3</sup> HNO<sub>3</sub> at 100°C

(B) Log (|j<sub>corr</sub>\*|) for X1CrNiSi18-15-4 (triangles) and X2CrNi18-10 (circles) SS as a function of V(V) concentration in 4 mol dm<sup>-3</sup> HNO<sub>3</sub> at 100°C

One can notice that the values of ( $E_{corr}$ ,  $j_{corr}^*$ ) obtained in the different concentrations in V(V) can be superimposed with the polarization curve obtained in 4 mol dm<sup>-3</sup> HNO<sub>3</sub> at 100 °C (Fig. 6) and this is also valid for the X2CrNi18-10 SS.

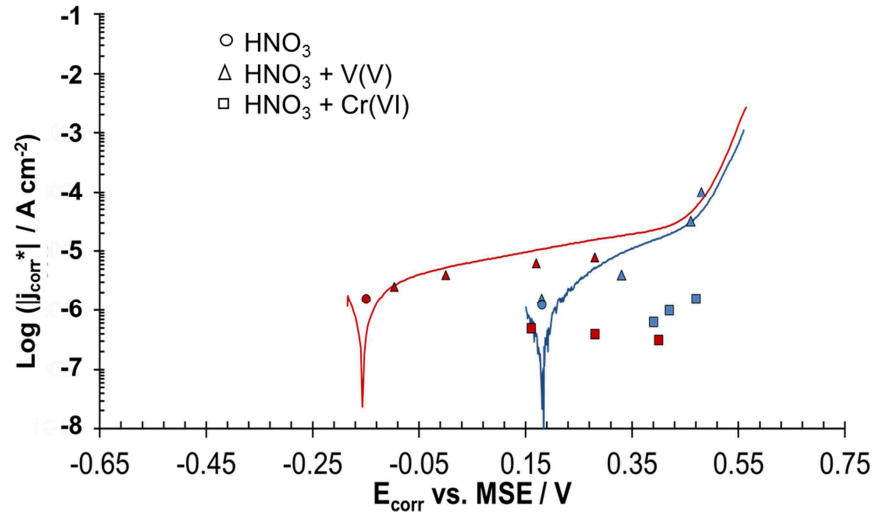


Fig. 6. Red : X1CrNiSi18-15-4 SS polarization curve (line) performed in  $4 \text{ mol dm}^{-3} \text{ HNO}_3$  at  $T = 100$  °C ( $v = 0.2 \text{ mV s}^{-1}$ ) and  $E_{\text{corr}}$  values recorded in pure  $\text{HNO}_3$  (circles),  $\text{HNO}_3$  containing V(V) (triangles) and  $\text{HNO}_3$  containing Cr(VI) (squares)

Blue : X2CrNi18-10 SS polarization curve (line) performed in  $4 \text{ mol dm}^{-3} \text{ HNO}_3$  at  $T = 100$  °C ( $v = 0.2 \text{ mV s}^{-1}$ ) and  $E_{\text{corr}}$  values recorded in pure  $\text{HNO}_3$  (circles)  $\text{HNO}_3$  containing V(V) (triangles) and  $\text{HNO}_3$  containing Cr(VI) (squares)

This result first shown by Plante *et al.* [17] would imply that the oxidation branch of these alloys is not significantly affected by the presence of oxidizing species, and that knowing their  $E_{\text{corr}}$  in given conditions would enable the determination of  $j_{\text{corr}}$ . Other oxidizing species investigated throughout literature ascertained in Plante *et al.*'s work [17] lead to the same conclusion. Regardless of their nature, the anodic current measured at a given potential was found to be unique [17]. The present work confirms that V(V) shifts the  $E_{\text{corr}}$  value without modifying the anodic reaction of the material such that the anodic reaction rate vs. potential curve is independent of the presence of oxidizing ions.

### 3.2.2. Cr(VI)

The Cr(VI) is a more specific case of an oxidizing ion with an original interaction with the alloy. The addition of Cr(VI) species in  $\text{HNO}_3$  has been massively studied [3-5, 7, 10, 13, 15,

34, 35] probably because it requires a very low concentration to shift X2CrNiN18-10 type SS in transpassive dissolution. Fig. 7A displays polarization curves obtained for the X1CrNiSi18-15-4 SS (A) in 4 mol dm<sup>-3</sup> HNO<sub>3</sub> at 100 °C for concentrations of Cr(VI) of 0(1), 9.6 10<sup>-5</sup>(2), 4.8 10<sup>-4</sup>(3) and 9.6 10<sup>-4</sup>(4) mol dm<sup>-3</sup>. Fig. 7B displays the example of polarization curves that were obtained for both SS in 4 mol dm<sup>-3</sup> HNO<sub>3</sub> at 100 °C for a concentration in Cr(VI) of 4.8 10<sup>-4</sup> mol dm<sup>-3</sup>. Fig. 8 ascertains values of E<sub>corr</sub> and j<sub>corr</sub>\* measured in these conditions.

Hexavalent chromium is involved in the H<sub>2</sub>CrO<sub>4</sub>/Cr<sup>3+</sup> redox couple that displays a very high standard potential of 1.40 V vs. SHE [32, 36]. The reduction reaction is described by the equation 9.

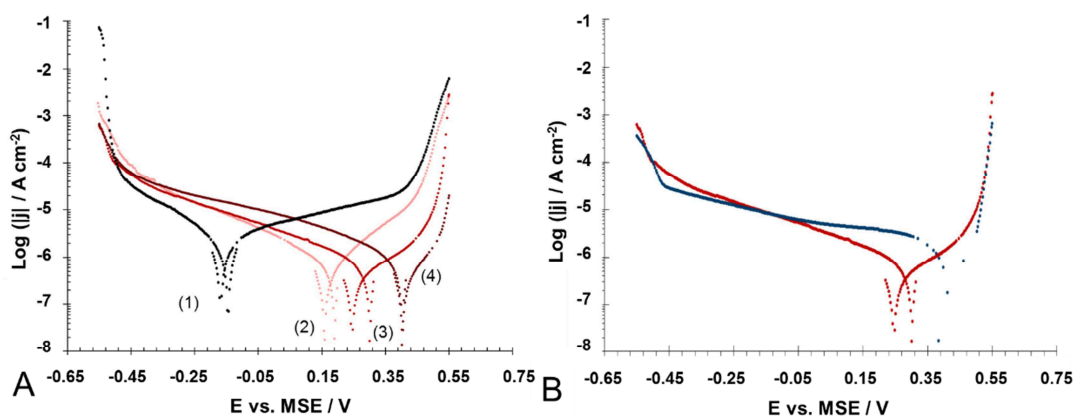
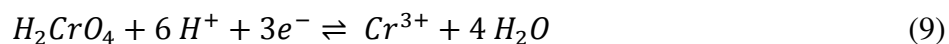


Fig. 7. Linear sweep voltammetry ( $v = 0.2 \text{ mV s}^{-1}$ ) performed in 4 mol dm<sup>-3</sup> HNO<sub>3</sub> at  $T = 100 \text{ }^{\circ}\text{C}$  for X1CrNiSi18-15-4 (A) SS with Cr(VI) 0(1), 9.6 10<sup>-5</sup>(2), 4.8 10<sup>-4</sup>(3), 9.6 10<sup>-4</sup>(4) mol dm<sup>-3</sup> and for X1CrNiSi18-15-4 and X2CrNiN18-10 (B) SS with Cr(VI) 4.8 10<sup>-4</sup> mol dm<sup>-3</sup>



# ***Après trois ans – Paul Verlaine***

## **Remerciements**

*J'adresse mes premiers remerciements aux membres de mon jury,  
Dont chacune des présences revêt un sens qui m'est singulier,  
Je n'éprouve pas seulement du respect pour l'importance de leur travail scientifique,  
Je leur suis redevable également pour leurs qualités humaines,  
Le chemin qu'ils ont su tracer pour que nous puissions les rejoindre un jour.*



*Pour leur soutien technique comme humain,  
Merci à Karine Rousseau, Christian Bataillon, Renaud Cornut, Olivier Genève,  
Kevin Ginestar, Frédéric Miserque et Michel Tabarant.  
La rigueur et la justesse de leur expertise m'ont permis de grandir en tant que scientifique.*



*Au partenaire industriel, Areva,  
pour le financement de la thèse,  
les jours passés, et les aventures à venir.*



*A Jérôme et Fred,  
avec qui j'ai réalisé à quel point j'aimais ce métier.*



*Someday I shall rise and leave my friends  
And seek you again through the world's far ends,  
You whom I found so fair  
My only god in the days that were.  
My eager feet shall find you again,  
Though the sullen years and the mark of pain  
Have changed you wholly; for I shall know  
How could I forget having loved you so?*

**Rupert Brooke**

*A mon directeur de thèse, Kevin Ogle.*

Merci d'avoir été cette voix unique, patiente et entière, guidée par la fascination d'une Science exigeante et sincère. Merci d'avoir ouvert les portes, abattu les cloisons, et soufflé dans les cabanes que je pensais des maisons.

*A Time to Talk – Robert Frost*



*A mon encadrante, Nathalie.*

Le temps que je réalise à quel point ces trois années m'avaient bouleversée et nous étions au bout de la jetée. J'étais là, j'avais grandi, sous le regard bienveillant que tu as toujours su m'accorder. Un voilier m'attendait.

*La fleur qui fait le printemps – Théophile Gautier*



*A mon encadrant, Benoit.*

De deux routes nous avons rarement choisi la même, mais à travers ta patience et ta gentillesse, je savais que les ponts à bâtir pour les relier feraient les plus belles constructions de cette incroyable aventure.

*J'arrive où je suis étranger – Louis Aragon*

*A mes Chefs de Service et de Laboratoire, Fabrice et Raphaël.*

C'est l'exercice le plus difficile au monde que d'emmener, suggérer, diriger. Et de traduire en quelques secondes le meilleur d'une personnalité. Comprendre ce qui suscite l'impulsion, jongler avec un millier de raisons, je crois avoir appris de vous bien plus que vous n'en avez eu l'impression.

*L'indulgence* – René-François Sully Prudhomme



*A tous ceux qui étaient là pour moi, les équipes du SCCME et de l'I2E.*

Des milliers de sourires que vous m'avez adressés, pas un seul ne s'est évanoui, chacun d'eux m'a servi, comme une terre que l'on sème, à cultiver une meilleure version de moi-même.

*J'ai plus de souvenirs que si j'avais mille ans* – Charles Baudelaire



*A des collègues, qui sont devenus des amis, qui sont devenus des proches.*

Je n'ai presque aucun mot, vous avez tout su de moi, à la minute où nos trajectoires se sont interceptées.

*A mon ami Alfred T* – Alfred de Musset



*A mes amis.*

Qu'ils soient au bout de la rue, ou au bout du monde, que l'on se retrouve chaque jour, chaque an, chaque mois, je danse, je pense, chaque fois que je les vois. Et ces trois années n'auraient eu aucun sens en leur absence.

*J'ai cueilli cette fleur pour toi sur la colline* – Victor Hugo

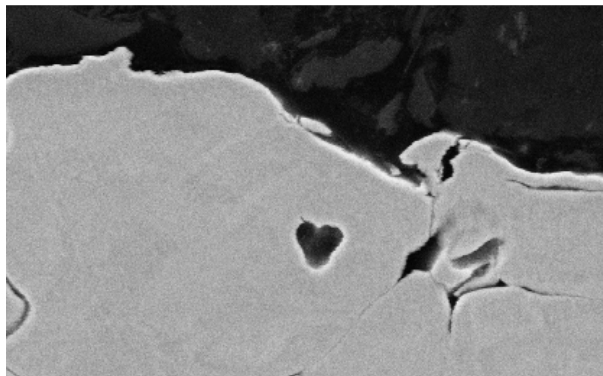
*A ma famille.*

J'ai voulu devenir docteur, comme ma mère. Elle qui pensait que je ne devais ça qu'à mon père.

*Avec le même amour* – Emile Verhaeren



*Et à ceux qui ont mis pied sur le pont mon bateau,  
Qui m'ont donné la force de traverser ces eaux,  
A la vitesse d'un cheval au galop.*



*En 1095 jours, et autant de doutes.*





# T

## ABLE OF CONTENTS

1.	Introduction (English and French)	1
2.	State of the art	8
2.1.	Industrial context, history of development, fabrication and metallurgy of the Uranus S1N SS	8
2.1.1.	Context – Electrolyte and materials	8
2.1.2.	History of the development of the Uranus S1N SS	10
2.1.3.	Metallurgy – fabrication of how is the Si in the bulk material	12
2.1.3.1.	Fabrication	12
2.1.3.2.	Chemical composition	13
2.2.	The metal-electrolyte interface that pilots the corrosion rate of the material	13
2.3.	The passive layer and the electrochemical behavior of austenitic stainless steels in acidic media	15
2.4.	Conclusion	17
3.	Experimentals	19
3.1.	Materials	19
3.1.1.	Experimental strategy	19
3.1.2.	Stainless steels samples	19
3.2.	Atomic emission spectroelectrochemistry	19
3.2.1.	Experimental strategy	19
3.2.2.	Experimental device	20
3.3.	Combining <i>in situ</i> and <i>ex situ</i> analysis	22
3.3.1.	200 mL reactor electrochemistry measurements	23
3.3.2.	Optical microscopy and scanning electron microscopy	23
3.3.3.	X-ray photoelectron spectroscopy	24
3.3.4.	Transmission electron microscopy and energy dispersive X-ray spectroscopy	25

4.	Results	26
4.1.	Silicon enrichment of an austenitic stainless steel – impact on electrochemical behavior in concentrated nitric acid with oxidizing ions	26
4.1.1.	Introduction, the flaws in the literature	26
4.1.2.	Experimental strategy	27
4.1.3.	Main results	28
4.1.4.	Conclusion	35
4.1.5.	Publication to be submitted	36
4.2.	A direct measurement of the activation potential of stainless steels in nitric acid	63
4.2.1.	An introduction to the activation potential	63
4.2.2.	Experimental strategy	66
4.2.3.	Main results	67
4.2.4.	Conclusion	72
4.2.5.	Publication	72
4.3.	Dissolution and passivation of a silicon-rich austenitic stainless steel during active-passive cycles in sulfuric and nitric acid	73
4.3.1.	Kinetics parameters determination and stoichiometry identification	73
4.3.2.	Main results	76
4.3.3.	Conclusion	85
4.3.4.	Publication	86
4.4.	The kinetics of transpassive dissolution chemistry of stainless steels in nitric acid: The impact of Si	87
4.4.1.	On the origin of the intergranular attack	87
4.4.2.	In situ analysis of the transpassive dissolution	89
4.4.3.	Main results	90
4.4.4.	Conclusion	95
4.4.5.	Publication	95
5.	Conclusion (English and French)	96

6. Symbols	107
7. References	108
Annexe. Unachieved experiments	118
1. Impact of an argon flow in the electrolyte on the corrosion potential of the 304L and the Uranus S1N SS	118
1.1. Experimentals	118
1.2. Results and discussion	118
1.3. Perspectives	119
2. Ratio of the reduction current density between the two SS in 4 mol dm <sup>-3</sup> HNO <sub>3</sub> at 100°C	120
2.1. Experimentals	120
2.2. Results and discussion	120
2.3. Perspectives	121
3. Electrochemical microscopy: determining the reduction mechanisms and characterization of the passive layer's conductivity	122
3.1. Feedback mode	123
3.2. Generator-collector mode	125
4. Why is the selective dissolution invisible during active-passive cycles in HNO <sub>3</sub> ?	126
4.1. A quick reminder of the results	126
4.2. Is the AESEC technique sensitive enough?	126
4.3. Perspectives	128
5. AESEC transpassive measurements versus SCIANS model	129
5.1. State of the art	129
5.2. Results	130
5.3. Conclusions	134
6. References of the unachieved experiments section	136
About the author	138





# INTRODUCTION

*I shall be telling this with a sigh  
Somewhere ages and ages hence:  
Two roads diverged in a wood, and I,  
I took the one less traveled by,  
And that has made all the difference.*

***Robert Frost***

*Quand j'étais jeune et fier et que j'ouvrais mes ailes,  
Les ailes de mon âme à tous les vents des mers,  
Les voiles emportaient ma pensée avec elles,  
Et mes rêves flottaient sur tous les flots amers.*

***Alphonse de Lamartine***



# I NTRODUCTION (EN)

1. Yves Bréchet [1] used to say that corrosion is the evil conscience of metallurgists,

... a price to pay for this free electron gas ensuring metallic cohesion and attractive properties of materials. Too often metallurgists and corrosionists have been ignoring each other. The first ones see corrosion as a wound asking for a remedy provided *a posteriori* or for an *a priori* foresight. The second ones are convinced that everything is said of an alloy as soon as its composition is known, and everything is said of its corrosion resistance as soon as the environment is identified. The idea that corrosion of a certain material in a given environment couldn't be approached by a single point of view has motivated deeply the present work.

This thesis work investigated the corrosion behavior of the Uranus S1N stainless steel (SS), an austenitic SS that was enriched in silicon (4 wt. %). The Si enrichment has proven to provide a satisfying resistance to corrosion in hot and concentrated nitric acid,  $\text{HNO}_3$ , containing oxidizing species. In this case, these species come from the recycling process of the nuclear spent fuel. This process enables an optimized use of nuclear energy resources, and provides a way to reuse up to 96% of the spent fuel. In France, it results from the recycling process of nuclear fuel an important saving of the natural uranium resources. Furthermore, it enables to extract the ultimate wastes that can be then glazed and stored in a limited volume and controlled radiotoxicity. One of the first steps of the process consists in the immersion of the fuel assembly (preliminarily sheared) in concentrated nearly boiling  $\text{HNO}_3$ . The fuel assembly dissolves, releasing in solution many species such as uranium, plutonium, minor actinides, and fission products. These species enhance the oxidizing character of  $\text{HNO}_3$ , which is already an oxidizing agent, as the nitrogenous species it contains may already reduce at high potentials.

With the Si enrichment, the Uranus S1N SS revealed to be a good candidate for such environment [2]. Firstly, when oxidizing species are added to the environment, its corrosion rate is lower than for the 304L SS, which is a very similar alloy but without Si [3, 4]. Secondly, even when conditions are so oxidizing that the passivity of the steel breaks down and the material enters in its “transpassive domain”, the Uranus S1N SS’s surface remains homogeneously dissolved, while the 304L SS displays a localized attack of the surface at grain boundaries called intergranular corrosion [4-10]. On the other hand, the Uranus S1N SS dissolves at higher rates than the 304L when the environment is less oxidizing, for example in pure  $\text{HNO}_3$  [11-13]. This paradox, among others that will be discussed later, motivated further investigations on the role of Si in the corrosion resistance properties of the Uranus S1N in hot and concentrated  $\text{HNO}_3$  containing oxidizing species.

The dissolution rate of stainless steels is drastically lowered thanks to a particular oxide interface spontaneously created at the surface, called the passive layer. Investigating this interface is therefore a crucial aspect for the material lifetime forecasting. In the case of the Uranus S1N SS, the Si revealed to be present in high concentration in the passive layer [4, 6]. It is therefore natural to examine how Si at the interface between the alloy and the environment impacts its resistance to corrosion. Four main issues arise from it:

1. How can Si preserve the SS passivity, even in very oxidizing conditions? In particular, the impact of Si on the reduction reaction –mechanisms and kinetics- and on the oxidation reaction will be identified.
2. How does Si influence the stability of the passive layer (thermodynamics)? More precisely, how does Si modify the required energy for the formation of the passive layer?
3. Are the kinetics of passive layer formation impacted by the presence of Si?

4. Does Si play a role during the passive-transpassive transition when the potential is elevated (corresponding to very oxidizing conditions)?

To explore these four issues, the comparison with the 304L SS was used, as it presents a similar composition to the Uranus S1N SS but with a low concentration in Si (0.3 wt. %). Electrochemistry tools were mainly used to measure *in situ* the characteristics of the metal-electrolyte interface. Electrochemistry, as an interdisciplinary science that describes chemical transformations involving electronic transfers, was complemented by classical metallurgists' means such as *ex situ* surface analysis. Another particularity of the present work was the use of a chemical analysis of the electrolyte online with the electrochemistry measurement, enabling the simultaneous measurement of both electrical and quantitative chemical analysis.

Four publishing projects were made out of this multiscale and multidisciplinary approach. Therefore, a particular format of dissertation was chosen. Firstly, a state of the art will bring the reader from the industrial context to the interest found in the study of the passive layer. An experimental section will help the reader understanding the four chapters that will follow. Each chapter will be introduced by several paragraphs explaining the flaws in the state of the art and/or the calculations and methods and the experimental strategy the chapter is based on. Results will be synthetized and conclusions given, then the associated publication project containing the exhaustive results will state in its latest version, either published or ready to be submitted. One of the goals of this presentation format was to highlight both the academic dimension of the present work and the industrial interest. Aiming also at this last purpose, unachieved experiments will be discussed in a separate final part, in order to raise further questions and perspectives related to the four main issues of the thesis. Eventually, the reader will eventually find conclusions and general perspectives at the end of this dissertation.

# **I**NTRODUCTION (FR)

**1. « La corrosion est la mauvaise conscience du métallurgiste, le prix à payer pour ce gaz d'électrons libres qui assure la cohésion métallique et les propriétés attractives des métaux. [...] Trop souvent les métallurgistes et les corrosionnistes s'ignorent mutuellement.**

Les uns considèrent la corrosion comme une plaie qui demande certes un remède, mais un remède que l'on apporte *a posteriori* ou une méfiance *a priori*. Les autres sont persuadés que l'on a tout dit d'un alliage quand on a donné sa composition et de sa tenue à la corrosion quand on a spécifié le milieu. », Yves Bréchet [1]. L'idée que l'on ne pouvait appréhender la corrosion d'un matériau dans un milieu donné par un unique point de vue fût un véritable moteur du présent travail de thèse.

Ces travaux se sont intéressés au comportement en corrosion d'un acier austénitique inoxydable enrichi en silicium (3,5 % m.), l'acier Uranus S1N. Cet enrichissement est à l'origine d'une tenue en corrosion satisfaisante de l'acier dans un milieu auquel il est destiné, l'acide nitrique chaud et concentré contenant des espèces oxydantes, que l'on retrouve notamment au cours du procédé de traitement-recyclage du combustible nucléaire usé.

Le traitement-recyclage du combustible nucléaire usé permet de tendre vers une production optimisée (en termes de ressources) de l'énergie nucléaire, et offre la possibilité de récupérer et de réutiliser jusqu'à 96 % du combustible usé. L'ensemble des procédés du traitement-recyclage du combustible nucléaire usé aboutit ainsi, en France, à une économie annuelle importante des ressources naturelles en uranium. Par ailleurs, les déchets ultimes issus de ces procédés sont vitrifiés et stockés dans un volume limité, avec une radiotoxicité maîtrisée. Une des premières étapes de ce traitement-recyclage consiste à plonger les assemblages de combustible cisailés dans une solution d'acide nitrique concentré à une température proche de l'ébullition. Au cours de cette dissolution, de nombreuses espèces

issues du combustible à recycler (uranium, plutonium, actinides mineurs, produits de fission) vont se trouver en solution sous forme ionique. Si l'acide nitrique est à lui seul un oxydant, c'est-à-dire contenant des espèces azotées capables de se réduire à des potentiels élevés, la présence de ces ions métalliques peut encore augmenter son pouvoir oxydant. Or l'enrichissement en Si dont a bénéficié l'acier Uranus S1N fait de lui un candidat satisfaisant pour les installations contenant ce type d'électrolyte [2]. D'une part, en présence d'espèces oxydantes, il présente une vitesse de corrosion plus faible qu'un alliage homologue sans Si tel que l'acier 304L (également utilisé pour les installations de traitement recyclage du combustible usé) [3, 4]. D'autre part, même lorsqu'il est soumis à un électrolyte si oxydant qu'il se trouve porté dans son domaine transpassif, sa corrosion demeure généralisée à l'ensemble de la surface, et l'on observe aucune attaque localisée de type intergranulaire contrairement à l'acier 304L [4-10]. Parallèlement à ces propriétés, l'acier Uranus S1N se dissout plus rapidement que son homologue sans Si dans des conditions moins oxydantes, comme en acide nitrique seul par exemple [11-13]. Ce paradoxe (et d'autres motivations non détaillées ici) a donc conduit à la nécessité d'apporter de nouveaux éléments de compréhension sur le rôle du Si dans les propriétés de tenue en corrosion de l'acier Uranus S1N en milieu acide nitrique chaud et concentré et en présence d'ions oxydants. C'est l'objectif principal de ce travail de thèse.

C'est grâce à une interface d'oxydes particulière spontanément présente à la surface d'un acier inoxydable, la couche passive, que la vitesse de corrosion de ce dernier est ralentie. La connaissance de cette interface est donc d'intérêt pour mieux appréhender la durée de vie du matériau du point de vue de la corrosion. En outre, le Si de l'acier Uranus S1N se trouve être présent dans cette couche passive en grande quantité [4, 6]. On peut donc légitimement s'interroger sur la manière dont ce Si présent dans les oxydes peut ou non impacter le phénomène de passivité. Dans ce travail, cette interrogation a été traitée sous différents angles



au travers de quatre questions majeures qui ont structuré ce travail de thèse. Ces quatre questions ont permis de balayer l'ensemble des composantes de la corrosion pouvant être affectées par la couche passive, de la cinétique de réduction du milieu à l'interface métal-électrolyte au mécanisme de rupture de passivité à haut potentiel (transpassif), en passant par une détermination des caractéristiques thermodynamiques et cinétiques de cette interface :

5. Comment le Si préserve-t-il la passivité de l'acier en conditions oxydantes sévères ?

En effet, comme discuté plus haut, il apparaît important de pouvoir comprendre pourquoi l'acier Uranus S1N reste passif en milieu acide nitrique contenant des ions oxydants, alors que d'autres aciers (comme l'acier 304L) vont perdre cette passivité en étant portés dans leur domaine transpassif (avec une corrosion de type intergranulaire). En particulier, c'est l'influence du Si sur les mécanismes et cinétiques de réduction et d'oxydation qui est analysée à travers ce premier volet.

6. Le Si modifie-t-il la formation de la couche passive sur le plan thermodynamique ?

En étudiant notamment si le Si modifie l'énergie (au travers du potentiel électrochimique) nécessaire à la formation de la couche passive.

7. Le Si impacte-t-il la cinétique de formation-dissolution de cette couche passive ?

8. Le Si joue-t-il un rôle dans le mécanisme de la transition passif-transpassif lorsque l'acier est porté à plus haut potentiel ?

La réponse à ces différentes questions s'est principalement reposée sur la comparaison de l'acier Uranus S1N avec l'acier 304L dont la composition est proche mais qui n'est que très faiblement allié au Si (0,3 %m.) et également plus faiblement allié au nickel (10 % m.). Sur le plan des outils, c'est l'électrochimie qui a été choisie comme outil principal d'étude de l'interface *in situ* entre le matériau et son milieu. Science interdisciplinaire décrivant les transformations chimiques de la matière mettant en jeu des échanges d'énergie électrique, elle a été complétée par d'autres outils plus classiquement utilisés en métallurgie permettant

l'analyse chimique et morphologique des surfaces, la plupart du temps *ex situ*. Au cœur de ces travaux, le couplage de la mesure électrochimique à une technique d'analyse chimique élémentaire en ligne a permis d'acquérir *in situ* des informations originales, à la fois électriques et chimiques, sur le comportement de l'interface métal-électrolyte.

A travers cette approche à la fois multi-échelles et pluridisciplinaire, quatre publications ont été réalisées (publications publiée ou à soumettre). Un format de rédaction particulier s'est articulé autour de ces quatre projets. Le texte s'ouvre sur un état de l'art général visant à expliquer les orientations de recherche choisies pour ce travail. Il est suivi d'une partie expérimentale à part entière. Puis, chacun des quatre chapitres est introduit par un état de l'art dédié à l'expérience proposée, une explication de la stratégie expérimentale adoptée, et un résumé de ses résultats et conclusions principaux. Chacun de ces quatre chapitre ayant donné lieu à une publication (trois publiées et une à soumettre), les textes associés sont joints. Le lecteur trouvera à la suite un recueil d'expériences inachevées pouvant éclairer ou soulever de nouvelles questions et perspectives. Enfin, une conclusion et une proposition générale de perspectives seront apportées. A l'image de cette première introduction, une traduction française sera proposée pour la conclusion et perspectives.



# STATE OF THE ART

*A Man may make a Remark—  
In itself—a quiet thing  
That may furnish the Fuse unto a Spark  
In dormant nature—lain—*

*Let us deport—with skill—  
Let us discourse—with care—  
Powder exists in Charcoal—  
Before it exists in Fire.*

*Emily Dickinson*

*Avant donc que d'écrire, apprenez à penser.  
Selon que notre idée est plus ou moins obscure,  
L'expression la suit, ou moins nette, ou plus pure.  
Ce que l'on conçoit bien s'énonce clairement,  
Et les mots pour le dire arrivent aisément.*

*Nicolas Boileau*



# **S** TATE OF THE ART

## **2. From the industrial context to the interest raised into the study of the passive layer**

### **2.1. Industrial context, history of development, fabrication and metallurgy of the Uranus S1N SS**

#### **2.1.1. Context – Electrolyte and materials**

In the present work, an austenitic stainless steel containing low amount of C and enriched in Si was studied. This SS called Uranus S1N was designed for hot and concentrated nitric acid in presence of oxidizing species. This very aggressive electrolyte is used in the recycling process of the nuclear waste, known as PUREX (Plutonium Uranium Refining by Extraction). This process was performed in 1945 and then first exploited in 1958 in Marcoule until 1997. It requires a first step of dissolution in  $\text{HNO}_3$  of the sheared nuclear waste material which contains mostly U, Pu, other actinides and fission products. Then, following a liquid-liquid extraction process, U and Pu are recycled. Over the whole process, the  $\text{HNO}_3$  temperature and concentration vary and lots of different metallic species might elevate its oxidizing character.

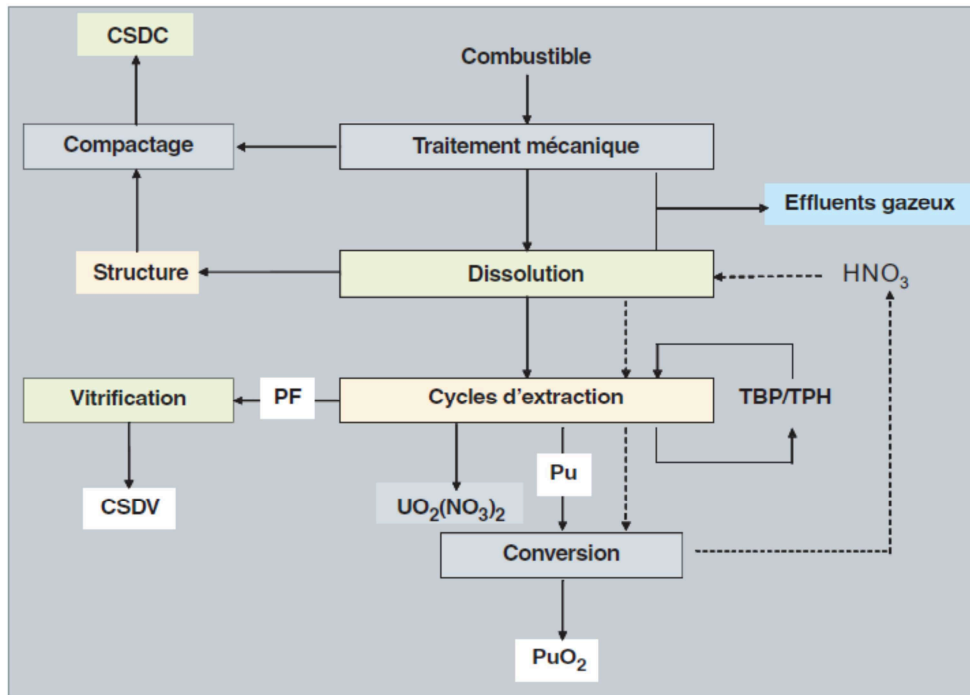


*Fig. 1. PUREX process main steps [14]*

Therefore, different materials can be chosen as good candidates to resist premature ageing of the different parts of the plant regarding their corrosion behavior in the different possible conditions (Fig. 2).

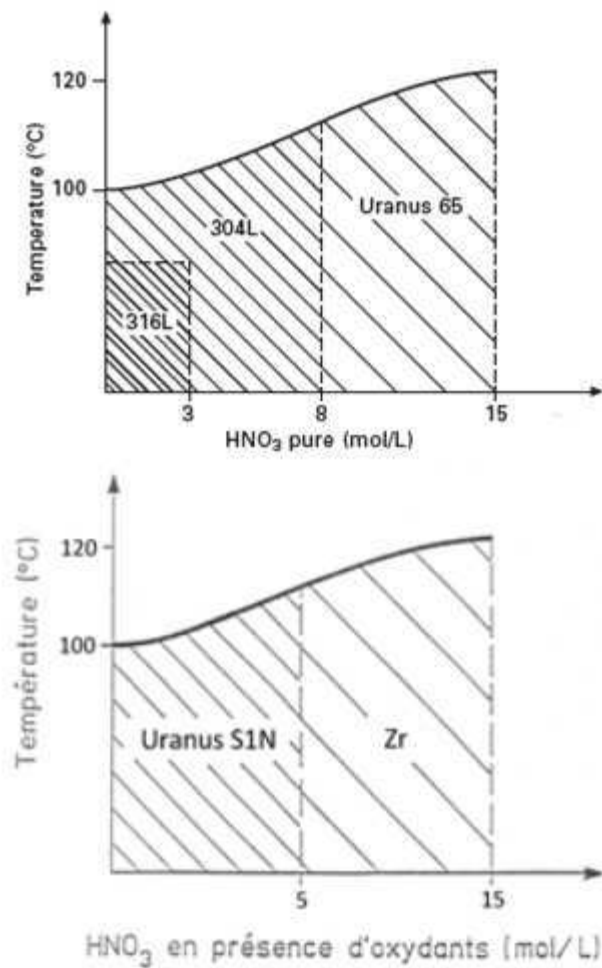


*Fig. 2. Possible materials depending on HNO<sub>3</sub> temperature, concentration, concentration in oxidizing species[2]*

SS containing low C such as AISI 304L, 316L and Uranus 65 are usually chosen for pure HNO<sub>3</sub> containing parts of the the plant, and Uranus S1N SS is especially designed for moderate concentrations in oxidizing species. Zr can also be used for the most aggressive electrolytes under certain circumstances.

### **2.1.2. History of the development of the Uranus S1N SS**

Low C austenitic SS containing Si were developed over the 60s because of the growing concerns about intergranular corrosion phenomenon observed for several materials in certain electrolytes (for example the 304L in the presence of oxidizing species). Numerous studies



can be found on the addition of Si in Fe-Cr-Ni alloys very similar to the 304L or 316L SS. It was shown that for alloys containing more than 16 wt.% in Cr and 14 wt.% in Ni, adding more than 2 wt.% in Si could efficiently prevent from the intergranular attack (IGC) [5, 10, 15]. An important decrease of the mass loss in the presence of Cr(VI) species is also measured as shown in Fig. 3 from Desestret *et al.* [3].

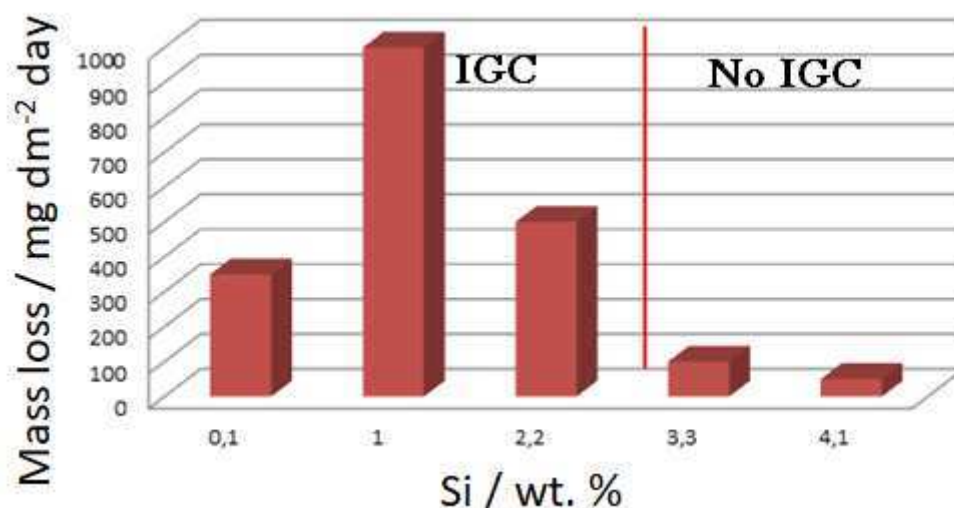
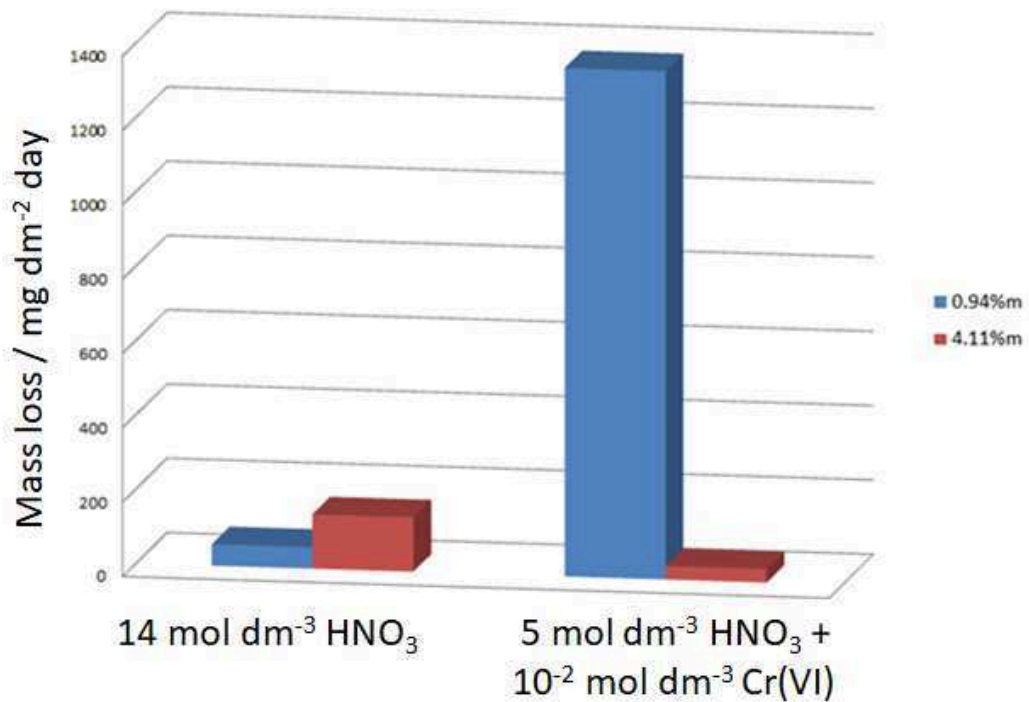


Fig. 3. Influence of the Si content on the mass loss of a 18Cr – 14Ni alloy in boiling  $5 \text{ mol dm}^{-3} \text{ HNO}_3$  containing Cr(VI) ( $2 \cdot 10^{-2} \text{ mol dm}^{-3}$ ) [3]

Similar results were found by Armijo and Holtzer in the 70s [4,16]. Also, Si tends to increase the corrosion rate of the alloy between 0.1 and 1 wt.%. At lower and higher contents, the corrosion rates are found to be very low, especially over 3 wt.%. This tendency could reveal a competition between two contrary effects provided by the Si, one that leads to an increase of the corrosion rate while the other tends to inhibit it.

The relative corrosion rate between two SS that contain respectively 0.94 and 4.11 wt.% varies depending on the presence of oxidizing species. It was shown by Ghiban and Cosmealta [12] that in pure  $\text{HNO}_3$  the Si-rich SS was dissolving at higher rate, as shown in Fig. 4 in  $14 \text{ mol dm}^{-3}$  boiling  $\text{HNO}_3$ . But when Cr(VI) is added, the opposite result is obtained and the low Si SS corrodes faster while displaying a high IGC morphology.



*Fig. 4. Corrosion rates obtained in 14 mol dm<sup>-3</sup> boiling HNO<sub>3</sub> and in 5 mol dm<sup>-3</sup> boiling HNO<sub>3</sub> containing 2.10<sup>-2</sup> mol dm<sup>-3</sup> of Cr(VI) depending on the Si content in an 18Cr-15Ni alloy [12]*

### 2.1.3. Metallurgy – Fabrication and how is the Si in the bulk material

#### 2.1.3.1. Fabrication

The Uranus S1N SS is a vacuum casted material because its composition has to be well controlled especially containing as few C as possible [17]. It is then casted in ingot before annealing and overhardening. It is maintained at a high temperature between 1000 and 1150°C then rapidly cooled to obtain a homogeneous austenitic phase where all the alloying elements, especially C and N, are in solid solution [18]. Carbonitrides are indeed soluble in austenite at high temperatures and this state can be maintained if the cooling is sufficiently rapid. Ferritic phase  $\delta$  can also appear for certain steels at higher temperatures than 1100°C and this phase can be preserved over the cooling, which could be a problem because of  $\sigma$  phase precipitation it would be responsible for. Therefore, an upper limit of temperature was

introduced for the annealing. The duration of heating is about 0.7 to 2.5 minutes per mm. The longer the heating, the lower the residual constraints, and short heating durations limit the growth of the grains [19].

#### **2.1.3.2. Chemical composition**

As Si content was fixed, then the other elements concentrations had to be adjusted. Si is an alpha stabilizing element like Cr. Therefore, the Ni concentration must be elevated in order to promote austenite  $\gamma$ . Ni also facilitates the plastic deformation [20]. Uranus S1N C content is maintained low ( $C < 0,015$  wt. %) and it also contains few Nb. Nb prevents from local carburization or nitrocarburization of Cr, known to promote IGC. In the 70s, few adjustments of the chemical formulation of the Uranus S1N were made, for example, Al was added to stabilize N [21]. Nb could also stabilize N at higher concentration, but the weldability would then have been affected.

### **2.2. The metal-electrolyte interface that pilots the corrosion rate of the material**

In order to understand the phenomena involved in the corrosion of the Uranus S1N SS, and especially to understand the impact of Si, the present work was specifically dedicated to the interface between the metal and the electrolyte. The Uranus S1N SS displays a typical oxide layer called passive layer that spontaneously covers its surface when immersed into an oxidizing electrolyte such as hot and concentrated  $\text{HNO}_3$ .

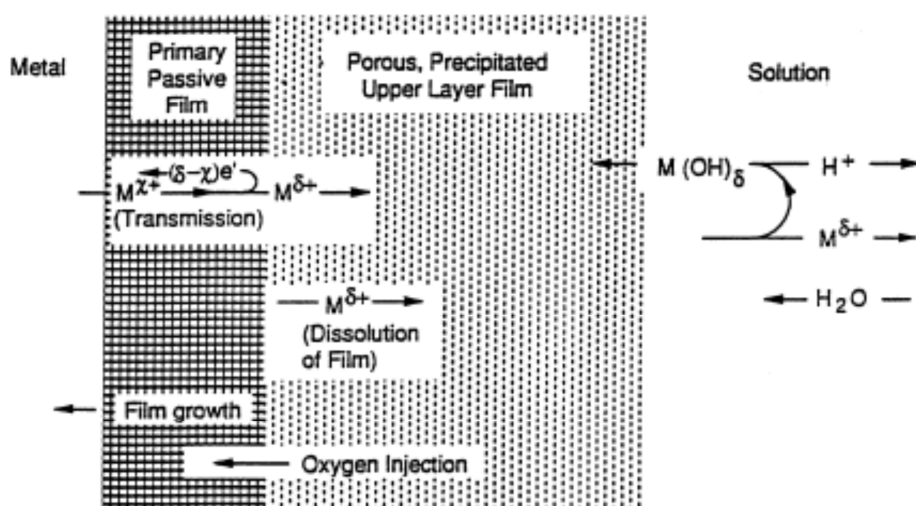


*Fig. 5. Schematic processes involved in the formation of a passive film at a metallic interface [22]*

Usually, passive layers of austenitic SS formed in  $\text{HNO}_3$  are nanometric layers composed by several alloying elements from the bulk material [22-24]. These oxides are organized in several layers as shown in Fig. 5 [22, 25, 26]. They ensure a protection for the SS against dissolution in the acidic medium [27-31]. Their chemical composition can be different from the bulk composition, because a selective dissolution occurs between the alloying elements [32-34]. In particular, for austenitic SS, Cr dissolution happens to be slower than Fe, and therefore a Cr rich oxide layer is established at the surface.

It was also shown that Si occupies an important place in the Uranus S1N oxide layer, as more than 30 at.% can be detected [6]. As indicated previously, this could be the result of a slower dissolution of Si versus Fe. However, this selectivity has never been clearly shown.

If the oxide layer enables to lower the dissolution rate of the material, it also may impact the cathodic reaction occurring simultaneously. This reaction needs indeed as much electron quantity as it is required for the oxidation to occur, and these electrons are provided nearby the metal electrolyte interface. The composition and structure of the passive layer therefore

can play a significant role on the mechanisms and kinetics of the reduction reaction. Based on this assumption, a large amount of studies have tried to elucidate the mechanisms involved in the  $\text{HNO}_3$  electrolyte reduction reactions on inert materials then at passive interfaces [35-40].

As the oxide layer might play such an important role both concerning cathodic anodic reactions, the great amount of Si in the Uranus S1N oxide layer naturally orientated the present work experimental strategy to a comparison with the 304L SS which composition is very similar but contains only 0.3 wt.% in Si. The general corrosion behavior of the 304L has been largely studied over the past decades [4-6, 9, 41-44] and sometimes compared to Si rich similar alloys [6]. One can notice that the Uranus S1N SS contains also more Ni (15 wt.% for the Uranus S1N whereas the 304L contains only around 10 wt.%). However, this element is never detected in the passive layer. According to the literature it is expected to be rapidly oxidized under a soluble form [45]. Moreover, the ratios between each elements are very comparable between the two stainless steels. A hypothesis will be thus made that the Ni will not impact drastically the corrosion behavior of the steel between the two compositions. The measured composition of the materials used in the present work will be detailed in the experimental section.

### **2.3. The passive layer and the electrochemical behavior of austenitic stainless steels in acidic media**

As previously mentioned, the passive layer is responsible for a limitation of the oxidation current density. On the anodic branch of a I-E curve of an austenitic SS in acidic medium, three domains of potential can be characterized, where the oxidation current density varies with the stability of the passive layer. This passive layer is almost inexistant in the active domain at low potentials, then starts to cover the surface and provides its protective property

in the passive domain, and eventually loses its stability when entering the transpassive domain at high potentials (Fig. 6). The electrochemical domain in which the material will remain is determined by equilibrium of electron exchanged between the cathodic and the anodic reactions. The nature of the cathodic process and its oxidizing character (that can be evaluated from its own equilibrium potential) is a determining factor for the passivity of the alloy. The cathodic process happening on the vicinity of the surface (at the surface or close), the passive layer has therefore a direct impact on the cathodic reaction. This reinforces the interlinked relationship between the cathodic and the anodic reaction and highlights the need for a better knowledge of the Si-rich passive layer.

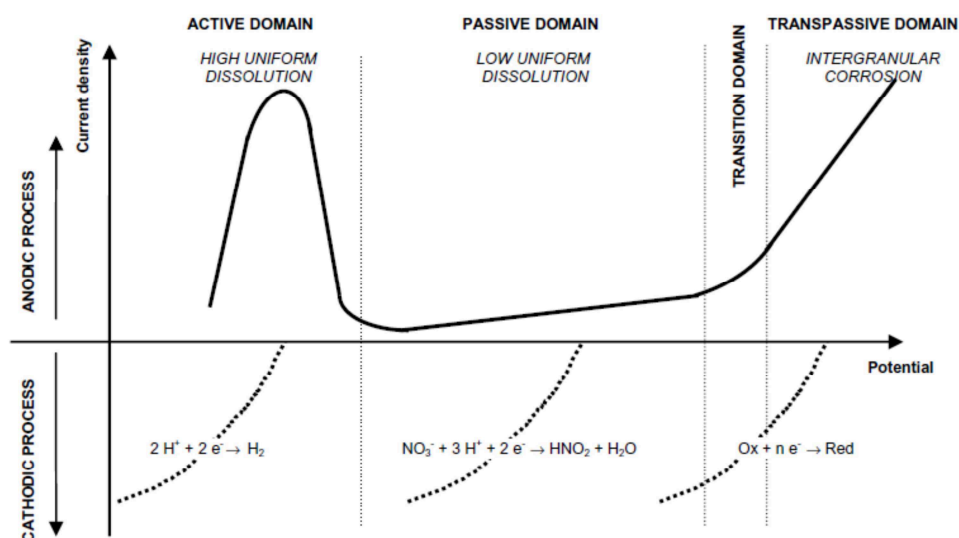


Fig. 6. Typical SS Evans diagram in different acidic electrolytes [2]

Because the cathodic and the anodic reactions are so connected, the present work will open on a general study of the impact of Si on the anodic and cathodic current densities from polarization curves in various  $\text{HNO}_3$  electrolytes, containing or not oxidizing species. This will enable to highlight the impact of the Si on the cathodic reaction (mechanism and kinetics) especially when oxidizing species will be added. It will also show how the passivity is

affected by the Si alloying. Then, to access thermodynamic and kinetic properties of the passive layer, the use of transitions between the three domains of potential will be used. For example, the passive-active transition will enable to access some thermodynamic properties of the oxide, and successive polarizations between these two domains will provide more information on the kinetics of formation of the oxide layer, for the first time *in situ* in  $\text{HNO}_3$ . The transpassive domain will be naturally chosen to study the inhibition of the intergranular corrosion, and the transients between passive and transpassive will help highlighting possible selective dissolution effects.

## **2.4. Conclusion**

The Uranus S1N was initially formulated for a specific use in hot and concentrated  $\text{HNO}_3$  in presence of oxidizing species; however the explanation on the origin of its satisfying behavior has never been clearly and completely elucidated.

The Si alloying indeed increases the dissolution rate of the steel in pure  $\text{HNO}_3$ , but when oxidizing species are added, it plays a more positive role, because the steel corrodes at lower rates than a regular 304L SS would do. The most probably hypothesis to explain this paradox is that the reduction reaction is kinetically lowered at the Si-rich surface, while the oxidation kinetics are on the otherside increased, and therefore the corrosion potential would remain passive even in highly oxidizing electrolytes. However, this was actually never clearly shown. Therefore, the first chapter of the present work will focus on elucidating the impact of Si on the electrochemical behavior of austenitic SS in pure  $\text{HNO}_3$  and containing oxidizing species. Both cathodic and anodic processes will be investigated through the use of polarization curves.

Furthermore, the passive layer of the Uranus S1N has barely been studied. It is only known to be a Si-rich oxide, probably made of mixed oxide silicates whose thickness and exact composition have never been determined. The second and third chapters of the thesis will focus on providing new insights in the properties of this passive layer, giving both thermodynamic and kinetic new information on the properties of the oxide layer.

Eventually, the transpassive dissolution of the Uranus S1N SS will be investigated. The inhibition of the IGC, while frequently observed in the literature, has found no clear explanation and limited number of hypothesis. Therefore, the last chapter of this present work will aim at providing new elements and hypothesis to explain what is observed in this region of potential when the electrolyte becomes sufficiently oxidizing.





# EXPERIMENTALS

*Up in the air and over the wall,  
Till I can see so wide,  
River and trees and cattle and all  
Over the countryside —  
Robert Louis Stevenson*

*Voulez-vous que verté vous dire ?  
Il n'est jouer qu'en maladie,  
Lettre vraie qu'en tragédie,  
Lâche homme que chevalereux,  
Orrible son que mélodie,  
Ne bien conseillé qu'amoureux.  
François Villon*



# EXPERIMENTALS

## 3. From hypothesis to proof

### 3.1. Materials

#### 3.1.1. Experimental strategy

As mentioned earlier, a similar stainless steel as the Uranus S1N but without Si was chosen to compare, the 304L SS. Even if the 304L SS contains less Ni, ratios between each element are really comparable between the two SS. Moreover, the literature about the 304L SS is sufficiently large.

#### 3.1.2. Stainless steels samples

Uranus S1N samples were prepared from a 35mm thick plate (moulding n° 12723) annealed at 1135°C. 304L samples were prepared from a 10mm thick plate (moulding n°372048) annealed between 1000 and 1100°C. Table 1 provides chemical compositions of the two materials used, determined at the beginning of the thesis using glowing discharge optical emission spectroscopy (GD OES).

*Table 1. Mass composition of the Uranus S1N and 304L SS determined using GD-OES between 10 and 40µm depth (wt. %)*

	Fe	Cr	Ni	Si	Mn	Add.
Uranus S1N	59,8	18,8	15,1	3,5	2,0	0,8
304L	70,3	17,8	9,5	0,3	1,5	0,6

## 3.2. Atomic emission spectroelectrochemistry

### 3.2.1. Experimental strategy

The study of the Uranus S1N SS passivity exploited the characterization of the three

domains of potentials that are the active, passive and transpassive states. An interesting method to investigate these three domains was to couple the electrochemical classical measurement to an online elementary analysis such as atomic emission spectroscopy using induced coupled plasma (ICP-AES). Coupling both techniques was motivated by the following assertions. The conventional electrochemical methods only measure currents and potentials from the redox system: anodic and cathodic current densities can't be distinguished nearby the corrosion potential. Moreover, it remains very difficult to distinguish the anodic current that will be involved in the passive layer formation from the part involved in the dissolution of the material. It has to be mentioned that few techniques enabling oxidation products detection such as ring disk electrode or scanning electron microscopy were nonetheless used in this type of study. Gravimetric measurements of the mass loss occurring over a potentiostatic or galvanostatic measurement could be of interest to separate the anodic from the cathodic contribution, however it is limited to a global mass loss and doesn't give access to any information upon the selectivity of the dissolution that occurs. To solve such problem, one could possibly analyze the solutions and analyze the passive layer formed by surface investigation means, however these informations are both ex situ and punctual, not giving any information on the kinetics for example.

### **3.2.2. Experimental device**

In the early 90s, Ogle et al. developed the Atomic emission spectroelectrochemistry (AESEC) [46]. They achieved coupling an ICP-AES to the electrochemical measurement as shown in Fig. 7 [47].

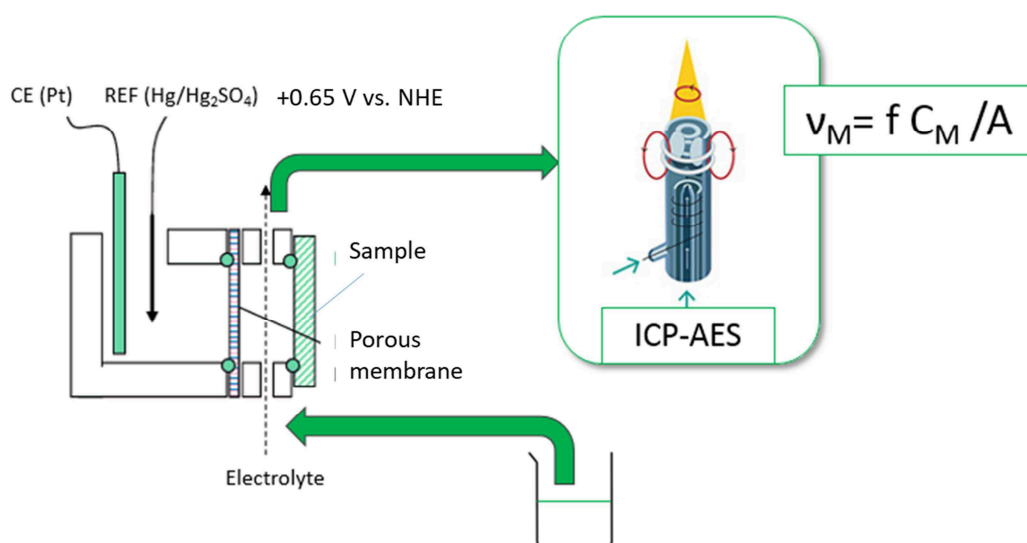


Fig. 7. Experimental AESEC device with  $v_M$ : dissolution rate of  $M$ ,  $f$ : flow rate,  $C_M$ :

concentration in  $M$ ,  $A$ : surface of the sample

The elemental analysis of the dissolved species is real time coupled to the electrochemical measurements that enable to:

- Distinguish anodic from cathodic current contribution,
- Distinguish current contribution to the passive layer formation from contribution to the dissolution
- Determine the possible selectivity of the dissolution

The electrolyte is brought from a reserve to the ICP-AES using a peristaltic pump whose rotation speed and capillaries diameter control the flow rate. The electrolyte in contact with the sample (working electrode) must be carefully controlled in terms of flow rate and volume. Therefore, the WE is in contact with a small volume of electrolyte separated from the rest of the cell by a porous membrane. In the biggest part of the cell can be set the counter and the reference electrodes that are respectively a small Pt grid and a small mercurous sulfate electrode. The smallest compartment has a volume of  $0,2 \text{ cm}^3$  and the surface of the electrode

in contact with the solution is 1 cm<sup>2</sup>. the sealing between the sample and the flow cell is ensured by a pneumatic compression. Toric joint prevents from leakage. The electrolyte is nebulized in a chamber before accessing the plasma where it is analyzed by two optical captors, one that is an adjustable monochromator and the other one which is a polychromator. The nebulizer and the chamber are chosen to minimize the residence time to enable the simultaneous measurements from both electrochemical and elemental analyses.

The data acquisition system is slightly modified from a regular ICP-AES data acquisition system, in order to collect on-line data from the potentiostat, and also get rid as much as possible of the hydrodynamics of the ICP device. However, when necessary, an additional mathematic correction of the hydrodynamics of the device will be performed. Detailed calculation will be explained later on. The whole acquisition system enables to measure on the same time scale the electrochemical measurements and the elemental analysis from the ICP. Each alloying element can be measured independently using the polychromator and the ICP-AES signal, after a classical standard calibration for each element of interest, can be translated into a dissolution rate  $v_M$  knowing the flow rate  $f$ , and surface of the sample. The experiments were realized with the electrochemical flow cell using plane SS samples as working electrodes. Average flow rate was 2.9 mL dm<sup>-3</sup> and was carefully measured after each experiment. The porous membrane was made of cellulose, and the electrolyte and sample could be heated from a water bath and heating copper block pressed on the sample but electrically isolated.

### 3.3. Combining *in situ* and *ex situ* analysis

To understand better the *in situ* results obtained with electrochemistry or AESEC, some *ex situ* surface analyses were performed.

### 3.3.1. 200 mL reactor electrochemistry measurements

For basic electrochemistry, a double jacketted reactor of 200 mL was used. In this reactor were put three electrodes. The working electrode was made of a bullet shape sample of the steel to be studied, a Pt grid was used as the counter electrode, and a mercurous sulfate electrode was used as a reference (+0.65 V vs. NHE) (Fig. 8).

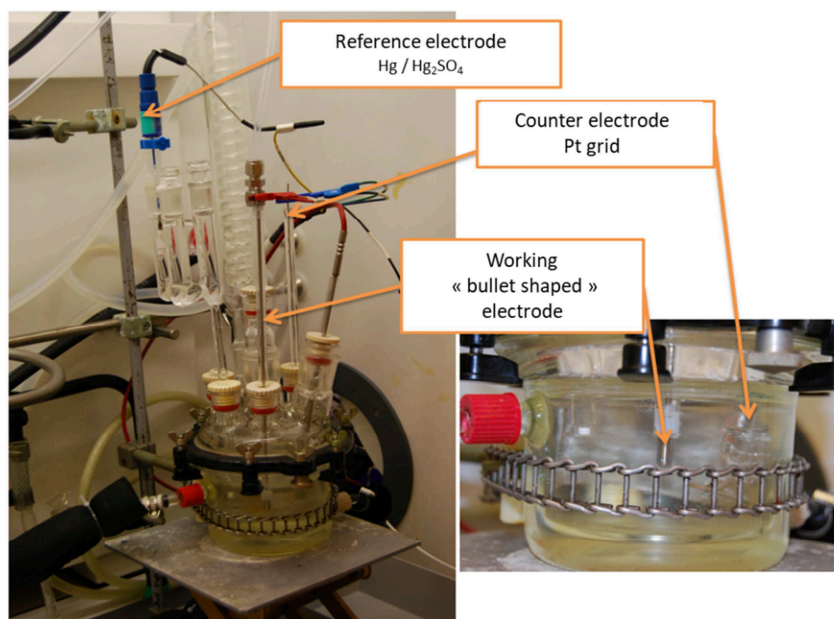


*Fig. 8. Picture of the experimental set-up for electrochemical measurements used in the first chapter*

The double jacketted reactor is heated by a thermostat using oil at 100°C. A VSP Potentiostat (BioLogic®) was dedicated to these experiments.

### 3.3.2. Optical microscopy and scanning electron microscopy

Optical and scanning electron microscopies enabled to observe the corrosion morphology of the samples, especially the intergranular attack that could occur in the transpassive domain of the steels. Observations were performed using a reverse optical microscope (Olympus GX51). Two scanning electron microscopes were used: SEM-Leo (Leo 1450 VP Zeiss) and SEM-FEG (Ultra 55 Zeiss).



### 3.3.3. X-ray photoelectron spectroscopy

X-ray photoelectron spectroscopy (XPS) is a well known technique associated to the study of the passive layers. In the present work, it has been largely used to analyze the chemical composition of the oxides in various types of conditions. Moreover, the XPS measurements give precious information about the close environment of the excited atoms. It enabled to confirm that the high content in Si in the oxide layer was or not associated to mixed silicates rather than pure SiO<sub>2</sub> for example [14]. The XPS measurements were performed using a Thermofisher Escalab 250 XI spectroscope, using a monochromatic X-ray source Al-K $\alpha$  (1486.6 eV). The instrument was calibrated in energy with the Ag Fermi level (0 eV) and the 3d<sup>5/2</sup> core level of metallic silver (368.3 eV). The C-1s signal was used to correct a possible charge effect: the CC/ CH contribution of C-1s spectra was fixed at 285.0 eV. The analysis zone consisted of a 900  $\mu$ m diameter spot. The data processing was performed using the commercially available *Avantage*<sup>TM</sup> software. For the fitting procedure, a Shirley background has been used and Lorentzian-Gaussian (L/G) ratio was fixed at 30 %. Main parameters used to decompose XPS spectra are presented in Table 2.

*Table 2. Parameters used for the deconvolution of XPS spectra (Avantage<sup>TM</sup> software)*

*Binding energies and full width at half maximum (FWHM)*

	[ Fe Ox ] / at. %		[ Cr Ox ] / at. %			[ Si Ox ] / at. %	
	Fe - 2p <sub>3/2</sub>	Fe - 2p <sub>3/2</sub>	Cr - 2p <sub>3/2</sub>	Cr - 2p <sub>3/2</sub>	Cr - 2p <sub>3/2</sub>	Si - 2p	Si - 2p
Binding energy / eV	709.69	712.07	576.26	577.32	578.99	102.05	102.65
FWHM / eV	2.36	2.93	1.08	1.92	1.71	1.36	1.32

### 3.3.4. Transmission electron microscopy and energy dispersive X-ray spectroscopy

Cross-sections of materials were analyzed using transmission electron microscopy (TEM) in high resolution imaging mode. In order to identify zones of interest on each sample, electron backscattered diffraction (EBSD) was performed at the surface of the materials prior to sample cross-section elaboration, using a scanning electron microscope field emission gun ZEISS Gemini 500 scanning electron microscope (SEM), a *Hikari Super* charge coupled device (CCD) camera, and OIM<sup>TM</sup> Data collection and OIM<sup>TM</sup> Analysis software for the acquisition and exploitation of the data. Cross-section TEM lamellas were thinned using focused ion beam (FIB) FEI Strata DB400 and analyzed with a FEI Tecnai Osiris TEM using a an accelerating voltage of 200 kV and equipped with ChemiSTEM<sup>TM</sup> and GIF Quantum® detectors X-ray energy dispersive spectroscopy (X-EDS).

One key point of the experimental strategy of the present work was therefore to associate *in situ* and *ex situ* results combined to the comparison between the two stainless steels whose Si content is different, and take advantage of the whole electrochemical anodic branch to investigate the impact of Si on the corrosion behavior of the Uranus S1N SS.

#### Note to the reader

The major parts of the experiments was actually performed by the student. AESEC and classical electrochemistry were directly performed by the student, and XPS and TEM-EDX were respectively performed in narrow collaboration with Frédéric Miserque (CEA/DEN/DANS/ DPC/SCCME/LECA) and Karine Rousseau (*Serma Technologies*). TEM-EDX analyses of the 304L SS in the transpassive domain had been performed by Karine Rousseau during the PhD thesis of Elsa Tcharkhtchi [33].



# RESULTS

*If it is true, what the Prophets write,  
That the heathen gods are all stocks and stones,  
Shall we, for the sake of being polite,  
Feed them with the juice of our marrow-bones?*

**William Blake**

*La lumière, le Temps, l'Espace, l'Énergie  
Furent jadis des dieux de la mythologie :  
La Physique a la sienne et nous les a ravis  
Sous l'autorité de sa Muse rigoureuse.  
Notre vie en est-elle ou moins ou plus heureuse,  
À ton avis?*

**Jacques Réda**



## **4.1. Silicon enrichment of an austenitic stainless steel – impact on electrochemical behavior in concentrated nitric acid with oxidizing ions**

### **4.1.1. Introduction, the flaws in the literature**

As it was shown in the State of the Art chapter, literature counts numerous studies about SS with or without Si alloying in various electrolytes. However, these studies are difficult to compare as the conditions are sometimes very different in temperatures, concentrations, etc. It also reveals some paradoxes. For example, the relationship between the spontaneous corrosion rate and the state of dissolution the steel is actually involved in (passive or transpassive) is not always clear. Armijo *et al.* [4] have shown that a Si-rich austenitic SS in presence of certain oxidizing species could remain passive while the Si-low SS was transpassivated. They formulated the hypothesis that the decrease of the reduction kinetics at the Si-rich interface was responsible for this phenomenon. It was also measured by Robin *et al.* [6] that the passive current density of the Uranus S1N was more intense than for the 304L SS in the same conditions.

Moreover, the most studied oxidizing species in the state of the art was Cr(VI). However, it was shown by Plante that Cr(VI) altered the anodic branch of the Si-rich SS [48], which complicates the interpretation of the results as long as the oxidizing species is not a simple oxidant species. (Fig. 9).

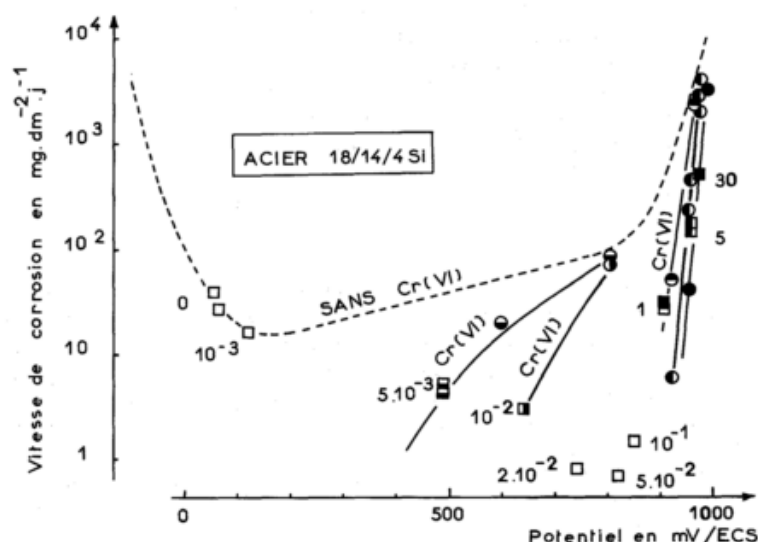


Fig. 9. Corrosion rate of a Si-rich SS as a function of potential in boiling  $5 \text{ mol dm}^{-3}$

$\text{HNO}_3$  with different concentrations in Cr(VI) (Plante [48]).

■ : at  $E_{\text{corr}}$  / ● : potentiostatic measurement / --- : polarization curve without Cr

Because of the decrease that Cr(VI) provokes on the oxidation current of the Si-rich SS, the Si-rich SS even corrodes at a lower rate in the presence of Cr(VI) than in pure  $\text{HNO}_3$  and obviously at a lower rate than the 304L SS. In fact, two phenomena are actually observed: one is the transpassive dissolution of the 304L triggered by the oxidizing character of the Cr(VI) that the Si-rich SS doesn't suffer from because of kinetically lowered reduction reaction, and the second one is the improved passivity of the Si-rich SS because of the Cr(VI).

#### 4.1.2. Experimental strategy

To distinguish these two phenomena, different oxidizing species were chosen. Three different electrolytes were then used: pure  $\text{HNO}_3$ ,  $\text{HNO}_3$  containing V(V),  $\text{HNO}_3$  containing Cr(VI). V(V) was chosen as a purely oxidizing ion, while Cr(VI) was chosen for the previously mentioned “enhancing passivity” property at the Si-rich surface. This first chapter aimed at bringing an overall sight of the impact of Si on the electrochemical behavior of SS in conditions close to the industrial electrolyte.

V(V) was chosen for its stability at 100°C under its fifth oxidation state, and for it can be assimilated to a pure oxidant that doesn't alter the passivity [35]. Historically, V(V) was also used to simulate Np species that can be found in the real conditions but that are more delicate to use because of their radioactivity.

As mentionned previously, the 304L SS is used as the material of comparison. XPS analyses, TEM and EDX measurements enabled to get general informations about the thickness and composition of the passive layers of both materials.

#### **4.1.3. Main results**

Fig. 10 displays the polarization curves obtained at 100°C in the three electrolytes for the Uranus S1N and the 304L SS.



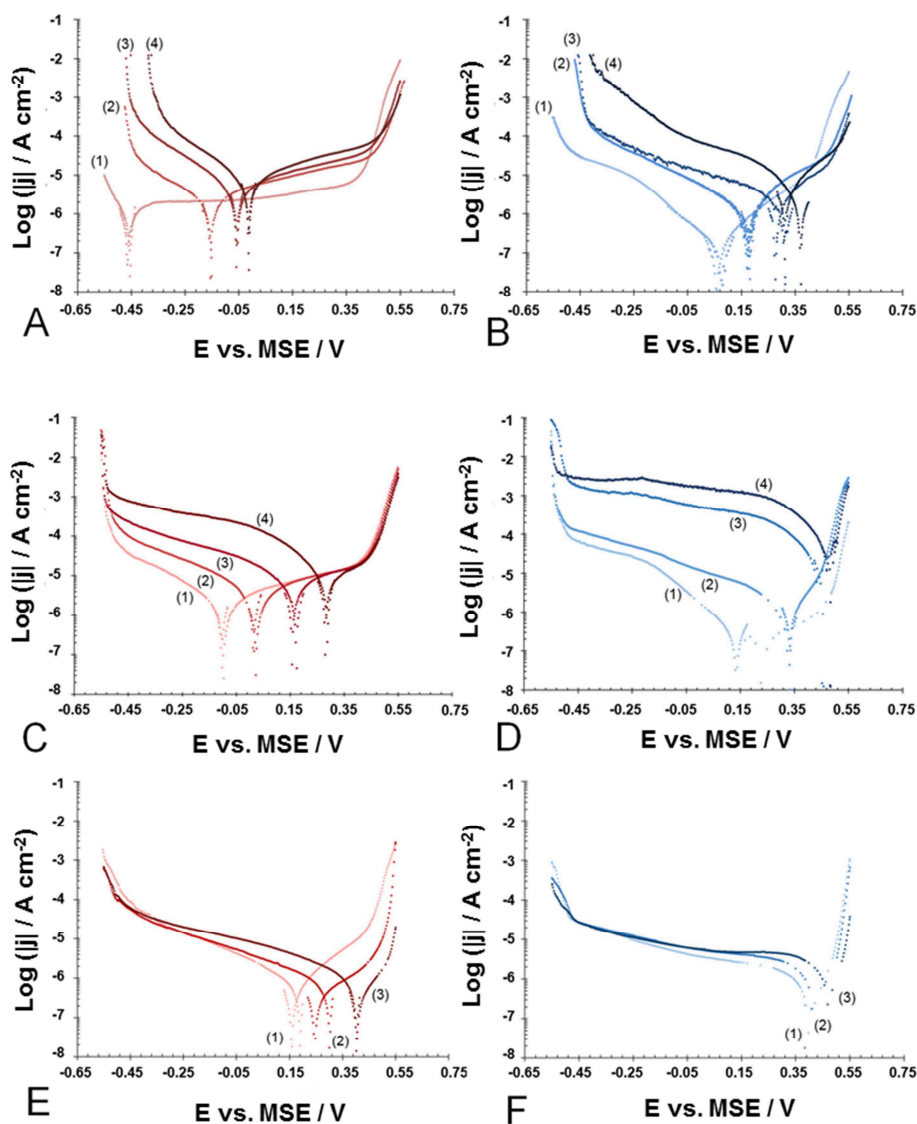


Fig. 10. Linear polarization curves ( $v = 0.2 \text{ mV s}^{-1}$ ) in  $4 \text{ mol dm}^{-3} \text{ HNO}_3$  at  $100^\circ \text{C}$  for the Uranus S1N SS (red) and 304L SS (blue) – natural convection

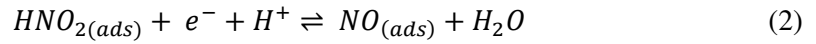
(A / B):  $\text{HNO}_3$  1 (1), 4 (2), 6 (3), 9 (4)  $\text{mol dm}^{-3}$

(C / D) :  $\text{HNO}_3$   $4 \text{ mol dm}^{-3}$  ; V(V)  $1.9 \cdot 10^{-4}$  (1),  $1.9 \cdot 10^{-3}$  (2),  $9.8 \cdot 10^{-3}$  (3),  
 $3.9 \cdot 10^{-2}$  (4)  $\text{mol dm}^{-3}$

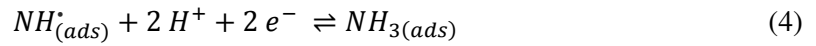
(E / F) :  $\text{HNO}_3$   $4 \text{ mol dm}^{-3}$  ; Cr(VI)  $9.6 \cdot 10^{-5}$  (1),  $4.8 \cdot 10^{-4}$  (2),  $9.6 \cdot 10^{-4}$  (3)  $\text{mol dm}^{-3}$

Firstly, the mechanism of the reduction reaction was investigated at the Uranus S1N SS surface through the shapes of the cathodic branches observed on the Uranus S1N polarization

curves. In pure  $\text{HNO}_3$  (between 1 and 9  $\text{mol dm}^{-3}$ ) Uranus S1N cathodic branches (Fig. 10A) display two  $\log (|j|)$  vs.  $E$ . slopes. These slopes could be associated to several reactions described in the literature [35, 40]. The first reaction, occurring between  $E_{\text{corr}}$  and -0.45 V vs. MSE could be the nitrous acid reduction reaction as described by Schmid [50] but without the autocatalytic reaction as shown by Benoit *et al.* [39] :

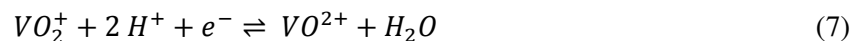


The second reaction, below -0.45 V vs. MSE would be ammoniac formation as described by Razygraev *et al.* [40] :

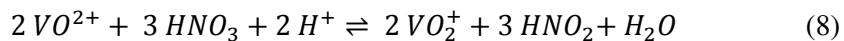


However, this second reaction could also be the first reactions (Eqs. 1 to 3) whose kinetics would be increased by the active domain of the SS. However, the activation potential measurements displayed in the second chapter of this work are closer to -0.64 V vs. MSE for the Uranus S1N in a 4  $\text{mol dm}^{-3}$   $\text{HNO}_3$  at 80°C, which seems to be much lower than the -0.45 V vs. MSE observed in Fig. 10. Also, at lower potentials than -0.60 V vs. MSE, the proton reduction reaction will be expected.

In the presence of V(V), the Uranus S1N cathodic branch shape (Fig. 10C) doesn't seem to be affected by the concentration in V(V). The reduction reaction of the V(V) species are supposed to be :



In the conditions of the experiments ( $4 \text{ mol dm}^{-3} \text{ HNO}_3$ ,  $100^\circ \text{C}$ ), this reaction is immediately followed by a reoxidation of  $VO^{2+}$  [51]:



Therefore, V(V) can be seen as a catalyzer for the nitric acid reduction reaction. In Fig. 10C it is difficult to conclude if the reduction reaction observed is consequently the nitric medium reduction reactions, the V(V) reduction reaction, or a mixed of both. In Fig. 11 are superimposed polarization curves of the Uranus S1N in  $4 \text{ mol dm}^{-3} \text{ HNO}_3$  at  $100^\circ \text{C}$  with and without V(V). From the very subtle modification of the slopes, Fig. 11 suggests that a mixed reduction reaction is observed, but that the  $\text{HNO}_3$  reduction reactions prevail.

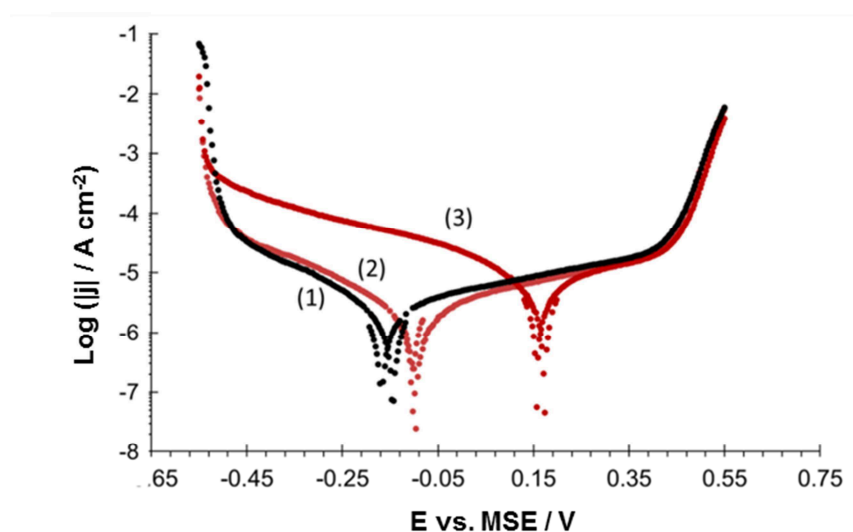
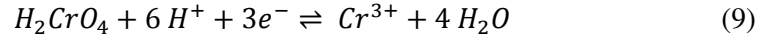


Fig. 11. Linear polarization curves of the Uranus S1N in  $4 \text{ mol dm}^{-3} \text{ HNO}_3$  at  $100^\circ \text{C}$

$\text{HNO}_3 \text{ } 4 \text{ mol dm}^{-3}$  (1)

$\text{HNO}_3 \text{ } 4 \text{ mol dm}^{-3} + \text{V(V)} \text{ } 1.9 \cdot 10^{-4} \text{ mol dm}^{-3}$  (2);  $+ \text{V(V)} \text{ } 9.8 \cdot 10^{-3} \text{ mol dm}^{-3}$  (3)

In the case of the Cr(VI) species(Fig. 11), the reduction reaction also seems to be independant from the concentration in terms of mechanism. The reduction reaction of Cr(VI) species are expected to follow Eq. 9:



According to the Pourbaix diagrams, the reduction reaction product,  $Cr^{3+}$ , is stable in the conditions of the experiment unlike for the V(V). Two possible reduction reactions can be then expected in Fig. 10E. First, it could be the reduction reaction of Cr(VI) as described by Eq. 9. The other hypothesis would be once again the reduction reaction of  $HNO_3$  prevailing but kinetically decreased by a local reinforcement of the passivity of the steel because of the reduction reaction of Cr(VI). Benoit *et al.* [36] tended to show that the passivity of a material could affect in this way the intensity of the  $HNO_3$  reduction reactions.

Then, the two materials are compared in the same conditions. Fig. 12 displays several superimpositions of the polarization curves obtained for the two materials in different conditions.

As the general aspect of the reduction reaction does not seem to vary, it can be thought that Si alloying does not affect the species involved in the reduction reaction (Fig. 12). However, it is clear that the Si decreases efficiently the kinetics of the reduction reaction. For each concentration of each electrolyte, the intensity of the reduction reaction is lower for the Uranus S1N.

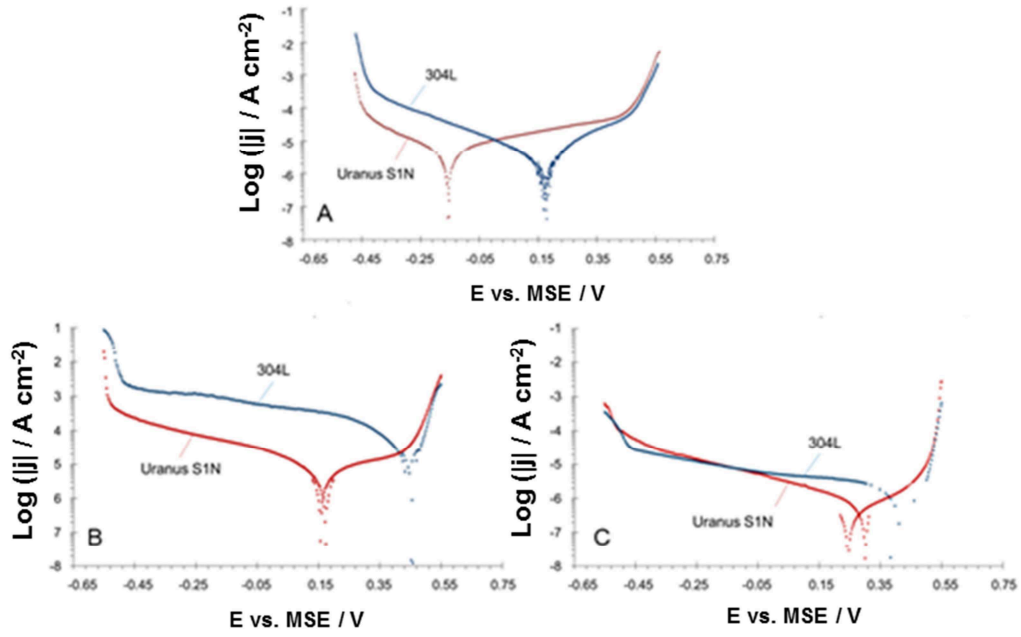


Fig. 12. Linear polarization curves of the Uranus S1N (red) and 304L SS (blue) in  $4 \text{ mol dm}^{-3}$   $\text{HNO}_3$  at  $100^\circ \text{C}$

(A)  $\text{HNO}_3$   $4 \text{ mol dm}^{-3}$

(B)  $\text{HNO}_3$   $4 \text{ mol dm}^{-3}$ ;  $\text{V(V)}$   $9.8 \cdot 10^{-3} \text{ mol dm}^{-3}$

(C)  $\text{HNO}_3$   $4 \text{ mol dm}^{-3}$ ;  $\text{Cr(VI)}$   $4.8 \cdot 10^{-4} \text{ mol dm}^{-3}$

Fig. 13 sums up the different  $E_{\text{corr}}$  and  $j_{\text{corr}}^*$  estimated from the polarization curves.  $j_{\text{corr}}^*$  is a Tafel extrapolation from the cathodic branch of the polarization curves.

Fig. 13 shows clearly that as the reduction reaction kinetics are lowered for the Uranus S1N, while the oxidation current is increased,  $E_{\text{corr}}$  is systematically lowered as compared to the 304L. As the transpassive transition  $E_{\text{tp}}$  is never really affected by the conditions, a mean value is represented in Fig. 13. Consequently, it is shown that as  $E_{\text{corr}}$  is lowered by the presence of Si, the Uranus S1N always remain passive in the present range of conditions, whereas the 304L is shifted to its transpassive domain.

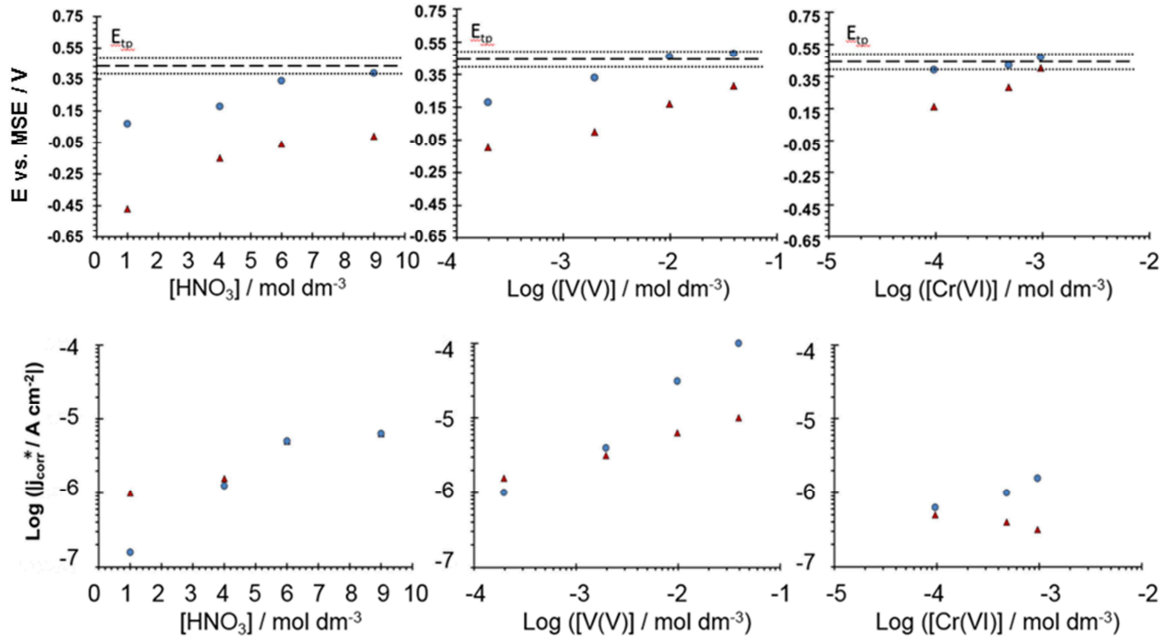


Fig. 13.  $E_{corr}$  et  $j_{corr}^*$  for Uranus S1N (red) and 304L (blue)

The direct consequence of this result is that the  $j_{corr}^*$  value of the 304L SS increases rapidly as soon as the material becomes transpassive, and the inversion between Uranus S1N and 304L corresponds exactly to the limit condition where the 304L will start being transpassive. These results confirm what was found by Armijo *et al.* [4].

In this first chapter, the specific case of the Cr(V) is also investigated. In Fig. 13 is clearly shown the decreasing  $j_{corr}^*$  for the Uranus S1N that is not observed in the case of the 304L SS. The Uranus S1N displays a very singular interaction with the Cr(VI). However, this phenomenon occurs apparently because the concentration in Cr(VI) are low, because in literature, higher concentrations were investigated using different Cr(VI) isotopes. They were meant to prove that Cr(VI) could reduce at the Uranus S1N surface, but they couldn't conclude [52].

#### 4.1.4. Conclusion

In this first chapter, polarization curves were performed in different electrolytes with both SS. It was shown that Si was capable of preserving the passivity of the Uranus S1N even in very oxidizing conditions. It is directly related to the fact that Si in the passive layer of the SS kinetically limits the reduction reaction while increasing the oxidation current. Therefore, the corrosion potential is largely decreased and the material remains passive even at high concentrations in oxidizing species. It clearly explains why the Si-rich SS corrode at higher rates than the 304L in pure  $\text{HNO}_3$  and at lower rates than the 304L when adding oxidizing species, because the 304L SS starts dissolving in its transpassive state.

The second conclusion involved the particular affinity of the Uranus S1N to Cr(VI) species. For low concentrations (less than  $0.1 \text{ g dm}^{-3}$ ), the passivity of the Uranus S1N improves, which is not the case for the 304L SS. One can think that other oxidizing species could display similar behavior, which highly stresses the importance of working with different oxidizing species.

#### **4.1.5. Publication (to be submitted)**

##### *Abstract*

The present work relies on linear sweep voltammetry to investigate the impact of a 3.5 wt. % addition of Si on the corrosion resistance of an 18Cr-15Ni stainless steel (SS) in 100 °C nitric acid, HNO<sub>3</sub>. The X1CrNiSi18-15-4 SS was compared to the X2CrNi18-10 SS in various types of conditions: pure concentrated HNO<sub>3</sub> with or without oxidizing species (V(V) and Cr(VI)). In pure HNO<sub>3</sub>, both SS are passive and the X1CrNiSi18-15-4 SS dissolves spontaneously faster than the X2CrNi18-10 SS. The addition of oxidizing species V(V) or Cr(VI) in the electrolyte leads to the opposite result: the X1CrNiSi18-15-4 stainless steel remains in the passive state, whereas the 18Cr-10Ni stainless steel is polarized in the transpassive state. As a consequence, the X1CrNiSi18-15-4 SS corrodes slower than the X2CrNi18-10 SS. All these observations are explained by the fact that the presence of Si in the oxide film slightly deteriorates the passivity of the stainless steel but also moderates the reduction processes. It keeps the corrosion potential of the X1CrNiSi18-15-4 SS low enough for the alloy to remain passive. A specific impact of the addition of Cr(VI) is also shown, as Cr(VI) seems to play a role on both cathodic and anodic processes, whereas V(V) mainly impacts the cathodic kinetics.

##### *1. Introduction*

Industrial devices involving nitric acid in their processes, such as in plants for spent nuclear fuel reprocessing, have to face material choice in regards to this constraining environment. Indeed, nitric acid, HNO<sub>3</sub>, acts both as an acid and an oxidizing agent. Some frequently chosen alloys such as several austenitic stainless steels (SS) present a satisfying corrosion resistance in nitric acid, especially when concentrated, because of a dissolution rate that can be lower than a few tens of micrometers per year. Each composition of alloy can be



dedicated to a specific environment in terms of temperature,  $\text{HNO}_3$  concentration and the possible presence of oxidizing species dissolved in the acid [1]. Oxidizing species refer to heavy metallic ions coming from the process itself that reduce at very high potentials. Their presence in the electrolyte ( $\text{HNO}_3$ ) raises the steady state potential of the alloys to values that could cause loss of passivity. Shifted to their transpassive domain of potential, they may undergo severe dissolution. High dissolution may also come along with surface heterogeneity, for example, the corrosion can be more intense at grain boundaries than at grain faces. It results from this phenomenon, called intergranular corrosion, a non-faradaic contribution to mass loss of the material, caused by grains being removed from the surface before they have actually dissolved into the electrolyte [2, 3]. To limit risks associated with such type of corrosion, the chemical composition of some SS was optimized. In particular, by the end of the 60s it was shown that the addition of Si had a major impact on the corrosion behavior of 18Cr-15Ni type SS [1, 4-9]. Very low-Si alloyed materials were performing satisfyingly, alloys containing around 1 wt. % severely degraded in concentrated  $\text{HNO}_3$ , but more than 1 wt.% Si addition revealed benefic in the presence of oxidizing species [10]. An X1CrNiSi18-15-4 SS was then developed to resist these specific conditions. In pure  $\text{HNO}_3$ , the X1CrNiSi18-15-4 SS dissolves more rapidly than the X2CrNi18-10 SS (more commonly referred to as 304L SS), but in presence of various oxidizing species, the X1CrNiSi18-15-4 dissolves much slower than the X2CrNi18-10 SS [10]. It proved to dissolve even slower than it did in pure  $\text{HNO}_3$  in the presence of Cr(VI) in the electrolyte [11]. Moreover, even in transpassive conditions, the X1CrNiSi18-15-4 SS does not undergo intergranular corrosion [4, 5, 7]. An assumption proposed by Camus *et al.* [12] is that Si enrichment over 1 wt. % levelled grain boundaries and grain faces energies at the surface of the material. However, this hypothesis was moderated by Armijo *et al.* [13] because even if low-Si alloys present more active grain boundaries than grain faces, they are not always subject to intergranular

corrosion. Nevertheless it was shown in previous work [13, 14] that the surface of X1CrNiSi18-15-4 SS was covered by an oxide layer containing much more silicon than the bulk material (over 30 at. %) in various conditions. Based on core level energies measured by X-ray photoelectron spectroscopy (XPS), Robin *et al.* [14] formulated the hypothesis that silicon is present in the layer as a Cr-Si oxide. If the exact chemistry and structure of this oxide layer remains unclear, it is nevertheless different from the Cr oxide that is usually analyzed at the X2CrNiN18-10 SS surface, which contains no enrichment in Si. As the passive layer acts as the interface at which corrosion reactions to proceed, such differences in the composition of passive layer between the X1CrNiSi18-15-4 and the X2CrNiN18-10 SS could be responsible for the differences in the corrosion behavior that have been discussed above. But this point seems not to have been discussed by many authors.

A lot of corrosion rate measurements of different SS in HNO<sub>3</sub> in various conditions of concentration and temperature, and with or without addition of oxidizing ions are available in the literature [10, 13-16]. However, only a few authors [13, 14, 17, 18] tried to express precisely the relationships between corrosion (dissolution rate and surface morphology) and electrochemical behavior of the alloys (corrosion potential, limits of passivity, reduction mechanisms and kinetics). The present work aims at measuring and explaining more exhaustively the electrochemical differences involved by with silicon enrichment of the 18Cr-15Ni type SS by comparing the X1CrNiSi18-15-4 SS and the X2CrNiN18-10 SS in various HNO<sub>3</sub> based electrolytes.

The following work will focus on three main types of electrolyte. First, the impact of the Si enrichment will be examined in pure HNO<sub>3</sub>. The concentration will be varied from 1 to 9 mol dm<sup>-3</sup> at a temperature of 100 °C. Then, V(V) and Cr(VI) will be added to a 4 mol dm<sup>-3</sup> HNO<sub>3</sub> electrolyte at 100 °C to increase the electrochemical potential of the electrolyte. Comparisons of corrosion currents and potentials for the two alloys in these three electrolytes

will help the establishment of a clear link between the pre-existing studies and it will be proposed some hypothesis to explain better the role of Si in the corrosion behavior of SS in HNO<sub>3</sub> environments.

## 2. Experimental

The experiments performed at 100°C. To ensure a better stability of this temperature, a system of thermocryostat (*LAUDA*) heating oil and jacketed 200 mL reactor was used.

### 2.1. Samples

Bullet shape samples (2 cm<sup>2</sup>) made out of X1CrNiSi18-15-4 SS and X2CrNiN18-10 SS were used in the present work for electrochemical measurements. Plane samples (20 mm x 20 mm x 1 mm) polished to diamond finish 0.03µm were used for XPS measurements. The elemental analysis of the steel have been performed by glow discharge optical emission spectroscopy (GD-OES) using a GD-Profilier from *Horiba Jobin-Yvon*. The bulk of the sample was clearly reached from 10 to 45 µm depth and the composition of the steel is averaged over two craters on different samples. This analysis is given in Table 1.

*Table 1. Mass composition of X1CrNiSi18-15-4 SS and X2CrNiN18-10 SS determined by GD-OES profiles performed on samples and averaged between 40 µm and 50 µm depth expressed in wt. %*

	Fe	Cr	Ni	Si	Mn	Add.
X1CrNiSi18-15-4 SS	59.76	18.79	15.08	3.54	1.97	0.18
X2CrNiN18-10 SS	70.35	17.78	9.51	0.34	1.46	0.16

The stainless steel samples used for linear polarization curves were cut into 2 cm<sup>2</sup> “bullet shaped” electrodes, ultrasonic cleaned with ethanol and acetone and then left at open circuit potential (OCP) in 4 mol dm<sup>-3</sup> 100°C HNO<sub>3</sub> for 24h prior to any measurement.

## 2.2. Electrolytes

A 18.2 MΩ cm water prepared with a *Millipore*<sup>TM</sup> system and HNO<sub>3</sub> 52.5 % (*VWR Chemicals*) were used for all the electrolytes. pH were measured using a *Mettler-Toledo* DL55 titrator and NaOH (*Sigma Aldrich*) 1 mol dm<sup>-3</sup> reagent. Preliminary study showed that desaerating nitric acid before the experiment had few impact on the X1CrNiSi18-15-4 SS electrochemical behavior. Considering this, the solutions were not desaerated. Nitric acid solutions containing V(V) were prepared with vanadium sulfate pentahydrate VOSO<sub>4</sub>·5H<sub>2</sub>O (*Sigma Aldrich*, 97.0 %) that were heated up to 100°C for 24 hours for V(IV) to be oxidized in V(V) and then controlled by UV-visible spectroscopy (Cary ‘50 scan’ *Varian* spectroscope). For hexavalent chromium solutions, anhydrous potassium dichromate K<sub>2</sub>Cr<sub>2</sub>O<sub>7</sub> (*Sigma Aldrich*, 99.9 %) was weighed and added to the electrolytes.

## 2.3. Electrochemistry measurement

### 2.3.1. Experiments

A three electrodes cell was used. Samples were used as working electrodes (X1CrNiSi18-15-4 SS or X2CrNi18-10 SS), counter electrode was made of a platinum grid, and reference electrode was a mercury-mercurous sulphate electrode (MSE) provided by *Radiometer* (E=+0.65 V vs NHE in sat'd K<sub>2</sub>SO<sub>4</sub>). A *Biologic* VSP potentiostat performed the experiments, functioning in the potentiodynamic linear polarization mode at 0.2 mV s<sup>-1</sup> scan rate and recorded by *EC-Lab* software V10.37. This scan rate was chosen to be as close as possible to quasi-stationary conditions and perform experiments in a reasonable amount of time. Polarization was performed in two distinct measurements. The first measurement was

started 30 mV above OCP and followed a cathodic sweep direction down to -0.45 V vs. MSE. The second measurement was started after 24 h OCP. It was started 30 mV below OCP and followed an anodic sweep up to +0.55 V vs. MSE. During the OCP period between the two measurements, the potential of the sample usually reached almost perfectly its initial value prior to the first scan.

### 2.3.2. Determination of parameters

Several parameters were extracted from the electrochemical measurements presented. Firstly, the corrosion potentials, corresponding to a measured current density  $j = 0$ , and called  $E_{\text{corr}}$  will be compared. In most of cases, as said before, the OCP of the sample reached almost perfectly its initial value in the 24 h OCP period, therefore  $E_{\text{corr}}$  measurements displayed a very small uncertainty (inferior to 5 mV) except for few experiments on the X2CrNiN18-10 SS that lead to an uncertainty for  $\pm 40$  mV.

Secondly, during a linear polarization measurement, it is possible under specific conditions [19] to distinguish on a semi-log scale at both side of  $E_{\text{corr}}$  two slopes (usually called Tafel slopes) that would bring to the measurement of  $j_{\text{corr}}$ , corresponding to the instantaneous dissolution rate of the material. However, in the case of passive materials, the anodic Tafel slope is usually inexistent. Moreover, when the reduction reaction involves complex mechanisms, as it will be shown in the case of  $\text{HNO}_3$ , cathodic Tafel slope is also rigorously difficult to establish. Nevertheless, it was proposed in the present work to define a  $j_{\text{corr}}^*$  that provides a qualitative information on the relative dissolution rates of the alloys.  $j_{\text{corr}}^*$  was determined as the intersection between a cathodic slope identified on at least one decade and  $x = E_{\text{corr}}$ .

Eventually, the passivity breakdown at high potentials, usually called transpassive domain transition, was associated to a potential  $E_{\text{tp}}$  identified at the intersection between the passive

domain slope (when measurable) and the transpassive domain slope. The uncertainty associated with  $E_{tp}$  was found to be about  $\pm 40$  mV.

#### 2.4. X-ray photoelectron spectroscopy measurements

XPS analyses were carried out with a *ThermoFisher Escalab 250 XI* spectrometer using a monochromatic X-ray Al K $\alpha$  source. The instrument was calibrated in energy with the Ag Fermi level (0 eV) and the 3d<sup>5/2</sup> core level of metallic silver (368.3 eV). The C-1s signal was used to correct a possible charge effect: the CC/ CH contribution of C-1s spectra was fixed at 285.0 eV. The analysis zone consisted of a 900  $\mu$ m diameter spot. The data processing was performed using the commercially available *Avantage<sup>TM</sup>* software. For the fitting procedure, a Shirley background has been used and Lorentzian-Gaussian (L/G) ratio was fixed at 30 %. Main parameters used to decompose XPS spectra are presented in Table 2.

Table 2. Parameters used for the deconvolution of XPS spectra (*Avantage<sup>TM</sup>* software)

*Binding energies and full width at half maximum (FWHM)*

	[ Fe Ox ] / at. %		[ Cr Ox ] / at. %			[ Si Ox ] / at. %	
	Fe - 2p <sub>3/2</sub>	Fe - 2p <sub>3/2</sub>	Cr - 2p <sub>3/2</sub>	Cr - 2p <sub>3/2</sub>	Cr - 2p <sub>3/2</sub>	Si - 2p	Si - 2p
Binding energy / eV	709.69	712.07	576.26	577.32	578.99	102.05	102.65
FWHM / eV	2.36	2.93	1.08	1.92	1.71	1.36	1.32

## 2.5. Transmission electron microscopy and energy dispersive X-ray spectroscopy

Cross-sections of materials passivated in 4 mol dm<sup>-3</sup> HNO<sub>3</sub> at 100 °C were analyzed using transmission electron microscopy (TEM) in high resolution imaging mode. These studies were performed by *Serma Technologies* (France). In order to identify zones of interest on each sample, electron backscattered diffraction (EBSD) was performed at the surface of the materials prior to sample cross-section elaboration, using a scanning electron microscope field emission gun *ZEISS Gemini 500* scanning electron microscope (SEM), a *Hikari Super* charge coupled device (CCD) camera, and OIM<sup>TM</sup> Data collection and OIM<sup>TM</sup> Analysis software for the acquisition and exploitation of the data. Cross-section TEM lamellas were thinned using focused ion beam (FIB) *FEI Strata DB400* and analyzed with a *FEI Tecnai Osiris* TEM using a an accelerating voltage of 200 kV and equipped with ChemiSTEM<sup>TM</sup> and GIF Quantum® detectors X-ray energy dispersive spectroscopy (X-EDS)

## 3. Results and discussion

### 3.1. Impact of Si on the passive layer of SS

Both SS materials are covered by an oxide film with similar morphology after exposure to 4 mol dm<sup>-3</sup> HNO<sub>3</sub> electrolyte at 100°C for 24 hrs at open circuit. This is seen clearly by comparing the cross sections of the X1CrNiSi18-15-4 SS (Fig. 1A) and the X2CrNiN18-10 SS (Fig. 1B). In both cases, the oxide film is continuous over the surface. Fig. 1 also seems to demonstrate the amorphous character of the passive layer [20]. The X2CrNiN18-10 SS shows localized zones where Cr was found to penetrate about 10-20 nm (white arrow on Fig. 1). No such penetration zones were detected for the X1CrNiSi18-15-4 SS.

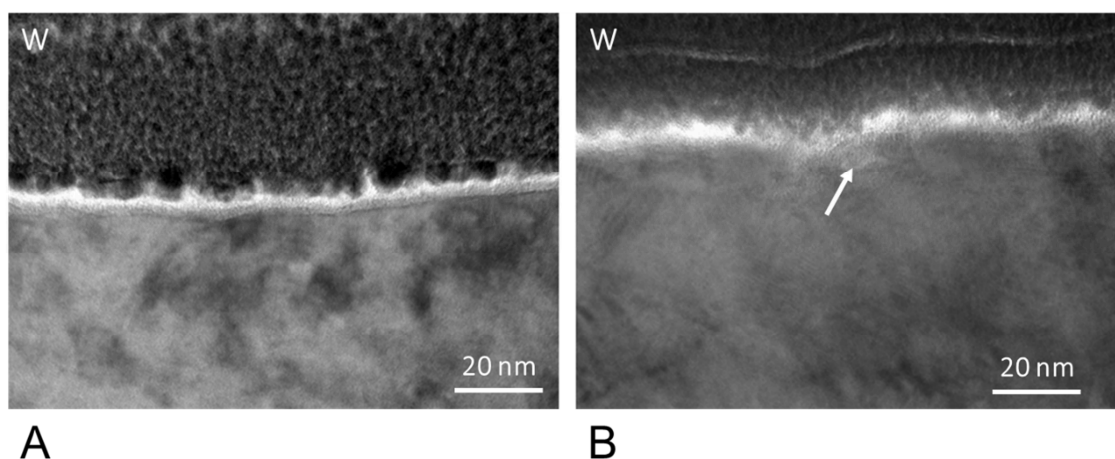


*Fig.1. Cross section of passive layers established on X1CrNiSi18-15-4 (A) and X2CrNiN18-10 (B) SS in 4 mol dm<sup>-3</sup> 100°C HNO<sub>3</sub> for 24 hours and observed using transmission electron microscopy (TEM)*

*Table 3. XPS measurements on passive layers established for 24 hours in 4 mol dm<sup>-3</sup> HNO<sub>3</sub> at 100 °C (averaged over 10 experiments)*

		[ Fe Ox ] / at. %	[ Cr Ox ] / at. %	[ Si Ox ] / at. %
HNO <sub>3</sub> 4 mol dm <sup>-3</sup>	X1CrNiSi18- 15-4	26 ± 4	46 ± 4	28 ± 3
	X2CrNiN18- 10	41 ± 4	59 ± 5	None

Chemical compositions of the passive layers were obtained using XPS on the same samples (Table 3): the X2CrNiN18-10 SS surface was mainly composed of Cr (59 at. %) while the X1CrNiSi18-15-4 SS, contained mainly Cr (46 at. %) and Si (28 at. %). As mentioned previously, and already found in literature [14, 21], the passive layer formed at a Si enriched alloy's surface is also enriched in Cr but also in Si in higher concentration than the



bulk material. Moreover, a core level energy lower than 104 eV was found for Si-2p at the X1CrNiSi18-15-4 SS's surface. This indicates that Si atoms are not bonded to O under the form of SiO<sub>2</sub>. Robin *et al.* [14] highlighted that this particular structure of the X1CrNiSi18-15-4 SS oxide was probably due to a mixed silicate oxide.

In conclusion, Si seems to impact the chemical composition of the oxide layer, morphological properties being mainly similar. This composition difference may impact the electrical properties provided by the oxide layer, and therefore, the corrosion behavior. Therefore, both anodic and cathodic contributions characteristics will be compared in pure HNO<sub>3</sub> and using oxidizing species for both SS.

### 3.2. Impact of Si in pure HNO<sub>3</sub>

Typical linear polarization curves obtained in 100 °C pure HNO<sub>3</sub> for X1CrNiSi18-15-4 SS and X2CrNi18-10 SS are displayed on Fig. 2 for concentrations of 1 mol dm<sup>-3</sup> (A), 4 mol dm<sup>-3</sup> (B) and 6 mol dm<sup>-3</sup> HNO<sub>3</sub> (C). Red curves represent X1CrNiSi18-15-4 SS and blue curves are associated to X2CrNi18-10 SS.

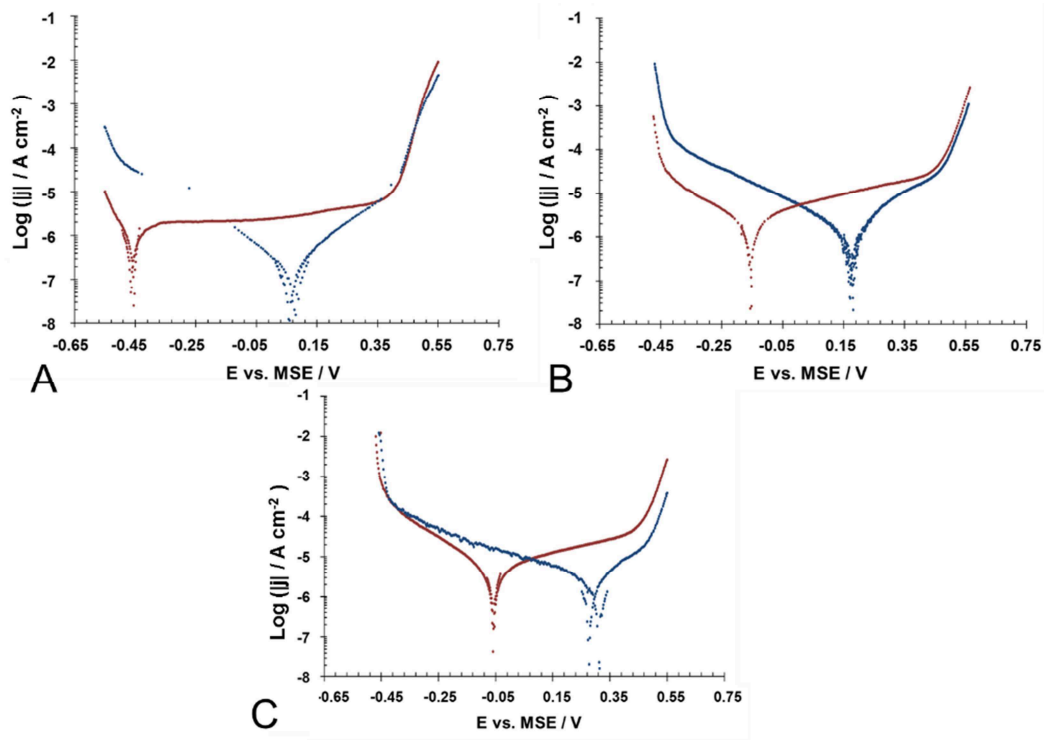
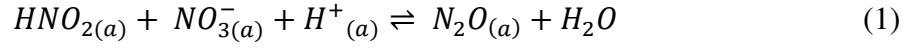
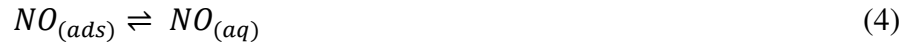
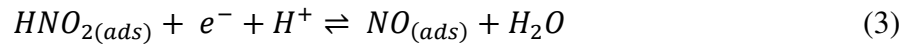


Fig. 2. Linear sweep voltammetry ( $v = 0.2 \text{ mV s}^{-1}$ ) performed at  $T = 100 \text{ }^{\circ}\text{C}$  for X1CrNiSi18-15-4 (red) and X2CrNiN18-10 (blue) SS in  $\text{HNO}_3$  1 (A), 4 (B), 6 (C)  $\text{mol dm}^{-3}$

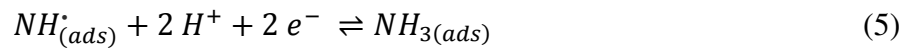
The shape of the cathodic branch and the cathodic Tafel slope does not differ significantly between the two steel samples, suggesting that the cathodic reaction is not significantly affected by the presence of Si (Fig. 2). The cathodic branch for both steel specimens at every  $\text{HNO}_3$  concentration displays two slopes. The first cathodic domain is detected between  $E_{\text{corr}}$  and  $-0.45 \text{ V vs. MSE}$  (almost  $-0.30 \text{ V vs. MSE}$  for the highest concentration) and the second domain starts below  $-0.45 \text{ V vs. MSE}$ . Concentrated  $\text{HNO}_3$  reduction reactions have been extensively investigated on various ranges of materials from platinum to stainless steel [22-27]. In concentrated  $\text{HNO}_3$ , various nitrogenous species were shown to be in equilibrium, as described exhaustively by various authors [22-27]. Briefly, the nitrosonium ion,  $\text{NO}^{3-}$ , being in equilibrium with nitrous acid  $\text{HNO}_2$  according to Eq. 1,  $\text{HNO}_2$  has been shown to be, between  $-0.45$  and  $-0.25 \text{ V vs. MSE}$ , one of the main electroactive species reducing at a SS surface [27].



The reduction reaction of  $HNO_2$  is given by Eqs. 2 to 4. It reduces into N(II) species such as nitrogen monoxide, NO, which after desorbing (Eq. 4) may be reoxidized by  $HNO_3$  close to the interface. In the case these third oxidation state species produced by this reoxidation would reduce again, the overall reduction process becomes autocatalytic (also called Schmid's mechanism), and this autocatalytic behavior depends on the nature of the interface [23, 24]. Benoit *et al.* [26] showed that the autocatalytic behavior was not triggered at the 304L SS surface.



Between -0.60 and -0.45 V vs. MSE, ammonia formation is expected to happen according to Razygraev *et al.* [27] (Eqs. 5 to 7)



$NH^*_{(ads)}$  being itself produced by a number of different equilibria of the  $HNO_3$  electrolyte. At lower potentials than -0.60 V vs. MSE, the proton reduction reaction is expected. In the present work, polarization curves were performed at higher potentials, therefore this reaction is never observed. Fig. 2 seems to reveal previously mentioned mechanisms consistent with

literature in terms of potentials (Eqs 1-3 and 4-6), although further investigations should confirm the nature of reduced species.

The Si alloying is not responsible for any significant modification of the reduction mechanism, however, the reduction current density of the X2CrNi18-10 SS is systematically between 0.5 to 1 decade higher than for the X1CrNiSi18-15-4 SS in Fig. 2 and Table 4. Si contained in the passive layer seems to inhibit  $\text{HNO}_2$  reduction, as described by Armijo *et al.* [13]. The results of Fig. 2 fully support this hypothesis, showing a similar mechanism with a decreased reaction rate.

Table 4. Values of cathodic current 100 mV below  $E_{corr} / \mu A cm^{-2}$ , cathodic Tafel slope / mV dec<sup>-1</sup>,  $E_{tp}$  vs. MSE / V, passive current 100 mV below  $E_{tp} / \mu A cm^{-2}$  and transpassive current 100 mV above  $E_{tp} / mA cm^{-2}$  for both SS in the exhaustive range of conditions tested for the present work at 100 °C

100°	HNO <sub>3</sub> / mol dm <sup>-3</sup>	V(V) / mol dm <sup>-3</sup>	Cr(VI) / mol dm <sup>-3</sup>	$E_{corr}$ vs. MSE / V	Cathodic current 100mV below $E_{corr} / \mu A$ cm <sup>-2</sup>	Cathodic Tafel slope / mV dec <sup>-1</sup>	$E_{tp}$ vs. MSE / V	Passive current 100mV below $E_{tp} / \mu A cm^{-2}$	Transpassive current 100mV above $E_{tp} / mA$ cm <sup>-2</sup>
X1CrNiSi18-15-4	1	-	-	-0.47	8.9	-19.6	0.44	6.0	5.00
	4	-	-	-0.15	4.4	-17.9	0.45	19.0	1.15
	6	-	-	-0.06	13.0	-19.5	0.45	27.0	2.60
	9	-	-	-0.01	21.0	-20.6	0.47	43.4	1.20
	4	$1.96 \cdot 10^{-4}$	-	-0.097	4.1	-17.2	0.44	12.3	2.80
	4	$1.96 \cdot 10^{-3}$	-	0	11.2	-19.4	0.44	12.4	2.80
	4	$0.0098$	-	0.17	14.9	-19.7	0.44	12.4	2.70
	4	0.039	-	0.28	32.0	-21.6	0.44	12.5	2.70
	4	-	$9.6 \cdot 10^{-4}$	0.16	1.7	-16.9	0.44	5.0	0.55
	4	-	0.019	0.28	1.7	-17	0.48	1.1	0.55
	4	-	0.029	0.4	1.7	-17.1	0.51	-	0.02
X2CrNiN18-10	1	-	-	0.07	0.5	-15.6	0.45	4.8	3.75
	4	-	-	0.18	3.8	-17.9	0.47	3.4	0.69
	6	-	-	0.34	5.5	-15.9	0.45	-	0.38
	9	-	-	0.39	20.0	-20.5	0.44	-	0.23
	4	$1.96 \cdot 10^{-4}$	-	0.18	1.1	-16.3	0.46	5.0	2.90
	4	$1.96 \cdot 10^{-3}$	-	0.33	2.9	-17	0.45	-	2.80
	4	$0.0098$	-	0.46	77.0	-23	-	-	2.80
	4	0.039	-	0.48	240.0	-26	-	-	2.70
	4	-	$9.6 \cdot 10^{-4}$	0.39	1.6	-16.9	-	-	0.96
	4	-	0.019	0.42	2.5	-17	-	-	0.96
	4	-	0.029	0.47	3.3	-17	-	-	0.03

The passive current density is also affected by the presence of Si, the mean passive current density of the X1CrNiSi18-15-4 SS being markedly higher than for the X2CrNiN18-10 SS. For example, Table 4 shows that in 4 mol dm<sup>-3</sup> HNO<sub>3</sub> the passive current density value 100mV below  $E_{tp}$  is 5 times higher for the X1CrNiSi18-15-4 SS than for the alloy without Si.

The combined inhibition of the cathodic reaction and activation of the anodic reaction by Si alloying, causes the corrosion potential  $E_{corr}$  of the X1CrNiSi18-15-4 SS to be systematically lower than for X2CrNiN18-10 SS. This applies to the whole range of conditions tested as shown on Fig. 3.

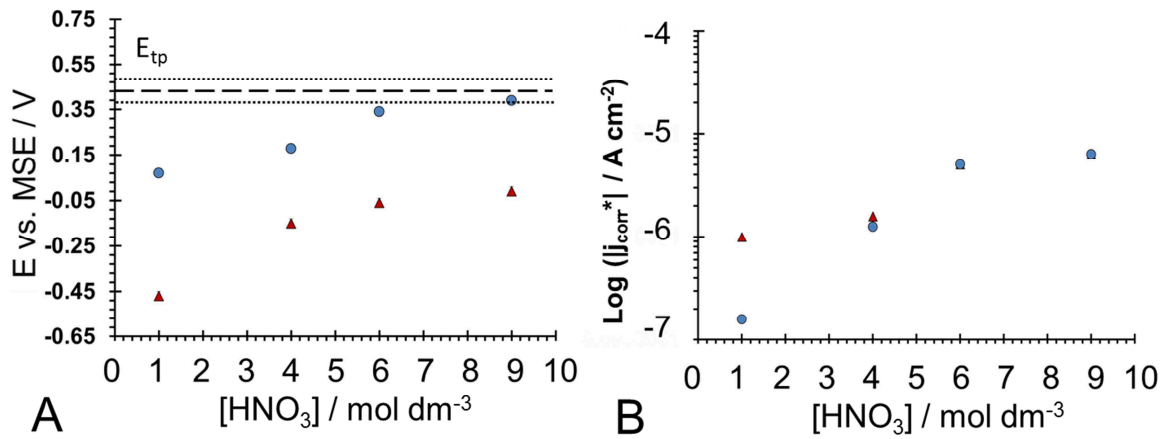


Fig. 3. (A)  $E_{corr}$  measured for X1CrNiSi18-15-4 (triangles) and X2CrNiN18-10 (circles)

SS as a function of HNO<sub>3</sub> concentration at 100°C

(B) Log ( $|j_{corr}^*|$ ) for X1CrNiSi18-15-4 (triangles) and X2CrNiN18-10 (circles) SS as a

function of HNO<sub>3</sub> concentration at 100°C

According to Eqs. 1 to 6, this cathodic inhibition could either result from a modification of the charge transfer properties at the X1CrNiSi18-15-4 SS interface, or from an alteration in the adsorption capability of the X1CrNiSi18-15-4 SS surface.

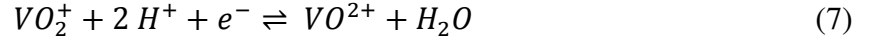
It can be noticed that the measurements of  $j_{\text{corr}}^*$  (Fig. 3) are consistent with dissolution rates ascertained in literature [10, 13]. For example, Desestret *et al.* [10] found a mass loss of  $20 \text{ mg cm}^{-2}$  per day in boiling  $5 \text{ mol dm}^{-3} \text{ HNO}_3$ . Based on the Fe molar mass of  $53.46 \text{ g mol}^{-1}$ , on the density of the X1CrNiSi18-15-4 SS of  $7.81 \text{ g cm}^{-3}$ , and on an averaged value of number of electrons exchanged  $n_e$  of 2.7, the value  $j_{\text{corr}}^* = 1.5 \cdot 10^{-6} \text{ A cm}^{-2}$  found in  $100^\circ\text{C}$   $4 \text{ mol dm}^{-3} \text{ HNO}_3$  leads to a mass loss of  $26 \text{ mg cm}^{-2}$  per day.

$E_{\text{tp}}$  was not influenced by the presence of Si as indicated in Fig. 2. This value is usually associated with the transition of Cr(III) to Cr(VI) in the passive layer. However, it was demonstrated that, on artificial Fe-Cr oxides [28], Fe(III) oxides in acidic electrolyte lowers the Cr(III)/Cr(VI) transition rate [29]. Values for  $E_{\text{tp}}$  were found identical within a small variance of 20 mV ( $0.45 \pm 0.2 \text{ V vs. MSE}$ ) in all concentrations for both steels although a slight difference in the transpassive currents were observed. For example, in  $4 \text{ mol dm}^{-3} \text{ HNO}_3$  at  $0.55 \text{ V vs. MSE}$ , current density recorded for the X1CrNiSi18-15-4 SS 100 mV above  $E_{\text{tp}}$  is  $1.15 \text{ mA cm}^{-2}$  while the X2CrNiN18-10 SS displays a current density of  $0.70 \text{ mA cm}^{-2}$ . The difference was expected to increase slightly with nitric acid concentration and this may be due to pH as demonstrated by Schmuki *et al.* [28], but was found to be almost steady between 0.5 and 2 mA in the whole range of conditions tested (Table 4).

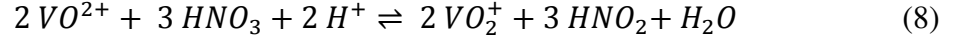
### 3.3. Impact of Si in the presence of oxidizing species

#### 3.3.1. V(V)

Oxidizing species are known to increase the corrosion rate of SS in  $\text{HNO}_3$  [1-3, 5, 11, 15-18]. V(V) has been historically used as an oxidizing agent for simulating redox couple of pentavalent neptunium  $\text{NpO}_2^{2+}/\text{NpO}_2^+$  in nuclear fuel treatment-recycling electrolytes [30]. Pentavalent vanadium is involved in the  $\text{VO}_2^+/\text{VO}^{2+}$  redox couple through the Eq. 7 (31), whose standard equilibrium potential is predicted to be  $1.04 \text{ V vs. SHE}$  [32].



At 100 °C in the conditions of the present work ( $HNO_3$  4 mol  $dm^{-3}$ ) V(V) is expected to be stable [33]. The oxidation of V(IV) was described by Irisawa *et al.* [33] as:



This reaction can directly enhance the reactions described by Eqs. 1 to 3 in which case V(IV) would be considered a catalysis for the reduction of  $HNO_3$ .

In the presence of V(V) in 4 mol  $dm^{-3}$   $HNO_3$  at 100 °C , the X1CrNiSi18-15-4 SS, originally designed for such specific electrolyte ( $HNO_3$  containing oxidizing species), displays typical polarization curves as shown on Fig. 4A for concentrations in V(V) of 0(1),  $1.9 \cdot 10^{-4}$ (2),  $1.9 \cdot 10^{-3}$ (3),  $9.8 \cdot 10^{-3}$ (4) and  $3.9 \cdot 10^{-2}$ (5) mol  $dm^{-3}$ . A comparison with the X2CrNiN18-10 SS is given on Fig. 4B in 4 mol  $dm^{-3}$   $HNO_3$  at 100 °C for a concentration in V(V) of  $1.9 \cdot 10^{-3}$  mol  $dm^{-3}$ .

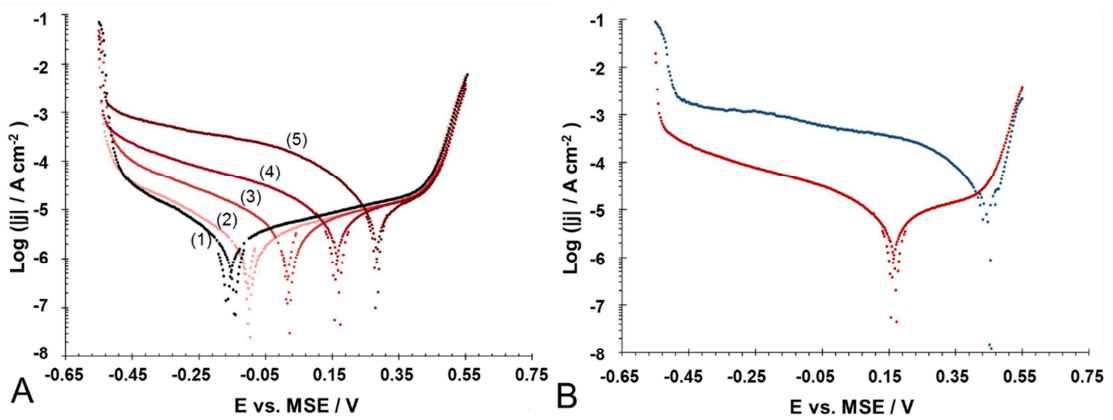


Fig. 4. Linear sweep voltammetry ( $v = 0.2 \text{ mV s}^{-1}$ ) performed in 4 mol  $dm^{-3}$   $HNO_3$  at  $T = 100 \text{ }^{\circ}\text{C}$  for X1CrNiSi18-15-4 (A) with V(V) at 0 (1),  $1.9 \cdot 10^{-4}$ (2),  $1.9 \cdot 10^{-3}$ (3),  $9.8 \cdot 10^{-3}$ (4),  $3.9 \cdot 10^{-2}$ (5) mol  $dm^{-3}$  and for X1CrNiSi18-15-4 and X2CrNiN18-10 (B) SS with V(V) at  $1.9 \cdot 10^{-3}$  mol  $dm^{-3}$

The nature of the cathodic current in Fig. 4 contains contribution from the reduction of V(V) as well as  $HNO_2$  reduction. However, in the case of the X1CrNiSi18-15-4 SS, the shape



of the cathodic curve in presence of V(V) is very similar to pure HNO<sub>3</sub> (Fig 4A) and the cathodic Tafel slopes were found to be of  $18.6 \pm 2.5 \text{ mV dec}^{-1}$  (Table 4) in the whole range of conditions tested.

The shape of the reduction curves and the cathodic Tafel slopes are similar for both SS (Fig. 4B, Table 4) suggesting that the overall reduction mechanism of the electrolyte containing V(V) is comparable between the two alloys and therefore not influenced by the Si alloying. Similar to what was observed in the case of pure HNO<sub>3</sub>, for the same concentrations, cathodic current density is also systematically higher for the X2CrNi18-10 SS than for the X1CrNiSi18-15-4 SS. This would once again support an inhibiting effect of the Si on the cathodic reactions. The passive current density of the X1CrNiSi18-15-4 SS is once again generally higher than for the X2CrNi18-10 SS with a similar effect on  $E_{\text{corr}}$  (Fig. 5) as was observed for HNO<sub>3</sub> alone in Fig. 2. At the lowest concentration in V(V),  $1.9 \cdot 10^{-4} \text{ mol dm}^{-3}$ , the passive current 100 mV below  $E_{\text{tp}}$  was found to be 2 times higher for the X1CrNiSi18-15-4 SS than for the X2CrNi18-10 SS. However, at higher concentrations in V(V), the transpassive transition was too close to determine properly the same difference.

It is clear from Figs. 3 and 5 that when HNO<sub>3</sub> or V(V) concentrations are sufficiently high, or when Cr(VI) species are added, the  $j_{\text{corr}}^*$  is lower for X1CrNiSi18-15-4 SS than for X2CrNi18-10 SS and that this inversion matches perfectly the threshold of transpassive domain. Therefore, as a direct consequence of the presence of Si, the X1CrNiSi18-15-4 SS remains passive even while the X2CrNi18-10 SS is shifted into its transpassive domain and starts to dissolve at a much higher rate.

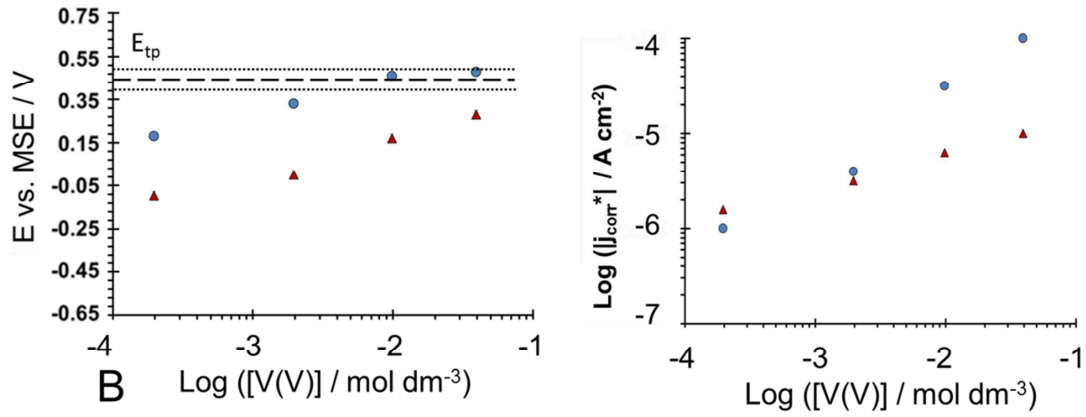


Fig. 5. (A)  $E_{corr}$  measured for X1CrNiSi18-15-4 (triangles) and X2CrNiN18-10 (circles) SS as a function of V(V) concentration in 4 mol dm<sup>-3</sup> HNO<sub>3</sub> at 100°C

(B) Log (|j<sub>corr</sub>\*|) for X1CrNiSi18-15-4 (triangles) and X2CrNiN18-10 (circles) SS as a function of V(V) concentration in 4 mol dm<sup>-3</sup> HNO<sub>3</sub> at 100°C

One can notice that the values of ( $E_{corr}$ ,  $j_{corr}^*$ ) obtained in the different concentrations in V(V) can be superimposed with the polarization curve obtained in 4 mol dm<sup>-3</sup> HNO<sub>3</sub> at 100 °C (Fig. 6) and this is also valid for the X2CrNiN18-10 SS.

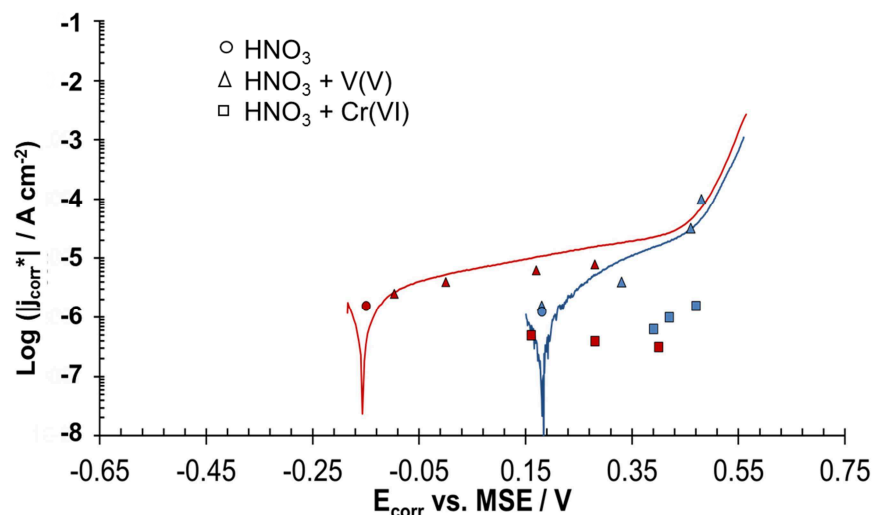


Fig. 6. Red : X1CrNiSi18-15-4 SS polarization curve (line) performed in  $4 \text{ mol dm}^{-3} \text{ HNO}_3$  at  $T = 100$  °C ( $v = 0.2 \text{ mV s}^{-1}$ ) and  $E_{\text{corr}}$  values recorded in pure  $\text{HNO}_3$  (circles),  $\text{HNO}_3$  containing V(V) (triangles) and  $\text{HNO}_3$  containing Cr(VI) (squares)

Blue : X2CrNi18-10 SS polarization curve (line) performed in  $4 \text{ mol dm}^{-3} \text{ HNO}_3$  at  $T = 100$  °C ( $v = 0.2 \text{ mV s}^{-1}$ ) and  $E_{\text{corr}}$  values recorded in pure  $\text{HNO}_3$  (circles)  $\text{HNO}_3$  containing V(V) (triangles) and  $\text{HNO}_3$  containing Cr(VI) (squares)

This result first shown by Plante *et al.* [17] would imply that the oxidation branch of these alloys is not significantly affected by the presence of oxidizing species, and that knowing their  $E_{\text{corr}}$  in given conditions would enable the determination of  $j_{\text{corr}}$ . Other oxidizing species investigated throughout literature ascertained in Plante *et al.*'s work [17] lead to the same conclusion. Regardless of their nature, the anodic current measured at a given potential was found to be unique [17]. The present work confirms that V(V) shifts the  $E_{\text{corr}}$  value without modifying the anodic reaction of the material such that the anodic reaction rate vs. potential curve is independent of the presence of oxidizing ions.

### 3.2.2. Cr(VI)

The Cr(VI) is a more specific case of an oxidizing ion with an original interaction with the alloy. The addition of Cr(VI) species in  $\text{HNO}_3$  has been massively studied [3-5, 7, 10, 13, 15,

34, 35] probably because it requires a very low concentration to shift X2CrNiN18-10 type SS in transpassive dissolution. Fig. 7A displays polarization curves obtained for the X1CrNiSi18-15-4 SS (A) in 4 mol dm<sup>-3</sup> HNO<sub>3</sub> at 100 °C for concentrations of Cr(VI) of 0(1), 9.6 10<sup>-5</sup>(2), 4.8 10<sup>-4</sup>(3) and 9.6 10<sup>-4</sup>(4) mol dm<sup>-3</sup>. Fig. 7B displays the example of polarization curves that were obtained for both SS in 4 mol dm<sup>-3</sup> HNO<sub>3</sub> at 100 °C for a concentration in Cr(VI) of 4.8 10<sup>-4</sup> mol dm<sup>-3</sup>. Fig. 8 ascertains values of E<sub>corr</sub> and j<sub>corr</sub>\* measured in these conditions.

Hexavalent chromium is involved in the H<sub>2</sub>CrO<sub>4</sub>/Cr<sup>3+</sup> redox couple that displays a very high standard potential of 1.40 V vs. SHE [32, 36]. The reduction reaction is described by the equation 9.

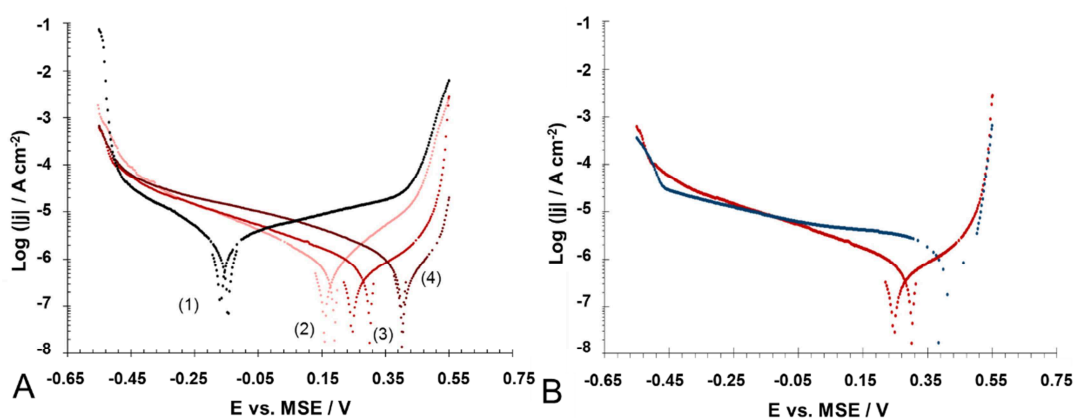
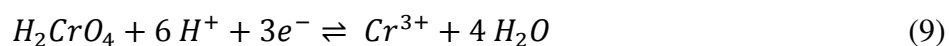


Fig. 7. Linear sweep voltammetry ( $v = 0.2 \text{ mV s}^{-1}$ ) performed in 4 mol dm<sup>-3</sup> HNO<sub>3</sub> at  $T = 100 \text{ }^{\circ}\text{C}$  for X1CrNiSi18-15-4 (A) SS with Cr(VI) 0(1), 9.6 10<sup>-5</sup>(2), 4.8 10<sup>-4</sup>(3), 9.6 10<sup>-4</sup>(4) mol dm<sup>-3</sup> and for X1CrNiSi18-15-4 and X2CrNiN18-10 (B) SS with Cr(VI) 4.8 10<sup>-4</sup> mol dm<sup>-3</sup>

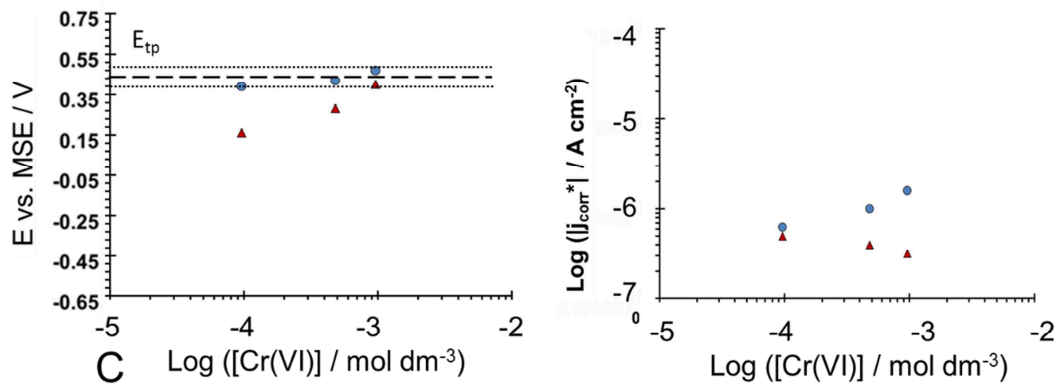


Fig. 8. (A)  $E_{corr}$  measured for X1CrNiSi18-15-4 (triangles) and X2CrNi18-10 (circles) SS as a function of Cr(VI) concentration in  $4 \text{ mol dm}^{-3} \text{ HNO}_3$  at  $100^\circ\text{C}$

(B)  $\text{Log} (|j_{corr}^*|)$  for X1CrNiSi18-15-4 (triangles) and X2CrNi18-10 (circles) SS as a function of Cr(VI) concentration in  $4 \text{ mol dm}^{-3} \text{ HNO}_3$  at  $100^\circ\text{C}$

In the presence of Cr(VI), the cathodic current was about 3 times lower (Table 4) than for pure  $\text{HNO}_3$  or  $\text{HNO}_3 + \text{V(V)}$ . The currents recorded in the cathodic region almost superimpose between concentrations and between the two SS. As for the V(V), it is unclear if the reaction that is observed between 0.15 and -0.45 V vs. MSE is associated with the reduction of the Cr(VI) or with the  $\text{HNO}_2$  reduction reaction, but the cathodic Tafel slopes do not seem to be drastically affected (variance of the cathodic Tafel slopes is of  $2.6 \text{ mV dec}^{-1}$  in the whole range of conditions tested). The tenuous increase of cathodic current density with Cr(VI) concentration indicates that a limitation, either by diffusion or charge transfer, exists at very low concentrations. This could be the result of an enhancement of the passivity of the alloy by the reduction of Cr(VI). As a consequence of this enhancement, the  $\text{HNO}_2$  reduction reaction (Eqs. 2 to 4) kinetics could be drastically lowered, which would be consistent with Benoit *et al.* [26]. However, at much higher concentrations in Cr(VI) (about 20 times higher at least), the use of radioisotope  $^{51}\text{Cr}$  by Desestret *et al.* [12] did not reveal any incorporation of Cr(VI) into the passive film on X1CrNiSi18-15-4 SS.

Main conclusion for the case of Cr(VI) is that this oxidizing species, unlike V(V), does not enhance HNO<sub>3</sub> reduction for either alloy, the opposite effect being observed.

More striking electrochemical differences between the two SS can be observed in the anodic region of the measurement. Figs. 7A and 8 clearly demonstrate a decrease of the  $j_{\text{corr}}^*$  with the increase of Cr(VI) in a range of low concentrations, consistent with the literature [17]. This effect is not as clear for X2CrNi18-10 SS, where  $j_{\text{corr}}^*$  keeps increasing with the increasing concentration in HNO<sub>3</sub>. Nagano *et al.* [18] presented consistent results by varying the Si content of a 15Cr-13Ni SS in similar electrolyte for a Si enrichment of 4.15 wt. %.

Fig. 8 and Table 4 also show that  $E_{\text{tp}}$  of the X1CrNiSi18-15-4 SS is anodically shifted by 70 mV with increasing Cr(VI) concentration (between  $9.6 \cdot 10^{-4}$  and  $2.9 \cdot 10^{-2} \text{ mol dm}^{-3}$  in Cr(VI) species). The effect is more tenuous for the X2CrNi18-10 SS but the quantification is delicate since the alloy is already transpassive as shown in Fig. 8. When all the experiments of the present work are put on the same  $j$ - $E$  diagram (Fig. 6), it becomes clear that the presence of Cr(VI) induces a significant modification of the anodic behavior of the alloys, and that the effect is even more important for X1CrNiSi18-15-4 SS. As Cr(III) is the oxidation state of Cr predicted by the Pourbaix diagrams [32] to be stable in a large range of potentials at pH = 0, it was expected by a few authors that the reduction of Cr(VI) could directly enhance the passivity of the SS by producing extra Cr<sub>2</sub>O<sub>3</sub> at the surface. However, as mentioned before, previous investigations [12] did not see this enhancement of passivity at low Cr(VI) concentrations.

#### 4. Conclusion

The present work aimed at identifying the origin of the differences on the corrosion behavior of SS in HNO<sub>3</sub> induced by the presence of Si in the alloy. Linear sweep voltammetry

at low scan rate enabled to distinguish the effect of Si on the anodic and cathodic reactions by comparing X1CrNiSi18-15-4 SS to X2CrNiN18-10 SS.

Firstly, it was shown that an important Si enrichment in the oxide layer of the steel may have great consequences on the mechanisms and kinetics of both reduction of the electrolyte and oxidation of the material.

It was shown in pure  $\text{HNO}_3$  or in the case of oxidizing species as  $\text{V(V)}$  that Si lowers the cathodic reaction kinetics.

As a direct consequence of this phenomenon,  $E_{\text{corr}}$  is lowered by Si alloying. Therefore, in conditions where the X2CrNiN18-10 SS is shifted into its transpassive domain, the X1CrNiSi18-15-4 SS remains passive, even if the comparison of the  $j_{\text{corr}}^*$  confirmed that the Si-rich oxide may not be as protective as the passive layer identified at the X2CrNiN18-10 SS surface.

The break of passivity at high potentials  $E_{\text{tp}}$  does not depend on the silicon enrichment, except in presence of  $\text{Cr(VI)}$  which is revealed to have a very singular affinity to the X1CrNiSi18-15-4 SS interface.

Consistent with literature,  $\text{Cr(VI)}$  revealed a modification of the anodic answer of the X1CrNiSi18-15-4 SS, lowering its dissolution rate. Even if the hypothesis of  $\text{Cr(VI)}$  reducing into a stable  $\text{Cr(III)}$  product was never shown, this specific interaction between X1CrNiSi18-15-4 SS interface and  $\text{Cr(VI)}$  highlights the importance of understanding various types of reduction reactions at this X1CrNiSi18-15-4 SS interface.

## 5. Acknowledgements

The authors would like to thank Areva for partial financing this work.

## REFERENCES

1. P. Fauvet, Nuclear corrosion science and engineering, 679, Woodhead Publishing, Cambridge (2012).
2. B. Gwinner, M. Auroy, F. Balbaud-Célérrier, P. Fauvet, N. Larabi-Gruet, P. Laghoutaris and R. Robin, Corrosion Science, 107, 60 (2016).
3. V. Bague, S. Chachoua, Q. T. Tran and P. Fauvet, Journal of Nuclear Materials, 392, 396 (2009).
4. T. Honda, T. Yokosuka and Y. Arai, Corrosion 97 (1997).
5. Y. Kuriki, M. Tamura, N. Yamanouchi and K. Kiuchi, Third International Conference on Nuclear Fuel Reprocessing and Waste Management. RECOD '91 Proceedings, 1049 (1991).
6. S. Kass, J. D. Grozier and F. L. Shubert, Transactions ASM, 69 (1963).
7. B. E. Wilde, Corrosion, 44, 699 (1988).
8. O. V. Kasparova and Y. V. Baldokhin, 60 (2011).
9. R. R. Kirchheiner, F. Hofmann, T. H. Hofmann and G. Rudolph, Corrosion 86, 120 (1986).
10. A. Desestret, Materiaux et Techniques, S. I. R. P. E. (1977).
11. G. Plante and G. Chaudron, C.R. Acad. Sc. Paris, 261, 994 (1965).
12. A. Camus, A. Desestret, M. Froment and P. Guiraldenq, Comptes Rendus Hebdomadaires Des Seances De l'Academie Des Sciences Serie C, 264, 425 (1967).
13. J. S. Armijo and B. E. Wilde, Corrosion Science, 8, 649 (1968).



14. R. Robin, F. Miserque, *Journal of Nuclear Materials*, 375, 65-71 (2008).
15. A. R. Perrin and K. T. Aust, *Materials Science and Engineering*, 51, 165 (1981).
16. O. V. Kasparova, V. Cihal, V. M. Milman, I. Kasova, S. D. Bogolyubskii and N. M. Ostrikova, *Protection of Metals*, 27, 5, 554-562 (1991).
17. G. Plante, *Contributions à l'étude de la passivité d'aciers inoxydables en milieu nitrique bouillant*, Université de Paris (1969).
18. N. Hiroo, K. Haruhiko and U. Noriaki, *Center for Cooperative Research Gifu University*, research report, 28 (1998).
19. D. Landolt, *Corrosion et chimie de surfaces des métaux*, Presses polytechniques et universitaires romandes (1997).
20. V. Maurice and P. Marcus, *Electrochimica Acta*, 84, 129 (2012).
21. C. A. Della Rovere, J. H. Alano, R. Silva, P. A. P. Nascente, J. Otubo and S. E. Kuri, *Materials Chemistry and Physics*, 133, 668 (2012).
22. P. Fauvet, F. Balbaud, R. Robin, Q. T. Tran, A. Mugnier and D. Espinoux, *Journal of Nuclear Materials*, 375, 52 (2008).
23. F. Balbaud, *Mécanisme de corrosion de l'acier inoxydable Z3 CN 18.10 en présence de condensats nitriques*, Université Pierre et Marie Curie (1998).
24. D. Sicsic, F. Balbaud-Celerier and B. Tribollet, *European Journal of Inorganic Chemistry*, 6174 (2014).
25. R. Lange, E. Maisonhaute, R. Robin and V. Vivier, *Electrochemistry Communications*, 29, 25 (2013).

26. M. Benoit, Modélisation de la cinétique de réduction de l'acide nitrique concentré sur acier inoxydable 304L, Université Pierre et Marie Curie (2016).
27. V. P. Razygraev, M. V. Lebedeva, S. A. Kabakchi, E. Y. B. Ponomareva, R. S. and L. P. Lobanova, Journal of Applied Chemistry USSR, 61 (1988).
28. P. Schmuki, S. Virtanen, H. S. Isaacs, M. P. Ryan, A. J. Davenport, H. Böhm and T. Stenberg, Journal of The Electrochemical Society, 145, 791 (1998).
29. M. Bojinov, G. Fabricius, T. Laitinen and T. Saario, Electrochimica Acta, 44, 4331 (1999).
30. T. Motooka, C. Kato and M. Yamamoto, Zairyo-to-Kankyo, 59, 18 (2010).
31. P. Martin and P. Alena, IOP Conference Series: Materials Science and Engineering, 9, 012074 (2010).
32. M. Pourbaix, Atlas of electrochemical equilibria in aqueous solutions, Pergamon Press (1966).
33. E. Irisawa, M. Seki, F. Ueno, C. Kato, T. Motooka and H. Abe, Global 2015, Paris (2015).
34. D.-Y. Lin and T.-C. Chang, Materials Science and Engineering: A, 359, 396 (2003).
35. J. Stolarz, J. Le Coze and A. Desestret, Colloque de Physique, 51, 1641-1645 (1990).
36. B. Beverskog and I. Puigdomenech, Corrosion Science, 39, 43 (1997)



## **4.2. A Direct Measurement of the Activation Potential of Stainless Steels in Nitric Acid**

### **4.2.1. An introduction to the activation potential**

As mentioned in the state of the art, it sounded truly important to bring some more information about the oxide layer of the Uranus S1N SS. In this second chapter, the thermodynamics of the oxide were investigated through the transition between passive and active state directly in  $\text{HNO}_3$ . This type of characterization used to be investigated on a wide range of metals and alloys [53-58] and the first attempt was very likely to have been made by Friedrich Flade in 1911 [59] on Fe. The activation potential is therefore sometimes called « Flade potential » (however, this denomination is more appropriate to pure Fe).

There are two kinds of measurements to access the value of the activation potential in acidic medium. Historically, the experiment proposed by Flade relies on the spontaneous activation of Fe in sulfuric acid. Similar behavior was observed for Fe-Cr alloys. The typical E vs. Time curve obtained in these conditions is shown in Fig. 14 and enables to estimate the activation potential.

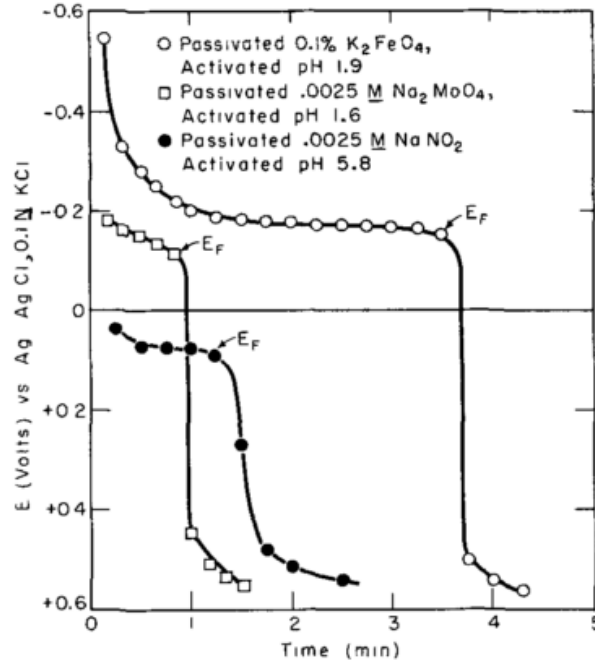


*Fig. 14. E vs. Time typical curve for an Fe electrode (passive at  $t=0$ ) in  $H_2SO_4$ : measurement of the Flade potential during a spontaneous activation (Uhlig et al. [55])*

The second possibility to measure the activation potential is to use linear polarization in the cathodic direction, and identify the transition between passive and active state. But both of these methods can only be easily performed in pure acids with a low potential reduction reaction such as the proton reduction reaction. Otherwise, the anodic current in the active domain of the steel will be lower than the cathodic current and the active domain will not appear, or the material will not spontaneously activate. It explains why most of the studies in the state of the art performed the measurements in low concentrated  $H_2SO_4$ .

In the state of the art, numerous measurements for the activation potential of Fe, Fe-Cr, or Fe-Cr-Ni alloys are displayed as a function of pH. Vetter [60] ascertained many results of the literature to show that a linear dependence is usually found between the pH and  $E_a$  for a given material (Fig. 15) because  $E_a$  follows a Nernst-type evolution with pH.

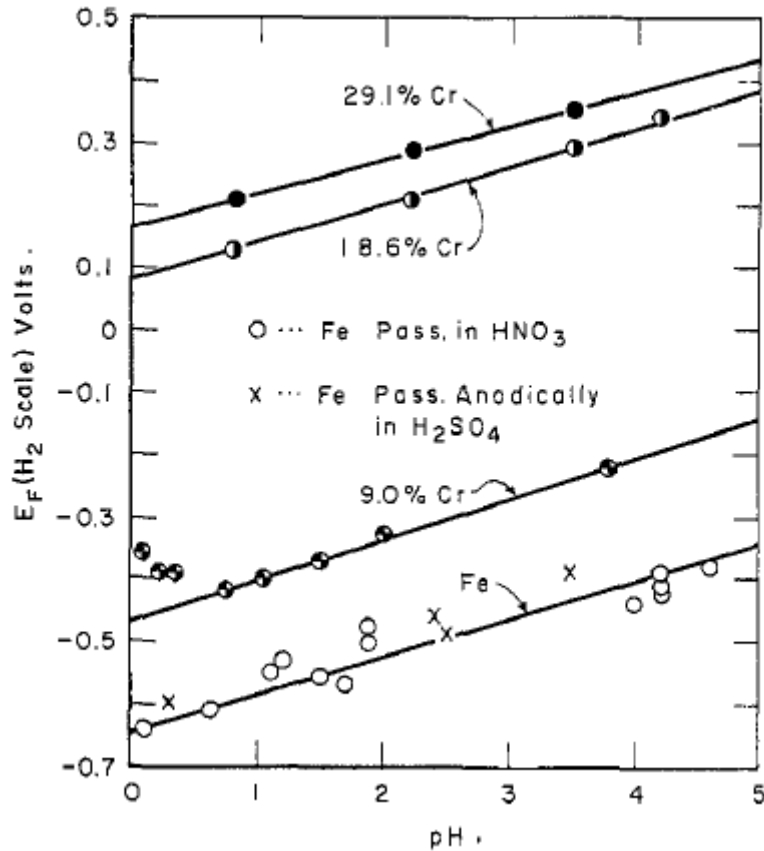


Fig. 15. Activation potential of Fe-Cr alloys in  $H_2SO_4$  as a function of pH at 25°C (Uhlig et al. [61] spontaneous activation)

Baroux [1] precized that in very acidic envrionments, kinetical effects must also be taken into account because of the competition between the formation and dissolution of the oxide.

In  $HNO_3$ , the reduction reaction occurs at a high potential, and consequently the cathodic current is largely superior to the anodic current in the passive-active region. To measure  $E_a$ , several methods are ascertained in the literature. A mass loss measurement after several potentiostatic polarizations at different values are one of them. However, this is quite a long and fastidious way of performing the measurement, and the precision of the measurement will depend on the step between each polarization potential. It is also possible to measure indirectly the activation of the material with an appropriate reduction reaction whose kinetics would be increased by the activity of the bare surface [58]. Adding some chlorides in the

electrolyte also helps increasing the anodic current in the active domain enough for it to overreach the cathodic current, however this type of measurement comes with uncertainties both on the mechanism of passivity breakdown and precision of the measurement [62].

#### 4.2.2. Experimental strategy

In this second chapter, the AESEC technique turned out to be a very convenient mean to measure  $E_a$ . pH and temperature were controlled and varied, and both Uranus S1N and 304L were tested. By performing  $0.2 \text{ mV s}^{-1}$  polarization curves, the current was recorded between the OCP and  $-0.9 \text{ V vs. MSE}$ . At the end of the experiment, the potentiostat recorded several hundreds of negative  $\text{mA cm}^{-2}$ . Simultaneously, the ICP was able to record the increase of the dissolution equivalent current associated to the active dissolution of the material. At the end of the experiment, this anodic equivalent current reaches only few  $\text{mA cm}^{-2}$  which is much lower than the reduction current. The hydrodynamics of the set-up were corrected according to previous work [46, 63-65] in a way the external current could be convoluted and superimposed in a more accurate time scale on the ICP results. One could notice that the other way of doing the calculation could be more intuitive (deconvolute the ICP signals), but this would introduce loss of information due to the need of a pretreatment of the data (smoothing of the signals).

Several  $\text{HNO}_3$  concentrations were used from 2 to  $6 \text{ mol dm}^{-3}$ . The proton activity was then estimated from Fallet *et al.* [66]. Temperatures from ambient to  $80^\circ\text{C}$  were for the first time recorded as well. However, it can be noticed that due to the thin capillaries, a heat loss could have been accused and is not taken into account in the present work.  $80^\circ\text{C}$  was a very delicate temperature to perform the experiment because of the membrane that could turn permeable. This explains why the measurement at this temperature was kept as short as possible.

XPS analyses were used for different conditions of passivation both in HNO<sub>3</sub> and H<sub>2</sub>SO<sub>4</sub> in order to relate our measurements to the literature.

ICP-AES data treatment associated to the present work are described in the following equations :

$$v_M = f \frac{C_M}{A} \quad (10)$$

$$j_M = F \frac{v_M z_M}{M_M} \quad (11)$$

with  $f$  being the flow rate,  $C_M$  concentration in M,  $A$  surface of the sample,  $F$  the Faraday constant,  $z_M$  the oxidation state of M and  $M_M$  its molar mass.

#### 4.2.3. Main results

Fig. 16 displays the typical activation measurement on the Uranus S1N in HNO<sub>3</sub>. The external current  $j_e^*$  reaches -31 mA cm<sup>-2</sup> at -0.9 V vs. MSE, whereas the anodic dissolution equivalent current only reach few mA cm<sup>-2</sup>, remaining undetectable if the measurement was purely electrochemical.



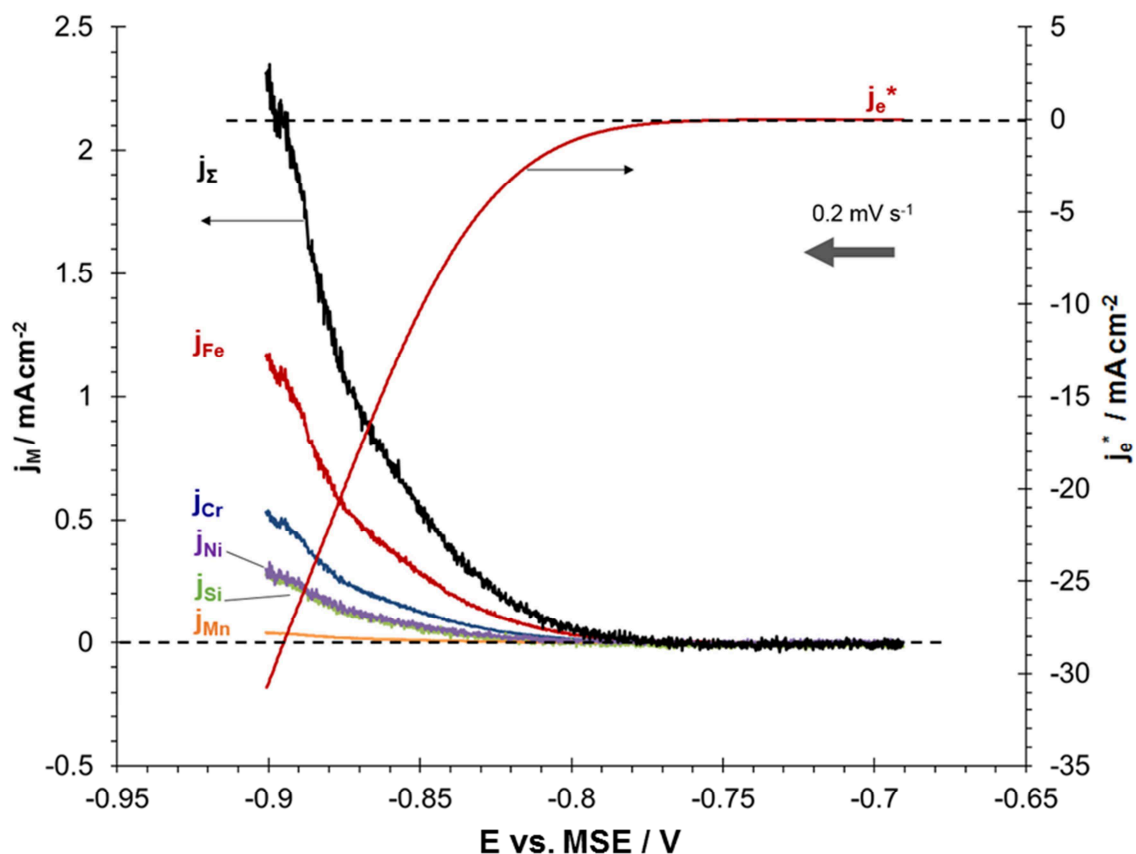


Fig. 16. Elemental dissolution currents  $j_M$ , total dissolution current  $j_\Sigma$  and external current  $j_e^*$  as a function of potential for the Uranus S1N SS in  $4 \text{ mol dm}^{-3} \text{ HNO}_3$ ,  $28^\circ\text{C}$ , cathodic direction, scan rate:  $V = 0.2 \text{ mV s}^{-1}$  (black:  $j_\Sigma$  ; red:  $j_{Fe}$ ; blue:  $j_{Cr}$ ; purple:  $j_{Ni}$ ; green:  $j_{Si}$ ; orange:  $j_{Mn}$ ; red curve on the secondary y-axis:  $j_e^*$ ).

In the passive domain, at higher potentials than  $0.75 \text{ V vs. MSE}$ ), the dissolution currents are lower than the detection limits. An empirical criterion has to be chosen to determine  $E_a$ . Based on the non-selectivity of the dissolution observed for Mn, which also has the lowest detection limit, it was considered that  $E_a$  was reached when  $j_{Mn}$  was overreaching five times the detection limit of Mn. But it was verified that other criteria were leading to very similar results.

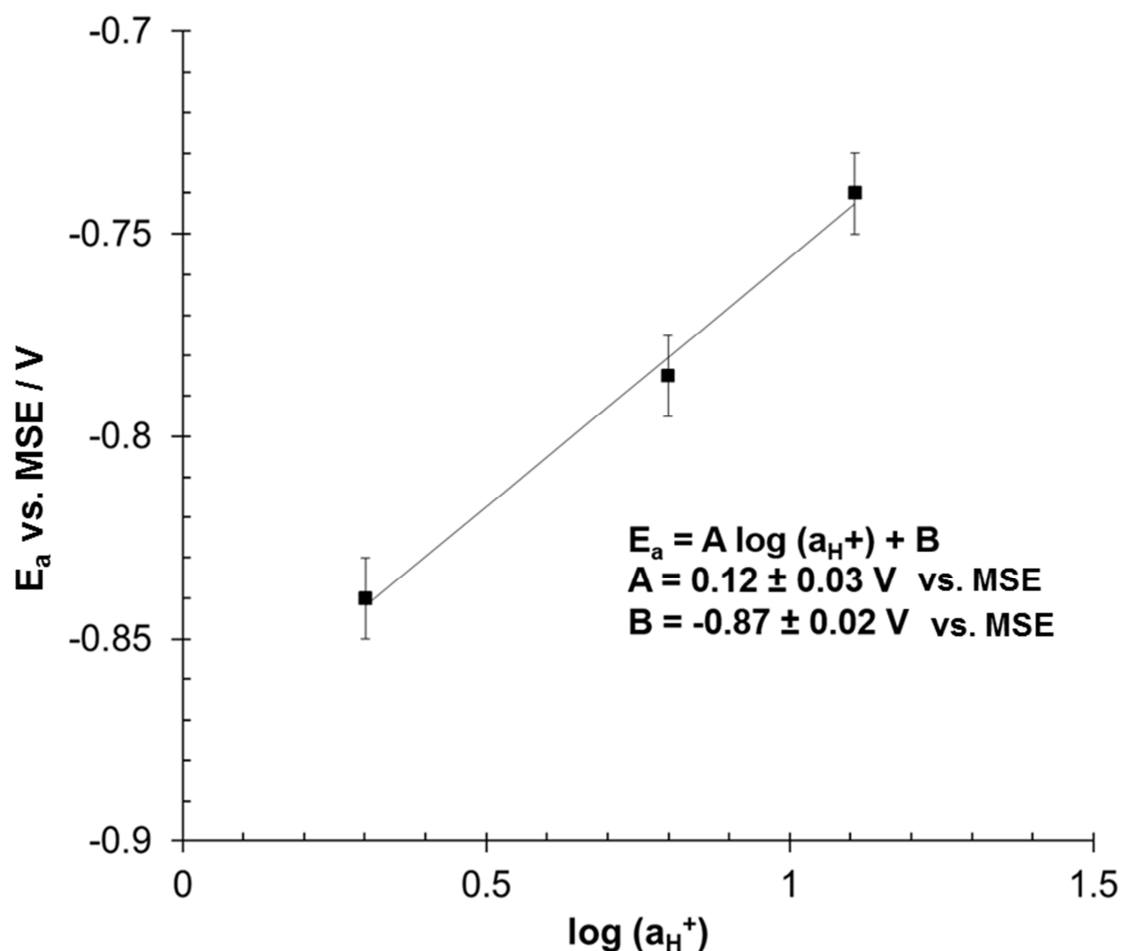


Fig. 17. Activation potential of the Uranus S1N SS in  $HNO_3$  depending on the pH at 28 °C

At 28°C the concentration of the electrolyte was varied between 2 and 6 mol dm<sup>-3</sup>. The curve obtained is shown in Fig. 17. The slope is perfectly comparable to what Rocha *et al.* [53] found in  $H_2SO_4$  using linear polarization method, and is twice the value of the slope found by Uhlig *et al.* and Feller *et al.* [56, 61] using spontaneous activation. But such a difference had already been identified by the same authors. The best hypothesis to explain this factor 2 relies on the mechanism of the reduction of the oxide which could be more or less homogeneous depending on the method of measurement.

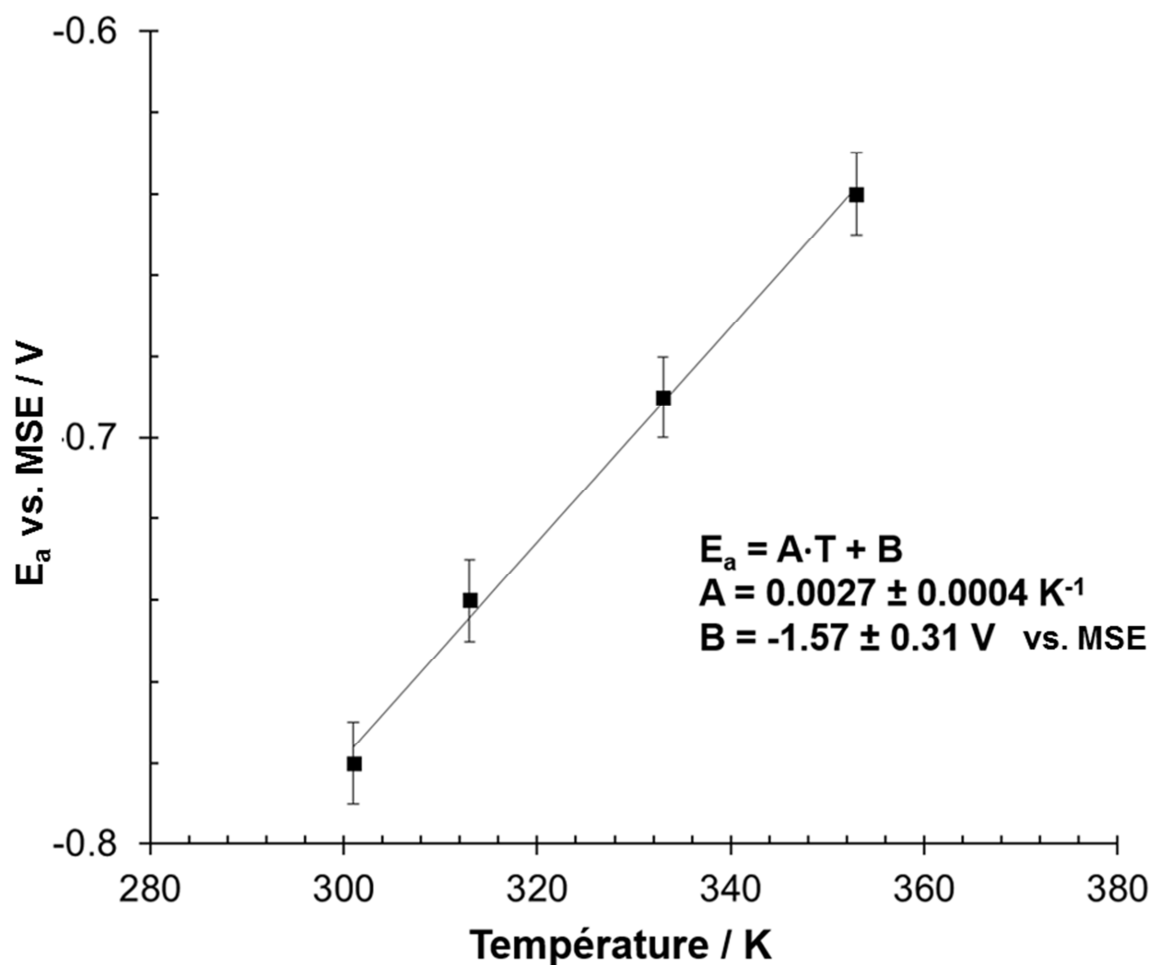


Fig. 18. Activation potential of the Uranus S1N SS in  $4 \text{ mol dm}^{-3} \text{ HNO}_3$  depending on the temperature

For the second experiment, a concentration  $n$  of  $4 \text{ mol dm}^{-3}$  was fixed, then  $E_a$  was recorded at different temperatures of the Uranus S1N SS (Fig. 18). Temperature dependence had never been clearly investigated but a linear dependance was found in the present work as shown in Fig. 18, and is quite coherent if  $E_a$  evolves following Nernst equation at fixed pH. The coefficient of the slope remains however difficult to explain because both measurements do not correlate well. However, further investigations and a better heat control could probably lead to very satisfying results.

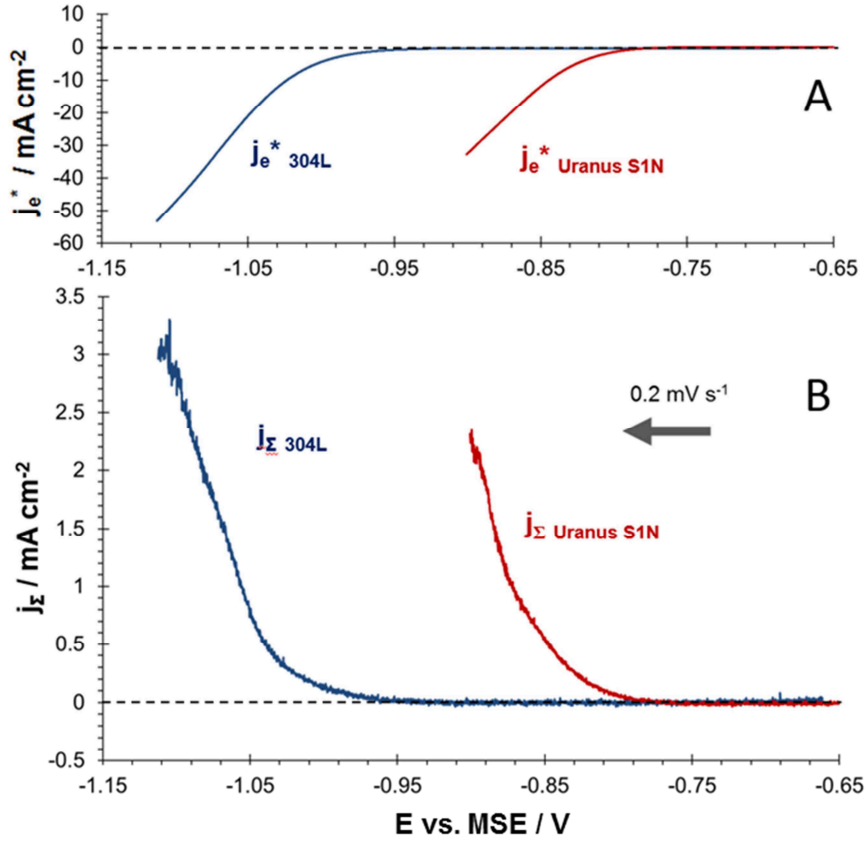


Fig. 19. Elemental dissolution currents  $j_M$ , total dissolution current  $j_\Sigma$  and external current  $j_e^*$  as a function of potential for the Uranus S1N SS and 304L SS in 4 mol dm<sup>-3</sup> HNO<sub>3</sub>, 28°C, cathodic direction, scan rate:  $V = 0.2 \text{ mV s}^{-1}$

Eventually, the impact of Si on  $E_a$  was evaluated by comparison to the 304L SS in the same condition, at 4 mol dm<sup>-3</sup>, 28 °C. Fig. 19 reveals that they are separated by almost 200 mV. Thermodynamically, it would suggest that the Uranus S1N oxide layer requires less energy ( $E_a$  is higher) to reduce than the oxide layer of the 304L SS. It was quite surprising given the fact that the passive-active transition was usually attributed to the reduction of  $\text{Cr(III)} \rightarrow \text{Cr(II)}$ , but stresses the importance of Si in this mechanism. Vetter explained that  $E_a^\circ$  that can be extracted from Fig. 17 for example could be associated to the  $E^\circ$  of an oxide electrode and ascertained several values, such as  $\text{Cr/Cr}_2\text{O}_3$  at -1,25 V vs. MSE [60]. By assuming that the slope  $E_a$  vs. pH will be identical for both SS, Fig. 19 would suggest that  $E_a^\circ$

of the 304L SS would value around -1,10 V vs. MSE. It would then fit satisfyingly to the value given by Vetter for  $E^\circ(\text{Cr}/\text{Cr}_2\text{O}_3)$ .

Nevertheless, XPS measurements tend to show that Cr is involved in a totally different type of oxide in the two SS. If the 304L SS will be very likely to be covered by  $\text{Cr}_2\text{O}_3$ , the Uranus S1N SS turns out to be more likely covered by mixed Cr-Fe silicates. It would then not be very surprising if  $E_a^\circ$  was indeed associated to this oxide.  $E^\circ(\text{Si}/\text{SiO}_2) < E^\circ(\text{Cr}/\text{Cr}_2\text{O}_3)$  according to Vetter, however  $E_a^\circ$  of the Uranus S1N SS is higher than for the 304L SS. As mentioned before, the kinetics aspects of the dissolution of the passive layer should be taken into account.

#### 4.2.4. Conclusion

AESEC enabled for the very first time to measure in situ the activation potential of the Uranus S1N in  $\text{HNO}_3$  both depending on pH and temperature. Si was shown to impact directly the energy required for the reduction of the oxide layer.

From an industrial point of view, the risk for the steel to be brought to its active domain remains minimum because of the very oxidizing operating conditions. However, the temperature dependence found enables to extrapolate the value of  $E_a$  at higher temperatures. At  $100^\circ\text{C}$ ,  $E_a$  would probably reach around -0.60 V vs. MSE in  $4 \text{ mol dm}^{-3} \text{HNO}_3$  while the  $E_{\text{corr}}$  (as seen in chapter 1) would be of -0.15 V vs. MSE. But in internal references, it was shown that under certain circumstances ( $C_{\text{H}^+} = 2,5 \text{ mol dm}^{-3}$ ,  $C_{\text{NO}_3^-} = 5 \text{ mol dm}^{-3}$ ) the activation occurs at values around -0.25 V vs. MSE while the  $E_{\text{corr}}$  is -0.15 V vs. ESM which is actually more risky. It is therefore important to have an easy mean to evaluate  $E_a$  in different conditions.

#### 4.2.5. Publication - A Direct Measurement of the Activation Potential of Stainless Steels in Nitric Acid, Journal of The Electrochemical Society, 164 (9) C481-C487 (2017)



## A Direct Measurement of the Activation Potential of Stainless Steels in Nitric Acid

B. Laurent,<sup>a</sup> N. Gruet,<sup>a</sup> B. Gwinner,<sup>a</sup> F. Miserque,<sup>a</sup> M. Tabarant,<sup>b</sup> and K. Ogle<sup>c,\*</sup>

<sup>a</sup>Den-SERVICE de la Corrosion et du Comportement des Matériaux dans leur Environnement (SCCME), CEA, Université Paris-Saclay, F-91191 Gif-sur-Yvette, France

<sup>b</sup>Den-SERVICE d'Etudes Analytiques et de Réactivité des Surfaces (SEARS), CEA, Université Paris-Saclay, F-91191 Gif sur Yvette, France

<sup>c</sup>Paris Sciences et Lettres, Chimie ParisTech, IRCP-CNRS, 75005 Paris, France

The rate of anodic dissolution and the associated activation potential that characterizes the passive-active transition of stainless steels have been measured directly for the first time in nitric acid. The anodic dissolution current under cathodic polarization in pure nitric acid, in absence of chlorides, is masked by intense cathodic hydrogen reduction. In this work, atomic emission spectroelectrochemistry (AESEC) was used to record simultaneously the dissolution rate of the individual alloying elements of stainless steels as well as the overall cathodic current. This methodology has been used to quantify the influence of several parameters on the activation potential: nitric acid concentration, temperature, and the addition of silicon in the steel composition.

© The Author(s) 2017. Published by ECS. This is an open access article distributed under the terms of the Creative Commons Attribution 4.0 License (CC BY, <http://creativecommons.org/licenses/by/4.0/>), which permits unrestricted reuse of the work in any medium, provided the original work is properly cited. [DOI: 10.1149/2.0081709jes] All rights reserved.



Manuscript submitted April 26, 2017; revised manuscript received June 6, 2017. Published June 23, 2017.

Nitric acid,  $\text{HNO}_3$ , is a widely-used electrolyte in nuclear reprocessing plants for spent nuclear fuel.<sup>1,2</sup> In addition to its acidic properties,  $\text{HNO}_3$  is a strong oxidizing agent and therefore material choice for the industrial devices must follow strict specifications. Some austenitic stainless steels (SS) such as the 18Cr-10Ni type SS are frequently chosen because of their high corrosion resistance in concentrated nitric acid.<sup>1</sup>

The cathodic and anodic reactions of stainless steel in concentrated nitric acid have been the object of numerous investigations.<sup>3-7</sup> Cathodic processes involved in austenitic SS corrosion in concentrated nitric acid have been investigated since the beginning of the 20<sup>th</sup> century.<sup>6,8-10</sup> However, in the very low range of potentials of interest for the present work, the proton reduction reaction is expected to prevail.<sup>6</sup>

The anodic reactions of stainless steel in the active state have proven difficult to investigate due to the fact that stainless steel is spontaneously passive in concentrated nitric acid, and when polarized to the active potential domain, the high cathodic current completely masks the anodic current. Under certain conditions, the potential of nitric acid can find itself closer to the active domain. Some other acidic electrolytes such as  $\text{H}_2\text{SO}_4$  or  $\text{HCl}$  have more clearly shown a spontaneous activation of SS in spite of high initial open circuit potentials<sup>11,12</sup> or when polarized for a long time close to the active domain.<sup>13</sup> This supports an interest into exploring the passive layer stability on the edge of the active dissolution. When the electrode potential becomes increasingly cathodic and approaches the active state, the oxides making up the passive film become thinner, less protective, and the dissolution rate of the steel increases. In general, the thickness of the passive film is determined by a steady state between film growth and film dissolution. To a first approximation, the rate of film growth will decrease with decreasing potential, while film dissolution is less dependent on potential and more a function of electrolyte pH. Although the oxidation rate of the stainless steel should, in theory, decrease with decreasing potential, the rate of elemental dissolution will increase due to the decreased thickness of the passive film. The potential below which the dissolution rate becomes measurable is referred to as the “activation potential”,  $E_a$ .

Many studies of the “activation potential” have been made on various materials including pure iron,<sup>11,12</sup> iron-chromium alloys<sup>12,14</sup> and more complex alloys involving nickel and other elements.<sup>16,17</sup> They lead to an establishment of a linear dependence between the activation potential and the logarithm of the proton activity. These measurements have mostly been performed in sulfuric acid using linear

sweep voltammetry.<sup>12,14,18</sup> This is possible because there is a sufficiently wide electrochemical window to measure active dissolution at low potentials without interference from cathodic reactions. Frankenthal et al.<sup>18</sup> showed that an accurate measurement of  $E_a$  was possible to within a few millivolts. However, in nitric acid, no cathodic loop behavior (total current that becomes positive over a short range of potentials in the active domain of the steel) can be observed because overall current is strongly negative. Such a method is not appropriate for concentrated nitric acid due to the high cathodic current in the active potential domain. Measurements of  $E_a$  can also be based on the spontaneous activation behavior of stainless steels in sulfuric acid.<sup>15,17</sup> After a passivation polarization of the sample in sulfuric acid, the potential at which passivity decays spontaneously to an active potential on shutting off this anodic polarization has been also called the “Flade potential”.<sup>16,19</sup> Once again, this method cannot be applied to nitric acid because the sample is spontaneously passive. It must also be noticed that using a voltammetric linear scan may have an impact on the mechanism of passivity breakdown in the case of chromium rich passive layers.<sup>18</sup> King and Uhlig<sup>12</sup> highlighted that linear scan measurements doubled the slope  $E_a = f(\text{pH})$  and that this difference could be related to differing chemical equilibria accompanying the breakdown of passivity.

In several references, samples were passivated in nitric acid and their activation potential was then studied in sulfuric acid.<sup>11,20</sup> According to these authors, stainless steel passivated in  $\text{HNO}_3$  and in  $\text{H}_2\text{SO}_4$  show a very similar behavior. However, they were not able to perform the in situ measurement since below the corrosion potential, the contribution of the anodic dissolution (active and passive) of the sample to the overall electrochemical current is completely masked by the cathodic reduction of nitrate. The use of chlorides<sup>23</sup> provided a way to increase anodic current density and thus a chance to observe an anodic contribution greater than the reduction current at low potentials, which was a proof of the active dissolution, but did not permit easily the determination of the activation potential. A few attempts have been made at measuring the activation potential by gravimetry in a discontinuous way to measure this anodic dissolution rate below the corrosion potential. The material was polarized at low potentials where the reduction reaction is intense, and the weight loss recorded after several hours of polarization.<sup>3,21</sup> Such a method raises the issue of the solution chemical equilibria over the measurement time. It requires a massive electrode that releases a high quantity of metallic ions, while at the same time the counter electrode, in the same reactor, can highly disturb gas equilibria in the environment. The analysis of the increasing cathodic current during a long-term polarization of samples in  $\text{HCl}$  enabled Moshaweh and Burstein<sup>13</sup> to identify the activation of SS under high cathodic currents. Activation

\*Electrochemical Society Member.

<sup>†</sup>E-mail: [kevin.ogle@chimie-paristech.fr](mailto:kevin.ogle@chimie-paristech.fr)

**Table I.** Mass composition of Si-rich and 304L SS determined by GD-OES profiles performed on samples and averaged between 10  $\mu\text{m}$  and 40  $\mu\text{m}$  depth expressed in wt%.

	Fe	Cr	Ni	Si	Mn	Add.
Si-rich SS	59.8	18.8	15.1	3.5	2.0	0.8
304L SS	70.3	17.8	9.5	0.3	1.5	0.6

was deduced qualitatively and indirectly by observing the enhancement of the cathodic hydrogen reduction due to the exposed metallic surface.

In this work, a novel method of directly measuring the activation potential of stainless steel in  $\text{HNO}_3$  will be presented using atomic emission spectroelectrochemistry (AESEC). In this way, the anodic dissolution of the stainless steel was measured directly despite a cathodic current which is orders of magnitude larger. The variation of the activation potential was measured as a function of nitric acid concentration, temperature and silicon concentration of the steel and interpreted in terms of oxide stability. Previous work concerning the application of AESEC to stainless steel was essentially limited to the case of sulfuric acid,  $\text{H}_2\text{SO}_4$ . Briefly, the electrochemical kinetics of dissolution in the active state were investigated in the earliest AESEC publication.<sup>22</sup>

### Experimental

**Materials.**—18Cr-15Ni-3.5Si SS (designated in the present work as Si-rich SS) and 18Cr-10Ni SS (designated in the present work as 304L SS) were used in this work for AESEC measurements. The specimens were cut into squares of 20 mm  $\times$  20 mm  $\times$  1 mm. The elemental analysis of the steel was performed by glow discharge optical emission spectroscopy (GD-OES) using a GD-Profilier from Horiba-Jobin Yvon. From the signals given by the GD-OES, the bulk of the sample was clearly reached from 10 to 40  $\mu\text{m}$  depth and the composition of the steel was averaged over two craters on different samples. This analysis is given in Table I. Si-rich and 304L SS are very similar stainless steels in composition, except for silicon and nickel. Relative ratios between major elements Fe, Cr and Ni are comparable. Prior to any use, the specimens were cleaned with ethanol and acetone in an ultrasonic bath, then polished to a mirror finish with 0.03  $\mu\text{m}$  diamond paste. Polishing ensures good sealing in the AESEC flow cell and allows possible ex situ surface analysis of the sample if required. All samples were then left for passivation at open circuit potential for 24 h in nitric acid at the desired concentration and at room temperature in separate beakers. The passive film was then analyzed by X-ray photoelectron spectroscopy prior to any AESEC measurement.

**Electrolytes.**—Deionized water (18.2 M $\Omega$  cm) was prepared with a Millipore system and used for all electrolytes. Nitric acid 68% (Sigma Aldrich) was used to prepare the solutions. pH of each solution was verified using a Mettler-Toledo DL55 titrator and 1 mol dm<sup>-3</sup> (reagent grade, Sigma Aldrich). All glassware was protected with a paraffin film to avoid any hazardous contamination.

The experiments were performed in a temperature range of 28 to 80°C (301 to 353 K) using a recirculating water system connected to a thermocryostat (LAUDA) constant temperature bath. Water from the bath was circulated through a hollow copper block connected to the rear of the working electrode so that the electrode was heated

directly. The electrolyte reservoir was also heated in the constant temperature bath. Electrical isolation between the block and the sample was designed to prevent both current leakage and ensure heat transfer.

**Electrochemical measurements.**—The AESEC flow cell has been described in detail in previous publications.<sup>22,27</sup> It consists of a three-electrode cell with the stainless steel specimen as the working electrode (Si-rich SS or 304L SS), a small platinum grid as a counter electrode, a mercury-mercurous sulfate reference electrode (MSE,  $E = +0.65$  V vs. SHE in saturated  $\text{K}_2\text{SO}_4$ ). The flow cell consists of a small volume working electrode compartment (approximately 0.2 cm<sup>3</sup>) with electrolyte input at the bottom and output at the top. The flow rate was measured accurately (1% precision) for each experiment and nominally 3 cm<sup>3</sup> min<sup>-1</sup>. The reference and counter electrodes were in a separate compartment separated from the working electrode by a porous membrane to allow passage of electrical current but avoid bulk mixing of the two solutions. A Gamry Reference 600 potentiostat functioning in the potentiodynamic linear polarization mode was used to measure electrochemical current density  $j_e$  with a 0.2 mV s<sup>-1</sup> scan rate. It should be mentioned that using a dynamic measurement could impact the values obtained,<sup>12,13</sup> however, the slow scan rate used here enables the measurement of electrical current at a quasi-stationary state of the electrochemical reactions within a reasonable total time of experiment. The analog outputs of the potentiostat were fed into the A/D converter and data acquisition software of the ICP-OES spectrometer so that the ICP-OES intensity data and the electrochemical data were on exactly the same time scale.

**Atomic emission spectroelectrochemistry.**—The experimental set-up including data acquisition has been described in detail in Ogle et al.<sup>22</sup> Briefly, the working electrode releases ions into the electrolyte in the flow cell. The electrolyte is then continuously fed into the plasma of the ICP-OES where the emission intensities of the different ions are measured simultaneously. These emission intensities were converted into concentration using standard ICP-OES calibration techniques. Electrolyte transport was implemented via a peristaltic pump. Electrolyte transfer into the plasma was realized via a concentric glass nebulizer and a cyclonic spray chamber. The ICP-OES used in this work was an Ultima 2C from Horiba Jobin Yvon consisting of a 40.68 MHz inductively coupled Ar plasma, operating at 1 kW and interfaced to independent polychromator and monochromator optical modules. A 50 cm focal length Paschen-Runge polychromator was used equipped with an array of photomultiplier tube detectors at given wavelengths allowing the measurement of up to 50 preselected elements simultaneously. Emission wavelengths were chosen for maximum sensitivity and low interferences. The monochromator (1 m focal length) with a Czerny–Turner configuration is dedicated for high spectral resolution of a single element. In the present work, the monochromator was used to monitor the Cr signal. Wavelengths used for each element and corresponding detection limits are given in Table II.

**AESEC data treatment.**—For each element M, instantaneous dissolution rate  $v_M$  and current  $j_M$  are calculated from the instantaneous elemental concentration  $C_M$ :<sup>22</sup>

$$v_M = f \frac{C_M}{A} \quad [1]$$

$$j_M = F \frac{v_M z_M}{M_M} \quad [2]$$

**Table II.** Wavelengths used for each major element of the two stainless steels, corresponding atomic weights and detection limits associated (averaged over 10 experiments).

	Fe	Cr	Ni	Si	Mn
Wavelength / nm	259.940	283.563	231.604	251.611	257.610
Atomic weight / g mol <sup>-1</sup>	55.8	51.9	58.7	28.1	54.9
Detection limit $C_{3\sigma}$ / $\mu\text{g dm}^{-3}$	12.1	7.3	27.3	30	1.0



**Table III.** Parameters used for the deconvolution of XPS spectra (Avantage software). Binding energies and full width at half maximum (FWHM).

	[Fe Ox] / at. %		[Cr Ox] / at. %			[Si Ox] / at. %	
	Fe - 2p <sup>3/2</sup>	Fe - 2p <sup>3/2</sup>	Cr - 2p <sup>3/2</sup>	Cr - 2p <sup>3/2</sup>	Cr - 2p <sup>3/2</sup>	Si - 2p	Si - 2p
Binding energy / eV	709.69	712.07	576.26	577.32	578.99	102.05	102.65
FWHM / eV	2.36	2.93	1.08	1.92	1.71	1.36	1.32

where  $f$  is the flow rate of the electrolyte,  $A$  the surface area,  $F$  the Faraday constant,  $z_M$  the oxidation state of the element  $M$ , and  $M_M$  its molar weight. Total dissolution current  $j_\Sigma$  can be defined as the sum of major elements dissolution currents:

$$j_\Sigma = \sum j_M \quad [3]$$

and  $j_\Sigma$  will be compared to electrical current  $j_e^*$  which is obtained by convoluting the electrical current measured by the potentiostat,  $j_e$ , using an experimental transfer function  $h(t)$ , where  $h(t)$  represents the distribution of residence times in the flow cell.<sup>27</sup> Complex physical processes contribute to the broadening of  $h(t)$ . These processes include diffusion from the surface into the flowing electrolyte stream, mixing in the channel flow cell, spreading out during the laminar flow in the capillaries between the cell and the spectrometer, and the complicated nebulization system itself. Despite this complexity, an empirical function was simulated in the form of a log-normal distribution after an experimental measurement.<sup>24,27</sup> This convolution treatment is necessary to compare electrochemical current with elementary equivalent currents that are estimated from the elementary concentration transients in solution. The convolution integral is:<sup>22</sup>

$$j_e^*(t) = \int_0^t j_e(\tau) h(t - \tau) d\tau \quad [4]$$

The detection limits  $3\sigma$  are calculated as following:

$$C_{3\sigma} = 3 \frac{\sigma_{\text{blank}}}{\alpha} \quad [5]$$

where  $\sigma_{\text{blank}}$  is standard deviation of the background and  $\alpha$  the sensitivity factor calculated from the calibration curves of each element at their specific wavelength.

**X-ray photoelectron spectroscopy (XPS).**—XPS analyses were carried out with a Thermofisher Escalab 250 XI spectrometer using a

monochromatic X-ray Al K $\alpha$  source. The instrument was calibrated in energy with the silver Fermi level (0 eV) and the 3d<sup>5/2</sup> core level of metallic silver (368.3 eV). The C-1s signal was used to correct a possible charge effect: the CC/CH contribution of C-1s spectra was fixed at 285.0 eV. The analysis zone consisted of a 900  $\mu\text{m}$  diameter spot. No etching of the surface was done before the experiment. The data processing was performed using the commercially available Avantage software. The main parameters used to decompose XPS spectra into the various contributions of major elements of the alloy are presented in Table III.

## Results and Discussion

**Anodic dissolution below the corrosion potential.**—The AESEC method permits a direct measurement of the anodic dissolution of metals even when they cannot be detected in the electrical current. A typical example of this for the Si-rich stainless steel in HNO<sub>3</sub> is given in Fig. 1. A cathodic linear polarization sweep was performed beginning at the open circuit potential of  $0.19 \pm 0.01$  V vs. MSE where the steel is passive. As no significant dissolution rate is measured between the open circuit potential and  $-0.70$  V vs. MSE, only a  $-0.70$  V to  $-0.90$  V vs. MSE range of potential is presented in Fig. 1. Shown as a function of potential are the electrical current,  $j_e^*$ , and the elemental currents,  $j_M$ , and the sum of the elemental currents  $j_\Sigma$ . Fig. 2 shows  $j_e^*$ ,  $j_M$ , and  $j_\Sigma$  on a semilogarithmic scale. Ammonia, NH<sub>3</sub>, can be expected to be produced below 0.05 V vs. NHE ( $-0.60$  V vs. MSE).<sup>7</sup> However, in the same region the proton reduction reaction should also take place and dominate.<sup>7</sup> As the potential decreases in the cathodic direction,  $j_e^*$  increases systematically approaching  $-31$  mA cm<sup>-2</sup> at  $-0.9$  V vs. MSE reflecting the reduction of H<sup>+</sup> to H<sub>2</sub>. Supporting the idea that the proton reduction is the major reaction, two Tafel slopes of  $-40$  mV and  $-120$  mV per decade can be read

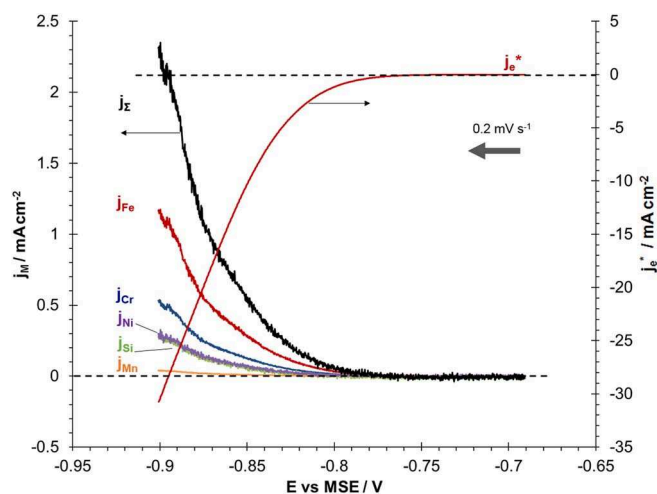


**Figure 1.** Elemental dissolution currents  $j_M$ , total dissolution current  $j_\Sigma$  and external current  $j_e^*$  as a function of potential for Si-rich SS in 4 mol dm<sup>-3</sup> HNO<sub>3</sub>, 28°C, cathodic direction, scan rate:  $V = 0.2$  mV s<sup>-1</sup> (black:  $j_\Sigma$ ; red:  $j_e^*$ ; blue:  $j_{Cr}$ ; purple:  $j_{Ni}$ ; green:  $j_{Si}$ ; orange:  $j_{Mn}$ ; red curve on the secondary y-axis:  $j_e^*$ ).

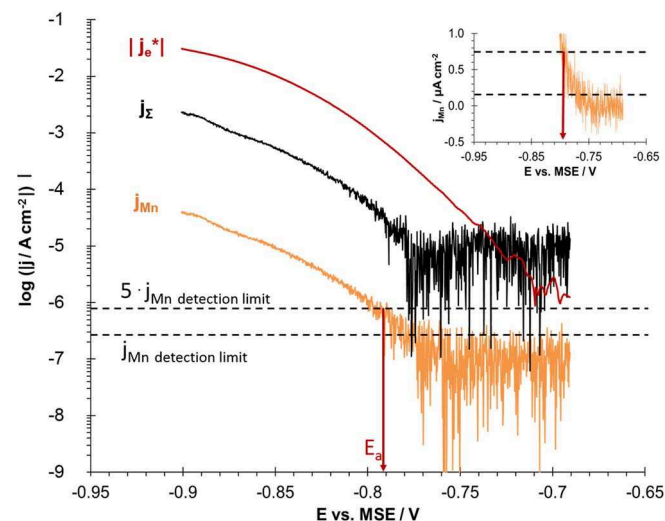


**Figure 2.** Log ( $|j_e^*|$ ) (red), log ( $|j_\Sigma|$ ) (black), and log ( $|j_{Mn}|$ ) (orange) as a function of potential during linear sweep voltammetry of Si-rich SS in 4 mol dm<sup>-3</sup> HNO<sub>3</sub>, 28°C, cathodic direction, scan rate:  $V = 0.2$  mV s<sup>-1</sup>. Dashed lines represent the  $j_{Mn}$  detection limit (lower line) and five times its value (upper line) given as a criterion for  $E_a$ . The inset on top gives the linear representation of  $j_{Mn}$  as a function of potential and  $j_{Mn}$  detection limit.



on  $|j_e^*|$  in Fig. 2 that are usually assimilated, respectively, to Volmer-Herovskiy and Volmer-Tafel proton reduction mechanisms on metals in acidic environment.<sup>28</sup>

Fig. 1 gives as a function of potential,  $j_e^*$  and the elemental dissolution currents of the alloying elements ( $j_M$ , where  $M = \text{Fe, Cr, Ni, Si, Mn}$ ). Like the cathodic current, the elemental dissolution currents,  $j_M$ , also increase monotonically as the potential decreases below  $-0.7$  V vs. MSE. Expressed as equivalent faradaic currents, their sum  $j_\Sigma$  is also shown by way of comparison to  $j_e^*$  (Fig. 2). Their systematic increase clearly demonstrates the loss of passivity as the potential becomes increasingly cathodic. Note however that at the final point,  $-0.9$  V vs. MSE,  $j_\Sigma$  is only  $2.4 \text{ mA cm}^{-2}$  which is quite negligible as compared to the  $-31 \text{ mA cm}^{-2}$  of  $j_e^*$ . This demonstrates the capacity of the AESEC technique to quantitatively detect very low anodic dissolution rates under circumstances when the electrochemical interface is dominated by the cathodic reaction. The activation transient of the stainless steel is not visible in the conventional polarization curve of  $j_e^*$  vs.  $E$ .

The operative definition of the activation potential  $E_a$  used in this work is shown in Fig. 2. The logarithm of  $|j_\Sigma|$  and  $|j_M|$  are plotted as a function of potential. As Mn is the alloying element with the lowest detection limit and is completely soluble in the  $\text{HNO}_3$  electrolytes used here, it is a logical candidate for the determination of  $E_a$ . The detection limit, expressed in  $\text{A cm}^{-2}$ , is  $1.5 \times 10^{-7} \text{ A cm}^{-2}$  and is shown in Fig. 2 (lower dashed line). Passive dissolution of the sample was not detectable by AESEC, being below the detection limit. Therefore,  $E_a$  is defined as the first potential where  $j_{\text{Mn}}$  rises to five times the detection limit (upper dashed line), in this case  $7.5 \times 10^{-7} \text{ A cm}^{-2}$ . This measurement is actually coherent with any similar measurement on all of the elemental signals and enables determination of  $E_a$  with a precision of  $\pm 10$  mV. Reproducibility of this measurement is also consistent with an uncertainty of 10 mV over 3 experiments in spite of an intense cathodic reaction that may lead to scatter in the dissolution rates.<sup>13</sup>

Anodic dissolution was demonstrated to be congruent by the results of Fig. 3. The dissolution rates of Cr, Ni, Si, and Mn in  $\mu\text{g s}^{-1} \text{ cm}^{-2}$  divided by the mass ratio of the chemical composition of the steel given in Table I, are plotted as a function of the Fe dissolution rate. The good superposition of all the dissolution rates as a function of  $v_{\text{Fe}}$  reveals

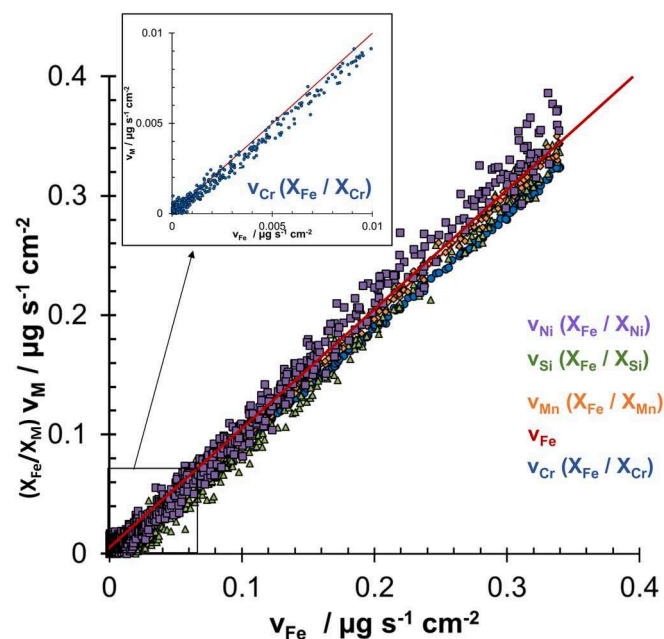


**Figure 3.** Elemental dissolution rates  $v_M$  multiplied by their bulk mass ratios on Fe for Si-rich SS in  $4 \text{ mol dm}^{-3} \text{ HNO}_3$ ,  $28^\circ\text{C}$  as a function of Fe dissolution rate,  $v_{\text{Fe}}$  over linear sweep voltammetry (cathodic direction, scan rate  $V = 0.2 \text{ mV s}^{-1}$ ).

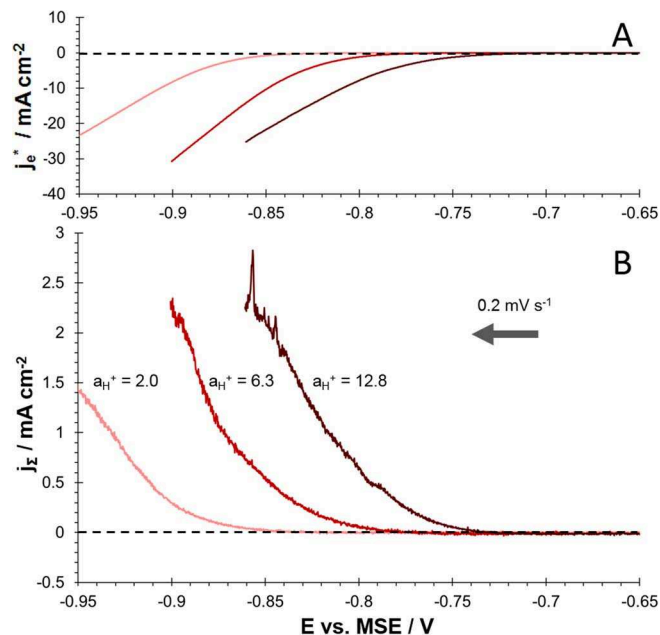


**Figure 4.**  $j_e^*$  (A) and corresponding  $j_\Sigma$  (B) over linear sweep voltammetry (cathodic direction, scan rate:  $V = 0.2 \text{ mV s}^{-1}$ ) of Si-rich SS performed in  $2 \text{ mol dm}^{-3} \text{ HNO}_3$  ( $a_{\text{H}^+} = 2.0$ );  $4 \text{ mol dm}^{-3} \text{ HNO}_3$  ( $a_{\text{H}^+} = 6.3$ );  $6 \text{ mol dm}^{-3} \text{ HNO}_3$  ( $a_{\text{H}^+} = 12.8$ ) at  $28^\circ\text{C}$ .

the non-selective nature of the active dissolution. It can be noticed that Mn presents a rigorously non-selective behavior with respect to Fe, which supports the choice of Mn as the reference element for  $E_a$  determination. The non-selective behavior for all M supports the conclusion that the active dissolution domain has been reached. One could expect an excess of Cr dissolution if Cr oxide were dissolving at the surface of the sample.<sup>33</sup> A zoom of the low current values (inset to Fig. 3) does not confirm this expectation. However, Cr deviation could be too small to be seen in Fig. 3, and therefore transient dissolution rate analysis should be more appropriate to measure any Cr enrichment. Such experiments were performed by Ogle et al.<sup>25</sup> in sulfuric acid using active-passive cycles.

**Activation potential depending on pH.**—Previous measurements of the activation potential demonstrated a proportional relationship between  $E_a$  and the pH in sulfuric acid for several materials from pure iron to various types of iron-based alloys.<sup>12-16,19,29</sup> AESEC measurements of  $E_a$  for the Si-rich SS in different concentrations of nitric acid enabled assessment of this relationship. Measurements of the activation potential of the Si-rich SS are shown in Fig. 4 for 2, 4 and 6  $\text{mol dm}^{-3} \text{ HNO}_3$ .

Due to their method of measurement, most of studies cited before were not able to measure  $E_a$  for high proton activities. As AESEC is able to work with concentrated electrolytes, measurement of  $E_a$  of the Si-rich SS was possible with the identical precision even for concentrations up to  $6 \text{ mol dm}^{-3}$ .

Each nitric acid concentration is associated with a certain proton activity which was calculated after Fallet's<sup>30</sup> work upon the stoichiometric activity coefficient of the proton in  $28^\circ\text{C}$  binary  $\text{HNO}_3$ - $\text{H}_2\text{O}$  solutions. This calculation takes into account the incomplete dissociation of the nitric acid. The resulting activities are given in Table IV.

**Table IV.** Activity of proton for  $\text{HNO}_3 = 2 \text{ mol dm}^{-3}$ ;  $4 \text{ mol dm}^{-3}$ ;  $6 \text{ mol dm}^{-3}$  at  $28^\circ\text{C}$  calculated after Fallet.<sup>30</sup>

$[\text{HNO}_3] / \text{mol dm}^{-3}$	2	4	6
$a_{\text{H}^+}$	2.0	6.3	12.8

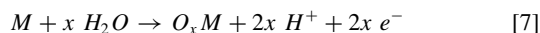
The total cathodic current  $j_e^*$  increased with increasing proton activity. This is not surprising since the proton reduction reaction is expected to dominate below  $-0.65$  V vs. MSE. If the cathodic reaction is enhanced by the activity of the proton, it can also be accelerated by the passivity breakdown of the working electrode. The activation potential increases with the activity of the proton  $a_{H^+}$  as shown in Fig. 4 with a slope of  $0.12 \text{ V} \pm 0.03 \text{ V}$  (Fig. 5). According to Rocha et al.'s measurements<sup>14</sup> on various iron-chromium alloys at room temperature, in the case of linear sweep voltammetry measurement, the activation potential of such alloys in sulfuric acid followed the Equation 5:

$$E_a = E_a^o + \frac{0,058}{n} \log a_{H^+} \quad [6]$$

with the  $n$  value of 0.5 as described in Rocha et al.,<sup>14</sup> which is an experimental value determined for an alloy that contains more than 15 wt% in chromium, the activation potential curve should display a slope of 0.116 ( $n = 0.5$ ). Uhlig and King<sup>11</sup> showed that in the case of pure iron,  $n = 1$ , leading to a Nernstian slope of  $E_a$  vs. pH for Fe dissolution in acidic electrolytes. They suggested that for Fe-Cr alloys, the passivity breakdown mechanism would have an impact on the  $n$ -value. When spontaneously activated in sulfuric acid,  $n = 1$ , but if activation was performed through linear polarization, they found a value of  $n = 0.5$ .

The results presented in Fig. 5 seem to be very similar to what was found in other electrolytes.<sup>11,16,18</sup> Therefore, the  $E_a$  of stainless steel in very concentrated nitric acid is comparable to sulfuric acid in terms of proton activity dependence.

The free enthalpy of formation may be accessed from the y-intercept of Fig. 5. Rocha et al.<sup>14</sup> defined this y-intercept as the standard activation potential  $E_a^o$  and measured  $-0.26$  V vs. SCE which is higher than  $-0.87$  vs. MSE found in the present work (by about 200 mV). Uhlig et al.<sup>12,29</sup> showed that a standard free enthalpy of formation,  $\Delta_r G^o$ , of the oxide can be obtained from the value of  $E_a^o$  and that it helps to assess the alloy's affinity to oxygen in the electrolyte. The calculation is based on the equation of oxide formation as follow:



where  $M$  is the metallic element considered. Such affinity might also depend strongly on the chemical composition and microstructure of the passive layer.

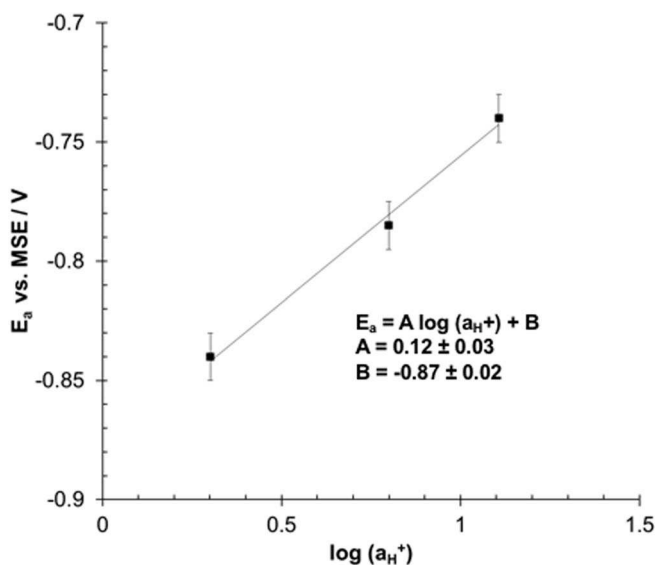


**Figure 5.** Activation potential of Si-rich SS as a function of the logarithm of the proton activity for  $HNO_3 = 2 \text{ mol dm}^{-3}$  ( $a_{H^+} = 2.0$ );  $4 \text{ mol dm}^{-3}$  ( $a_{H^+} = 6.3$ );  $6 \text{ mol dm}^{-3}$  ( $a_{H^+} = 12.8$ ) at  $28^\circ\text{C}$ .

**Table V.** XPS quantification in at. % of three passive layers compositions spontaneously established, concentration for  $HNO_3 = 2 \text{ mol dm}^{-3}$ ;  $4 \text{ mol dm}^{-3}$ ;  $6 \text{ mol dm}^{-3}$  (associated to their respective activity of the proton) and in sulfuric acid, concentration  $H^+ = 4 \text{ mol dm}^{-3}$  at  $28^\circ\text{C}$  and in  $2 \text{ mol dm}^{-3}$   $H_2SO_4$  at  $28^\circ\text{C}$ .

	[Fe Ox]/at. %	[Cr Ox]/at. %	[Si Ox]/at. %
Nitric acid ( $a_{H^+} = 2.0$ )	21	49	30
Nitric acid ( $a_{H^+} = 6.3$ )	19	54	27
Nitric acid ( $a_{H^+} = 12.8$ )	22	44	34
Sulfuric acid	27	44	29
Sulfuric acid $2 \text{ mol dm}^{-3}$			

These considerations lead to the idea that the oxide formation kinetics could be related to a specific oxide layer. Therefore, the value of  $E_a^o$  could be explained by a different passive layer that is preferentially formed in the three different concentrations. XPS quantifications were performed for passive layers formed at Si-rich SS surface in the three nitric acid concentrations at  $28^\circ\text{C}$  and in sulfuric acid  $2 \text{ mol dm}^{-3}$  at  $28^\circ\text{C}$ . The results ascertained in Table V present relative concentrations in iron, chromium and silicon oxides regarding levels  $Fe-2p^{3/2}$ ,  $Cr-2p^{3/2}$  and  $Si-2p$ .

The differences between nitric and sulfuric electrolytes are not considered as significant and the results also demonstrate a reproducible passive layer composition in all nitric electrolytes. The oxide film's nature and thickness (relatively evaluated by the ratio of oxide and metallic peaks' areas) do not seem to be sensitive to the concentration or nature of the electrolyte. It is very likely that the solubilities of all species in the oxide layer increase with the proton activity. The concentration of nitrates could also play a role but was not investigated in the present work.

**Activation potential depending on temperature.**—The proportional relationship between  $E_a$  and pH has been assimilated to a Nernst type equation by several authors.<sup>12,20</sup> It can then be expected that  $E_a$  also depends linearly on temperature. AESEC measurements of the  $E_a$  of Si-rich SS were performed in  $4 \text{ mol dm}^{-3}$   $HNO_3$  at different temperatures. Fig. 6 displays the total dissolution rates obtained for

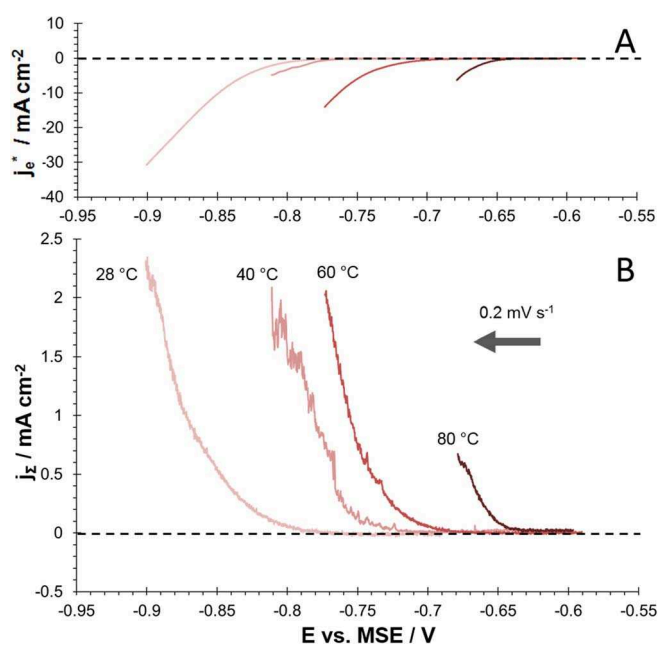


**Figure 6.**  $j_e^*$  (A) and corresponding  $j_\Sigma$  (B) over linear sweep voltammetry (cathodic direction, scan rate  $V = 0.2 \text{ mV s}^{-1}$ ) of the Si-rich SS  $4 \text{ mol dm}^{-3}$   $HNO_3$  at  $T = 28^\circ\text{C}$ ,  $40^\circ\text{C}$ ,  $60^\circ\text{C}$  and  $80^\circ\text{C}$ .

**Table VI.** XPS quantification of two passive layer compositions spontaneously established on Si-rich and 304L stainless steels in 4 mol dm<sup>-3</sup> HNO<sub>3</sub> at 28°C expressed in at. %.

	[Fe Ox]/at. %	[Cr Ox]/at. %	[Si Ox]/at. %
Si-rich SS	19	54	27
304L SS	40	60	0

the temperatures of 28°C, 40°C, 60°C and 80°C (respectively 301 K, 313 K, 333 K and 353 K).

$E_a$  is between  $-0.75$  and  $-0.60$  V vs. MSE in these conditions. The higher the temperature, the higher the dissolution rate measured at a given potential, resulting in a shift of  $E_a$  to higher potential. With increasing temperature,  $j_e^*$  also increases. This may be considered as a consequence of temperature elevation under the hypothesis of hydrogen reduction whose reaction rate follows the Butler-Volmer equation.

When the  $E_a$  values extracted from Fig. 6 are plotted as a function of temperature, a proportionality factor of  $0.0027 \text{ V/K} \pm 0.0004$  is observed (Fig. 7). For a better legibility of the calculation, temperatures have been converted from degrees Celsius to Kelvin. Under the hypothesis of a Nernst type evolution of  $E_a$  vs.  $T$ , the slope of the curve of Fig. 7 will depend on several parameters such as the activities of the elements in the alloy and the number of electrons exchanged. These parameters cannot be determined easily. Nevertheless, the linear dependence between  $E_a$  and temperature is demonstrated through the present work.

**Activation potential depending on the silicon content in the alloy.**—The silicon enrichment of 18Cr-10Ni type SS has been shown to provide a homogeneous corrosion morphology in very oxidizing electrolytes.<sup>10,31</sup> In the present work, XPS measurements of the Si-rich SS confirmed a significant presence of silicon in the passive layer which is also higher than in its bulk composition (Table VI). As compared to the 304L stainless steel, which is a 18Cr-10Ni type SS with 0.34 wt% of silicon in its composition (Table I), Si-rich SS presents a chemically different oxide layer. The chromium rich 304L SS's passive layer, Cr<sub>2</sub>O<sub>3</sub>, was quantified by XPS measurements displayed in Table VI.

The oxide peak energies measured for silicon suggest that the alloy is oxidized into some mixed iron-chromium silicates whose chemistry is not easy to determine. Similar conclusions can be found in Robin et al.<sup>32</sup> The activation potentials of such different passive layers may

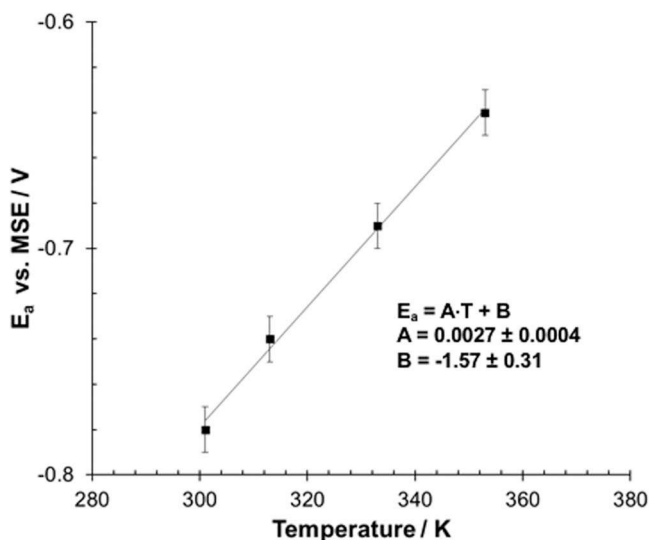


**Figure 7.** Activation potential of the Si-rich SS as a function of the temperature in 4 mol dm<sup>-3</sup> HNO<sub>3</sub> at  $T = 28^\circ\text{C}$ ,  $40^\circ\text{C}$ ,  $60^\circ\text{C}$  and  $80^\circ\text{C}$ .

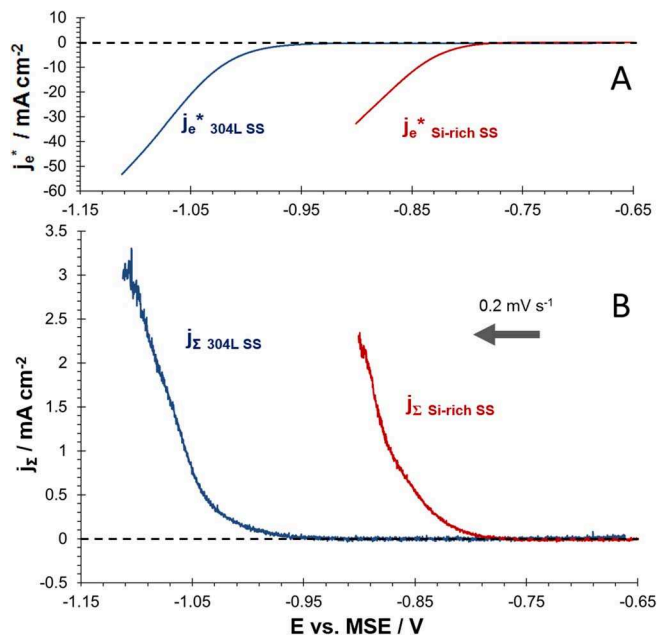


**Figure 8.**  $j_e^*$  (A) and corresponding  $j_c$  (B) over linear sweep voltammetry (cathodic direction, scan rate  $V = 0.2 \text{ mV s}^{-1}$ ) of Si-rich SS (red) and 304L SS (blue) in 4 mol dm<sup>-3</sup> HNO<sub>3</sub> at  $T = 28^\circ\text{C}$ .

provide information about their respective properties in nitric acid, for example their affinity to oxygen.

The activation potentials of the 304L SS were measured by AESEC and compared in the same conditions as the Si-rich SS.

Fig. 8 shows the total dissolution currents measured for the 304L SS during the activation of the sample as compared to the Si-rich SS's in a 4 mol dm<sup>-3</sup> HNO<sub>3</sub> at 28°C. The reduction reaction increases shortly after the break of passivity occurs, as observed in Fig. 6. Considering that the interface reactivity is deeply modified by the break of passivity, one can expect an increase of the reduction kinetics regardless of the reduced species.

A gap of about 200 mV appears between  $E_a$  of the 304L ( $-0.95$  V vs. MSE) and Si rich stainless steel ( $-0.78$  V vs. MSE). The equilibrium potential of the couple Cr(III)/Cr(II) is  $-0.41$  V vs. NHE<sup>35,36</sup> corresponding to  $-1.06$  V vs. MSE and is consistent with  $E_a$  of 304L SS. However, if the active dissolution was only the consequence of Cr(III) reduction, such a large difference in  $E_a$  between these two very similar alloys would not be expected. Given the XPS results, it is very likely that Si lowers the free enthalpy of formation of the oxides,  $\Delta_f G^\circ$ . Such a result is not trivial, since Vetter<sup>34</sup> listed some standard potentials of oxide electrodes calculated from  $\Delta_f G^\circ$  and the Si oxide electrode ( $-1.51$  V vs. MSE) has a lower potential than Cr ( $-1.25$  V vs. MSE).

## Conclusions

The AESEC technique was used to measure the activation potential,  $E_a$ , corresponding to the passive to active transition of stainless steel under conditions of net cathodic reaction rate by analyzing the anodic dissolution rate directly and independently from the cathodic reaction. The value of  $E_a$  in a given environment gives information on the alloy's affinity to oxygen and thus the stability of the oxides formed. The relationship between  $E_a$  and temperature was demonstrated from 28°C to 80°C and hydrogen ion activity from 2 to 12.8.

It was confirmed by XPS measurements that the initial passive layer is similar for all conditions in terms of thickness, structure and chemistry, enhancing the hypothesis of both an increase of the oxide solubility with the proton activity and an impact of the nitrates on the oxygen interaction with the alloy.

A linear dependence between the activation potential and pH was found, similar to what has been found in the literature in other electrolytes. The slope of this linear dependence was found to be very similar to that in sulfuric acid, although the standard activation potential was shifted to lower values. This shift might be explained by several parameters including the nature of the electrolyte (impact of  $\text{NO}_3^-$ ).

A linear dependence was found between the activation potential and the temperature (28°C to 80°C). The general tendency of this evolution would be in good agreement with a Nernst-type equation. However, determination of all parameters would require further investigations of activities of the alloyed elements.

It was shown that silicon in the stainless steel increases the value of the activation potential. The passive layer displays a higher activation potential as it contains less chromium and more silicon. It is proposed that Si lowers the affinity of the alloy to oxygen.

### References

1. P. Fauvet, in *Nuclear corrosion science and engineering*, p. 679, Woodhead Publishing, Cambridge (2012).
2. A. Desestret, in *Materiaux et Techniques*, S. I. R. P. E. (1977).
3. E. Tcharkhtchi-Gillard, M. Benoit, P. Clavier, B. Gwinner, F. Miserque, and V. Vivier, *Corrosion Science*, **107**, 182 (2016).
4. M. Ozawa, O. Yamamura, and K. Gonda, *Journal of Nuclear Science and Technology*, **22**, 68 (2012).
5. B. Raj and U. K. Mudali, *Progress in Nuclear Energy*, **48**, 283 (2006).
6. F. Balbaud, *European Journal of Inorganic Chemistry*, 665 (2000).
7. D. Siesic, F. Balbaud-Celier, and B. Tribollet, *European Journal of Inorganic Chemistry*, 6174 (2014).
8. K. J. Vetter, *Zeitschrift für Elektrochemie, Berichte der Bunsengesellschaft für physikalische Chemie*, **63**, 1189 (1959).
9. G. Schmid and G. Krichel, *Berichte der Bunsengesellschaft für physikalische Chemie*, **68**, 677 (1964).
10. P. Fauvet, F. Balbaud, R. Robin, Q. T. Tran, A. Mugnier, and D. Espinoux, *Journal of Nuclear Materials*, **375**, 52 (2008).
11. H. H. Uhlig and P. F. King, *Journal of The Electrochemical Society*, **106**, 1 (1959).
12. P. F. King and H. H. Uhlig, *The Journal of Physical Chemistry*, **63**, 2026 (1959).
13. A. R. Moshaweh and R. Burstein, *Corrosion Science*, **113**, 126 (2016).
14. H.-J. Rocha and G. Lennartz, *Archiv für den Eisenhüttenwesen*, 117 (1955).
15. P. Lorbeer and W. J. Lorenz, *Corrosion Science*, **21**, 79 (1981).
16. H. G. Feller and H. H. Uhlig, *Journal of The Electrochemical Society*, **107**, 864 (1960).
17. W. S. Hwang, J. J. Lee, W. S. Yang, and S. C. Na, *Materials Science Forum*, **544-545**, 423 (2007).
18. R. P. Frankenthal, *Journal of The Electrochemical Society*, **114**, 542 (1967).
19. F. Flade, *Zeitschrift für Physikalische Chemie*, **6**, 513 (1911).
20. U. F. Franck, *Zeitschrift für Naturforschung*, **4a**, 378 (1949).
21. G. Plante, Contributions à l'étude de la passivité d'aciers inoxydables en milieu nitrique bouillant., in *Thesis*, Université de Paris (1969).
22. K. Ogle and S. Weber, *Journal of The Electrochemical Society*, **147**, 1770 (2000).
23. D. G. Kolman, D. K. Ford, D. P. Butt, and T. O. Nelson, *Corrosion Science*, **39**, 2067 (1997).
24. K. Ogle, J. Baeyens, J. Swiatowska, and P. Volovitch, *Electrochimica Acta*, **54**, 5163 (2009).
25. K. Ogle, M. Mokaddem, and P. Volovitch, *Electrochimica Acta*, **55**, 913 (2010).
26. K. Ogle, A. Tomandl, and N. Meddahi, in *Innovative Pre-Treatment Techniques to Prevent Corrosion of Metallic Surfaces*, p. 158, Woodhead Publishing, Washington (2007).
27. V. Shkirskiy, P. Keil, H. Hintze-Bruening, F. Leroux, P. Volovitch, and K. Ogle, *Electrochimica Acta*, **184**, 203 (2015).
28. T. Shinagawa, A. T. Garcia-Esparza, and K. Takanabe, *Scientific Reports*, **5**, 13801 (2015).
29. H. H. Uhlig, *Zeitschrift für Elektrochemie, Berichte der Bunsengesellschaft für physikalische Chemie*, **62**, 626 (1958).
30. A. Fallet, Influence des ions oxydants issus de la dissolution du combustible nucléaire usé sur le comportement des matériaux de structures, in *Thesis*, Université de Montpellier (2016).
31. J. Stolarz, J. Le Coze, and A. Desestret, *Colloque de Physique*, 51 (1990).
32. R. Robin, F. Miserque, and V. Spagnol, *Journal of Nuclear Materials*, **375**, 65 (2008).
33. I. Olefjord and B.-O. Elfstrom, *Corrosion*, **39**, 46 (1982).
34. K. J. Vetter, in *Electrochemical Kinetics*, p. 753, Academic Press, New York (1967).
35. M. Pourbaix, *Atlas of electrochemical equilibria in aqueous solutions*, Pergamon Press, New York (1966).
36. B. Beverskog and I. Puigdomenech, *Corrosion Science*, **39**(1), 43 (1997).



### **4.3. Dissolution and passivation of a silicon-rich austenitic stainless steel during active-passive cycles in sulfuric and nitric acid**

#### **4.3.1. Kinetics parameters determination and stoichiometry identification**

At this point, chemical composition and organization of the oxide layer of the Uranus S1N SS is still unclear. If the chapter II enabled to collect some thermodynamic information about this oxide, this third chapter aims at providing some kinetic properties of the formation and dissolution of the passive layer, and elucidate its chemical composition.

##### **4.3.1.1. Passivation kinetics in acidic media**

In the case of the Uranus S1N, the state of the art concerning the formation or dissolution of the oxide layer in acidic media is nearly inexistent. In a more general way, the passive interface of alloys can be considered as the result of a selective dissolution of the alloying elements. If Fe is taken as the reference element for example, Ni will be expected to dissolve faster, and Cr and Si will on the contrary accumulate at the surface. thus, when the steady state is reached, the alloy is covered by a Cr-Si rich layer [67]. Among the different studies about the selective dissolution of Cr versus Fe [68-70], Ogle *et al.* [63] first attempted to visualize it *in situ* using the AESEC and the 304L SS. In their work, the active and passive domains of the steel were exploited to form and dissolve successively the oxide layer. This experiment aimed at analyzing the signals obtained and their relative congruence to identify the enrichment in Cr over the transients.

They used  $\text{H}_2\text{SO}_4$ , at  $2 \text{ mol dm}^{-3}$  at room temperature because this acid, as said in 4.2., enables the active dissolution to occur, and therefore the stainless steel can be stabilized reversely in its active and passive domains. A few seconds polarization enables to activate then passivate the sample as shown in Fig. 14. Similar experiments are presented in this third



chapter, because they can not only provide information about the selective dissolution but also about the kinetics of formation and dissolution of the passive layer. Given the kinetic character of this study, it is possible to remove the descending background of the signal,  $\psi$  from the dissolution signals during the passivation of the sample (Eq. 12). This function is associated to the evacuation of the elements in the plasma over time. Details of the calculation were given in previous work [63-65] :

$$\psi(t) = Y/2[1 - \text{erf}\{\beta^{1/2} \ln\left(\frac{t}{t_c}\right) - 1/2\beta^{-1/2} \quad (12)$$

With  $Y$  = mean value of the signal before passivation,  $\beta = 0,99 \pm 0,02$  s et  $t_c = 14 \pm 0,5$  s [64].

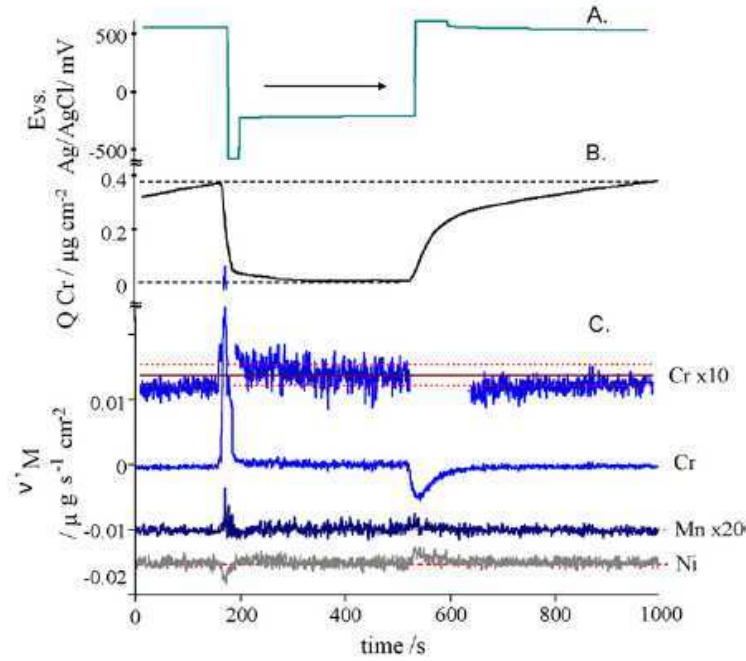


*Fig. 14. Active passive cycles experiment (Ogle et al. [63]) on 304L SS*

*in  $2 \text{ mol dm}^{-3} \text{H}_2\text{SO}_4$  at room temperature*

*(A) Active passive cycle potential vs. time*

*(B) Cr enrichment vs. time*

*(C) Cr, Mn and Ni excesses vs. time*

In this third step of the thesis, the enrichment in Cr and Si at the surface during the passivation of the Uranus S1N in H<sub>2</sub>SO<sub>4</sub> was calculated. The impact of these enrichments on the decrease of the dissolution during passivation was then evaluated. In a second time, similar experiment in HNO<sub>3</sub> was also attempted. Because of the highly oxidizing nature of the acid, it required few adjustments to perform the experiment. The polarization in the active domain had to be maintained instead of observing a stable active dissolution. The passivation could be done at polarized potential or at open circuit potential. Several experiments were conducted but proved to bring to very similar results. As in previous work, the XPS analyses enabled to establish some parallels between H<sub>2</sub>SO<sub>4</sub> and HNO<sub>3</sub>.

The calculations associated to the following results are :

$$v_M^o = (X_{Fe}/X_M) v_M \quad (13)$$

$$v'_M = \frac{X_M}{X_{Fe}} v_{Fe} - v_M \quad (14)$$

$$Q_M(t) = \int_0^t v'_M(t) dt \quad (15)$$

With X<sub>M</sub> mass fraction of M in the bulk composition of the steel,  $v'_M$  the excess dissolution of M versus Fe,  $Q_M$  relative enrichment in M at the surface.

#### 4.3.1.2. Stoichiometry of the oxide

As mentionned several times before, XPS have proven that the Si in the oxide layer of the Uranus S1N SS [14] was very likely to be involved in mixed silicate. They are few studies about natural Fe-Cr silicates studied with XPS [59] that could confirm the binding energies shifts observed. Fe silicates were observed in the case of Fe-Si alloys [60-62] because Fe core level energy displayed a slight shift, *a priori* not detected for the Uranus S1N by Robin *et al.* [6]. To provide new information about the stoichiometry and composition of the passive



layer, this third chapter used the AESEC Cr and Si enrichments quantifications and compared them to ex situ analyses such as XPS and EDX.

#### **4.3.2. Main results**

Fig. 20 shows a typical active-passive cycle performed on the Uranus S1N SS in 2 mol dm<sup>-3</sup> H<sub>2</sub>SO<sub>4</sub> at ambient temperature. The four periods of the cycle were numbered on the potential plot: periods (1), (3) and (1') correspond to open circuit measurements, whereas during periods (2) and (4), potentiostatic pulses of 10 secondes were applied for the activation and passivation triggering.  $v_{Cr}^{\circ}$  corresponds to the normalized signal of Cr, dissolution rate of Cr divided by its ratio on Fe in the bulk composition of the alloy (Table 1).  $v_{Fe}$  can be then compared to  $v_{Cr}^{\circ}$ , and a clear excess of Cr during activation is detected, corresponding to the dissolution of the rich Cr layer. On the contrary, during the passivation, a enrichment of Cr is detected. Similar results were obtained for Si (Fig. 21) which was very satisfying.

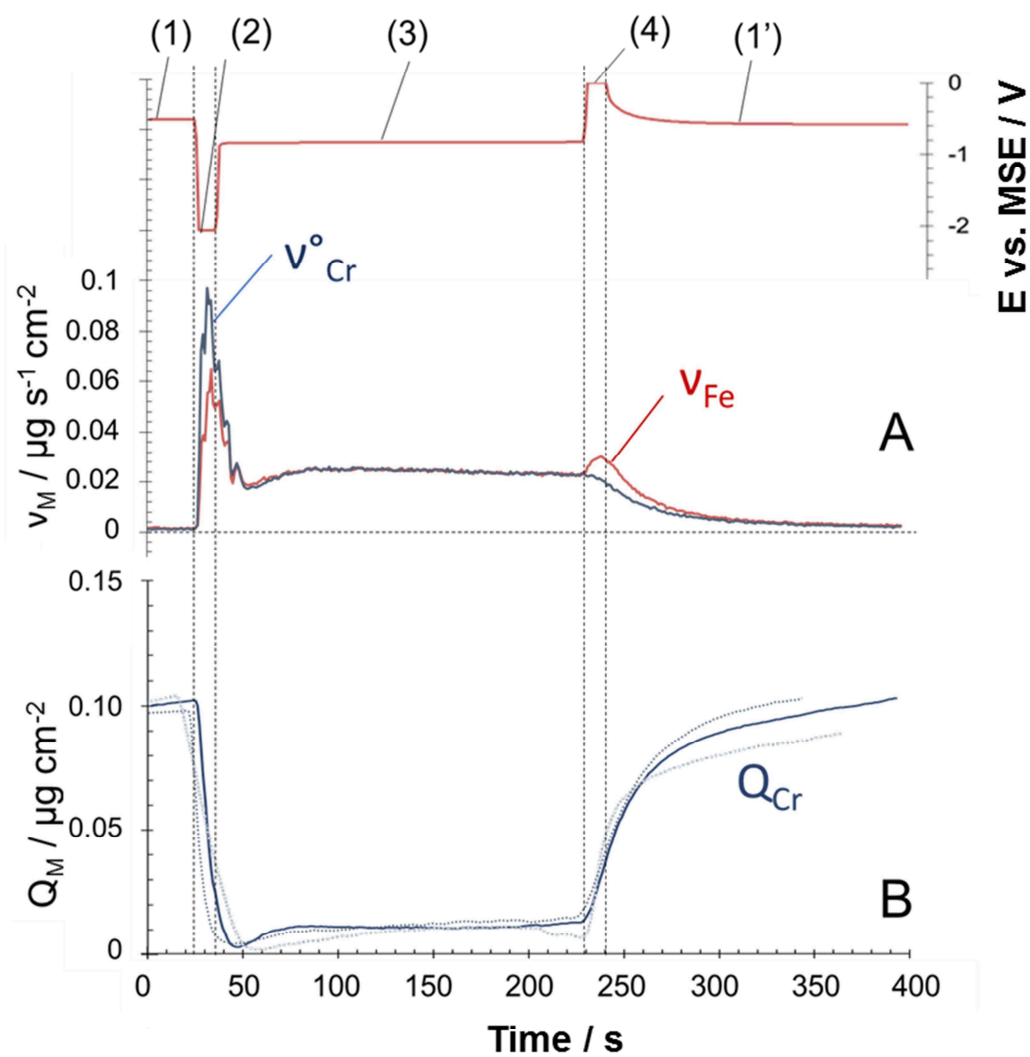


Fig. 20. Active passive cycle on the Uranus SIN SS in  $2 \text{ mol dm}^{-3} \text{ H}_2\text{SO}_4$  at room temperature

(A)  $v_{\text{Fe}}$  and  $v_{\text{Cr}}^{\circ}$

(B)  $Q_{\text{Cr}}$  (three consecutive cycles superimposed)

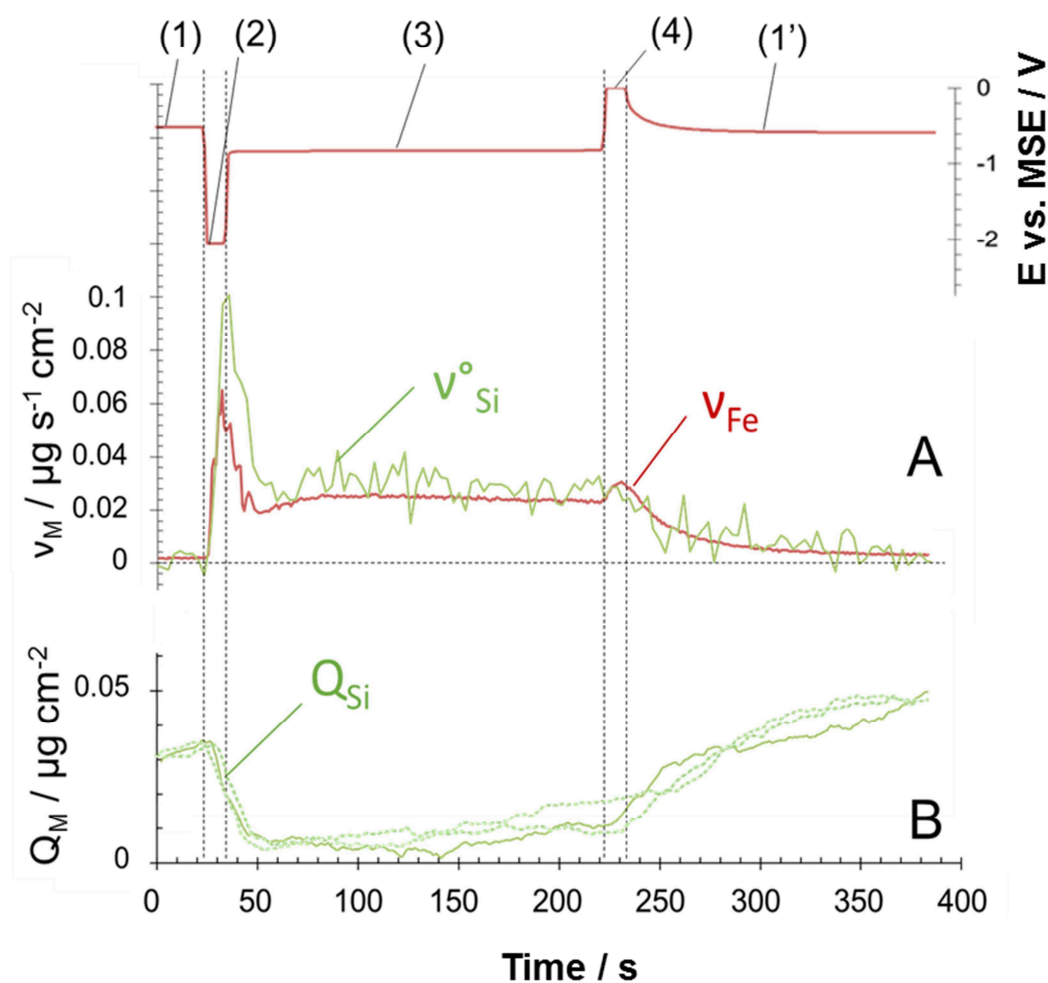


Fig. 21. Active-passive cycle on the Uranus SIN SS in  $2 \text{ mol dm}^{-3} \text{ H}_2\text{SO}_4$  at room temperature

(A)  $v_{\text{Fe}}$  and  $v^{\circ}_{\text{Si}}$

(B)  $Q_{\text{Si}}$  (three consecutive cycles superimposed)

#### 4.3.2.1. Kinetics of passivation in $\text{H}_2\text{SO}_4$ versus $\text{HNO}_3$

Figs. 20 et 21 provide precious information about the kinetics of passivation of the Uranus SIN. In these conditions, it seems that the first efficient passivation seems to last only few hundreds of seconds. It is possible to characterize this efficiency by plotting the total

dissolution rate  $v_{\Sigma}$  during passivation as a function of  $Q_{Cr}$ . Fig. 22 displays the comparison obtained between the Uranus S1N and the 304L SS (Fig. 22).

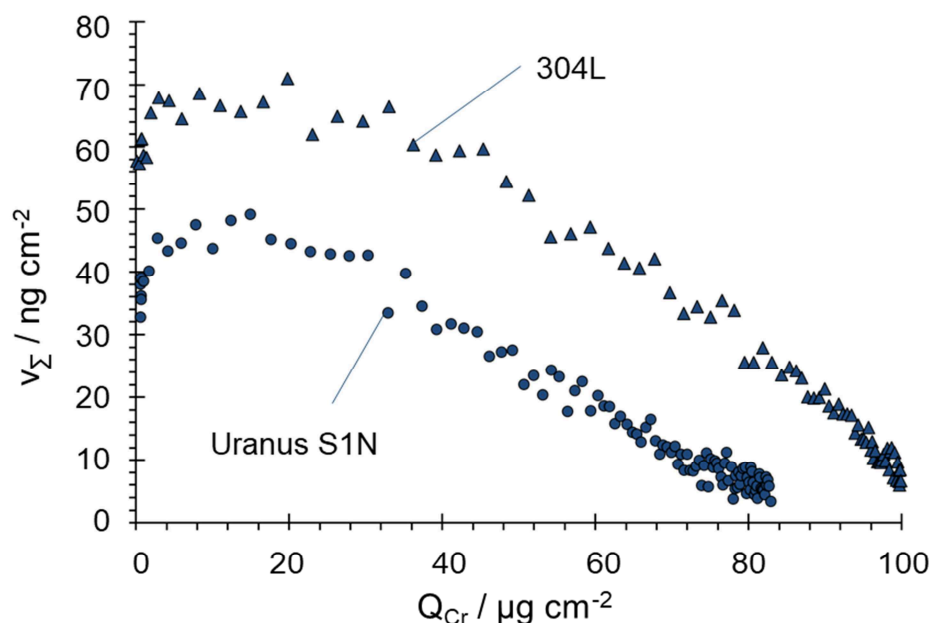
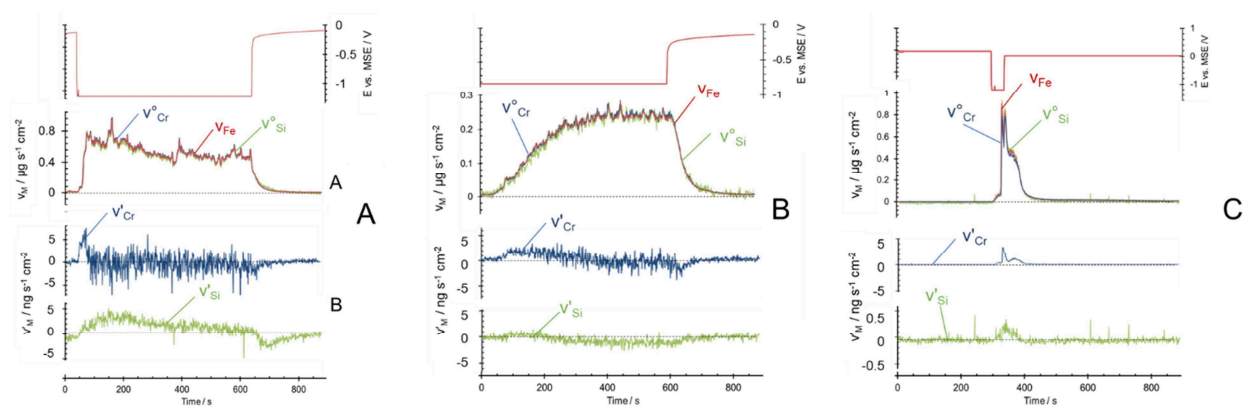


Fig. 22.  $v_{\Sigma}$  as a function of  $Q_{Cr}$  during the passivation period for the two stainless teels in  $2 \text{ mol dm}^{-3} \text{ H}_2\text{SO}_4$  at room temperature

The observation of these curves in their descending part (passivation of the alloy) show that both SS present a passivation transient that is very similar and not affected by the presence of Si, except for that the maximum value of  $Q_{Cr}$  is naturally lower for the Uranus S1N as the surface also enriches in Si. In a first approximation, Cr seems to be the main responsible for the diminishing dissolution rate of the alloy during the passivation.

Then, the experiment was attempted to be performed in  $\text{HNO}_3$ . The SS is maintained potentiostatically in its active domain and the following passivation can be obtained either by a releasing of the potential of by the polarization at a given value of potential ( $E = 0.0 \text{ V vs. MSE}$ ). Fig. 23 shows the results obtained for the three different experiments tried and the excess Cr and Si measured over the transients.



*Fig. 23. Active passive cycles obtained for the Uranus S1N SS in 4 mol dm<sup>-3</sup> HNO<sub>3</sub> at room temperature*

*(A) Potentiostatic activation 600 s ( $E = -1.2$  V vs. MSE) then spontaneous passivation*

*(B) Potentiostatic activation 600 s ( $E = -0.8$  V vs. MSE) then spontaneous passivation*

*(C) Potentiostatic activation 30 s ( $E = -1.2$  V vs. MSE) then potentiostatic passivation 600s ( $E = 0.0$  V vs. MSE)*

For the three possible experiments, successive active and passive states are observed. But no clear selective dissolution is detected. Even a slight opposite selectivity is measured but at a very low amount, and the origin of this phenomenon was not determined.

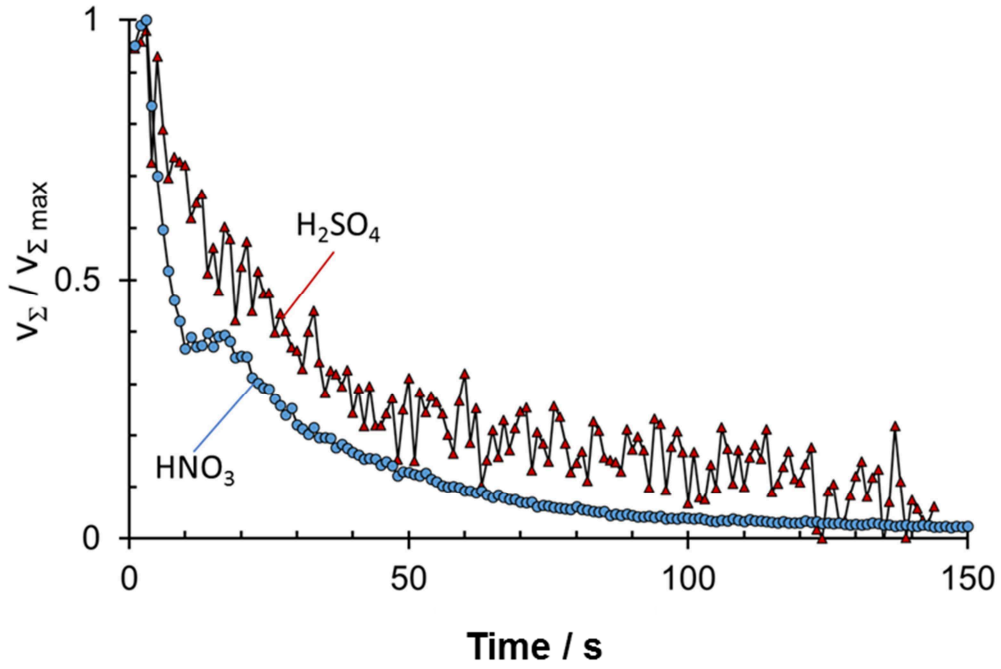


Fig. 24. Comparison of the evolution of the dissolution rate of the Uranus S1N SS in 2 mol  $\text{dm}^{-3}$   $\text{H}_2\text{SO}_4$  and 4 mol  $\text{dm}^{-3}$   $\text{HNO}_3$  4mol  $\text{dm}^{-3}$  at room temperature

Fig. 24 shows that the passivation kinetics of the Uranus S1N SS seems identical between the two electrolytes even if the dissolution is more intense during the active dissolution. It is still unclear why the selective dissolution was not detectable. A paragraph in the unachieved experiment will later explain why it cannot be a lack of sensitivity in the AESEC device.

#### 4.3.2.2. Oxides formed at the surface, chemistry and thickness

From Figs. 20 et 21 can be estimated that the surface of the Uranus S1N during the passivation in  $\text{H}_2\text{SO}_4$  is enriched in  $80 \pm 10$  ng in Cr and  $30 \pm 10$  ng in Si (for a surface of 1  $\text{cm}^2$ ). After converting these amounts in moles, the molar ratio  $\frac{n_{\text{Cr}}}{n_{\text{Si}}}$  values  $1.4 \pm 0.2$ . Then several XPS measurements were made in different conditions of passivation and compared to this result.

Table 3 ascertains the different relative quantifications of the chemistry of the passive layers obtained for both SS. It is shown that in H<sub>2</sub>SO<sub>4</sub>, the ratio  $\frac{n_{Cr}}{n_{Si}}$  values  $1.5 \pm 0.2$ , it is very coherent with the AESEC measurements.

*Table 3. XPS relative quantification of the chemistry of the passive layer established on Uranus S1N and 304L SS, averaged over several samples (8 to 10) during variable amounts of time (10 mins and 24 hrs) at the OCP, at 28°C and 100°C in two different electrolytes*

		[ Fe Ox ] / at. %	[ Cr Ox ] / at. %	[ Si Ox ] / at. %
H <sub>2</sub> SO <sub>4</sub> (2 mol dm <sup>-3</sup> )	Uranus S1N	24 ± 4	45 ± 3	31 ± 3
	304L	45 ± 5	55 ± 5	-
HNO <sub>3</sub> (4 mol dm <sup>-3</sup> )	Uranus S1N	26 ± 4	46 ± 4	28 ± 3
	304L	41 ± 4	59 ± 5	-

Moreover, when the Cr-2p<sub>3/2</sub> obtained are compared between both SS, it is systematically shown that the core level of the oxide Cr contribution is shifted to lower values in the case of the Uranus S1N (Fig. 25). Binding energy associated to the Si-2p is also decreased. This phenomenon had already been reported in the literature for the Si-2p [6]. This can be associated to the presence of Cr silicates. Indeed, similar results were found in the literature concerning Fe and Zn silicates [72, 75].

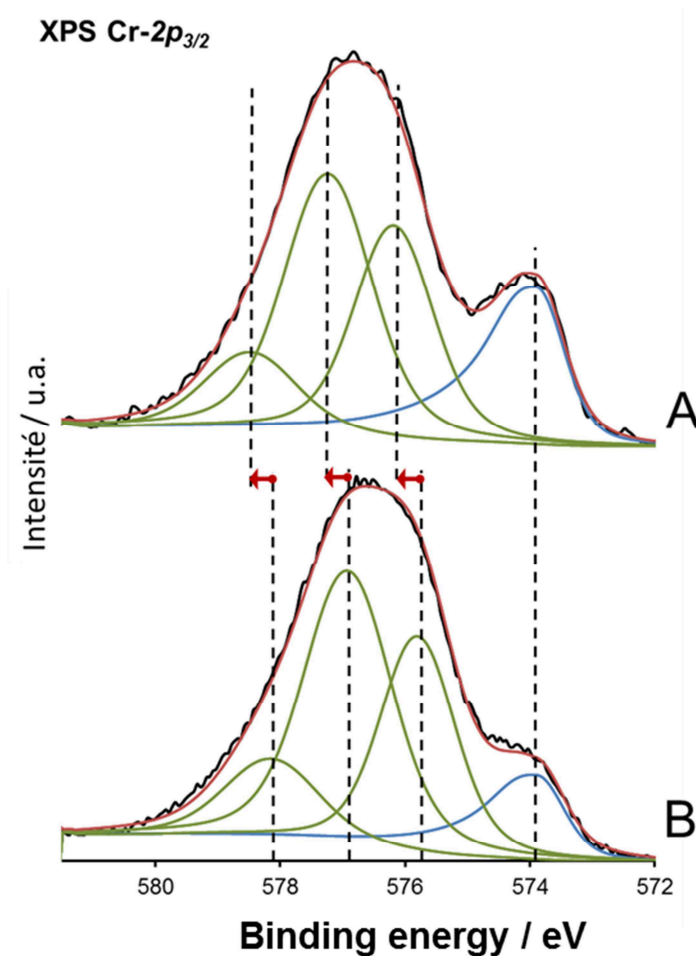


Fig. 25. Intensity as a function of binding energy obtained by XPS for the Cr-2p<sub>3/2</sub> corresponding energies, fitted with Advantage<sup>TM</sup>

(A) Uranus S1N

(B) 304L

These measurements were independent from the nature of the electrolyte and the other conditions used in terms of duration and temperature.

It was then tried to spot possible heterogeneities in the passive layer because so far, both AESEC and XPS results are averaged over the whole thickness of the passive layer.

Therefore, FIB thin blades were analyzed with a TEM and EDX profiles were performed on the Uranus S1N after a passivation of 24 hrs in HNO<sub>3</sub> 4 mol dm<sup>-3</sup> at (Fig. 26). It is then shown



in Fig. 26 an imperfect congruence between Cr and Si over the first nanometers depth. More precisely, it reveals at the extreme surface of the sample a domain where Si overails clearly on Cr.

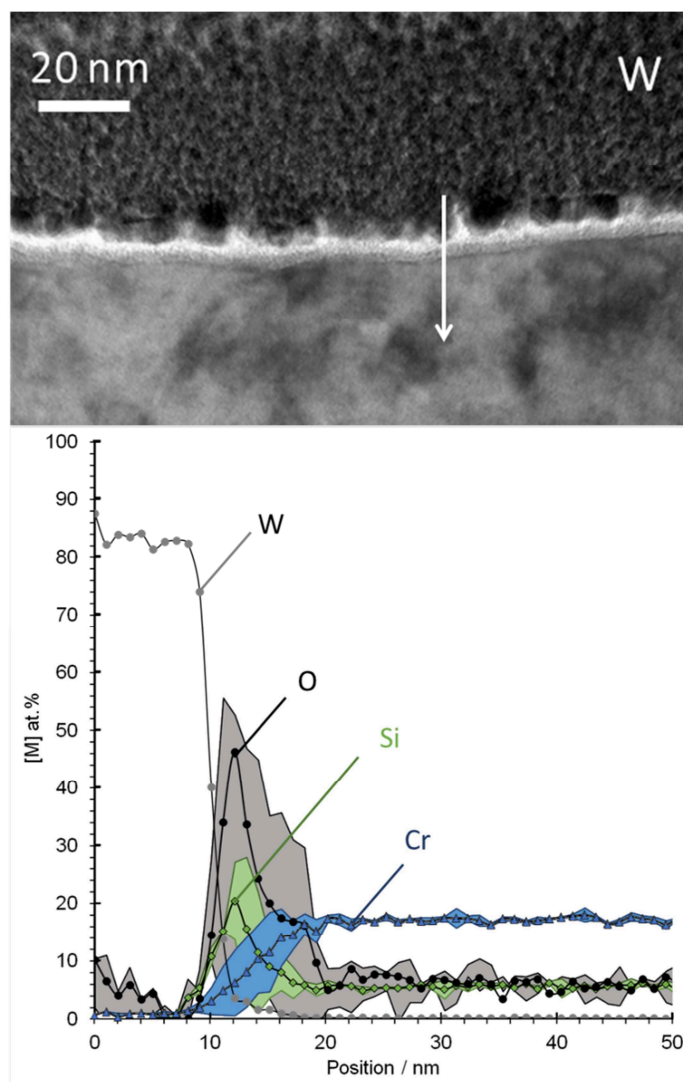


*Fig. 26. TEM-EDX analysis of the passive layer established on Uranus S1N in  $4 \text{ mol dm}^{-3}$   $\text{HNO}_3$  at  $100^\circ\text{C}$  for 24 hrs. Colored zones give an estimation of the standard deviation over more than 10 measurements on 2 different samples*

Regarding the fact that AESEC and XPS (in all sort of conditions) clearly show that the overall Cr amount is greater than Si, these results prove that the oxide layer of the Uranus S1N is organized into at least two layers of a different  $\frac{n_{\text{Cr}}}{n_{\text{Si}}}$  ratio. The two ratios can be statistically

determined based on the EDX profiles. On the outermost part of the layer, a ratio of  $\frac{n_{Cr}}{n_{Si}} = 0.7 \pm 0.1$  is found, and the inner part of the layer displays a ratio of  $\frac{n_{Cr}}{n_{Si}} = 2.1 \pm 0.3$ . It has to be satisfyingly noticed that the mean of these two ratios corresponds exactly to the result found by AESEC and XPS.

As these measurements are very consistent with each other, they also show that the nature of the electrolyte, duration and temperature of passivation has no influence on the overall result. However, few differences exist in the measurement of the thickness of the layer. First, it is shown that XPS measured the same relative quantifications either for 10 mins passivation and 24 hrs with the same ratios between the metal and the oxide contributions for each element. This would suggest that after 10 mins passivation the maximum thickness of the passive layer is reached. On the other hand, the thickness of the film dissolved in the AESEC device can also be estimated by dividing the 100 ng Cr dissolved by an average density of  $5.21 \text{ g dm}^{-3}$  (which corresponds, in first approximation, to the density of the  $\text{Cr}_2\text{O}_3$ ). From this calculation is estimated a thickness of 0.2 nm. This surprising result is however in the order of magnitude of what was found by Ogle *et al.* [63] on the 304L. Eventually, the TEM analyses revealed (Fig. 26) a 3 nm thick passive layer, more coherent with other results of the literature (between 1 and 3 nm) [76, 77]. This difference could be very interesting to investigate using longer times of passivation with the AESEC device. At  $t = 400 \text{ s}$  in Fig. 20, one can wonder if the  $Q_{Cr}$  was still increasing.

#### 4.3.3. Conclusion

Thanks to the AESEC, transients between active and passive states enabled to characterize the kinetics of formation and dissolution of the passive layer, and revealed the Si enrichment in it. Nevertheless, Cr was shown to be better responsible for the decrease of the dissolution rate during the passivation as the kinetics seem to be very comparable between the two steels.

The quantification of the elements in the passive layer appeared very similar to what was found by XPS. EDX results added more precise information, revealing an extreme surface where Si prevails. Statistical ratios of (Cr : 2 ; Si : 3) and (Cr : 2 ; Si : 1) were thus found for respectively the outer and the inner parts of the oxide. These stoichiometries are coherent with a silicate structure in which Si is quadrivalent and the average ratio of the two parts of the oxide layer was found to be congruent to what was measured by AESEC and XPS.

**4.3.4. Publication - Dissolution and Passivation of a Silicon-Rich Austenitic Stainless Steel during Active-Passive Cycles in Sulfuric and Nitric Acid, Journal of The Electrochemical Society, 164 (13) C892-C900 (2017)**



# Dissolution and Passivation of a Silicon-Rich Austenitic Stainless Steel during Active-Passive Cycles in Sulfuric and Nitric Acid

Barbara Laurent,<sup>a,b,\*</sup> Nathalie Gruet,<sup>a</sup> Benoit Gwinner,<sup>a</sup> Frederic Miserque,<sup>a</sup> Karine Rousseau,<sup>c</sup> and Kevin Ogle<sup>b,\*\*,z</sup>

<sup>a</sup>Commissariat à l'Energie Atomique, Den-Serve de la Corrosion et du Comportement des Matériaux dans leur Environnement, Université Paris-Saclay, F-91191 Gif-sur-Yvette, France

<sup>b</sup>Chimie-ParisTech, PSL Research University, IRCP-CNRS, 75005 Paris, France

<sup>c</sup>Serma Technologies, BHT, Bâtiment 52, 38040 Grenoble, France

The high Si containing X1CrNiSi18-15-4 stainless steel (SS) spontaneously forms a protective oxide film that is mostly composed of mixed chromium and silicon oxides. This film ensures a good durability of the industrial facilities the alloy was designed for, containing very acidic electrolytes such as hot and concentrated nitric acid, HNO<sub>3</sub>, in presence of oxidizing species. In the present work, the chemistry of the oxide formed and the passivation kinetics of the alloy in sulfuric acid, H<sub>2</sub>SO<sub>4</sub>, and for the first time in HNO<sub>3</sub>, were monitored by atomic emission spectroelectrochemistry (AESEC) over successive activation and passivation cycles of the material. X1CrNiSi18-15-4 SS was compared to a low Si containing SS, the X2CrNi18-10 SS. It was found that a similar quantity and rate of passive film was formed during passivation, and dissolved during activation. Reproducible results were obtained over several active-passive cycles. The excess Cr was correlated with the dissolution rate decay during passivation. The Si/Cr ratio of the passive film was determined by X-ray photoelectron spectroscopy, energy dispersive X-ray spectroscopy (performed using transmission electron microscopy), and AESEC giving similar results within experimental error. The EDX profile suggest that the passive film consists of a Si rich outer and Cr rich inner layer.

© The Author(s) 2017. Published by ECS. This is an open access article distributed under the terms of the Creative Commons Attribution 4.0 License (CC BY, <http://creativecommons.org/licenses/by/4.0/>), which permits unrestricted reuse of the work in any medium, provided the original work is properly cited. [DOI: 10.1149/2.1531713jes] All rights reserved.



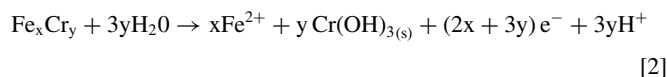
Manuscript submitted August 10, 2017; revised manuscript received October 17, 2017. Published November 7, 2017.

The passivation of iron in nitric acid was first noted by Keir in 1790,<sup>1</sup> followed soon after by Berzelius and Hisinger<sup>2</sup> and Schönbein<sup>3</sup> between 1807 and 1836. In 1837, Faraday, in correspondence with Schönbein,<sup>4</sup> made the first enunciation of the oxide-skin theory which has been extended to many materials ever since. Nowadays, corrosion prediction of stainless steels (SS) in acidic environment arises directly from the characterization of their passive layer, constitutive of the metal-electrolyte interface,<sup>5,6</sup> whose chemistry and morphology determine the electrochemical behavior of the material in a given environment. This oxide layer of SS makes these alloys a very appropriate material choice for acidic environments. Nitric acid, HNO<sub>3</sub>, is used extensively for nuclear retreatment and the nuclear retreatment plants rely on the use of 18Cr-10Ni type SS such as the 304L SS (X2CrNi18-10).<sup>7</sup> It has been demonstrated that a 3.5% Si composition improves the corrosion resistance of stainless steel in hot, concentrated nitric acid in the presence of oxidizing species although the origin of this improved performance has yet to be elucidated.<sup>37</sup>

It is generally acknowledged that the passive film has a bilayer structure with electron exchange occurring across the outer layer with the environment, and cation transfer across the inner layer. The dissolution rate of the material<sup>8,9</sup> in the passive state is limited by cation transfer across the inner layer. The formation of the passive film depends on the electrochemical potential of the material/electrolyte combination. In the active domain, Fe and the alloying elements are expected to dissolve in proportions respecting the bulk material (congruent dissolution), following the oxidation reaction of the metal:<sup>8</sup>



In the passive potential domain however, insoluble oxides of Cr(III) are formed. These oxides remain on the surface as a Cr(III) oxide film while the other elements dissolve via a process of selective dissolution.<sup>10-12</sup> Thus a Cr enriched surface film results according to the following stoichiometry:

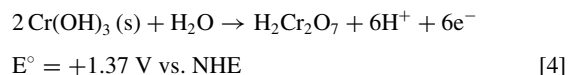


The potential domain where the oxides of Cr are protective is called the passive domain and is the most interesting for industrial applications.<sup>7</sup> However, under certain conditions, this passivity can be broken at very low or at very high potentials, called respectively 'active' and 'transpassive' domains.

The transition from the passive to the active state may be characterized by the reduction of the passive film to yield soluble Cr<sup>2+</sup>.<sup>17</sup>



The transition from the passive to the transpassive state is usually associated with the oxidation of Cr(III) to Cr(VI)<sup>13</sup> and Cr(VI) species are expected to be soluble in HNO<sub>3</sub>.<sup>17</sup>



A 4 mol dm<sup>-3</sup> HNO<sub>3</sub> solution at 100°C displays an equilibrium state potential on a platinum wire of 1.20 V vs. NHE<sup>14</sup> which enables 18Cr-10Ni type SS to be passive. However, due to the industrial processes that can be performed in HNO<sub>3</sub>, oxidizing species may be present that increase the potential of the electrolyte, leading to the possibility of a passivity breakdown following Eq. 4.<sup>7,15,16</sup> A high silicon enrichment (over 1 wt%) of a 18Cr-15Ni SS proved to lower the risk associated with such passivity breakdown in the presence of oxidizing species.<sup>18-24,37</sup> The X1CrNiSi18-15-4 SS (composition given in Table I) was designed for these kinds of electrolytes, where its dissolution rate was shown to be lower than for the X2CrNi18-10 SS. It is however not the case in pure HNO<sub>3</sub>, where the X1CrNiSi18-15-4 SS dissolves more rapidly than the X2CrNi18-10 SS, and this is probably due to the properties of the particular passive layer of the X1CrNiSi18-15-4 SS. This film is composed of a silicon rich oxide, very likely chromium silicate whose stoichiometry and thickness have not been clearly determined,<sup>36</sup> nor observed in situ over the very first seconds of formation. A first attempt of characterization of this oxide layer was made in previous work,<sup>25</sup> through the measurement of the activation potential, which should be directly related to E° of Eq. 3. For the X1CrNiSi18-15-4 SS, the activation potential was higher than E° for Eq. 3, highlighting the thermodynamic differences between a pure chromium oxide and a mixed Si-Cr oxide.

\*Electrochemical Society Student Member.

\*\*Electrochemical Society Member.

<sup>z</sup>E-mail: [kevin.ogle@chimie-paristech.fr](mailto:kevin.ogle@chimie-paristech.fr)

**Table I.** Mass composition of X1CrNiSi18-15-4 and X2CrNi18-10 SS determined by GDOES profiles performed on samples and averaged between 40  $\mu\text{m}$  and 50  $\mu\text{m}$  depth expressed in wt %.

	Fe	Cr	Ni	Si	Mn	Cu	Mo	Add.
X1CrNiSi18-15-4 SS	59.76	18.79	15.08	3.54	1.97	0.18	0.05	0.68
X2CrNi18-10 SS	70.35	17.78	9.51	0.34	1.46	0.16	0.19	0.21

Among the numerous possibilities to investigate the passivation of metals *in situ*, for example via surface analysis,<sup>6,26,27</sup> Ogle et al.<sup>28</sup> proposed an innovative protocol by monitoring the elemental dissolution of SS during the cyclic formation and dissolution of passive films in sulfuric acid,  $\text{H}_2\text{SO}_4$ , for low-Si containing SS, (X2CrNi18-10 SS). This method relied on the atomic emission spectroelectrochemistry (AESEC) technique where an electrochemical flow cell is coupled to an inductively coupled plasma atomic emission spectrometer (ICP-AES). When dissolving, metal ions of the sample are transported downstream to the ICP-AES where they can be analyzed in real time giving the rate of elemental dissolution directly, and giving precious information on the kinetics of passivation indirectly via mass balance. Ogle et al.<sup>28</sup> proved that it was possible in  $\text{H}_2\text{SO}_4$  for the X2CrNi18-10 SS, to switch reversibly from active to passive domains using short polarization pulses. Both states were stable over a few hundred seconds. Simultaneously, they recorded and analyzed the dissolution of each major element of the SS as a function of time during the cycles. From a mass balance, the Cr enrichment of the passive layer was quantified during the cycles, representing a growth of the passive film during passivation and a loss of the passive film during activation.

The present work aims at determining if the high concentration of Si in the passive layer of the X1CrNiSi18-15-4 SS impacts the kinetics of passivation of the material and extends this earlier work to nitric acid. It must be noted that performing similar experiments in concentrated  $\text{HNO}_3$  comes with several difficulties.  $\text{HNO}_3$  is both an acid and a strong oxidizing agent, reducing through numerous cathodic processes at high potentials.<sup>14,29</sup> Therefore, in concentrated  $\text{HNO}_3$ , SS will usually undergo spontaneous passivation and it is rarely possible to observe a stable active dissolution of the material without adding chlorides for example.<sup>30</sup> In the potential range of the active domain of SS, the overall current is strongly cathodic. Therefore, the observation of the active dissolution of SS in  $\text{HNO}_3$  must be performed under controlled polarization conditions of the sample (potentiostatic or galvanostatic mode), activation and passivation being the transient periods between open circuit potential and polarized activation.

The experimental strategy of the present work is to investigate the impact of silicon on the oxide layer of stainless steels, by comparing the X1CrNiSi18-15-4 SS and the X2CrNi18-10 SS oxide layers in  $\text{H}_2\text{SO}_4$ , and establish some parallels with  $\text{HNO}_3$  using *in situ* and *ex situ* techniques. The X2CrNi18-10 SS alloy was chosen as a reference material for this work because its composition is similar to the materials used in the nuclear retreatment facilities containing hot and concentrated acids. The impact of Ni concentration in the composition of the steel on the formation and dissolution of the passive layer is usually considered to be insignificant, Ni serving to stabilize the austenitic phase without affecting the corrosion resistance.<sup>31</sup> Based on these results, a structure for the oxide layer of the X1CrNiSi18-15-4 SS is proposed and characterized by its  $n_{\text{Cr}}/n_{\text{Si}}$  molar ratio.

## Experimental

**Materials and electrolytes.**—X1CrNiSi18-15-4 SS and X2CrNi18-10 SS used in the present work were cut into 20 mm  $\times$  20 mm  $\times$  1 mm samples. The elemental analyses of the steels were performed by glow discharge optical emission spectroscopy (GDOES) using a GD-Profilier from Horiba Jobin-Yvon. From the signals given by the GDOES, the bulk of the sample was reached between 40 and 50  $\mu\text{m}$  depth and the composition of the steel was averaged over two craters on different samples. This analysis is given in Table I. X1CrNiSi18-15-4 and X2CrNi18-10 SS are very similar SS in composition, except for silicon and nickel. Prior to analysis, samples were cleaned with ethanol and acetone in an ultrasonic bath, then polished to 0.03  $\mu\text{m}$  diamond finish. Polishing ensured good sealing in the AESEC flow cell and allowed *ex situ* surface analysis of the sample as required.

Deionized water (18.2 M $\Omega$  cm) was prepared with a Millipore system and used for all electrolytes. Sulfuric acid 96% and nitric acid 68% (Sigma Aldrich) were used to prepare the solutions. All glassware was protected with a paraffin film to avoid any hazardous contamination.

**X-ray photoelectron spectroscopy (XPS).**—XPS analyses were carried out with a Thermofisher Escalab 250 XI spectrometer using a monochromatic X-ray Al K $\alpha$  source. The instrument was calibrated in energy with the Ag Fermi level (0 eV) and the 3d<sub>5/2</sub> core level of metallic silver (368.3 eV). The C-1s signal was used to correct a possible charge effect: the CC/CH contribution of C-1s spectra was fixed at 285.0 eV. The analysis zone consisted of a 900  $\mu\text{m}$  diameter spot. The data processing was performed using the commercially available Avantage software. For the fitting procedure, a Shirley background has been used and Lorentzian-Gaussian (L/G) ratio was fixed at 30%. Main parameters used to decompose XPS spectra are presented in Table II.

**Transmission electron microscopy (TEM) and X-ray energy dispersive spectroscopy (X-EDS).**—Cross-sections of materials passivated in 4 mol dm<sup>-3</sup>  $\text{HNO}_3$  at 100°C were analyzed using transmission electron microscopy (TEM) in high resolution imaging mode. These studies were performed by Serma Technologies (France). In order to identify zones of interest on each sample, electron backscattered diffraction (EBSD) was performed at the surface of the materials prior to sample cross-section elaboration, using a scanning electron microscope field emission gun Gemini 500 (ZEISS) scanning electron microscope (SEM), a Hikari Super charge coupled device (CCD) camera, and OIM data collection and analysis software for the acquisition and treatment of the data. Cross-section TEM lamellas were thinned using focused ion beam (FIB) FEI Strata DB400 and analyzed with a FEI Tecnai Osiris TEM using an accelerating voltage of 200 kV and equipped with ChemiSTEM and GIF Quantum detectors X-ray energy dispersive spectroscopy (X-EDS).

**Electrochemistry and flow cell.**—The AESEC flow cell has been described in detail previously.<sup>32,33</sup> The flow cell consisted of a small volume working electrode compartment (approximately 0.2 cm<sup>3</sup>) with electrolyte input at the bottom and output at the top. The flow rate was measured accurately (1% precision) for each experiment and nominally 3 cm<sup>3</sup> min<sup>-1</sup>. Counter and reference electrodes were in a larger compartment separated from the working electrode by a porous membrane to allow passage of electrical current but avoid bulk mixing

**Table II.** Parameters used for the deconvolution of XPS spectra (Avantage software) Binding energies and full width at half maximum (FWHM).

	Fe oxide contributions		Cr oxide contributions			Si oxide contributions	
	Fe - 2p <sub>3/2</sub>	Fe - 2p <sub>3/2</sub>	Cr - 2p <sub>3/2</sub>	Cr - 2p <sub>3/2</sub>	Cr - 2p <sub>3/2</sub>	Si - 2p <sub>3/2</sub>	Si - 2p <sub>1/2</sub>
Binding Energy/eV	709.7 $\pm$ 0.3	712.1 $\pm$ 0.3	576.3 $\pm$ 0.3	577.3 $\pm$ 0.3	579.0 $\pm$ 0.3	102.1 $\pm$ 0.3	102.7 $\pm$ 0.3
FWHM/eV	2.36	2.93	1.08	1.92	1.71	1.36	1.32

**Table III.** Wavelengths used for each major element of the two stainless steels, corresponding atomic weights and detection limits associated (averaged over 10 experiments).

	Fe	Cr	Ni	Si	Mn
Wavelength/nm	259.940	283.563	231.604	251.611	257.610
Detection limit in H <sub>2</sub> SO <sub>4</sub> C <sub>3σ</sub> /μg dm <sup>-3</sup>	2.3	0.12	4.4	3.6	1.9
Detection limit in HNO <sub>3</sub> C <sub>3σ</sub> /μg dm <sup>-3</sup>	12.1	7.3	27.3	30	1.0

of the two solutions. An analysis of the solution contained in the second compartment ensured a negligible quantity of metallic ions passed through the membrane. The working electrode was the stainless steel specimen, the counter electrode was a Pt grid, and the reference electrode was a Hg/Hg<sub>2</sub>SO<sub>4</sub> electrode (MSE, E = +0.65 V vs. NHE in saturated K<sub>2</sub>SO<sub>4</sub>). A Gamry Reference 600 potentiostat functioning in the potentiostatic mode was used to control the potential and measure the electrochemical current density,  $j_e$ . The analog outputs of the potentiostat were fed into the A/D converter and data acquisition software of the ICP-AES spectrometer so that the ICP-AES intensity data and the electrochemical data were on exactly the same time scale.

The AESEC experiments were performed at a temperature of 28°C (301 K) using a recirculating water system connected to a thermocryostat (Lauda) constant temperature bath. Water from the bath was circulated through a hollow copper block connected to the rear of the working electrode (SS studied) so that the electrode was heated directly. Electrical isolation between the block and the sample was designed to prevent both current leakage and ensure heat transfer. Spontaneous passivation of samples for other surface analysis (several XPS and TEM-EDX measurements) was performed at 100°C (373 K) in a 200 mL jacketed reactor using similar recirculating oil system connected to a thermocryostat (Lauda).

Polarization curves were performed at a scan rate of 0.2 mV s<sup>-1</sup> in the anodic direction using the flowcell for both SS in H<sub>2</sub>SO<sub>4</sub> and HNO<sub>3</sub> electrolytes of comparable protonic concentration (C<sub>H</sub><sup>+</sup> = 2 mol dm<sup>-3</sup>).

**Atomic emission spectroelectrochemistry.**—The experimental set-up including data acquisition has also been described in detail previously.<sup>32</sup> Briefly, the working electrode releases ions into the electrolyte in the flow cell which is then continuously fed into the plasma of the ICP-AES where the emission intensities of the different ions are measured simultaneously. These emission intensities are converted into concentration using standard ICP-AES calibration techniques. Electrolyte transport is done using a peristaltic pump and the input to the plasma uses a concentric glass nebulizer and a cyclonic spray chamber. The ICP-AES used in this work was an Ultima 2C from Horiba Jobin-Yvon consisting of a 40.68 MHz inductively coupled Ar plasma, operating at 1 kW and interfaced to independent polychromator and monochromator optical modules. A 50 cm focal length Paschen-Runge polychromator was used equipped with an array of photomultiplier tube detectors at given wavelengths allowing the measurement of 30 preselected elements simultaneously. Emission wavelengths were chosen for maximum sensitivity and low interferences. The monochromator (1 m focal length) with a Czerny–Turner configuration was dedicated for high spectral resolution of a single element. In the present work, the monochromator was used to monitor the Cr signal. Wavelengths used for each element and corresponding typical detection limits are given in Table III. Note that the detection limit was measured for each experiment and may vary depending on the conditions of the plasma.

**AESEC data treatment.**—For each element M, the instantaneous dissolution rate  $v_M$  was calculated from the instantaneous elemental concentration C<sub>M</sub>:<sup>32</sup>

$$v_M = f \frac{C_M}{A} \quad [5]$$

where  $f$  is the flow rate of the electrolyte and  $A$  is the surface area of the working electrode. The total dissolution rate  $v_\Sigma$  can be defined as the sum of the dissolution rates of the measured elements:

$$v_\Sigma = \sum v_M \quad [6]$$

The detection limits  $3\sigma$  are calculated as following (Table III):

$$C_{3\sigma} = 3 \frac{\sigma_{blank}}{\alpha} \quad [7]$$

where  $\sigma_{blank}$  is standard deviation of the background and  $\alpha$  sensitivity factor calculated from the calibration curves of each element at their specific wavelength. To facilitate comparison with the electrochemical current density,  $j_e$ , it is sometimes convenient to present the dissolution rate data as an equivalent faradaic current,  $j_M$ ,

$$j_M = n_{eM} F v_M \quad [8]$$

where  $n_{eM}$  is the number of electrons transferred in the dissolution reaction of M and  $F$  is the Faraday constant.  $j_\Sigma$  designates the sum of elemental current densities equivalent to Eq. 6.

The AESEC technique reveals whether or not a dissolution reaction is congruent or incongruent by comparing the composition of the electrolyte with that of the bulk metal. To this end the dissolution rate of an element, M, may be normalized to the bulk composition of the alloy:

$$v_M^\circ = (X_{Fe}/X_M) v_M \quad [9]$$

where  $X_M$  is the mass fraction of element M as determined by GDOES bulk analysis. For perfectly congruent dissolution,  $v_M^\circ = v_{Fe}$  while  $v_M^\circ > v_{Fe}$  implies an excess of M is dissolving and  $v_M^\circ < v_{Fe}$  implies that M is building up on the surface.

In the case of incongruent dissolution, it is possible to calculate the quantity of excess M remaining on the surface. The method of estimating Q<sub>M</sub> was developed in detail previously.<sup>28</sup> The rate of excess M building up on the surface may be defined as:

$$v'_M = \frac{X_M}{X_{Fe}} v_{Fe} - v_M \quad [10]$$

In this work, the surface enrichment of the alloy component M, Q<sub>M</sub>, may be obtained by integration of  $v'_M$ .

$$Q_M(t) = \int_0^t v'_M(t) dt \quad [11]$$

over the time period,  $t$ . In this work, we will use Eq. 11 to estimate the enrichments of Cr and Si on the surface during passivation and their subsequent dissolution during reactivation. It will be shown that these elements, in their oxidized form, are the principal components of the passive film and thusly, the AESEC methodology provides a real time quantitative kinetic analysis of passive film growth and dissolution. Further the extent of passivation (Eq. 11) may be correlated directly with the elemental dissolution rates (Eqs. 5 and 6).

## Results and Discussion

### Comparison of polarization curves of SS in H<sub>2</sub>SO<sub>4</sub> and HNO<sub>3</sub>.

An overview of the activation and passivation of a stainless steel specimen may be obtained by consideration of the elemental AESEC polarization curve, shown for the two grades of SS in 4 mol dm<sup>-3</sup> HNO<sub>3</sub> at room temperature in Fig. 1. The elemental AESEC polarization curve presents the conventional polarization curve,  $j_e$  vs.  $E$ , as well as the total elemental dissolution current density,  $j_\Sigma$  (that takes into



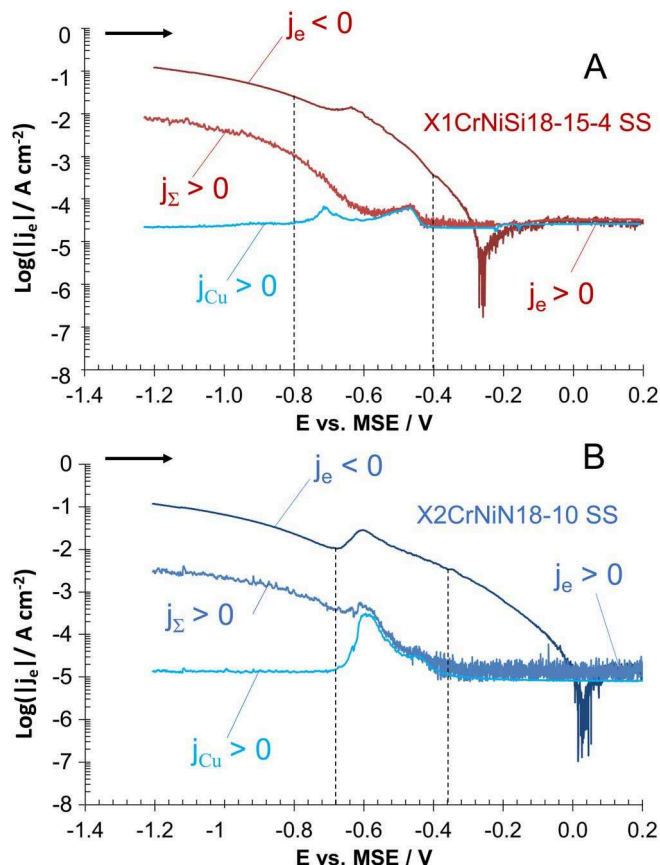


**Figure 1.**  $j_e$ ,  $j_\Sigma$  and  $j_{Cu}$  as a function of potential recorded during a linear sweep voltammetry performed on X1CrNiSi18-15-4 (A) and X2CrNiN18-10 SS (B) at  $0.2 \text{ mV s}^{-1}$  scan rate in  $4 \text{ mol dm}^{-3} \text{ HNO}_3$   $T = 25^\circ \text{C}$ .

account elemental current densities of Fe, Cr, Ni, Si, Mn, Cu), and the dissolution current density of Cu,  $j_{Cu}$ . The latter is represented separately in Fig. 1 as it is clear that all of the elements dissolved together except for Cu. In  $\text{HNO}_3$ , the cathodic reduction reaction can be distinguished as two main regions separated by a short peak of current for both SS around  $-0.60 \pm 0.20 \text{ V vs. MSE}$ . The electrical current density,  $j_e$ , of both steels superimpose accurately below  $-0.80 \text{ V vs. MSE}$  and differ above. A selective dissolution clearly occurs below  $-0.80 \text{ V vs. MSE}$  (dissolution of Cu is close to zero), then Cu dissolution occurs in two peaks between  $-0.80$  and  $-0.38 \text{ V vs. MSE}$  as it is shown in Fig. 1. Cu dissolution was detected in  $\text{H}_2\text{SO}_4$  around the same potentials by Ogle et al.<sup>35</sup> and Ruel et al.<sup>36</sup> but in the present work, the dissolution occurred systematically in two peaks whose origin is still unclear. However, as a result of this selective dissolution, a Cu-rich layer can be expected to exist below  $-0.80 \text{ V vs. MSE}$  where then dissolves between  $-0.80$  and  $-0.38 \text{ V vs. MSE}$ . It should be noted that this is quite consistent with thermodynamics as the transition  $\text{Cu}(0) \rightarrow \text{Cu}(\text{II})$  is expected around  $-0.40 \text{ V vs. MSE}$ .<sup>38</sup> At this Cu-rich surface, an enhancement of hydrogen reduction occurs<sup>29,30</sup> and this explains why both SS display exactly the same current density in this region. Right after the Cu-rich layer dissolution, given the potential domain, the reduction of nitric species is very likely to occur and the current density obtained is quite large.<sup>14</sup>

The results in Fig. 1 highlight the necessity of elemental rate data for the system SS/ $\text{HNO}_3$  as the active to passive transition is not at all detectable in the  $j_e$  vs.  $E$  curve but appears clearly as a decrease in the elemental dissolution rate over a potential range of approximately  $-1 \text{ V}$  to  $-0.6 \text{ V}$ . In this same potential range, the electrical current density,  $j_e$ , is cathodic and on the order of several hundred  $\text{mA cm}^{-2}$  while the anodic current associated with the passive to active transition,  $j_\Sigma$ , is less than  $1 \text{ mA cm}^{-2}$  and was therefore completely masked. Also

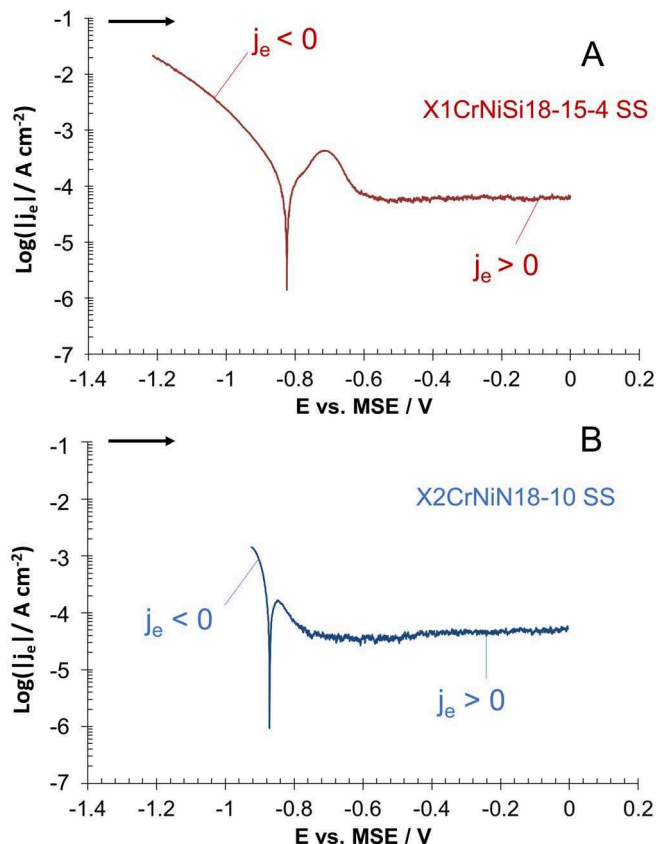


**Figure 2.**  $j_e$  as a function of potential recorded during a linear sweep voltammetry performed on X1CrNiSi18-15-4 (A) and X2CrNiN18-10 SS (B) at  $0.2 \text{ mV s}^{-1}$  scan rate in  $2 \text{ mol dm}^{-3} \text{ H}_2\text{SO}_4$   $T = 25^\circ \text{C}$ .

resulting from this intense reduction reaction, the potentials corresponding to  $j_e = 0$  are shifted anodically well into the passive domain. These values are very close to the open circuit potentials that were measured prior to the potential sweep. This result illustrates that SS in  $\text{HNO}_3$  spontaneously passivates and remains passive in  $\text{HNO}_3$ .

Previous measurements of the activation potential for the passive to active transition gave a value of  $-0.84 \pm 0.01 \text{ V vs. MSE}$  in  $4 \text{ mol dm}^{-3} \text{ HNO}_3$ <sup>25</sup> for the X1CrNiSi18-15-4 SS. In contrast, the results of Fig. 1 indicate that the opposite transition, active to passive, is shifted in the cathodic direction for the formation of the passive film as compared to the dissolution of the passive film. The same tendency was pointed out by Lorbeer et al.<sup>34</sup> on the active-passive and passive-active transitions of Fe in  $\text{H}_2\text{SO}_4$ .

Identical experiments were conducted for SS in  $2 \text{ mol dm}^{-3} \text{ H}_2\text{SO}_4$  at room temperature, however as this system has been investigated in detail previously,<sup>28</sup> only the conventional polarization curve ( $j_e$  vs.  $E$ ) are shown in Fig. 2. The active-passive transitions for both steels are clearly observed in  $\text{H}_2\text{SO}_4$  occurring between  $-0.90$  and  $-0.50 \text{ V vs. MSE}$ . However, the anodic maxima for the two cases is very close to the  $j_e = 0$  potential indicating that the cathodic current is quite large in this potential domain.

The effect of Si on the electrochemical behavior of SS may be determined by inspection of Figs. 1 and 2. First, the shape of the cathodic curves is very similar but the reduction reaction after Cu dissolution seems to be kinetically lowered for X1CrNiSi18-15-4 in both electrolytes. Second, in both electrolytes, the passive current of the X1CrNiSi18-15-4 SS is higher than for the X2CrNiN18-10 SS (respectively recorded  $260 \pm 50$  and  $125 \pm 50 \text{ nA cm}^{-2}$ ). This is consistent with both electrochemical and gravimetric measurements performed in different parametrical studies<sup>39–42</sup> showing that the X1CrNiSi18-15-4 SS in pure  $\text{HNO}_3$  dissolves more rapidly than the X2CrNiN18-10 SS.

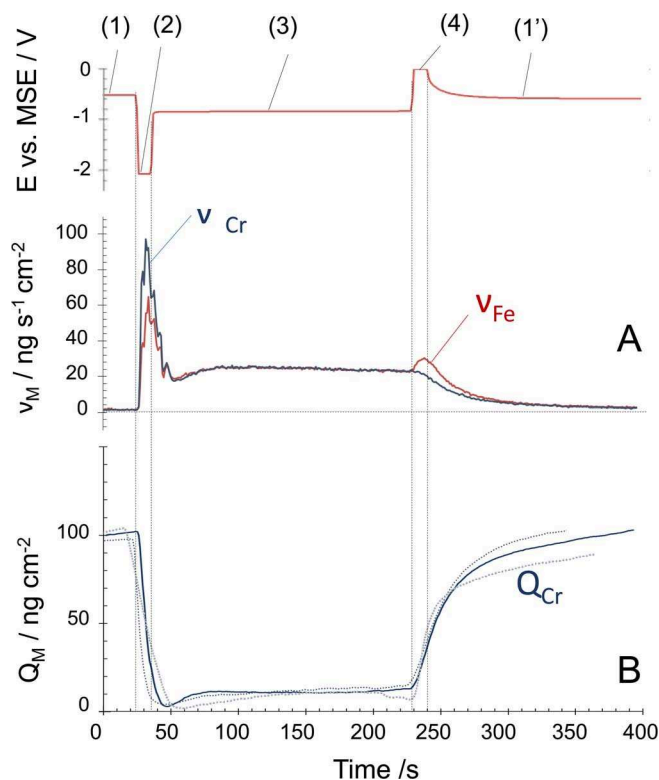


**Figure 3.** (A) Representative active-passive cycles for the X1CrNiSi18-15-4 SS in 2 mol dm<sup>-3</sup> H<sub>2</sub>SO<sub>4</sub> T = 25°C. A/ $v_{Fe}$  and  $v_{Cr}^{\circ}$  vs. time. (B)  $Q_{Cr}$  vs. time (3 cycles superimposed.).

This suggests that the oxide layer formed at the X1CrNiSi18-15-4 SS surface is less protective than for the X2CrNi18-10.

#### The kinetics of dissolution and passivation of SS in H<sub>2</sub>SO<sub>4</sub>—

Passive film formation and dissolution was performed in H<sub>2</sub>SO<sub>4</sub> during potentiostatic passivation and activation cycles, following the protocol of a previous publication.<sup>28</sup> A single active-passive cycle for X2CrNi18-10 SS in 2 mol dm<sup>-3</sup> H<sub>2</sub>SO<sub>4</sub> is presented in Fig. 3A and 4A. Shown are the dissolution rate of Fe,  $v_{Fe}$ , and the Cr and Si dissolution rates normalized to the Fe bulk composition,  $v_M^{\circ}$ , via Eq. 9. A single activation-passivation cycle is divided into four time periods: (1) open circuit in passive domain; (2) activation, potentiostatic pulse at -2.0 V vs. MSE for 10 s; (3) open circuit in the active domain; (4) passivation, potentiostatic pulse at 0.0 V vs. MSE for 10 s; (1') return to (1). The active and passive potentials for this work were chosen as -2.0 V and 0.0 V respectively. For both steels and both electrolytes, 0 V vs. MSE appears in the passive domain and is sufficiently low to avoid any risk of transpassive dissolution (Fig. 2). A potential of -2.0 V vs. MSE was chosen for the activation as it is well below the passive-active transition. The effect of potential and polarization time will be discussed later.

During period (1), the passivity of the alloy is evident as all  $v_M^{\circ}$  are nearly zero and  $E_{oc} = -0.50 \pm 0.05$  V vs. MSE, consistent with the passive state (Fig. 2). In period (2), a sharp dissolution peak is observed, indicative of the enhanced dissolution following a cathodic activation. This is followed in period (3) by a steady increase in  $v_M^{\circ}$  until a stable dissolution rate is obtained after approximately 200 s. During this period,  $E_{oc} = -0.82 \pm 0.05$  V vs. MSE also consistent with the active state. Period (4) is characterized by a peak in the  $v_{Fe}$  whereas Cr and Si showed simply a steady decrease in intensity. This cycle was repeated four times and gave reproducible results.

Congruent dissolution during the active period 3 is clearly indicated as  $v_M^{\circ} = v_{Fe}$  for both M = Cr and Si. This is consistent with the definition of the active domain as the oxide film formation rate

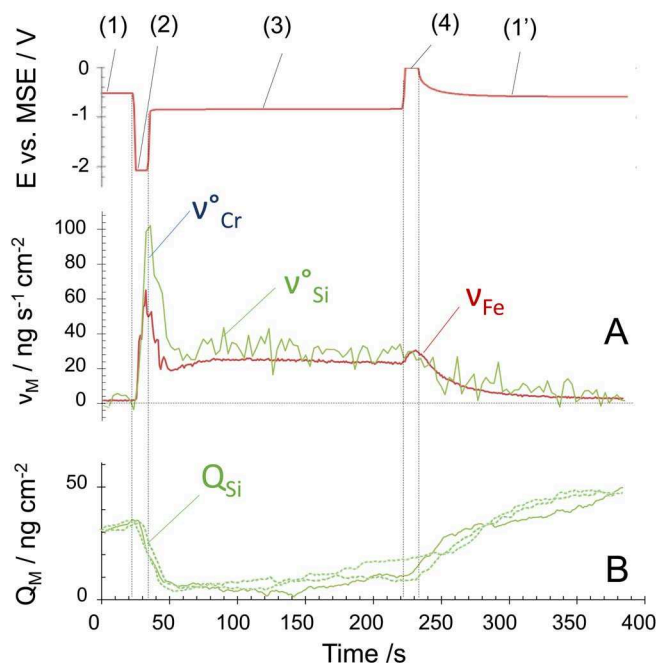


**Figure 4.** (A) Representative active-passive cycles for the X1CrNiSi18-15-4 SS in 2 mol dm<sup>-3</sup> H<sub>2</sub>SO<sub>4</sub> T = 25°C. A/ $v_{Fe}$  and  $v_{Si}^{\circ}$  vs. time. (B)  $Q_{Si}$  vs. time (3 cycles superimposed.).

should be negligible as compared to the dissolution rate.<sup>43</sup> It should be noted that using Fe as the reference element in Eq. 9 assumes that Fe is not contributing to the passive layer and that all oxidized Fe goes into solution. This hypothesis was confirmed by using Mn as the reference element (not shown), since soluble Mn(II) is expected to be the predominant Mn species across the entire range of applied potentials.<sup>17</sup> In nitric acid, it was found that  $v_{Mn}^{\circ}/v_{Fe} = 0.95 \pm 0.06$ , demonstrating that Fe is a suitable reference element for this calculation, identical to the situation in H<sub>2</sub>SO<sub>4</sub>.<sup>28</sup> Fe has been identified in the external layer of the passive film in various acidic electrolytes in several cases.<sup>49,50</sup> However, the observation of Fe oxide in the passive film by XPS in H<sub>2</sub>SO<sub>4</sub> and HNO<sub>3</sub> remains tenuous.<sup>37,44</sup> Yang et al.<sup>51</sup> even found that Fe(II) was no longer detectable after 24 hours in the passive film formed in acidic electrolytes containing chlorides.

The important point to note in Fig. 3A and 4A is that a positive excess dissolution for both elements was recorded during activation of the surface. For the activation  $v_{Cr}^{\circ} > v_{Fe}$  and  $v_{Si}^{\circ} > v_{Fe}$  suggesting an excess dissolution of Cr and Si. This result is consistent with the dissolution of a pre-existing passive layer enriched in Cr and Si. No significant selective dissolution of Si was detected for the X2CrNi18-10 SS, consistent with the absence of Si in the oxide layer of this alloy. The opposite behavior is observed during passivation as Cr. There is a significant peak in  $v_{Fe}$  while  $v_{Cr}^{\circ}$  and  $v_{Si}^{\circ}$  simply decrease. This is consistent with the preferential dissolution of Fe with Cr and Si remain on the surface contributing to the formation of the passive layer. Throughout the passivation cycle,  $v_{Cr}^{\circ} < v_{Fe}$  and  $v_{Si}^{\circ} < v_{Fe}$  suggesting that Cr is building up on the surface again in the form of a Cr enriched passive film. This behavior was not observed for Ni nor for Mn.

The quantification of Cr and Si in the passive film may be achieved by mass balance (Eqs. 10 and 11). This is shown for X1CrNiSi18-15-4 SS in Fig. 3B and Fig. 4B were the surface excesses of Cr and Si,  $Q_{Cr}$  and  $Q_{Si}$ , (Eq. 11) are given as a function of time. The results of three consecutive cycles are superimposed. From the graph,  $Q_{Cr}$  cycles between 0 and 100 ng cm<sup>-2</sup> while  $Q_{Si}$  cycles between 0 and 50 ng cm<sup>-2</sup>. For the activation period (2) (t = 30 to 60 s) there is a clear decrease in  $Q_{Cr}$  and  $Q_{Si}$  associated with the dissolution of the passive film. There is no indication of film formation in the active period (3) and Cr and Si dissolution are congruent with Fe. However, film



formation occurs in the passivation period (4) and continues slowly during the open circuit passive period (1'). Note that the growth of the passive film expressed in excess Cr observed in periods (4) and (1') are within a few percent of the dissolution of the passive film in period (2).

The maximum quantity of excess Cr and Si ( $\Delta Q_{Cr_{max}}$  and  $\Delta Q_{Si_{max}}$ ) did not vary within experimental reproducibility ( $\pm 10\%$ ) with the potentials and times of either activation or passivation as shown by the results of Table IV. Also shown in Table IV is the faradaic yield for passivation calculated as the ratio of the integrated external current,  $\Delta n_{e_{ext}}$ , and the hypothetical current determined from elemental dissolution,  $\Delta n_{e_{ICP}}$ :

$$\Delta n_{e_{ext}} = \frac{1}{F} \int_{t_1}^{t_2} j_e dt \quad [12]$$

$$\Delta n_{e_{ICP}} = \int_{t_1}^{t_2} \left( \frac{2v_{Fe}}{M_{Fe}} + \frac{3v_{Cr}}{M_{Cr}} + \frac{2v_{Ni}}{M_{Ni}} + \frac{4v_{Si}}{M_{Si}} \right) dt + 4 \frac{Q_{Si}}{M_{Si}} + 3 \frac{Q_{Cr}}{M_{Cr}} \quad [13]$$

where  $t_1$  and  $t_2$  refer to the beginning and end of the passivation period (4) with a total time of 100 seconds, and  $M_M$  the molar mass of M. The comparison leads to very coherent results as the average ratio of the ionic dissolution to electrochemical current,  $\Delta n_{e_{ICP}}/\Delta n_{e_{ext}} = 0.9 \pm 0.1$ . This means that the entire current recorded by the potentiostat can be assigned to the dissolution of the material and the formation of the passive film within a 10% error. This result also highlights the high reliability of the quantitative measurement of the AESEC. Note that the  $v_M$  values in Eq. 13 were corrected for the descending background of the concentration due to the residence time distribution as described previously.<sup>28</sup>

The quantity of Cr determined in this work is curiously small as compared to what would usually be expected for a passive film. A very rough estimate of the thickness may be made from the approximately  $100 \text{ ng cm}^{-2}$  Cr using the density of bulk  $\text{Cr}_2\text{O}_3$  ( $5.21 \text{ g cm}^{-3}$ ) and assuming a uniform distribution on the surface. This leads to a hypothetical thickness of only 0.2 nm, consistent with previous work.<sup>28</sup> This is very small as compared to values reported in the literature<sup>52,53</sup> and in fact is far from the 3 nm observed on the TE micrographs to be discussed later. For the most part however ex situ analysis has been done for films that were prepared after significantly longer passivation times and under more severe conditions. One possible explanation of the anomalously small value of the passive layer thickness is that the formation of the passive film occurs in two steps: (1) the very rapid formation of a "prepassive film",<sup>53,54</sup> followed by (2) a much slower growth of the film. Vetter<sup>12</sup> showed that for passive iron a steady-state thickness of the passive film was reached asymptotically with time. In order to be detected by the ICP-AES, the dissolution/film formation reactions have to rise above the detection limit of the spectrometer and it is conceivable that only the very first instants of film formation yield such a high rate. Once the proto film is formed, the rate of dissolution would slow considerably. In fact, this is observed in Fig. 3 where the passive film continues to grow even after the applied potential has been stopped.

These results allow us to correlate the dissolution (corrosion) rate of the steel with the quantity of excess Cr in the passive film. During active dissolution ( $Q_{Cr} = 0$ ), the open circuit potentials (OCP) of both materials are very close ( $-0.84 \pm 0.05 \text{ V vs. MSE}$  for the X2CrNiN18-10 SS and  $-0.82 \pm 0.05 \text{ V vs. MSE}$  for the X1CrNiSi18-15-4 SS). However,  $v_\Sigma$  differs by 30% between the two alloys ( $60 \text{ ng s}^{-1} \text{ cm}^{-2}$  for the X2CrNiN18-10 SS and  $40 \text{ ng s}^{-1} \text{ cm}^{-2}$  for the X1CrNiSi18-15-4 SS). This means that the spontaneous corrosion rate of the X2CrNiN18-10 SS is more severe than that of X1CrNiSi18-15-4 SS at the same potential in  $\text{H}_2\text{SO}_4$ . This was not obvious based on Fig. 2 as the  $j_e = 0$  potential for X1CrNiSi18-15-4 SS active-passive transition is shifted by about +200 mV (anodic) as compared to X2CrNiN18-10 SS.

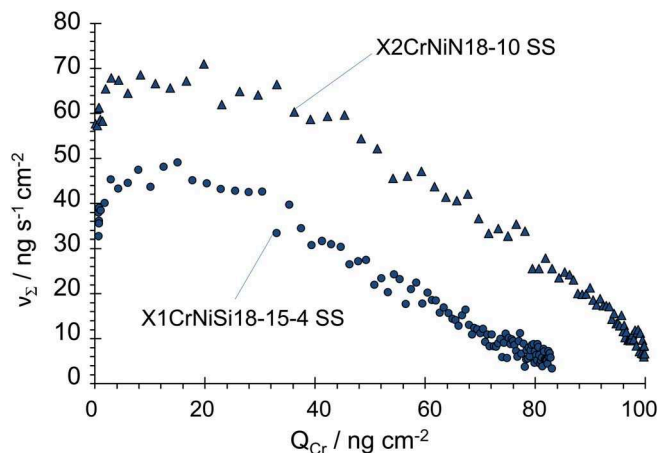


**Figure 5.**  $v_\Sigma$  as a function of  $Q_{Cr}$  for the X1CrNiSi18-15-4 and the X2CrNiN18-10 SS over a typical passivation period (4)  $\rightarrow$  (1') in  $2 \text{ mol dm}^{-3} \text{ H}_2\text{SO}_4$   $T = 25^\circ\text{C}$ .

In Fig. 5,  $v_\Sigma$  is shown as a function of  $Q_{Cr}$  for both materials in  $\text{H}_2\text{SO}_4$ . Note that the  $v_M$  values in Eq. 12 were corrected for the descending background of concentration as described in reference.<sup>28</sup> It is seen that the early stages of passive film formation ( $Q_{Cr} < 5 \text{ ng cm}^{-2}$ ) are associated with an increased dissolution rate which then remains stable until about  $30 \text{ ng cm}^{-2}$ . This represents the increase in dissolution rate observed initially when the passivation potential is applied. Beyond this, the progressive passivation of the surface takes place and the dissolution rate drops off until  $80 \text{ ng cm}^{-2}$  for 3.5 wt% Si and  $100 \text{ ng cm}^{-2}$  for 0.3 wt% Si. Although Si contributes to the passive layer of the X1CrNiSi18-15-4 SS, Fig. 5 presents very similar slopes  $v_\Sigma = f(Q_{Cr})$ . Furthermore, the addition of Si in the composition of SS does not seem to affect the slope  $v_\Sigma$  vs.  $Q_{Cr}$  during passivation, however, it shifts the final value of  $Q_{Cr}$  to  $20 \text{ ng cm}^{-2}$  as Si occupies the surface along with Cr.

**The kinetics of dissolution and passivation of X1CrNiSi18-15-4 SS in  $\text{HNO}_3$ .**—Active-passive cycles in  $\text{HNO}_3$  were attempted despite the difficulties inherent in this electrolyte. The SS was polarized in the active domain for two different values of potential ( $-1.20 \text{ V vs. MSE}$  in Fig. 6A and  $-0.8 \text{ V vs. MSE}$  in Fig. 6B) for 600 s and then allowed to passivate spontaneously at the open circuit potential as shown in Fig. 6. At the active polarization potentials of  $-1.20$  and  $-0.8 \text{ V vs. MSE}$ , all  $v_M$  increase similar to the situation for  $\text{H}_2\text{SO}_4$  (Fig. 3), however the accelerated dissolution yields nearly a 10-fold enhancement in the dissolution rates, even in the case of  $-0.8 \text{ V vs. MSE}$ . Elemental dissolution was congruent as indicated by the fact that  $v^\circ_{Cr} = v_{Fe}$  throughout the cycles. Right after releasing the potential and measuring its open circuit value, all  $v_M$  decrease slowly toward the detection limit.

Unlike the situation in  $\text{H}_2\text{SO}_4$ , it is clear from Fig. 6 that within experimental error of about 1%,  $v^\circ_{Cr} = v_{Fe}$  throughout the active-passive cycles. It is therefore not possible to extract reliable information on Cr enrichment on the surface during passivation or their excess dissolution during activation under the conditions investigated here. The  $v^\circ_{Si}$  differs in some places from  $v_{Fe}$  (indicated with a \* in Fig. 6), however, these variations are in different points of the cycle in Figs. 6A and 6B, and they do not correlate with the onset of the potential steps, and therefore no further attempt was made to interpret them.

The results of Fig. 6 yield, for the first time, a kinetic measurement in real time for the spontaneous passivation of SS in  $\text{HNO}_3$ . This is shown in Fig. 6 by the decrease of the elemental dissolution rates with time when the potential is released to open circuit after activating the alloy. As an aid to comparison between the two electrolytes, Fig. 7 gives the normalized rate,  $v_\Sigma/v_{\Sigma_{max}}$ , corrected for the decreasing background, as recorded during passivation of X1CrNiSi18-15-4 SS

**Table IV.** Results obtained over active-passive cycles on X1CrNiSi18-15-4 SS in 2 mol dm<sup>-3</sup> H<sub>2</sub>SO<sub>4</sub> at 25°C depending on various times and values of activation and passivation each repeated between one and five times.

Activation		Passivation		$\Delta n/\text{nmol cm}^{-2}$			$\Delta Q_{M_{\text{max}}}$	
$\Delta t/\text{s}$	E vs. MSE/V	$\Delta t/\text{s}$	E vs. MSE/V	$\Delta n_{\text{eICP}}$	$\Delta n_{\text{eext}}$	$\Delta n_{\text{eext}}/\Delta n_{\text{eICP}}$	$\Delta Q_{\text{Cr}_{\text{max}}}/\text{ng cm}^{-2}$	$\Delta Q_{\text{Si}_{\text{max}}}/\text{ng cm}^{-2}$
100	-2	100	0	53	56	1.06	130	50
10	-2	10	0	59	46	0.75	100	40
10	-2	10	-0.20	50	52	1.03	100	40
10	-2	10	0.25	37	44	1.19	90	40
10	-1.8	10	0	57	63	0.81	130	50
50	-1.8	10	0	93	81	0.87	230	100
90	-1.8	10	0	71	52	0.73	200	80
10	-1.6	10	0	53	43	0.80	230	100
10	-1.2	10	0	44	40	0.90	150	50
50	-1.2	10	0	62	40	0.64	300	120
90	-1.2	10	0	66	58	0.88	290	150
Mean				60	52	0.89		
Standard deviation				16	12	0.16		

in H<sub>2</sub>SO<sub>4</sub> and HNO<sub>3</sub>. These curves reveal that the passivation kinetics of the X1CrNiSi18-15-4 SS are very similar in both electrolytes, which is consistent with the hypothesis of a very similar passive layer obtained at the end of passivation. This supports the idea that the results obtained in H<sub>2</sub>SO<sub>4</sub> are transposable to HNO<sub>3</sub>.

**Structure of the passive film on X1CrNiSi18-15-4 SS exposed to HNO<sub>3</sub>.**—XPS measurements were performed on both SS after

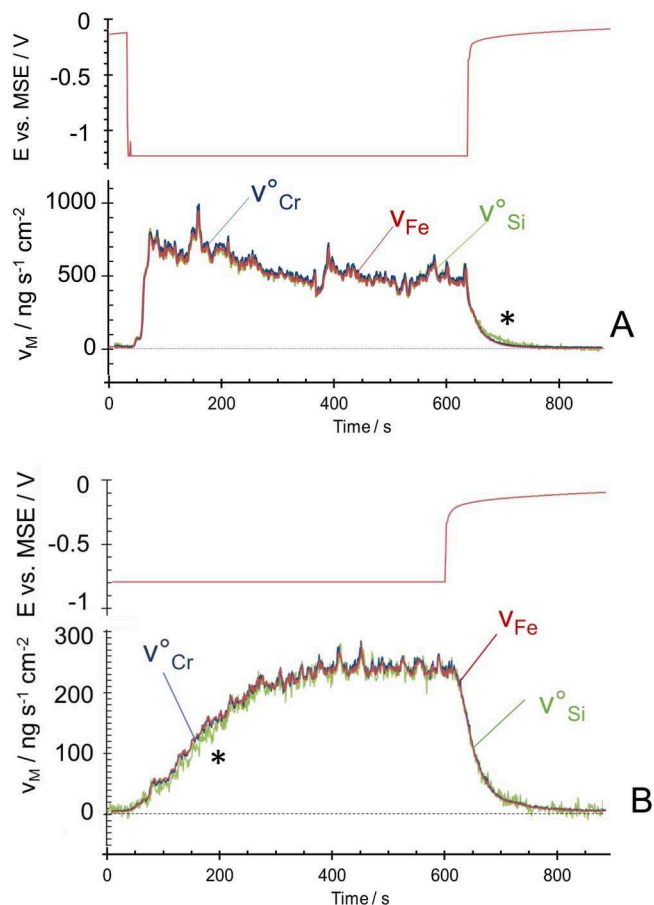


**Figure 6.**  $v_{\text{Fe}}$ ,  $v_{\text{Cr}}$  and  $v_{\text{Si}}$  vs. time for the X1CrNiSi18-15-4 SS monitored over a typical active – passive cycle in 4 mol dm<sup>-3</sup> HNO<sub>3</sub> T = 25°C (A) Activation potential of -1.2 V vs. MSE. (B) Activation potential of -0.8 V vs. MSE.

exposure to each electrolyte at 28°C and 100°C, and in HNO<sub>3</sub> for two different times of exposure (10 mins to 24 hours). As the results did not vary significantly between these conditions, typical spectra of Cr-2p<sub>3/2</sub> are shown in Fig. 8 and the quantitative average analyses are given in Table V.

The results are consistent with the literature for passive films formed in similar environments.<sup>36,43</sup> X1CrNiSi18-15-4 SS presents a high concentration of Si and Cr while X2CrNi18-10 SS surface is mainly enriched in Cr. Main differences in the chemical structure of the oxide layer concern Cr and Si. The Cr-2p<sub>3/2</sub> core level spectra for X2CrNi18-10 SS oxide layer presents a complex multiplet structure (Fig. 8B) with the typical range of energies corresponding to chromic oxide Cr<sub>2</sub>O<sub>3</sub>.<sup>45</sup> But for the X1CrNiSi18-15-4 SS oxide layer (Fig. 8B), Si-2p core level energies were shifted to lower values from the 103.5–104.0 eV range that is usually associated with SiO<sub>2</sub>.<sup>46</sup> For metal silicates, Si and associated metal elements core levels energies may shift as compared to pure metal oxides as it is the case of Fe silicate<sup>47</sup> or Zr silicate<sup>48</sup> in comparison to Fe or Zr oxide. In the present case, Cr-2p core levels energies seem to be shifted to higher values in the presence of Si in the oxide layer. Fig. 8 displays the comparison between the Cr-2p<sub>3/2</sub> photoelectron peaks for X1CrNiSi18-15-4 and X2CrNi18-10 SS. A chemical shift of 0.4 eV toward higher binding energy appears repetitively (over 8 experiments) for the oxide Cr contribution in the X1CrNiSi18-15-4 SS passive layer while the Cr metallic contribution is at the same binding energy for both SS. This result must be considered with great caution as the chemical shift is small. Nevertheless it is of the same order of magnitude as the shift found

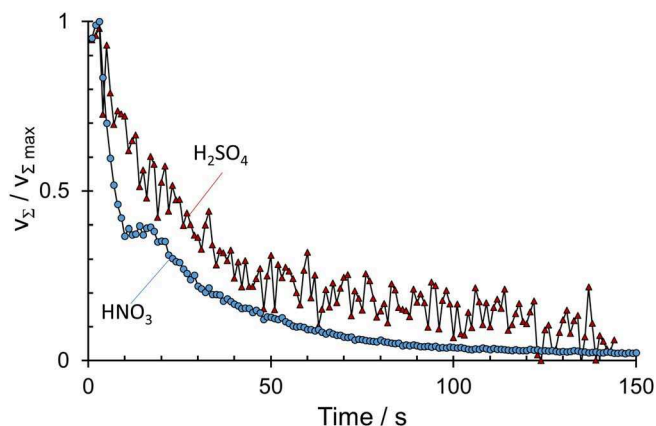


**Figure 7.**  $v_{\text{Si}}/v_{\text{Si}_{\text{max}}}$  as a function of time for X1CrNiSi18-15-4 SS during passivation in H<sub>2</sub>SO<sub>4</sub> (red triangles) and HNO<sub>3</sub> (blue circles) T = 25°C. The results have been corrected for the residence time distribution in the flow cell.

**Table V.** Relative quantification by XPS measurements on passive layers after 10 mins and 24 h immersion in H<sub>2</sub>SO<sub>4</sub> and HNO<sub>3</sub> (averaged over 3 experiments for H<sub>2</sub>SO<sub>4</sub>, 10 experiments for HNO<sub>3</sub>).

	[Fe Ox]/at. %	[Cr Ox]/at. %	[Si Ox]/at. %
X1CrNiSi18-15-4 H <sub>2</sub> SO <sub>4</sub> (2 mol dm <sup>-3</sup> ) 10 min – 28°C	28 ± 1	43 ± 2	30 ± 1
X2CrNiNi18-10 H <sub>2</sub> SO <sub>4</sub> (2 mol dm <sup>-3</sup> ) 10 min – 28°C	38 ± 8	62 ± 8	None
X1CrNiSi18-15-4 HNO <sub>3</sub> (4 mol dm <sup>-3</sup> ) 24 h – 100°C	22 ± 4	51 ± 5	27 ± 6
X1CrNiSi18-15-4 HNO <sub>3</sub> (4 mol dm <sup>-3</sup> ) 10 min – 28°C	26 ± 2	48 ± 1	26 ± 3
X2CrNiNi18-10 HNO <sub>3</sub> (4 mol dm <sup>-3</sup> ) 10 min – 28°C	41 ± 4	59 ± 5	none

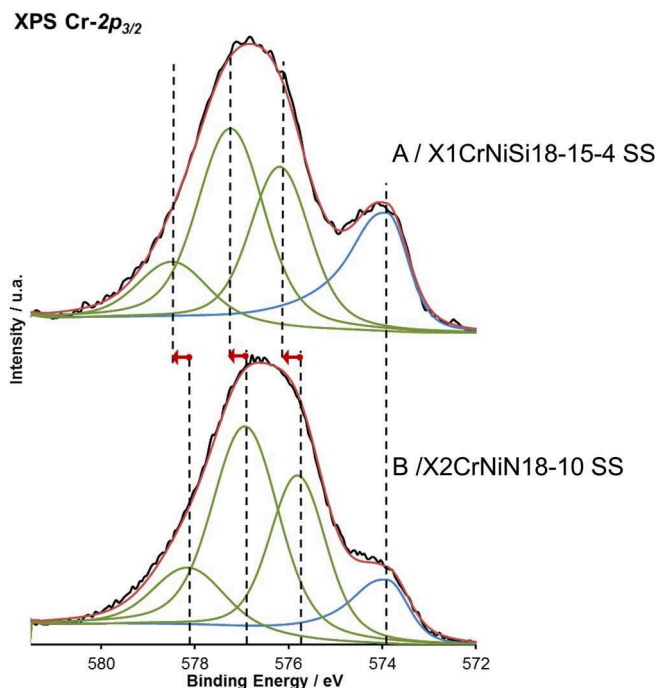
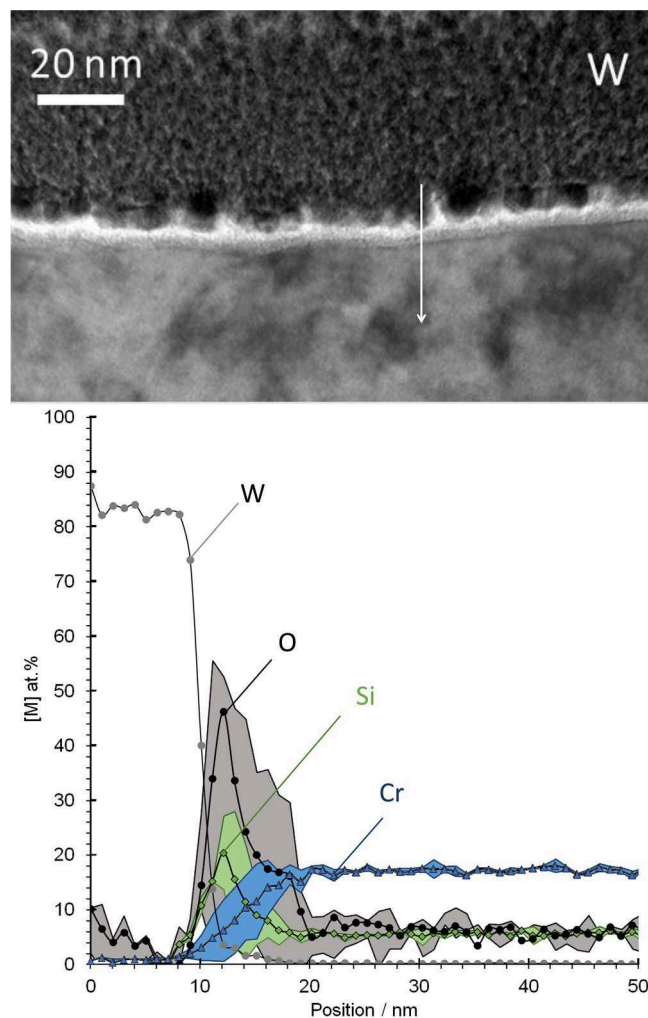
by Lee et al.<sup>47</sup> in the case of Fe silicates. The reproducibility of this result also supports the idea that Cr is actually involved in the silicate structure composing the oxide layer of the X1CrNiSi18-15-4 SS.

For the X1CrNiSi18-15-4 SS, XPS measurements reveal no drastic difference of chemical composition nor thickness between H<sub>2</sub>SO<sub>4</sub> and HNO<sub>3</sub>. Even without measuring the passive layer thickness on TEM micrographs, it was possible to compare ratios of metallic and oxidized contributions of the elements in the XPS spectra between the two electrolytes. As they were all congruent between different conditions of passivation, it was possible to conclude that the thickness of the X1CrNiSi18-15-4 SS passive layer was not impacted by the nature of the electrolyte. From TEM micrographs (Fig. 9), it was shown that the X1CrNiSi18-15-4 SS passive layer is about 3 to 4 nm thick, amorphous and regular over the surface.

To determine the stoichiometry of these oxides, a first idea would be to determine a ratio  $\frac{n_{Cr}}{n_{Si}}$  from both XPS measurements and AESEC measurements. AESEC measurements lead to total amounts of  $80 \pm 40$  ng cm<sup>-2</sup>, of Cr and of  $30 \pm 10$  ng cm<sup>-2</sup> of Si (from Fig. 4) to give  $n_{Cr} = n_{Si} = \frac{n_{Cr}}{n_{Si}} = 1.4 \pm 0.2$ . XPS gives  $\frac{n_{Cr}}{n_{Si}} = 1.5 \pm 0.2$  (for 8 measurements). Firstly, it can be noticed that AESEC and XPS lead to a very similar ratio. An averaged result of X-EDS measurements performed over 7 profiles on FIB cross section of a passive layer formed on the X1CrNiSi18-15-4 SS in HNO<sub>3</sub> at 100°C for 24 hours is presented on Fig. 9 (colored areas representing standard deviation obtained over the measurements). Fig. 9 reveal a reproducible outer

layer where Si prevails largely over Cr. X-EDS analysis revealed systematically the presence of Si at the extreme surface and a variation of the Cr/Si ratio over the few nanometers thick oxide layer, from the surface to the oxide-metal interface.

Because of the resolution of the X-EDS (0.5 nm), it is impossible to precisely position the transition between two possible regions. Nevertheless, as the increases of Cr and Si in the first nanometers of the oxide layer are clearly not proportional, and the high reproducibility of this result (for a total of 7 measurements on two different samples), the results clearly indicate an extreme surface zone where the atomic ratio  $\frac{n_{Cr}}{n_{Si}} < 1$  has been identified. This ratio was statistically measured at  $0.7 \pm 0.1$ .

**Figure 8.** Cr-2p<sub>3/2</sub> XPS spectra of X1CrNiSi18-15-4 and X2CrNiNi18-10 SS passive layers formed in 4 mol dm<sup>-3</sup> HNO<sub>3</sub>, T = 25°C for 24 hours highlighting a typical example of chemical shift of the oxide Cr contribution on the X1CrNiSi18-15-4 SS.**Figure 9.** X-EDS line scan (TEM) of the passive layer of X1CrNiSi18-15-4 SS: (upper) TEM cross section showing the passive film; (lower) EDS elemental analysis across the passive film formed in 4 mol dm<sup>-3</sup> HNO<sub>3</sub> T = 100°C for 24 hours. Two regions are observed where ratios Cr/Si are  $0.7 \pm 0.1$  and  $2.1 \pm 0.3$ .



Based on these three techniques (AESEC, XPS, TEM-X-EDS), it is proposed that a minimum of two layers of different oxide ratios exist. After X-EDS measurements, a ratio for the inner layer was measured in the region between  $n_{\text{Si}} > n_{\text{Cr}}$  and the region where the metal composition is reached and where  $\frac{n_{\text{Cr}}}{n_{\text{Si}}} = 3.6 \pm 0.1$ . In this inner layer, Cr appears as more concentrated and the atomic ratio calculated is  $2.1 \pm 0.3$  which remains lower than the value calculated in the bulk metal.

Given all the precautions mentioned, the following considerations must be taken as hypothesis to be confirmed. Nevertheless, if the two oxide regions are of the same thickness, one would expect an averaged ratio of  $1.4 \pm 0.2$  which would be consistent with AESEC and XPS to directly observe the two layers, supporting the hypothesis of a double layered oxide film for the X1CrNiSi18-15-4 SS. The outer layer would be composed of an oxide of a stoichiometry that could be (Cr: 2; Si: 3). A chromic oxide type  $\text{Cr}_2(\text{SiO}_3)_3$  is consistent with this stoichiometry, however this outer layer could also be hydrated.<sup>8</sup> The inner oxide stoichiometry would rather correspond to (Cr: 2; Si: 1) such as in  $\text{SiCr}_2\text{O}_5$ , for example.

### Conclusions

The direct observation by AESEC of Fe, Cr, and Si elemental dissolution during active – passive cycles is reported for two varieties of stainless steels in  $4 \text{ mol dm}^{-3} \text{ HNO}_3$  and  $2 \text{ mol dm}^{-3} \text{ H}_2\text{SO}_4$ . From a mass balance, it was possible to estimate the quantity of residual Cr and Si in the passive film for the case of  $\text{H}_2\text{SO}_4$ , and to follow its growth in real time during passivation as well as its dissolution during activation. It was shown in the present work that Si and Cr mainly contribute to the formation of the oxide layer of the X1CrNiSi18-15-4 SS. From these measurements, it was possible to calculate enrichments of Si and Cr in the passive layer and the results were consistent with XPS ex situ measurements performed in  $\text{H}_2\text{SO}_4$  and  $\text{HNO}_3$ .

TEM coupled with X-EDS line scans gave passive film compositions that were consistent with XPS and AESEC measurements in terms of molar ratio  $\frac{n_{\text{Cr}}}{n_{\text{Si}}}$  averaged through the entire passive film. However they revealed an outer region where Si prevails over Cr suggesting the passive film consists of an outer and inner layer with (Cr: 2; Si: 3) and a Cr rich inner layer (Cr: 2; Si: 1).

In  $\text{HNO}_3$ , no selective dissolution was detectable. It is assumed that this selective behavior exists as the passive layers analyzed by XPS are very similar for both acids.

It is concluded that Si enrichment of an X2CrNi18-10 type SS significantly modifies the chemistry of the passive layer. However, it still consists of a Cr-rich oxide with protective character for the material.

### Acknowledgments

Authors are grateful to Areva, S.A. for financial support, Dr. Michel Tabarant for the GDOES analysis, and Dr. Michel Keddad for helpful discussions.

### References

- J. Keir, *Philosophical Transactions of the Royal Society of London*, **80**, 359 (1790).
- W. Hisinger and J. J. Berzelius, *Gilberts Annalen*, **27**, 275 (1807).
- Ch. F. Schönbein and M. Faraday, *Philosophical Magazine*, **9**, 53 (1836).
- M. Faraday, *Experimental Researches in Electricity*, 2, Dover, New York (1965).
- C. L. McBee and J. Kruger, *Electrochimica Acta*, **17**, 1337 (1972).
- C. O. A. Olsson and D. Landolt, *Electrochimica Acta*, **48**, 1093 (2003).
- P. Fauvet, *Nuclear corrosion science and engineering*, 679, Woodhead Publishing, Cambridge (2012).
- H.-H. Strehblow, *Electrochimica Acta*, **212**, 630 (2016).
- D. D. Macdonald, *Pure Applied Chemistry*, **71**, 951 (1999).
- R. Kirchheim, B. Heine, S. Hofmann, and H. Hofsäuss, *Corrosion Science*, **31**, 573 (1990).
- M. Legrand, B. Diawara, J. J. Legendre, and P. Marcus, *Corrosion Science*, **44**, 773 (2002).
- K. J. Vetter, *Electrochemische Kinetik*, Springer-Verlag, Berlin-Göttingen-Heidelberg, 748 (1961).
- P. Schmuki, S. Virtanen, H. S. Isaacs, M. P. Ryan, A. J. Davenport, H. Böhm, and T. Stenberg, *Journal of The Electrochemical Society*, **145**, 791 (1998).
- F. Balbaud, *European Journal of Inorganic chemistry*, 665 (2000).
- M. Ozawa, O. Yamamura, and K. Gonda, *Journal of Nuclear Science and Technology*, **22**, 68 (2012).
- B. Raj and U. K. Mudali, *Progress in Nuclear Energy*, **48**, 283 (2006).
- M. Pourbaix, *Atlas of electrochemical equilibria in aqueous solutions*, Pergamon Press, Oxford (1966).
- A. Desestret, J. Ferriol, and G. Vallier, *Materiaux et Techniques*, **9**, 621 (1977).
- Y. Kuriki, M. Tamura, N. Yamanouchi, and K. Kiuchi, *Third International Conference on Nuclear Fuel Reprocessing and Waste Management*, xxii **1154**, 1049 (1991).
- O. V. Kasparova, Y. V. Baldokhin, and G. A. Kochetov, *Protection of Metals*, **38**, 176 (2002).
- G. Hochörtler and E. M. Horn, *Metallic corrosion*, **II**, 1447 (1981).
- B. Ghiban, S. Ciuca, I. Carceanu, N. Ghiban, and I. Nedelcu, *Metalurgia International*, **13**, 39 (2008).
- L. Y. Gurvich and A. D. Zhimov, *Protection of metals*, **31**, 231 (1995).
- T. Honda, T. Yokosuka, and Y. Arai, *Corrosion 97*, NACE (1997).
- B. Laurent, N. Gruet, B. Gwinner, F. Miserque, M. Tabarant, and K. Ogle, *Journal of the Electrochemical Society*, **164**(9), C481 (2017).
- S. Haupt and H. H. Strehblow, *Journal of Electroanalytical Chemistry*, **228**, 365 (1987).
- V. Maurice and P. Marcus, *Electrochimica Acta*, **84**, 129 (2012).
- K. Ogle, M. Mokaddem, and P. Volovitch, *Electrochimica Acta*, **55**, 913 (2010).
- V. P. Razygraev, M. V. Lebedeva, S. A. Kabakchi, E. Y. B. Ponomareva, R. S., and L. P. Lobanova, *Journal of Applied Chemistry USSR*, **61** (1988).
- D. G. Kolman, D. K. Ford, D. P. Butt, and T. O. Nelson, *Corrosion Science*, **39**, 2067 (1997).
- J. R. Myers, F. H. Beck, and M. G. Fontana, *Corrosion*, **9**(21), 277 (1965).
- K. Ogle and S. Weber, *Journal of the Electrochemical Society*, **147**, 1770 (2000).
- V. Shkirskiy, P. Keil, H. Hintze-Bruening, F. Leroux, P. Volovitch, and K. Ogle, *Electrochimica Acta*, **184**, 203 (2015).
- P. Lorbeer and W. J. Lorenz, *Corrosion Science*, **21**, 79 (1981).
- K. Ogle, J. Baeyens, J. Swiatowska, and P. Volovitch, *Electrochimica Acta*, **54**, 5163 (2010).
- F. Ruel, P. Volovitch, L. Peguet, A. Gaugain, and K. Ogle, *Corrosion*, **69**, 536 (2013).
- R. Robin, F. Miserque, and V. Spagnol, *Journal of Nuclear Materials*, **375**, 65 (2008).
- A. A. Hermas, K. Ogura, and T. Adachi, *Electrochimica Acta*, **40**, 837 (1995).
- J. S. Armijo and B. E. Wilde, *Corrosion Science*, **8**, 649 (1968).
- B. E. Wilde, *Corrosion*, **44**, 699 (1988).
- B. Ghiban and G. Cosmeleata, *Innovation stainless steel, European stainless steel conference 183* (1993).
- B. Ghiban and N. Ghiban, *Scientific Bulletin Series B: Chemistry and Materials Science*, **62**, 79 (2000).
- B. Baroux, *Passivity of Metals and Semiconductors*, Elsevier, Bombannes, France (1983) 531.
- E. Tcharkhtchi-Gillard, M. Benoit, P. Clavier, B. Gwinner, F. Miserque, and V. Vivier, *Corrosion Science*, **107**, 182 (2016).
- L. Marchetti, F. Miserque, S. Perrin, and M. Pijolat, *Surface and Interface Analysis*, **47**, 632 (2015).
- H. S. Nalwa, *Handbook of Surfaces and Interfaces of Materials*, (2001).
- Y. Lee, A. J. Bevol, and D. W. Lynch, *Surface Science*, **188**, 267 (1987).
- M. J. Guittet, J. P. Crocombette, and M. Gautier-Soyer, *Physical Review B*, **63**, 125117 (2001).
- V. Maurice, W. P. Yang, and P. Marcus, *Journal of the Electrochemical Society*, **143**(3), 1182 (1996).
- N. B. Hakiki, S. Boudin, B. Rondot, and M. Da Cunha Belo, *Corrosion Science*, **37**(11), 1809 (1995).
- W. P. Yang, D. Costa, and P. Marcus, *Journal of the Electrochemical Society*, **141**(1), 111 (1994).
- P. Marcus and J. M. Grimal, *Corrosion Science*, **33**, 805 (1992).
- V. Maurice, W. P. Yang, and P. Marcus, *Journal of the Electrochemical Society*, **145**, 909 (1998).
- R. Kirchheim, in *Modification of Passive films*, (P. Marcus, B. Baroux, and M. Keddad, eds.), *Institute of Materials*, London (1994).



## 4.4. The kinetics of transpassive dissolution chemistry of stainless steels in nitric acid: The impact of Si

### 4.4.1. On the origin of the intergranular corrosion

One of the particular consequence of the Si alloying in SS is the inhibition of the IGC when the addition in Si overcomes 1 wt. %. It has highly motivated the development of the Uranus S1N, because the IGC as a local type of corrosion was not quite desired. However since then, studies and model of the IGC have enabled to better predict the increasing of the dissolution rate due to the non-faradaic contribution of the grains removal at the surface of the steel [78].

It is though still unclear how Si can inhibit the IGC. It does exist a small range of Si addition between 0.5 and 1 wt. % where the IGC is on the contrary intensely promoted (Fig. 27) but at higher contents in Si, it totally disappears [12].

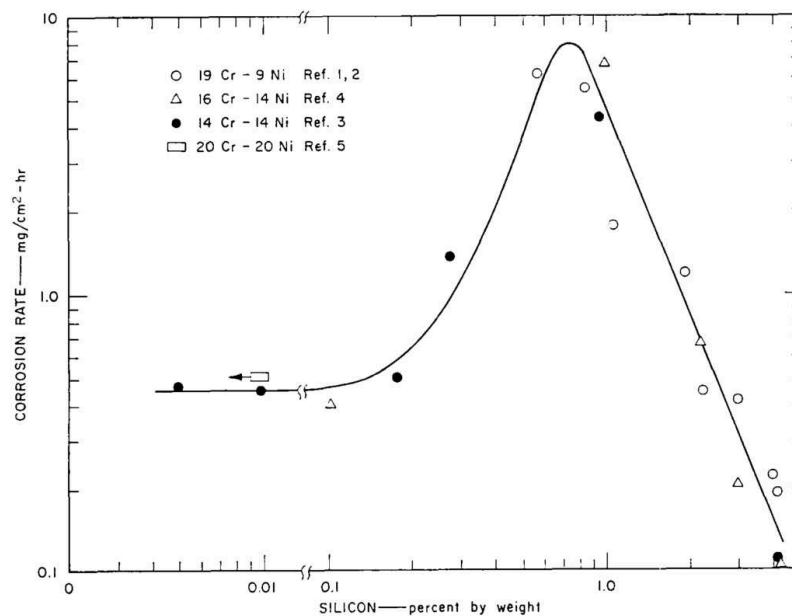


Fig. 27. Dissolution rates of several Fe-Cr-Ni alloys in boiling 5 mol dm<sup>-3</sup> HNO<sub>3</sub> as a function of Si content (Armijo et al. [11])

This maximum intensity of IGC was considered as a proof that Si was actually responsible for the inhibition or promotion of the IGC. Few attempts of measuring the reactivity or energy of the grain boundaries versus the grain faces were made but did not clearly prove the origin of the IGC. Desestret et al. [52] showed that the energy of the grain boundaries followed exactly the same trend as Fig. 27. This energy relies on local defects probably relying themselves on segregations and impurities at grain boundaries. But the nature of these segregation has never been clearly identified [79].

Another quite unexplored question in the literature is about the mechanism of the transpassivation. The loss of passivity is usually attributed to the oxidation of the trivalent Cr to the hexavalent Cr expected by the thermodynamics [80]. Cr(VI) species are then soluble and the oxide loses its protective properties causing the oxidation current to drastically increase. Studies showing that  $E_{tp}$  was independent from the Cr amount in the steel was an argument in favour of this theory [82] (Fig. 28) [11].

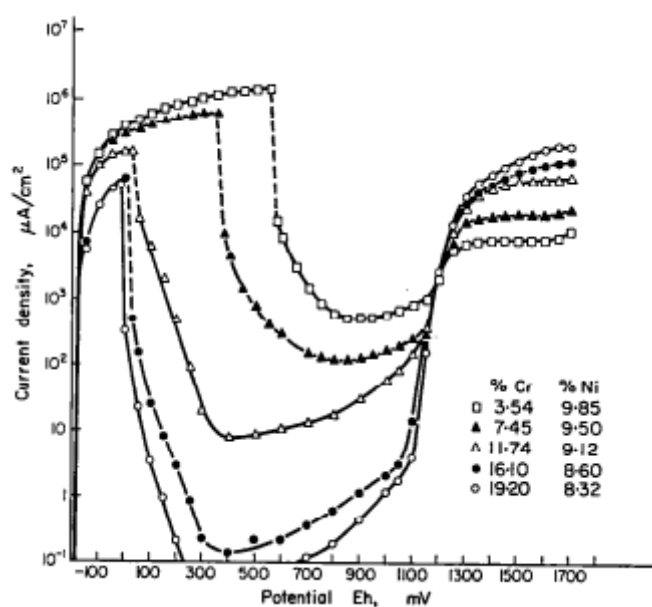


Fig. 28. I-E curves in  $2 \text{ mol dm}^{-3} \text{H}_2\text{SO}_4$  at  $90^\circ \text{C}$  for Fe-Cr-Ni alloys with variable Cr amounts [80]

It is shown in Fig. 18 that  $E_{ip}$  always reaches the value of the equilibrium for the redox couple  $Cr_2O_3/H_2CrO_4$  around 1.2 V vs. NHE [68]. Schmuki et al. [82] are of the only studies who formally identified the Cr oxidation on synthesized Fe-Cr.

#### **4.4.2. In situ analysis of the transpassive dissolution**

In a first part of the present last chapter, an experiment aiming at identifying the oxidation of each major alloying element of the steel is shown. Especially, the oxidation of Cr to its sixth valence state will be shown.

A study of the cross sections of the Uranus S1N (performed during the PhD thesis) and 304L (from original data of E. Tcharkhtchi [41]) after transpassivation enabled to compare the obtained corrosion morphologies and to analyze the chemical composition of the metal-oxide interface. An estimation of the in situ oxide-electrolyte interface is indeed delicate since at the very moment the transpassivation stops, any selective dissolution can occur changing the nature of the outermost part of the oxide layer. However, it is believed that the oxide-metal interface can keep information on the previous composition of the oxide-electrolyte interface. Associated to AESEC results, several hypothesis were formulated about the composition of this interface and compare it to what is found on the 304L SS.

In practical, it does exist two different possibilities to trigger the transpassive dissolution of SS. The first possibility consists into increasing the oxidizing power of the electrolyte by adding oxidizing species as it was done in the first chapter. However, the first chapter also showed that consequently, it will be impossible to study both SS in the same electrolyte since the 304L SS will require a lower oxidizing species concentration. This would introduce also the contribution of the reduction reaction since the dissolution would happen at the open circuit potential and thus, complicate the interpretation.



It was, therefore, chosen to use the second possibility to perform a transpassive dissolution of the SS which is by polarizing the sample. The polarization was done potentiostatically to not alter the kinetics of the dissolution. The same potential was chosen for both SS since their transpassive current densities were shown in the first chapter to almost superimpose.

#### 4.4.3. Main results

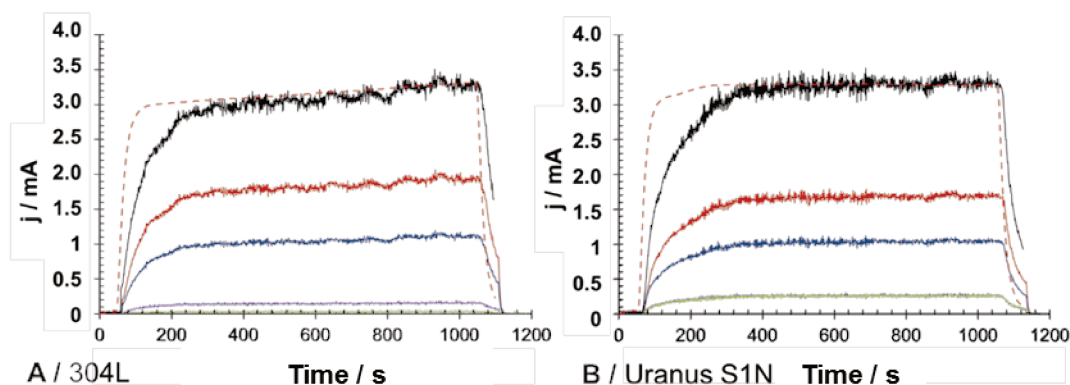


Fig. 29. Potentiostatic polarization ( $E = 0.65$  V vs. MSE) for the 304L SS in  $4 \text{ mol dm}^{-3} \text{ HNO}_3$  at  $40^\circ\text{C}$  with  $j_{\text{Fe}}$  (red),  $j_{\text{Cr}}$  (blue),  $j_{\text{Ni}}$  (purple),  $j_{\text{Z}}$  (black) et  $j_e^*$  (red dashed line)

First, a potentiostatic polarization at  $0.65$  V vs. MSE is performed on each SS in  $\text{HNO}_3$  for  $1000$  s at  $40^\circ\text{C}$ . The value of polarization was chosen to be in the transpassive domain but low enough to avoid the «  $2^{\text{nde}}$  passivity » observed in the literature at higher potentials than  $0.7$  V vs. MSE [83]. Under the effect of the potentiostatic polarization in their transpassive domain, their major alloying elements start to intensely dissolve (Fig. 29). According to the Faraday law, the dissolution rates can be translated into equivalent current. And if the right hypothesis is made on the oxidation state of each element taken into account, the total dissolution current will superimpose with the external current recorded by the potentiostat. As shown in Fig. 29, a unique combination of the oxidation states was found (Table 4). In particular, this method gives access to the direct observation of the  $\text{Cr(VI)}$  species forming during the transpassive state.

Table 4. Oxidation states obtained by correlation between  $j_e^*$  and  $j_L$  during transpassive dissolution of the 304L and Uranus S1N SS in  $4 \text{ mol dm}^{-3} \text{ HNO}_3$  at  $40^\circ\text{C}$  for 1000 s

	Fe	Cr	Ni	Si	Mn
Nombre d'oxydation	III	VI	II	IV	II

This experiment shows that the dissolution is equal in terms of oxidation states between the two SS. In the case of the 304L SS, a slight increase of the current over the experiment is observed. It is very likely to relate to the slight expand of the surface due to the preferential attack at the grain boundaries shown in Fig. 30.

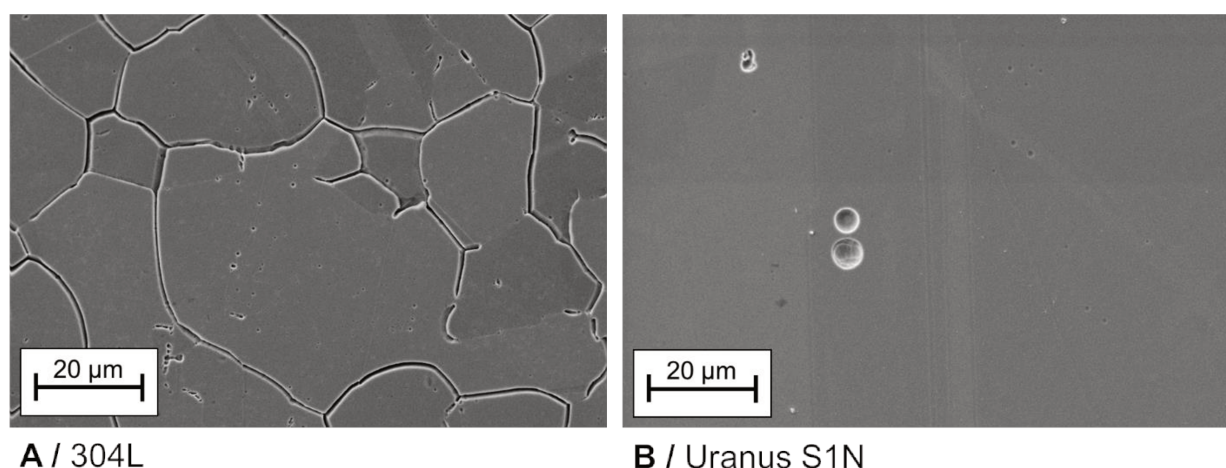


Fig. 30. SEM observation of the 304L (A) and Uranus S1N (B) SS after 1000 s transpassive polarization at  $0.65\text{V}$  vs. MSE in  $4 \text{ mol dm}^{-3} \text{ HNO}_3$  at  $40^\circ\text{C}$

Integrating the dissolution contributions in Fig. 29, it is possible to estimate a total amount of dissolved material for each SS. The 304L hence lost  $497,2 \pm 0,5 \mu\text{g}$  and the Uranus S1N lost  $508,9 \pm 0,5 \mu\text{g}$  which corresponds to a thickness decrease of  $0.64$  and  $0.70 \mu\text{m}$ . This values seems coherent with Fig. 30 since the grain boundaries are lightly attacked in the case

of the 304L SS. It can also be noticed that the thickness loss is about 200 times larger than the passive layer.

From previous observations and literature, the origin of the IGC could be directly related to heterogeneities at grain boundaries and to some extent, to a selective dissolution during the transpassive polarization [24]. It has to be mentioned that the EDX mappings, not shown in the present work, did not reveal on either of the SS, any apparent segregation at grain boundaries. But it was nevertheless decided to examine the selective character of the dissolution by investigating the very first seconds the sample are polarized into the transpassive domain. The normalized Cr dissolution rate is plotted in Fig. 31 as a function of the Fe dissolution rate.

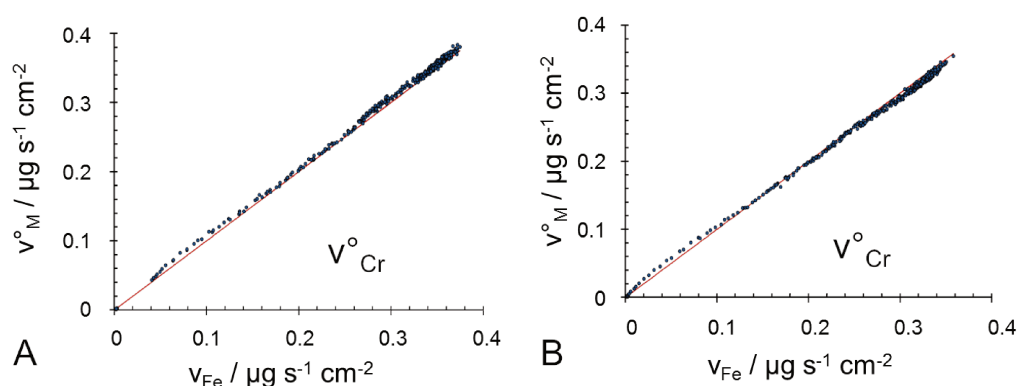


Fig. 31.  $v_{Cr}^o$  as a function of  $v_{Fe}$  for the 304L (A) and Uranus S1N (B) SS in 4 mol dm<sup>-3</sup> HNO<sub>3</sub> at 40°C over the first 100 first seconds of polarization at 0.65 V vs. MSE

First, for the two SS, the first phenomenon observed at the very beginning of the experiment is a slight excess in Cr. This excess is comparable for both SS and is related to the dissolution of the passive layer. The second phenomenon observed differs between the two SS. The 304L SS seems to display a more or less non selective dissolution, with a very tenuous preferential dissolution of Cr. On the other hand, the Uranus S1N SS showed a reproducible slight enrichment in Cr. Even if the uncertainty is elevated, the reproducibility of this result would

suggest that the interfaces of the 304L SS and the Uranus S1N SS during the transpassive dissolution may be completely different. The Uranus S1N would be covered with an oxide layer that is probably not protective since the current density is comparable to the 304L SS, but could be a homogenizer of the energy of the whole surface, preventing the preferential attack at grain boundaries.

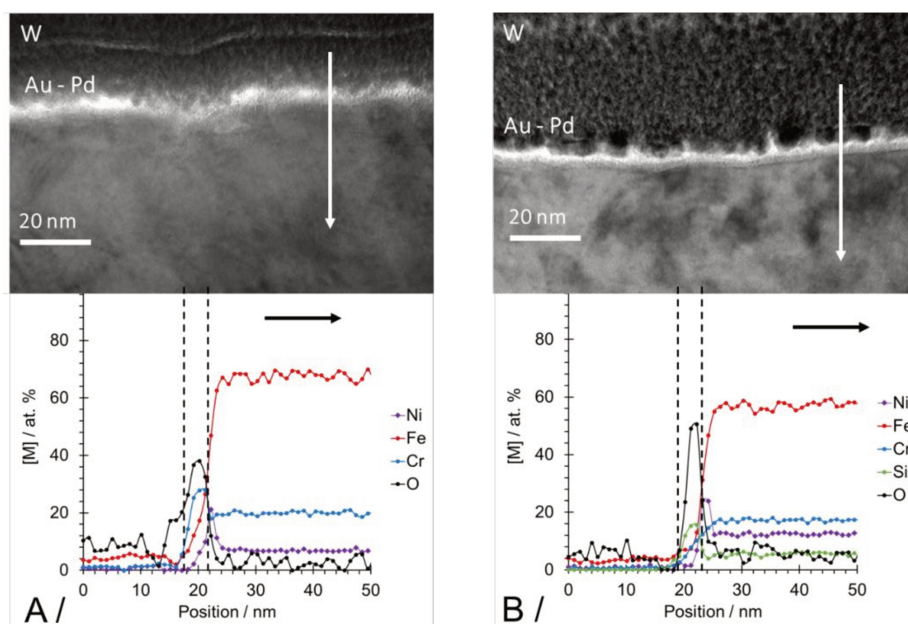


Fig. 32. TEM cross section analyses of the 304L (A) and Uranus S1N (B) SS and EDX profiles associated for a 24 hrs passivation in  $4 \text{ mol dm}^{-3} \text{ HNO}_3$  at  $100^\circ\text{C}$

Using EDX profiles, an attempt to confirm this hypothesis was made. Fig. 32 displays the passive layers of both SS in their passive initial state. Fig. 33 displays the same result after transpassive dissolution.

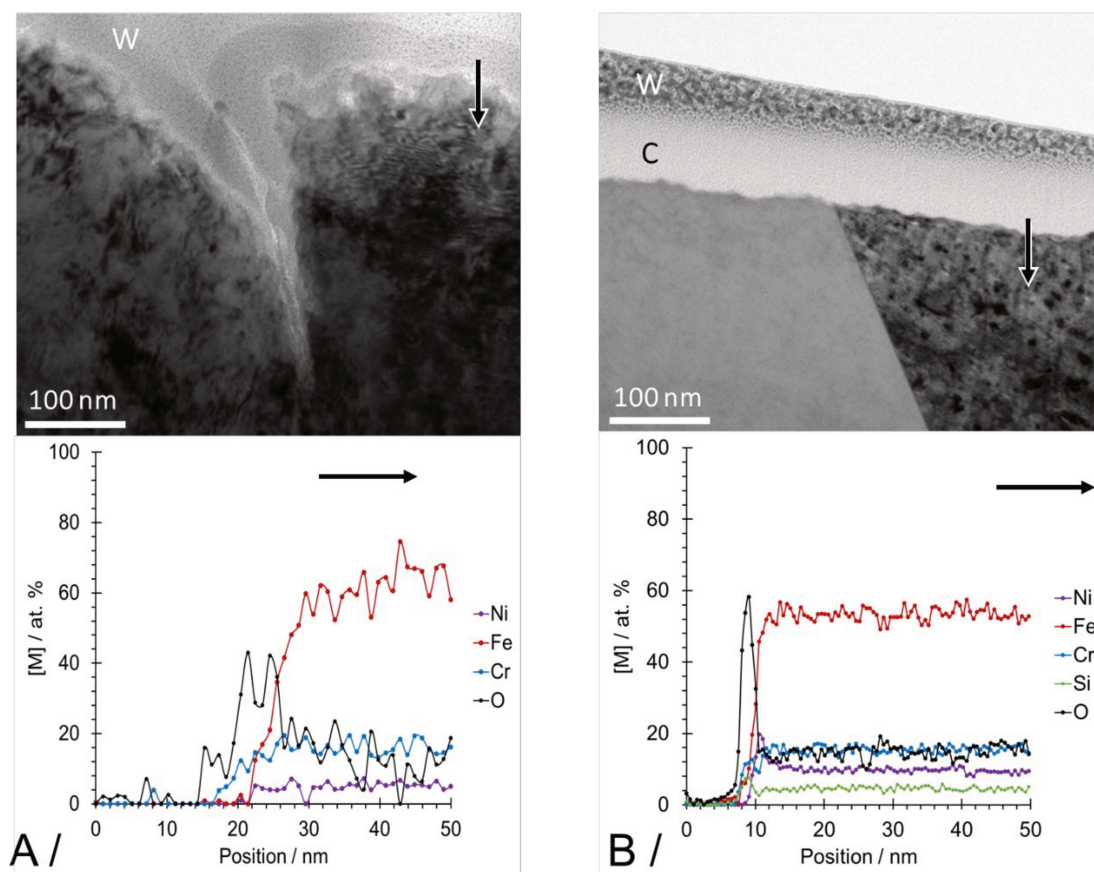


Fig. 33. TEM analyses of the 304L (A) and Uranus S1N (B) SS nearby a grain boundary and EDX analyses associated after a potentiostatic polarization at 0.65 V vs. MSE in 4 mol dm<sup>-3</sup> HNO<sub>3</sub> at 100°C for 1000 s

In the passive conditions, the EDX profile reveals a similar composition for both SS, with a Cr (or Cr-Si) rich oxide layer, and beneath this oxide layer, a relative enrichment in Ni. A priori this Ni enrichment would be related to the selective dissolution of this element, or in other words, to the presence of a Cr rich oxide layer. And the interesting result shown in Fig. 33 is that in the case of the Uranus S1N SS, the Ni enrichment is still visible after the transpassive polarization, and disappeared for the 304L SS. Although the selective dissolution is not identified by the AESEC because Ni comes with a high dispersion of the signal, this EDX result tend to prove that the Uranus S1N in situ interface is covered by a Cr rich layer, unlike the 304L SS.

The rugoses of the sample add some uncertainty to the EDX measurement shown in Fig. 33.

#### **4.4.4. Conclusion and perspectives**

New pieces of information were provided by this last chapter on the origin of the inhibition of the IGC by the Si. The AESEC firstly enabled to identify the Cr(VI) formation during the transpassive state, and that this phenomenon was exactly identical for both SS. But it also enabled to identify a tenuous selective dissolution of the Cr occurring in the passive-transpassive transients. TEM-EDX analyses then seemed to be in good agreement with the AESEC results, suggesting the existence of an oxide layer in situ that would not exist at the 304L SS surface during the transpassive polarization. It could be interesting to see if this oxide layer could to some extent protect the SS against preferential attack at grain boundaries by, for example, homogenizing the surface energy of the SS. Impedance spectroscopy associated with AESEC would be of great interest in this direction. Also, longer experiments detailed furtherly in the publication that follows and in the unachieved experiments would probably provide some more information about the evolution of the IGC for the 304L and its inhibition in the case of the Uranus S1N. Scanning electrochemical microscopy detailed in the unachieved experiments could also bring some information about the local conductivity of the interface during the transpassive polarization of the 304L SS.

#### **4.4.5. Publication - The kinetics of transpassive dissolution chemistry of stainless steels in nitric acid: The impact of Si, *Electrochimica Acta* 258, 653-661, (2017)**







# The kinetics of transpassive dissolution chemistry of stainless steels in nitric acid: The impact of Si

Barbara Laurent <sup>a, b</sup>, Nathalie Gruet <sup>b</sup>, Benoit Gwinner <sup>b</sup>, Frederic Miserque <sup>b</sup>,  
Karine Rousseau <sup>c</sup>, Kevin Ogle <sup>a, \*</sup>

<sup>a</sup> Chimie-ParisTech, PSL Research University, IRCP-CNRS, 11 rue Pierre et Marie Curie, 75005, Paris, France

<sup>b</sup> Commissariat à l'Energie Atomique, Den-Serve de la Corrosion et du Comportement des Matériaux dans leur Environnement, Université Paris-Saclay, F-91191, Gif-sur-Yvette, France

<sup>c</sup> Serma Technologies, BHT, Bâtiment 52, 7 Parvis Louis Néel, CS 20050, 38040, Grenoble, France

## ARTICLE INFO

### Article history:

Received 22 October 2017

Received in revised form

12 November 2017

Accepted 15 November 2017

Available online 16 November 2017

### Keywords:

Corrosion

Stainless steel

Intergranular

Transpassive

Spectroelectrochemistry

## ABSTRACT

Atomic emission spectroelectrochemistry was used to monitor the elemental dissolution of two stainless steels during transpassive polarization. A 304LN stainless steel (X2 CrNiN 18-10) was compared with a 3.5 wt% Si rich stainless steel (X1 CrNiSi 18-15-4) so as to elucidate the effect of Si on the dissolution mechanism. The enrichment in Si shifted the cathodic reaction to lower potentials explaining that in hot and concentrated nitric acid containing oxidizing species, 304LN SS corrodes more rapidly due to the transpassive break of passivity, while the 3.5 wt% Si SS remains passive. However, when polarized into the transpassive domain, preferential grain boundary corrosion was observed for the 304LN but not for the 3.5 wt% Si SS, despite having similar current densities. Congruent alloy dissolution was observed in the transpassive domain with the stoichiometry of Fe(III), Cr(VI) and Ni(II) yielding a faradaic yield of 100% at early times. For longer times, with the 304LN, the faradaic yield drop to 70% indicative of intergranular dissolution in which the cations released in the intergranular space were not detected by the ICP-AES. Transmission electron microscopy coupled with energy dispersive spectroscopy showed that the interface of the 3.5 wt% Si SS enriches in Cr during a polarization in the transpassive domain of the steel. No similar enrichment was detected for the 304LN.

© 2017 Elsevier Ltd. All rights reserved.

## 1. Introduction

Stainless steel may exist in at least three different states when in contact with an acidic electrolyte: the active state, the passive state, and the transpassive state. In recent work we demonstrated the use of atomic emission spectroelectrochemistry (AESEC) to follow the kinetics of dissolution of 304 LN and 3.5 wt% Si stainless steel (SS) in nitric and sulfuric acid in the active domain (cathodic to the open circuit potential) [1] and in the passive domain [2]. In the latter case, it was possible to monitor the kinetics of passive film formation and dissolution in real time. In this work, these earlier studies are extended to the transpassive domain for the same materials.

Nitric acid, HNO<sub>3</sub>, acts both as an acid and an oxidizing agent. Austenitic stainless steels (SS) 18Cr-10Ni types are usually

considered as sustainable candidates for industrial facilities performing processes that involve nitric reagent such as in nuclear retreatment cycle [3]. Such processes induce the dissolution of nuclear waste fuel and thus may involve a high concentration of various oxidizing species in the electrolyte which enhance the oxidizing nature of HNO<sub>3</sub>. The steady state potential of this hot and concentrated electrolyte with oxidizing species can reach very high values, and this implies a particular attention for the material choice. Even stainless steels may undergo severe dissolution rates and sometimes dissolve more rapidly at grain boundaries than at grain faces. This type of dissolution is obviously undesirable for the facilities to resist ageing. This localized type of corrosion, observed mainly when passivity breaks down at high potentials (transpassive domain of the steel), leads to grain removal at the surface which increases the exposed surface area. The grain removal adds a non-faradaic contribution to the mass loss of the material that is obviously an undesirable phenomenon. This motivated the optimization of stainless steels.

\* Corresponding author.

E-mail address: [kevin.ogle@chimie-paristech.fr](mailto:kevin.ogle@chimie-paristech.fr) (K. Ogle).



By the middle of the 20th century, it was shown that silicon enrichment over 1 wt % of a 18Cr–10Ni type SS (such as the 304LN SS) lowered the dissolution rate of the steel in nitric acid containing oxidizing species [4] and suppressed intergranular corrosion usually observed at the 304LN SS surface [2,5]. The Si rich 3.5 wt% Si SS was formulated and adopted for these environments based on a high number of mass loss measurements and morphological observations in various conditions [4–12]. However, electrochemical parameters were only taken into account by a few authors [13–15]. These authors showed [13–15] that in many HNO<sub>3</sub> electrolytes with or without oxidizing species, the Si enrichment lowered the corrosion potential, and as a result, in the same environment, 304LN SS was shifted to its transpassive domain, whereas the 3.5 wt% Si SS remained passive. This easily explained why mass loss measurements revealed a drastic difference between the 304LN SS and the 3.5 wt% Si SS in sufficiently oxidizing conditions. However, the absence of intergranular attack in the transpassive domain of the 3.5 wt% Si- SS remained unclear.

Several authors attempted to explain why intergranular corrosion was suppressed when Si was added [4,13,16–18]. Firstly, it was thought that a potential difference between grain faces and grain boundaries might be at the origin of the phenomenon, based on the high level of intergranular corrosion observed with a moderate Si enrichment (between 0.5 and 1 wt %). Possible galvanic effects resulting from this potential difference could explain the preferential attack of the grain boundaries, and this model could be adapted to higher or lower concentrations in Si. It was proposed by Desestret et al. [19] that the potential gradients were due to Si segregation at grain boundaries, that was expected to be very important between 0.5 and 1 wt %, then much lower above 1 wt % as for the 3.5 wt% Si SS. Armijo et al. [13] tended to support this hypothesis by measuring separately anodic currents of grain faces and grain boundaries for a Si enrichment of 0.95 wt %, however, neither of these authors were able to identify the Si segregation of these alloys at grain boundaries. Moreover, Armijo et al. [13] identified potential gradients for the lowest concentrations in Si without observing intergranular corrosion. Even though Desestret [19] highlighted an accurate correlation between grain boundaries energy and intergranular attack depending on Si enrichment, the specific origin of Si impact on the transpassive dissolution mechanism of SS remains unclear.

Therefore, there is considerable interest in understanding the transpassive dissolution behavior. The first aim of this work is to identify the impact of Si on the chemical aspects of the transpassive dissolution through the use of the atomic emission spectroelectrochemistry (AESEC). The methodology provides a very simple way to identify the oxidation states of the alloying elements when transpassive dissolution occurs, and thus propose a chemical dissolution mechanism. The second aim is to formulate an accurate explanation of the origin of intergranular attack inhibition by Si using transmission electron microscopy (TEM) coupled with energy dispersive X-ray spectroscopy (X-EDS) to compare metallurgical aspects of the 304LN and the 3.5 wt% Si SS grain boundaries and their respective surface morphology in the conditions of transpassive dissolution.

## 2. Experimental

### 2.1. Materials

3.5 wt% Si SS (X1 CrNiSi 18–15–4; DIN 1.4361) and 304LN (X2 CrNiN 18–10; DIN 1.4311) rolled stainless steel, quenched and annealed were used in the present work. The elemental analysis of the steels was performed by glow discharge optical emission spectroscopy (GD-OES) using a GD-Profilier from Horiba Jobin-Yvon.

**Table 1**

Mass composition of 3.5 wt% Si and 304LN SS determined by GD-OES profiles performed on samples and averaged between 10  $\mu$ m 40  $\mu$ m depth expressed in wt.%.

Abbreviation	European Norm	DIN W-Nr	Fe	Cr	Ni	Si	Mn	Add.
3.5 wt% Si SS	X1 CrNiSi 18–15–4	1.4361	59.8	18.8	15.1	3.5	2.0	0.8
304 LN	X2 CrNiN 18–10	1.4311	70.3	17.8	9.5	0.3	1.5	0.6

From the signals given by the GD-OES, the bulk of the sample was reached at 40  $\mu$ m depth and the composition of the steel was averaged over two craters on different samples. This analysis is given in Table 1.

Conventional electrochemical measurements were performed with bullet shaped samples of 2 cm<sup>2</sup>, unpolished, and cleaned with ethanol and acetone in an ultrasonic bath. AESEC experiments were performed using rectangular sheets of 20 mm  $\times$  20 mm  $\times$  1 mm samples. Prior to analysis, these samples were cleaned with ethanol and acetone in an ultrasonic bath, then polished to 0.03  $\mu$ m diamond finish. Polishing ensured good sealing in the AESEC flow cell and allowed *ex situ* surface analysis of the sample as required.

The 304LN SS alloy was chosen as a reference material for this work because its composition is the closest to the 3.5 wt% Si in the range of materials used in the nuclear retreatment facilities containing hot and concentrated acids. The impact of Ni concentration in the composition of the steel on the transpassive current density is usually considered to be insignificant, Ni serving to stabilize the austenitic phase without affecting the corrosion resistance [20].

Deionized water (18.2 M $\Omega$  cm) was prepared with a Millipore<sup>TM</sup> system and used for all electrolytes. Nitric acid 68% (Sigma Aldrich) was used to prepare the solutions. All glassware was protected with a paraffin film to avoid any hazardous contamination.

### 2.2. Conventional electrochemical measurements

Spontaneous passivation of samples for transmission electron microscopy (TEM) and X-ray energy dispersive spectroscopy (X-EDS) was performed at 100 °C (373 K) in a 0.2 dm<sup>−3</sup> jacketed reactor using similar recirculating oil system connected to a thermocryostat (Lauda). Conventional electrochemical measurements were performed at 100 °C in the same type of reactor. Samples were used as working electrodes (3.5 wt% SS or 304LN SS), counter electrode was made of a platinum grid, and reference electrode was a mercury-mercurous sulphate electrode (MSE) provided by Radiometer ( $E = +0.65$  V vs NHE in saturated K<sub>2</sub>SO<sub>4</sub>). A Biologic VSP potentiostat functioning in the potentiodynamic linear polarization mode at 0.2 mV s<sup>−1</sup> scan rate with the associated EC-Lab software V10.37 were used. This scan rate was chosen to be as close as possible to quasi-stationary conditions and perform experiments in a reasonable amount of time. Polarization was performed in two distinct measurements. The first measurement was started 30 mV above OCP and followed a cathodic sweep direction down to −0.45 V vs. MSE. The second measurement was started after 24 h OCP. It was started 30 mV below OCP and followed an anodic sweep up to +0.55 V vs. MSE. During the OCP period between the two measurements, the potential of the sample usually reached almost perfectly its initial value prior to the first scan.

### 2.3. AESEC measurements

The AESEC flow cell has been described in detail previously [21,22]. The flow cell consisted of a small volume working electrode compartment (approximately 0.2 cm<sup>3</sup>) with electrolyte input at the bottom and output at the top. The flow rate was measured accurately (1% precision) for each experiment and nominally

$3 \text{ cm}^3 \text{ min}^{-1}$ . Counter and reference electrodes were in a larger compartment separated from the working electrode by a porous membrane to allow passage of electrical current but avoid bulk mixing of the two solutions. An analysis of the solution contained in the second compartment ensured that a negligible quantity of metallic ions passed through the membrane. The working electrode was the stainless steel specimen. A  $1.0 \text{ cm}^2$  surface was exposed to the electrolyte defined by an o-ring. The counter electrode was a Pt grid and the reference electrode was a Hg/Hg<sub>2</sub>SO<sub>4</sub> electrode (MSE,  $E = +0.65 \text{ V}$  vs. NHE in saturated K<sub>2</sub>SO<sub>4</sub>). A Gamry Reference 600™ potentiostat functioning in the potentiostatic mode was used to control the potential and measure the electrochemical current density,  $j_e$ . Polarization curves were performed at a temperature of  $28^\circ \text{C}$  ( $301 \text{ K}$ ) using a recirculating water system connected to a thermocryostat (Lauda) constant temperature bath. Polarization curves were performed at a scan rate of  $0.2 \text{ mV s}^{-1}$  in the anodic direction using the flow cell for both stainless steel specimens. Potentiostatic polarizations were then performed at  $40^\circ \text{C}$  ( $313 \text{ K}$ ).

The experimental set-up including data acquisition has also been described in detail by Ogle et al. [21]. In summary, the working electrode releases ions into the electrolyte in the flow cell which is then continuously fed into the plasma of the ICP-AES where the emission intensities of the different ions are measured simultaneously. The analog outputs of the potentiostat were fed into the A/D converter and data acquisition software of the ICP-AES spectrometer so that the ICP-AES intensity data and the electrochemical data were on exactly the same time scale. These emission intensities are converted into concentration using standard ICP-AES calibration techniques. Electrolyte transport was maintained using a peristaltic pump. The input to the plasma uses a concentric glass nebulizer and a cyclonic spray chamber. The ICP-AES used in this work was an Ultima 2C™ from Horiba Jobin-Yvon consisting of a 40.68 MHz inductively coupled Ar plasma, operating at 1 kW and interfaced to independent polychromator and monochromator optical modules. A 50 cm focal length Paschen-Runge polychromator was used equipped with an array of photomultiplier tube detectors at given wavelengths allowing the measurement of up to 50 preselected elements simultaneously. Emission wavelengths were chosen for maximum sensitivity and low interferences. The monochromator (1 m focal length) with a Czerny–Turner configuration was dedicated for high spectral resolution of a single element. In the present work, the monochromator was used to monitor the Cr signal. Wavelengths used for each element and corresponding detection limits are given in Table 2.

#### 2.4. AESEC data treatment

For each element M, instantaneous dissolution rate  $v_M$  and current  $j_M$  were calculated from the instantaneous elemental concentration  $C_M$  [21]:

$$v_M = f \frac{C_M}{A} \quad (1)$$

**Table 2**

Wavelengths used for each major element of the two stainless steels, corresponding detection limits associated (averaged over 10 experiments).

	Fe	Cr	Ni	Si	Mn
Wavelength/nm	259.940	283.563	231.604	251.611	257.610
Detection limit $C_{3\sigma}/\mu\text{g dm}^{-3}$	4.1	5.3	27.3	30	0.8
Detection limit, equivalent current density/ $\mu\text{A cm}^{-2}$	0.7	2.9	4.4	20.0	0.1

$$j_M = F \frac{v_M z_M}{M_M} \quad (2)$$

where  $f$  is the flow rate of the electrolyte,  $A$  is the surface area,  $F$  the Faraday constant,  $z_M$  is the oxidation state of the element M and  $M_M$  its molar weight. Total dissolution current  $j_\Sigma$  can be defined as the sum of major elements dissolution currents:

$$j_\Sigma = \sum j_M \quad (3)$$

And  $j_\Sigma$  will be compared to electrical current  $j_e^*$  which is obtained by convoluting the electrical current measured by the potentiostat,  $j_e$ , using an experimental transfer function  $h(t)$ , where  $h(t)$  represents the distribution of residence times in the flow cell [21]. Complex physical processes contribute to the broadening of  $h(t)$ . These processes include diffusion from the surface into the flowing electrolyte stream, mixing in the channel flow cell, spreading out during the laminar flow in the capillaries between the cell and the spectrometer, and the complicated nebulization system itself. Despite this complexity, an empirical function was simulated in the form of a log-normal distribution after an experimental measurement [21,22]. A short pulse (10 mV during 0.5 s) was applied to a copper electrode in a  $2 \text{ mol dm}^{-3}$  deaerated HCl electrolyte under the same hydraulic conditions (length of tube, flow rate) as in the present experiments. This convolution treatment is necessary to compare electrochemical current with elementary equivalent currents that are estimated from the elementary concentration transients in solution. The convolution integral is:

$$j_e^*(t) = \int_0^t j_e(\tau) h(t - \tau) d\tau \quad (4)$$

The detection limits  $3\sigma$  are calculated as following:

$$C_{3\sigma} = 3 \frac{\sigma_{\text{blank}}}{\alpha} \quad (5)$$

where  $\sigma_{\text{blank}}$  is standard deviation of the background and  $\alpha$  the sensitivity factor calculated from the calibration curves of each element at their specific wavelength.

The AESEC technique reveals whether or not a dissolution reaction is congruent or incongruent by comparing the composition of the electrolyte with that of the bulk metal. To this end the dissolution rate of an element, M, may be normalized to the bulk composition of the alloy:

$$v_M^o = (X_{\text{Fe}}/X_M) v_M \quad (6)$$

where  $X_M$  is the mass fraction of element M as determined by GDOES bulk analysis. In this way,  $v_M^o$ . For perfectly congruent dissolution,  $v_M^o = v_{\text{Fe}}$  while  $v_M^o > v_{\text{Fe}}$  implies an excess of M is dissolving and  $v_M^o < v_{\text{Fe}}$  implies that M is building up on the surface.

#### 2.5. Transmission electron microscopy (TEM) and X-ray energy dispersive spectroscopy (X-EDS)

Cross-sections of materials were analyzed using transmission electron microscopy (TEM) in high resolution imaging mode. These studies were performed by Serma Technologies (France). In order to identify zones of interest on each sample, electron backscattered diffraction (EBSD) was performed at the surface of the materials prior to sample cross-section elaboration, using a scanning electron microscope field emission gun Gemini 500 (ZEISS) scanning electron microscope (SEM), a Hikari Super charge coupled device (CCD)

camera, and OIM<sup>TM</sup> data collection and OIM<sup>TM</sup> analysis software for the acquisition and treatment of the data. Cross-section TEM lamellas were thinned using focused ion beam (FIB) FEI<sup>TM</sup> Strata DB400 and analyzed with a FEI<sup>TM</sup> Tecnai Osiris TEM using an accelerating voltage of 200 kV and equipped with ChemiSTEM<sup>TM</sup> and GIF Quantum<sup>®</sup> detectors X-ray energy dispersive spectroscopy (X-EDS).

### 3. Results and discussion

#### 3.1. Preliminary results

Polarization curves of both steels were obtained in HNO<sub>3</sub> at 100 °C, the temperature of interest for the nuclear recycling industry, in a conventional electrochemical cell of 0.2 dm<sup>3</sup> (Fig. 1A) and in the AESEC flow cell at 28 °C in the AESEC flow cell (Fig. 1B). The anodic current is markedly reduced and less dependent on potential at 28 °C while the cathodic current is enhanced. The  $j = 0$  potential in the cathodic direction by approximately 100 mV.

Passivity breakdown at high potentials can be qualified by a transpassive potential,  $E_{tp}$ , identified at the intersection between the passive domain slope and the transpassive domain slope on a semi-log scale. For the present work, the uncertainty associated with  $E_{tp}$  was about  $\pm 20$  mV. Fig. 1 demonstrates that both steels in the two different sets of parameters display the same  $E_{tp}$ , within experimental error. At 100 °C  $E_{tp}$  was measured at  $0.45 \pm 0.02$  V vs. MSE, and at 28 °C it was measured at  $0.55 \pm 0.02$  V vs. MSE. This suggests that the 4 wt% Si does not affect the potential of the transpassive transition. Current densities observed at higher potentials than  $E_{tp}$  are very similar for both steels, although a slightly more intense current can be noticed for the 3.5 wt% Si SS, and the difference lowers as temperature increases. Therefore, as the AESEC flow cell admits a moderate heating of the sample and electrolyte, an intermediate temperature of 40 °C was chosen for all measurements performed with AESEC in the present work.

An applied potential  $E_0$  of 0.65 V vs. MSE was considered as relevant for the present work. Even though Fig. 1-A ends just before this value, extrapolation of the linear current density vs. potential shows that  $j_e$  will approach or exceed  $100 \text{ mA cm}^{-2}$  at 100 °C. Fig. 1-B estimates  $j_e$  at or below  $1 \text{ mA cm}^{-2}$  at 28 °C. Therefore, at 40 °C, a current density of several mA will be expected. In addition, a second passivity is sometimes observed at higher potentials than 0.7 V vs. MSE in sulfuric media for various Fe/Cr alloys [23,24].

#### 3.2. Determination of the chemical states of dissolution during transpassive polarization

The transpassive transition is usually associated with the oxidation of Cr(III) to Cr(VI), the latter being soluble in acidic media [24]. This transition may be predicted from equilibrium considerations of Cr [25] but Cr(VI) has rarely been experimentally identified. It is very likely that the same species were detected in previous work in H<sub>2</sub>SO<sub>4</sub> [26]. Schmuki et al. [27] used X-ray absorption near edge spectroscopy (XANES) to clarify the oxidation mechanism of Cr<sub>2</sub>O<sub>3</sub> in 1 mol dm<sup>−3</sup> H<sub>2</sub>SO<sub>4</sub> for a sputter-deposited mixed Cr<sub>2</sub>O<sub>3</sub>/Fe<sub>2</sub>O<sub>3</sub> oxide. Bojinov et al. [24] used ring-disk electrodes to detect Cr(VI) in H<sub>2</sub>SO<sub>4</sub>. In the present work, we used the correlation between the external convoluted current  $j_e^*$  recorded by the potentiostat and the total dissolution current,  $j_s$ , comprising dissolution currents of Fe, Cr, Ni, Si and Mn (Eq. (3), Mn not included because of the very low scale) to identify the oxidation state of the major elements in the 304LN and 3.5 wt% Si SS. As mentioned in the experimental section, a dissolution rate is measured for each major element of the material, and this dissolution rate can be converted into a current if the oxidation state,  $z_M$ , of the element is known, following Faraday's law (Eq. (2)). According to our results, an accurate correlation between  $j_e^*$  and  $j_s$  is found for a single combination of  $z_M$  values that are as ascertained in Table 3.

Furthermore, it can be concluded that Si does not affect the oxidation states of transpassive dissolution, since  $z_M$  are exactly the same for both materials.

#### 3.3. The role of Si in the inhibition of intergranular corrosion

In previous work, it was verified using X-ray photoelectron spectroscopy that a high Si enrichment at the 3.5 wt% Si SS surface was present in various acidic electrolytes [1]. This was a major difference between both materials that motivated an investigation for the consequences of the presence of Si on the intergranular attack of SS. These consequences could be either direct, for example if a Si enrichment is still present during the transpassive dissolution of the 3.5 wt% Si SS, or indirect, if Si modifies the behavior of the other alloying elements of the steel.

The 304LN SS and 3.5 wt% Si SS surfaces were observed after 1000 s polarization displayed in Fig. 2A and B respectively, with the corresponding SEM micrographs, shown in Fig. 3. The 1000 s polarization was performed in the AESEC flow cell in 4 mol dm<sup>−3</sup> 40 °C HNO<sub>3</sub> at 0.65 V vs. MSE. The 304LN SS clearly started to dissolve more rapidly at grain boundaries while the 3.5 wt% Si gave a relatively homogeneous dissolution. A few pits were observed in Fig. 3 but not on all samples tested. Using Faraday's law and results

**Table 3**

Oxidation states found by correlation between  $j_e^*$  and  $j_s$  during transpassive polarization of the 3.5 wt% Si and the 304LN SS in HNO<sub>3</sub> 4 mol dm<sup>−3</sup> at 40 °C.

	Fe	Cr	Ni	Si	Mn
Oxidation state	III	VI	II	IV	II

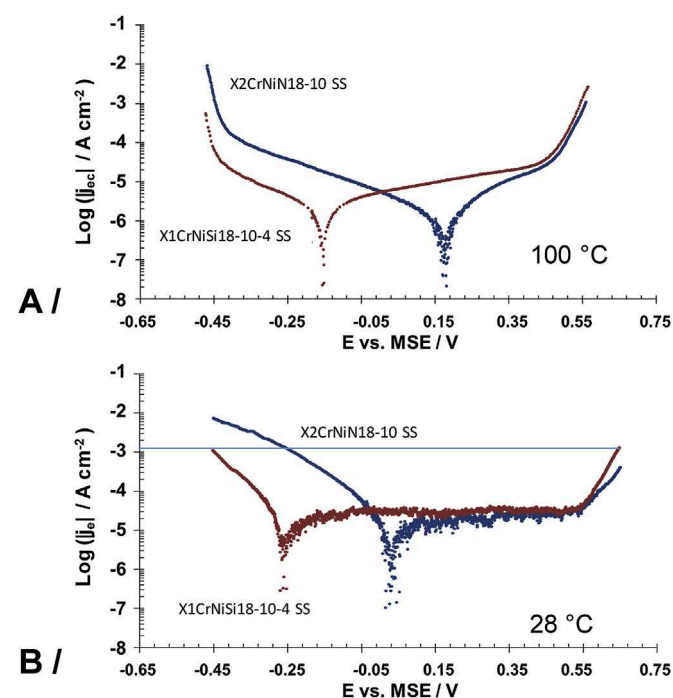


**Fig. 1.** Linear sweep voltammetry performed on 304LN and 3.5 wt% Si SS in 4 mol dm<sup>−3</sup> HNO<sub>3</sub> at 0.2 mV s<sup>−1</sup> for (A) T = 100 °C (conventional electrochemical cell) and (B) T = 28 °C (AESEC flow cell).

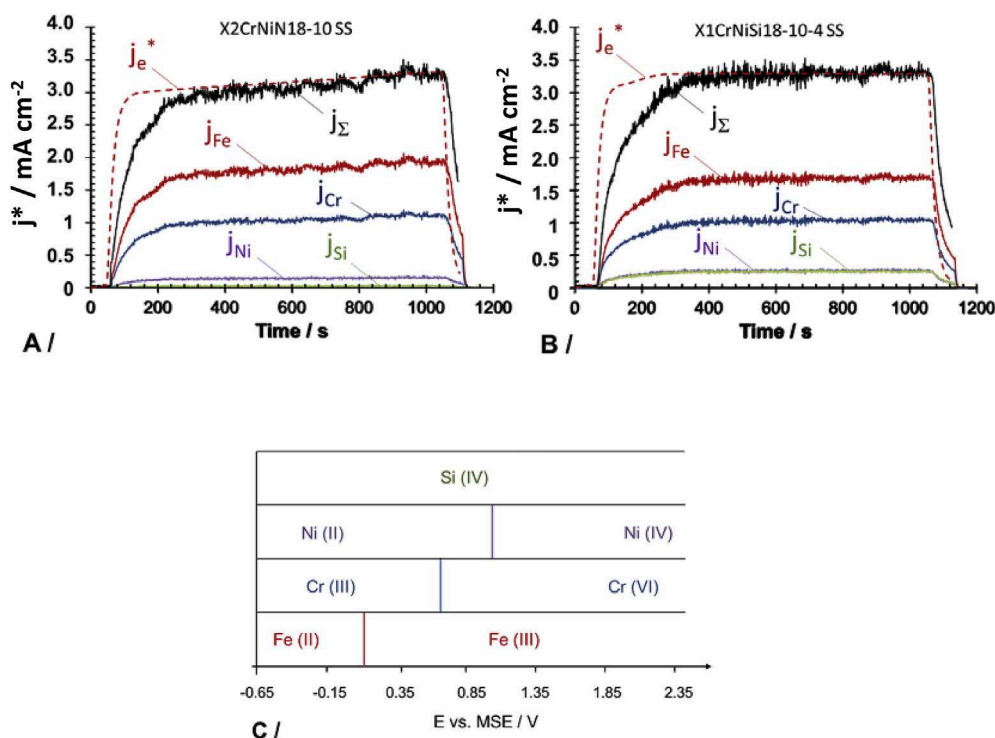


**Fig. 2.** 1000 s potentiostatic polarization at 0.65 V vs. MSE of 304LN (A) and 3.5 wt% Si (B) SS in 4 mol dm<sup>-3</sup> HNO<sub>3</sub>, pH = -0.80, at T = 40 °C.  $j_M$  (M = Fe, Cr, Ni, Si) elemental current contributions,  $j_\Sigma = \Sigma j_M$ ,  $j_e^*$  convoluted external current. (C) Oxidation states of major alloying elements between -0.65 and 2.35 V vs. MSE [34].

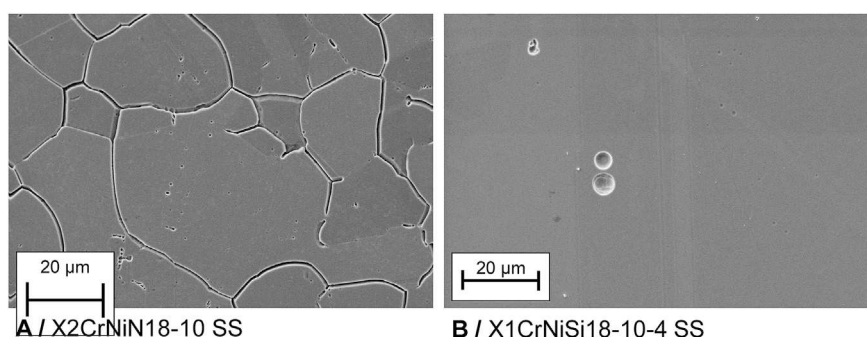


**Fig. 3.** Surface observation with SEM of 304LN (A) and 3.5 wt% Si (B) SS after 1000 s polarization at E = 0.65 V vs. MSE in 4 mol dm<sup>-3</sup> HNO<sub>3</sub> at T = 40 °C.

obtained with the AESEC, the mass of alloying elements dissolved was found to be nearly identical for the two alloys,  $497.2 \pm 0.5 \mu\text{g cm}^{-2}$  for the 304LN SS and  $508.9 \pm 0.5 \mu\text{g cm}^{-2}$  for the 3.5 wt % Si SS. Based on mass volumes of each element and using a total area of 1 cm<sup>2</sup>, this leads to a thickness decrease of about 0.64 μm for the 304LN SS and 0.70 μm for the 3.5 wt% Si SS. This is qualitatively consistent with the SEM observation of the 304LN SS whose grains are only lightly attacked. Nevertheless, as compared to the SS passive film of only few nanometers, the total dissolution is significant and this emphasizes the impact of Si on preventing a preferential dissolution of the grain boundaries. Armijo et al. [13] proved in the case of a 14Cr-14Ni-0.95Si that the current density of the grain boundaries in the passive range of potential could be ten times more important than for grain faces. It was shown in the same work and also for other alloys, such as 16Cr-14Ni or 19Cr-14Ni [9,28,29], that an alloy containing 0.95 wt % of Si displayed the most severe intergranular sensitivity. Nevertheless, this observation suggests that the origin of the intergranular corrosion could be related to the chemistry of the grain boundaries, the depletion of Cr

at grain boundaries due to the segregation of alloying elements such as Si being the most common hypothesis [29]. However, it has to be mentioned that X-EDS mappings in the transverse direction to grain boundaries for 304LN SS and 3.5 wt% Si SS of the present work (not shown here) revealed no significant segregation at grain boundaries for Si, Cu and Co, no other elements, e.g. P, N or Mo, were detected.

The results of Fig. 2 may be used to measure the degree of selectivity during transpassive dissolution of stainless steels in HNO<sub>3</sub>, giving information on the interface composition of SS during the transpassive dissolution. Before the experiment, open circuit potentials of the two alloys were found to be respectively 0.35 (A) and 0.32 (B) V vs. MSE which was in the passive domain of the alloys. The interface of both materials in this region of potential is known to be Cr enriched [30] which was confirmed by X-EDS analysis performed on the TEM cross sections of the 304LN SS and the 3.5 wt% Si SS, displayed in Fig. 4. A significant Ni enrichment appears in Fig. 4 below the passive layer. This enrichment results from the selective dissolution of Fe, Cr and Si [18]. However, it is



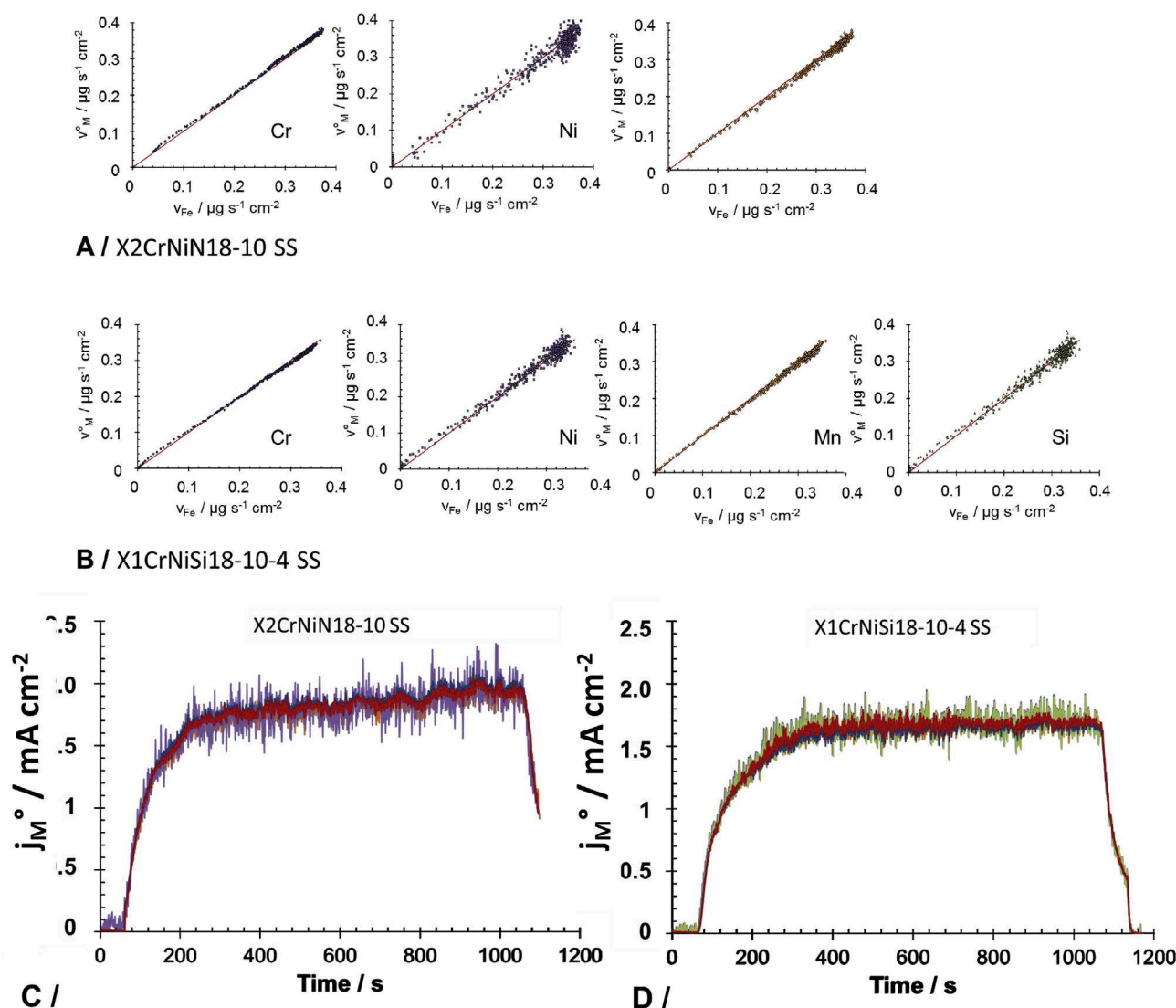


**Fig. 4.**  $j_M^0$  multiplied by their faradaic ratios on Fe for 304LN: (A) and 3.5 wt% Si (B) SS in 4 mol dm<sup>-3</sup> HNO<sub>3</sub> at T = 40 °C as a function of  $j_{Fe}$  over 500 first seconds of polarization at E = 0.65 V vs. MSE. (C/D) Same signals plotted as a function of time.

clear from Fig. 5 that  $v_{Ni}^0$  displays a poor signal to noise ratio that precludes detecting selective dissolution.

An investigation of congruent vs. incongruent dissolution for the major alloying elements, M, is displayed in Fig. 5. Shown are the  $v_M^0$  values as a function of  $j_{Fe}$  over the 500 first seconds of transpassive polarization for 304LN SS (A) and 3.5 wt% Si (B).

As mentioned before, during the passive-transpassive transition, the insoluble Cr(III) contained in the oxide layer is expected to oxidize into a soluble form of Cr(VI) [27]. This explains why for both materials, at the very beginning of the experiment, a slight excess of Cr versus Fe is detected (Fig. 5). Ni and Mn are expected to dissolve as Mn(II) and Ni(II) and no transition to a higher level of oxidation is expected over this potential range [31]. Their dissolution appears as non-selective with respect to Fe. Eventually, the scattering in the measurement of Si, comparable to Ni, makes it difficult to conclude as to whether or not there is selective dissolution of this element. Between  $v_{Fe} = 0.2$  and  $0.4 \mu\text{g s}^{-1} \text{cm}^{-2}$ , in the 50 s before the dissolution reaches its steady rate, a non-selective dissolution of Cr can be seen for the 304LN SS whereas a slight transitional inflexion is shown for the 3.5 wt% Si SS. Despite the high dispersion of points observed between 1 and 2 mA cm<sup>-2</sup>, the experiment was repeated

a second time, leading to the same tendency. It is possible that Si inhibits the oxidation of Cr during the passive-transpassive transition, leading to the presence of an *in situ* Cr(VI)-rich oxide layer.

Moreover, after the transpassive dissolution, a Ni enrichment was detected below the oxide layer for the 3.5 wt% Si SS by the X-EDS results (over 5 profiles for each SS) (Fig. 6B) and was undetectable for the X2CrNiSi18-10 SS (Fig. 6A). This enrichment could result from the selective dissolution of the elements at the surface, consistent with what is indicated by the AESEC measurements (Fig. 5), indicating the presence of an *in situ* oxide layer. It is widely agreed that a Cr(III) oxide is present in the passive film in the transpassive domain [31,32] based on *ex situ* measurements. A Cr-rich oxide layer is indeed observed for both SS in Fig. 6. But this result should be considered with precaution since *ex situ* analysis could be biased by an *a posteriori* oxidation of the surface.

It is still unclear how this Cr-rich interface could prevent the 3.5 wt% Si SS from being attacked preferentially at grain boundaries, unlike the 304LN SS. It could be the result of this specific interface homogenizing the surface energy as suggested by Froment [33] or Desestret [19].

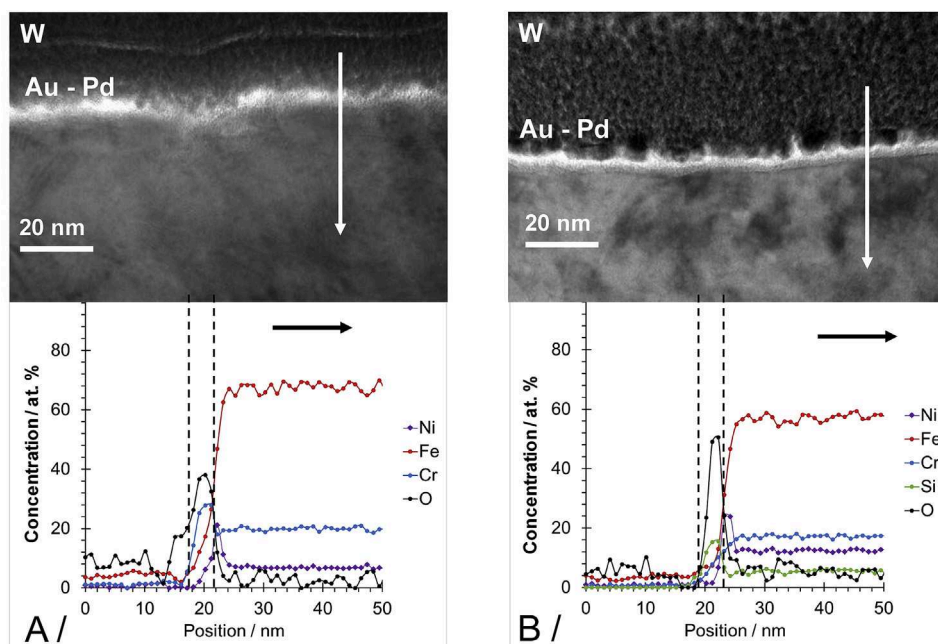


**Fig. 5.** Cross sections 304LN (A) and 3.5 wt% Si (B) SS in 4 mol dm<sup>-3</sup> for passive layers established in 4 mol dm<sup>-3</sup> HNO<sub>3</sub> at T = 100 °C for 24 hr observed using TEM and analyzed by X-EDS.

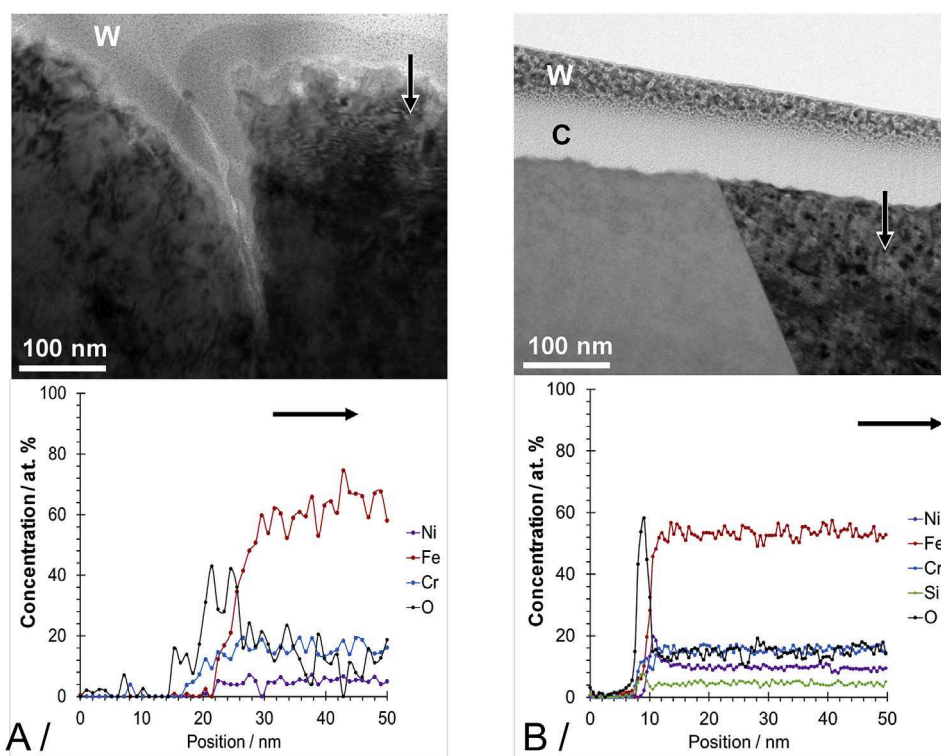


**Fig. 6.** Cross sections of grain boundary region observed by TEM and analyzed by X-EDS: (A) 304LN SS after 500 s polarization at E = 0.60 V vs. MSE in 4 mol dm<sup>-3</sup> HNO<sub>3</sub> at T = 100 °C and (B) 3.5 wt% Si SS after 1000 s polarization at E = 0.65 V vs. MSE in 4 mol dm<sup>-3</sup> HNO<sub>3</sub> at T = 100 °C.

### 3.4. Long term transpassive dissolution

AESEC was used to observe the transpassive dissolution of both 304LN SS and 3.5 wt% Si SS after several hours of polarization (Figs. 7 and 8). The polarization was continuous and the dissolution was recorded with the AESEC in the first and last 20 mins of

experiments. The spectrometer was calibrated separately for each measurement. During the 5 h of experiments, the electrolyte was kept flowing in the cell at 40 °C.

Comparison between short and long term exposure for the transpassive dissolution of 3.5 wt% Si SS is shown in Fig. 7 along with the associated surface structure observed with SEM.

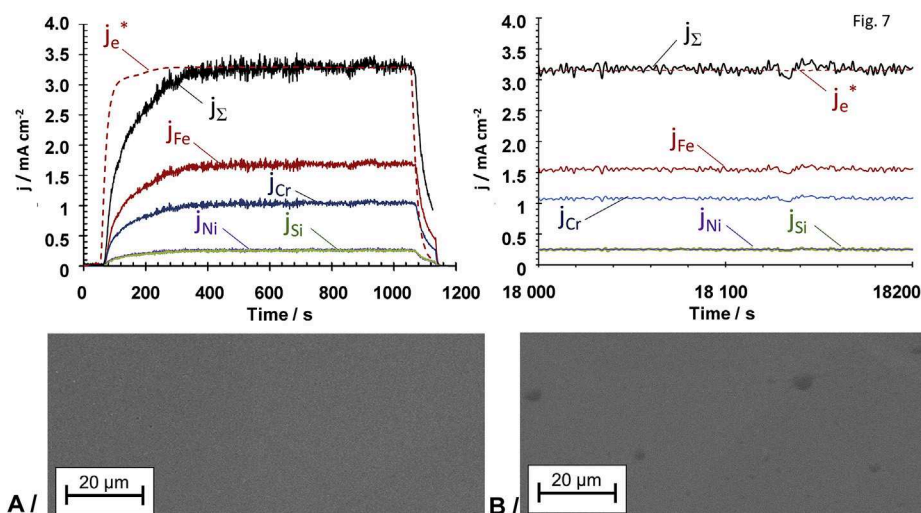


**Fig. 7.** Potentiostatic polarization at 0.65 V vs. MSE of 304LN SS in 4 mol dm<sup>-3</sup> HNO<sub>3</sub> at T = 40 °C.  $j_M$  (M = Fe, Cr, Ni, Si) elemental current contributions,  $j_\Sigma = \sum j_M$ ,  $j_e^*$  convoluted external current. Respective surface observations with SEM at  $t_0$  to  $t_0 + 1000$  s (A),  $t' = t_0 + 5$  hr to  $t' + 200$  s (B).

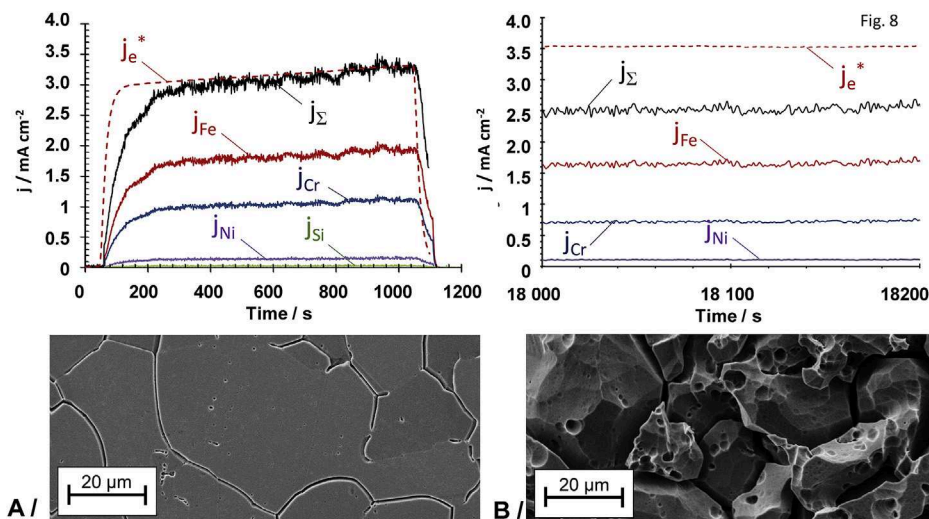


**Fig. 8.** Potentiostatic polarization at 0.65 V vs. MSE of 3.5 wt% Si SS in 4 mol dm<sup>-3</sup> HNO<sub>3</sub> at T = 40 °C.  $j_M$  (M = Fe, Cr, Ni, Si) elemental current contributions,  $j_\Sigma = \sum j_M$ ,  $j_e^*$  convoluted external current. Respective surface observations with SEM at  $t_0$  to  $t_0 + 1000$  s (A),  $t' = t_0 + 5$  hr to  $t' + 200$  s (B).

It is clear from Fig. 7 that the dissolution of the 3.5 wt% Si is exactly the same at  $t_0$  and  $t_0 + 5$  hr and that the surface is homogeneously dissolved. A very different result obtained for the 304LN SS is shown in Fig. 8.

The dissolution observed in Fig. 8 is still non-selective for all elements measured, but has significantly lowered. Consequently,  $j_\Sigma$  is no longer consistent with  $j_e^*$  at the end of the experiment, although the exact same parameters were used for the calculation. The surface expansion due to the intergranular attack was estimated from Fig. 9 (304LN SS after 5 hr experiment - cross section observed with SEM) between 114 and 137%. This value is consistent with the increase of  $j_e^*$ , 3.5 mA cm<sup>-2</sup> at the end of the experiment, which corresponds to +20% of the initial value. It is possible that this specific occluded surface morphology explains the low final value of  $j_\Sigma$ , ionic species from dissolution remaining in the porosity or occluded regions of the interface. If so, this experiment could prove extremely valuable in estimating quantitatively the progression of intergranular corrosion and surface porosity.

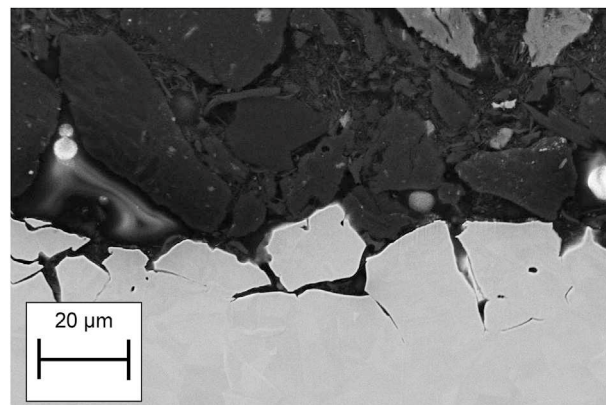


**Fig. 9.** Cross section of 304LN SS after 5 hr polarization at E = 0.65 V vs. MSE in 4 mol dm<sup>-3</sup> HNO<sub>3</sub> at T = 40 °C.



#### 4. Conclusions

In the present work, the role of Si alloying on the transpassive corrosion of stainless steel was investigated by comparing the dissolution behavior of 304LN SS and an 3.5 wt% Si SS using AESEC and *ex situ* surface analysis.

Linear polarization curves indicated that Si had limited impact on the electrochemical behavior of the material. Both 304LN SS and 3.5 wt% Si SS become transpassive at the same potential at 28 °C and 100 °C in 4 mol dm<sup>-3</sup> HNO<sub>3</sub> and similar current densities were measured.

Potentiostatic polarization of the stainless steel in 4 mol dm<sup>-3</sup> HNO<sub>3</sub> at 40 °C, revealed that Si alloying did not impact the dissolution of Cr in its hexavalent form. However, SEM observations confirmed that the 304LN SS was preferentially dissolved at grain boundaries whereas the 3.5 wt% Si SS displayed a homogeneous corrosion morphology. Attempts in the literature to explain this inhibition were based on possible depletion of Cr or segregation of impurities at grain boundaries but X-EDS mappings and profiles performed in the present work for both materials did not reveal such a phenomenon for the elements tested (Si, Cu, Co, P, Ni, Mo). An analysis of the selectivity of the dissolution was proposed based on the AESEC measurements.

In general, all the major elements of both materials displayed a non-selective dissolution. Both materials showed a slight excess of Cr dissolution during the first seconds of polarization when the chromium-rich passive layer is expected to dissolve as a result of the oxidation Cr(III) → Cr(VI). However, a negative excess of Cr was detected in a second step in the case of the 3.5 wt% Si SS, suggesting that the presence of Si could inhibit the dissolution of Cr during the transpassive dissolution. This was consistent with the observation of a relative enrichment in Ni below the interface for the 3.5 wt% Si SS similar to what was observed for the passive state, but not detected for the 304LN SS. The Ni enrichment could result from a local selective dissolution of Cr and Si. This could be a clue to a different *in situ* interface between the 3.5 wt% Si and the 304LN SS during their transpassive dissolution.

However, even if the interface of the 3.5 wt% Si was actually very different from the 304LN, for example if the surface of the 3.5 wt% Si SS was homogeneously covered by Cr(III) oxide, it remains unclear how this could protect grain boundaries from preferential dissolution.

A 5 hr polarization in the transpassive domain was performed for both SS, confirming the homogeneous dissolution of the 3.5 wt% Si SS and the grain removal occurring at the 304LN SS surface. The expansion of the surface measured on cross sections of the 304LN SS were consistent with the increasing of  $j_e^*$ , but the  $j_\Sigma$  probably due to the very occluded surface morphology observed at the end of the experiment.

#### Acknowledgements

Gratitude is extended to the industrial partner Areva for partial financing.

#### References

- [1] B. Laurent, N. Gruet, B. Gwinner, F. Miserque, M. Tabarant, K. Ogle, J. Electrochem. Soc. 164 (13) (2017) C892–C900.
- [2] B. Laurent, N. Gruet, B. Gwinner, F. Miserque, M. Tabarant, K. Ogle, J. Electrochem. Soc. 164 (9) (2017) C481–C487.
- [3] P. Fauvet, Nuclear Corrosion Science and Engineering, 679, Woodhead Publishing, Cambridge, 2012.
- [4] J. Stolarz, J. Le Coze, A. Desestret, in: 9th European Congress on Corrosion, Utrecht, 1, 1989.
- [5] A. Desestret, J. Ferriol, G. Vallier, Materiaux Tech. 9 (1977) 621–636.
- [6] B. Ghiban, S. Ciuca, I. Carceanu, N. Ghiban, I. Nedelcu, Metal. Int. 13 (2008) 39.
- [7] L. Vehovar, Kovine Zlitine Tehnol. 30 (1996) 245.
- [8] T. Honda, T. Yokosuka, Y. Arai, Corrosion 97 (1997).
- [9] B.E. Wilde, Corrosion 44 (1988) 699.
- [10] B. Ghiban, G. Cosmeleata, in: Innovation Stainless Steel, European Stainless Steel Conference, 1993.
- [11] B. Ghiban, N. Ghiban, Univ. "Politehnica" Buchar. Sci. Bull. Ser. B Chem. Mater. Sci. 62 (2000) 79.
- [12] R.R. Kirchheiner, F. Hofmann, T. Hoffmann, G. Rudolph, Mater. Perform. 26 (1987) 49.
- [13] J.S. Armijo, B.E. Wilde, Corros. Sci. 8 (1968) 649.
- [14] O. V. Kasparova and Y. V. Baldokhin, 60 (2011).
- [15] O.V. Kasparova, V. Cihal, V.M. Milman, I. Kasova, S.D. Bogolyubskii, N.M. Ostrikova, Prot. Met. 27 (1991) 554.
- [16] J. Stolarz, J. Le Coze, Colloq. Phys. C1 (1990) 1641.
- [17] A. Camus, A. Desestret, M. Froment, P. Guiraldenq, Comptes Rendus Hebd. Des. Seances De. l'Academie Des. Sci. Ser. C 264 (1967) 425.
- [18] N. Hiroo, K. Haruhiko, U. Noriaki, Cent. Coop. Res. Gifu Univ. 28 (1998).
- [19] A. Desestret, M. Froment, P. Guiraldenq, Mémoires Sci. Rev. métallurgie 66 (1969) 389.
- [20] J.R. Myers, F.H. Beck, M.G. Fontana, Corrosion 9 (21) (1965) 277–287.
- [21] K. Ogle, S. Weber, J. Electrochem. Soc. 147 (2000) 1770.
- [22] V. Shkirskiy, P. Maciel, J. Deconinck, K. Ogle, J. Electrochem. Soc. 163 (2016) C37.
- [23] K.J. Vetter, in: Electrochemische Kinetik, vol. 748, Springer-Verlag, Berlin-Göttingen-Heidelberg, 1961.
- [24] M. Bojinov, G. Fabricius, T. Laitinen, T. Saario, Electrochem. Acta 44 (1999) 4331.
- [25] B. Beverskog, I. Puigdomenech, Corros. Sci. 39 (1997) 43.
- [26] D. Hamm, K. Ogle, C.-O.A. Olsson, S. Weber, D. Landolt, Corros. Sci. 44 (2002) 7.
- [27] P. Schmuki, S. Virtanen, H.S. Isaacs, M.P. Ryan, A.J. Davenport, H. Böhm, T. Stenberg, J. Electrochem. Soc. 145 (1998) 791.
- [28] H. Coriou, J. Hure, G. Plante, Electrochim. Acta 5 (1961) 105.
- [29] A.R. Perrin, K.T. Aust, Mater. Sci. Eng. 51 (1981) 165.
- [30] I. Olefjord, B.-O. Elfstrom, Corrosion 38 (1982) 46.
- [31] M. Pourbaix, Atlas of Electrochemical Equilibria in Aqueous Solutions, Pergamon Press, Oxford, 1966.
- [32] R. Robin, F. Miserque, V. Spagnol, J. Nucl. Mater. 375 (2008) 65.
- [33] M. Froment, J. de Physique Colloques 36 (1975) C4.
- [34] H.-H. Strehblow, Electrochim. Acta 212 (2016) 630.





# CONCLUSION

Yes, your "never-never country"  
yes, your "edge of cultivation"  
And "no sense in going further"  
till I crossed the range to see.

**Rudyard Kipling**

La Nature est un temple où de vivants piliers  
Laissent parfois sortir de confuses paroles ;  
L'homme y passe à travers des forêts de symboles  
Qui l'observent avec des regards familiers.

**Charles Baudelaire**



## C ONCLUSION (EN)

The Uranus S1N SS is a satisfying material choice for industrial devices containing hot and concentrated  $\text{HNO}_3$  in presence of oxidizing species. The state of the art has shown that an important ( $> 1$  wt. %) Si enrichment gave interesting properties to a 18Cr-10Ni type SS in terms of corrosion resistance in such environment. In the presence of oxidizing species, the Uranus S1N dissolves slower than the 304L (X2CrNiN18-10) and is not preferentially attacked at grain boundaries when brought to its transpassive domain. However, in pure  $\text{HNO}_3$ , it tends to dissolve more rapidly. This paradox has not been extensively investigated in the literature as the published explanations rely almost exclusively on mass loss measurements. It could be naturally expected that the nature of the interface was responsible for this phenomenon. Therefore, the particular interface between the Uranus S1N and  $\text{HNO}_3$ , which was basically known to be an oxide layer of chromium silicates, was chosen as the main subject for the present work. By coupling in situ and ex situ techniques (electrochemistry classical tools and ex situ surface analysis) further investigations on this oxide layer were proposed, and its consequences on the corrosion behavior of the Uranus S1N SS in  $\text{HNO}_3$  containing oxidizing species were identified. In particular, an original coupling of electrochemical analysis and on line chemical measurement of the electrolyte, called AESEC (atomic emission spectroelectrochemistry), yields precise information on the thermodynamics and kinetics of formation and dissolution of this passive layer.

Firstly, an electrochemical set of experiments showed that main consequences of the Si enrichment on the alloy was to lower the kinetics of every reduction reactions happening in pure  $\text{HNO}_3$  and in  $\text{HNO}_3$  containing V(V) and Cr(VI) and elevating the oxidation kinetics, as compared to the 304L SS. These experiments confirmed that in pure  $\text{HNO}_3$  the corrosion current of the Uranus S1N SS was higher than for the 304L, because of increased oxidation

kinetics. But as the Si lowered the reduction kinetics, the corrosion potential was also lowered as compared to the 304L, which lead, in the case of  $\text{HNO}_3$  with V(V) (that mainly increased the oxidizing power of the electrolyte) to maintain the Uranus S1N SS passive while the 304L was driven into its transpassive domain, where a larger dissolution rate occurred. Moreover, the transpassive transition was observed for the 304L SS at a very low concentration in V(V) ( $10^{-2} \text{ mol dm}^{-3}$ ) which gave a threshold beyond which the Uranus S1N SS was becoming more resistant to corrosion than the 304L SS. Cr(VI) displayed a singular interaction to the Uranus S1N. At low values of concentrations ( $< 10^{-3} \text{ mol dm}^{-3}$ ) an enhancement of the SS passivity was observed, which was not the case for the 304L SS. This highlighted the possibility of different interactions between the Si-rich passive layer and the environment as compared to the passive layer formed by the 304L SS, and thus, the importance of knowing its properties and nature.

The thermodynamic properties of the oxides protection the Uranus S1N SS were firstly investigated through the measurement of the potential that was necessary to apply to reduce the passive layer. In the state of the art, this potential was called the “activation potential”,  $E_a$ , and it expresses the energy required to reduce the oxide formed.  $E_a$  was expected to evolve linearly with pH and temperature. Previous measurements in the literature were only made in sulfuric acid  $\text{H}_2\text{SO}_4$  where the main reduction reaction was the proton reduction, happening at low potentials, enabling to see the passive-active transition of the alloy. The intensity of the  $\text{HNO}_3$  reduction reaction did not allow to visualize this transition in situ. The use of AESEC enabled to cross this limitation and  $E_a$  was measured for concentrations from 2 to 6  $\text{mol dm}^{-3}$  and temperatures from 28 to 80 °C. The linear evolution of  $E_a$  with pH and temperature was consistent with literature, which made possible the identification of the effect of Si on the standard activation potential  $E_a^\circ$  of the Uranus S1N SS. According to the thermodynamics, standard activation potential of Si/SiO<sub>2</sub> was found to be

lower than Cr/Cr<sub>2</sub>O<sub>3</sub>. Surprisingly, the Uranus S1N SS displayed a higher  $E^{\circ}_a$ , indicating that Si tended to increase  $E^{\circ}_a$ . But as it was shown that the oxide was likely to be a mixed oxide silicate, therefore, it highlighted the importance of identifying the chemical nature of this oxide.

And the chemical nature of the oxide was obtained by combining AESEC with X-ray photoelectron spectroscopy (XPS) and energy dispersive spectroscopy based on transmission electron micrographs of alloys' cross sections (TEM-EDX). The formation and dissolution of the passive layer was examined using AESEC in H<sub>2</sub>SO<sub>4</sub> for both alloys. The selective dissolution of Cr and Si was evidenced during these cycles, and it was shown that Cr was a major factor determining the passivation of the alloy for both materials. Passivation kinetics were found to be very similar, although Si enrichment in the passive layer was for the first time perfectly detectable in the case of the Uranus S1N. The enrichment calculated with AESEC was consistent with the results given by XPS and EDX and it could be pointed out that this very thin film (< 1 nm) formed in few hundreds of seconds, displayed the same ratios Cr/Si than older films formed in 24 hours whose thickness was measured of 3 nm. The EDX measurements revealed the existence of an external layer mostly composed of Si while AESEC, XPS and mean EDX profile agreed on an overall oxide where Cr was the major element. This result proved the existence of at least two layers in the oxide film of the Uranus S1N, one which was composed of statistically 3 atoms of Si for 2 atoms of Cr in the outermost part of the film, and the other at the interface between oxide and metal which would be composed of 1 atom of Si for 2 atoms of Cr. This third set of experiments also revealed that a similar experiment of active-passive cycles was very difficult to perform in HNO<sub>3</sub>, but even if the selective dissolution was not observed during the activation or passivation phases, the passivation kinetics seemed to be consistent with H<sub>2</sub>SO<sub>4</sub>. One interesting aspect of this work could be, for example, to understand Si and Cr atoms

interactions with nitrogenous species, to determine how they could interact with their reduction reaction and explain the lowering of the reduction reaction kinetics that were observed in the first part of the present work. Electrochemical microscopy (SECM) could serve such a purpose for example.

The last part of the present work consisted in a better investigation of the transpassive dissolution of the Uranus S1N. The use of AESEC, by correlation between external current and dissolution current, enabled to formally identify the sixth valence state of Cr responsible for the passive-transpassive transition of SS. It also revealed that the major elements of both SS Fe, Cr, Ni, Si and Mn were oxidized at the same valence state. The analysis of transients at the beginning of the passive-transpassive transition tended to show a difference between the Uranus S1N and the 304L. Indeed, a small enrichment in Cr, very tenuous but reproducible, appeared for the Uranus S1N SS, supported by the persistence of a Ni enrichment below the outermost part of the interface revealed by EDX. In the case of the 304L SS, neither of these enrichment were observed with AESEC nor with EDX. With further investigations, if this phenomenon was not artefact, it could explain a role of Si in the absence of intergranular corrosion during transpassive dissolution of the Uranus S1N. Indeed, the alloy could be protected by a thin oxide layer which would not lower the dissolution rate efficiently but could be able to homogenize the energy at the surface and thus prevent preferential attack. More information could be extracted from local investigation of the surface in situ, for example with the use of impedance spectroscopy combined with AESEC, SECM or atomic force microscopy. The AESEC analysis of the dissolution for longer periods could also be of great interest to understand the reactions involved in the intergranular attack of the 304L SS. The metallurgy of grain boundaries should be furtherly explored as well, however the EDX mapping performed in the present work did not tend to reveal any chemical segregation at grain boundaries for any of the two SS.

Continued effort in this area should address the following questions: based on the first part of the present work, how is the passive layer interacting with more oxidizing species, especially in the case of highly noble redox couples whose reductant is stable in the electrolyte, or in the case of species that increase the reduction reaction of nitrogenous species? How is Si changing the adsorption properties of the passive layer towards nitrogenous species that could explain the lowering of the reduction reaction kinetics? What is the exact composition of the interface during the transpassive dissolution? And in the perspective of modelling the corrosion behavior of the Uranus S1N in various types of conditions, one could investigate the dielectric properties of the passive layer that was identified in the present work, and try to build an equivalent circuit of the system Uranus S1N – HNO<sub>3</sub>.

It has to be noticed eventually that the AESEC technique raises a lot of more general issues about the passive layer of SS that could be explored through different experiments. For example, the low equivalent thickness of the passive film measured during active-passive cycles seem to indicate that more information about the mechanisms involved in the formation and dissolution of the passive layer could be extracted from further measurements. These perspectives will probably correlate with the absence of selective dissolution in HNO<sub>3</sub> for these cycles. Overall, further experiments and calculations on transient phenomena could provide a large source of new information about the in situ mechanisms associated with the oxidation of alloys in very acidic electrolytes. Also, performing the experiments of the present work at higher temperatures could also be relevant for industrial aspects, but requires further technical adjustments of the device.



## C ONCLUSION (FR)

L'acier Uranus S1N est un bon matériau de structure des installations contenant de l'acide nitrique chaud et concentré et en présence d'ions oxydants. En effet, l'état de l'art montre que l'enrichissement important en Si dont il dispose lui confère de très bonnes propriétés de résistance à la corrosion dans ces milieux. Il y est dissout moins rapidement que son homologue sans Si, l'acier 304L, et ne présente pas d'attaque préférentielle significative aux joints de grains. Néanmoins, l'état de l'art montre que lorsqu'il est immergé en acide nitrique seul, sa dissolution est plus rapide que celle de l'acier 304L. Ce paradoxe a été finalement peu étudié dans l'état de l'art, reposant principalement sur une comparaison des deux aciers basée sur des mesures de vitesse de corrosion. On pouvait légitimement penser que cette différence de comportement était liée à la nature de l'interface, en particulier à la couche passive formée naturellement en surface. Il a ainsi été choisi de faire de la couche passive singulière de l'acier Uranus S1N, dont on sait principalement qu'elle est également riche en Si, l'objet d'étude principal de ces travaux de thèse. En couplant des techniques in situ (outils classiques de l'électrochimie) et ex situ (microscopie optique, à balayage, en transmission, XPS et SDL) usuellement utilisées dans les domaines de la corrosion et de la métallurgie, une identification plus complète de cette interface particulière a été proposée, et ses conséquences sur la corrosion de l'acier Uranus S1N en milieu nitrique et en présence d'ions oxydants mieux identifiées. En particulier, le couplage de l'analyse électrochimique avec l'analyse chimique élémentaire en ligne de l'électrolyte, AESEC, a permis d'accéder à des informations précieuses sur le comportement de la couche passive.

Dans un premier temps, une étude principalement électrochimique a permis de montrer que l'impact du Si sur la corrosion de l'acier Uranus S1N était principalement de ralentir les cinétiques de réduction et d'augmenter les cinétiques d'oxydation, et ce dans un large

domaine de conditions : en milieu acide nitrique seul à 100°C (pour des concentrations allant de 1 à 9 mol dm<sup>-3</sup>) et avec des ajouts de deux espèces oxydantes (vanadium pentavalent et chrome hexavalent). Il a été confirmé qu'en acide nitrique seul, le courant de corrosion de l'acier Uranus S1N est supérieur à celui du 304L, ceci étant lié à une augmentation des cinétiques d'oxydation par la présence du Si. Le vanadium pentavalent s'est avéré avoir une influence sur la corrosion des deux aciers d'une façon assez analogue à l'acide nitrique seul. L'impact du Si dans ce type de cas est ainsi lié à un ralentissement des cinétiques de réduction, limitant l'augmentation du  $E_{\text{corr}}$  et donc préservant le matériau d'une rupture de passivité à haut potentiel. Cette rupture transpassive est en revanche observée dans le cas de l'acier 304L à partir d'une concentration très faible de V(V) (10<sup>-2</sup> mol dm<sup>-3</sup>), ce qui conduit à une dissolution beaucoup plus importante de cet acier dans les mêmes conditions. D'autre part, le chrome hexavalent, montre une interaction tout à fait particulière avec l'acier Uranus S1N. En effet, aux faibles valeurs de concentration (inférieures à 10<sup>-3</sup> mol dm<sup>-3</sup>), celui-ci renforce la passivité de l'acier et diminue l'intensité du courant anodique observé. Ce phénomène est nettement moins observé pour l'acier 304L. Ceci montre que la couche passive de l'acier Uranus S1N interagit de manière différente avec l'électrolyte par rapport à l'acier 304L ce qui confirme l'importance de mieux en connaître la nature.

Une première voie pour caractériser cette couche passive riche en Si était de connaître le potentiel nécessaire à sa dissolution. Usuellement appelé potentiel d'activation, cette valeur traduit l'énergie nécessaire pour dissoudre la couche passive formée sur un acier. Ce potentiel d'activation est une fonction du pH et de la température. Si des études du potentiel d'activation de différents alliages Fe-Cr et même Fe-Cr-Ni avaient pu être effectuées dans l'acide sulfurique, où la réaction de réduction de l'eau, à bas potentiel, permet de visualiser la transition passif-actif par méthode électrochimique (sur une courbe I-E quasi-stationnaire classique), l'intensité importante de la réduction du milieu nitrique n'avait pas permis de

l'étudier dans l'acide nitrique. La mesure par la technique AESEC en milieu acide nitrique pour différentes concentrations (de 2 à 6 mol dm<sup>-3</sup>) et températures (de 28 à 80 °C) a permis de montrer que l'évolution du potentiel d'activation en fonction du pH et de la température, était similaire à celle obtenue en milieu sulfurique dans la littérature. Elle a pu également mettre en évidence un effet du Si sur la valeur du potentiel d'activation du matériau. Selon plusieurs auteurs, il est possible d'apparenter cette valeur au potentiel standard de formation de l'oxyde en question. Cela étant, on pouvait s'attendre à ce que le Si diminue le potentiel d'activation standard du matériau puisque le couple Si/SiO<sub>2</sub> possède un potentiel standard plus bas que celui de Cr/Cr<sub>2</sub>O<sub>3</sub>. Or il a été montré au cours du présent travail que le Si avait plutôt tendance à augmenter le potentiel d'activation standard du matériau. Cette étude a donc d'autant plus fortement souligné l'importance d'identifier la nature chimique de la couche passive de l'acier Uranus S1N.

Afin de déterminer cette nature, l'analyse de la formation et de la dissolution de la couche passive a été entreprise. En utilisant l'AESEC et la possibilité d'observer spontanément dans l'acide sulfurique la dissolution active des aciers, des cycles actif-passif ont été réalisés sur les aciers Uranus S1N et 304L afin d'observer la dissolution sélective du matériau au cours des phases d'activation et de passivation. Il a ainsi pu être montré que pour les deux aciers, l'enrichissement de la couche passive en chrome est un facteur déterminant de la passivation et que les cinétiques de passivation sont tout à fait comparables entre les deux aciers. Néanmoins, l'enrichissement de la couche passive en Si est non seulement détectable mais également quantifiable et conduit à une proportion Cr/Si tout à fait cohérente avec les analyses ex situ comme l'XPS ou l'EDX. Un point important qui a été ainsi montré est que la composition de la couche passive est réalisée en quelques centaines de secondes et qu'elle mesure a priori moins d'1 nm d'épaisseur (cohérent avec la littérature). Ceci est cohérent avec le fait qu'après 24 heures de passivation, la couche mesure environ 3 nm. Par ailleurs, si les

analyses AESEC et XPS s'accordent à montrer que le Cr est l'élément majoritaire constitutif de la couche passive, les analyses EDX sur lame mince examinée au MET montrent l'existence d'une couche plus riche en Si en extrême surface. Ce résultat reproductible a conduit à la conclusion qu'il existe au moins deux zones dans l'épaisseur de la couche passive de l'acier Uranus S1N. En extrême surface, un rapport de 3 atomes de Si pour 2 atomes de Cr a été déterminé, tandis qu'entre l'oxyde et le métal, un rapport de 1 atome de Si pour 2 atomes Cr a été plutôt trouvé. Enfin, l'étude a été conduite de façon analogue en acide nitrique, et bien que la sélectivité de la dissolution n'ait pas été détectée, les cinétiques de passivation semblent être parfaitement similaires entre les deux types d'acide. Une perspective particulièrement intéressante de ce travail, en lien avec les trois premières parties de ce travail de thèse, serait de comprendre les interactions des atomes de Si et de Cr avec les différentes espèces pouvant se réduire à la surface de l'acier dans le milieu nitrique. Il pourrait en effet être étudié si les propriétés de ralentissement des cinétiques de réduction de l'acier Uranus S1N peuvent être en lien avec la densité moins importante de Cr à l'interface oxyde-électrolyte, par exemple via l'utilisation de la microscopie électrochimique.

Il restait enfin à essayer de comprendre comment le Si pouvait, même en conditions transpassives, diminuer la corrosion intergranulaire. Dans un premier temps, l'utilisation de l'AESEC en corrélant le courant électrique mesuré par le potentiostat avec le courant de dissolution mesuré par l'ICP-AES a permis de démontrer que les deux alliages se dissolvaient suivant le même mécanisme chimique, c'est-à-dire que les éléments d'alliage majoritaires s'oxydaient aux mêmes valences. L'analyse des dissolutions transitoires lors de la rupture de passivité, ainsi que les profils EDX mesurés sur la couche passive ex situ des deux aciers semblent montrer qu'une différence existe in situ à l'interface oxyde-électrolyte. En effet, immédiatement après la dissolution détectable de la couche passive liée à l'oxydation du Cr trivalent qu'elle contient, un léger enrichissement en Cr semble se produire à la surface de

l'acier Uranus S1N qui n'est pas détecté à la surface de l'acier 304L. Les analyses EDX semblent confirmer cette idée puisque à l'interface oxyde-métal, un enrichissement relatif en Ni est détecté, témoin de la formation d'un oxyde riche en Cr en surface (par dissolution sélective), et cet enrichissement relatif est absent sur les mesures effectuées sur l'acier 304L. Malgré ce, la surface de la corrosion intergranulaire est particulièrement accidentée et il est possible que cela engendre des biais sur la mesure EDX. Toutefois si ce résultat était avéré, on pourrait imaginer que le rôle du Si dans la corrosion transpassive de l'acier Uranus S1N est de diminuer les hétérogénéités de réactivité de la surface par la formation d'un oxyde riche en Cr différent de ce qui se produit dans le cas de l'acier 304L. La dissolution de l'acier Uranus S1N demeure intense et non sélective mais ne se différencie pas aux joints de grain. Il manque néanmoins des éléments importants pour étayer cette hypothèse, qui pourraient être apportés par exemple par l'analyse locale de la conductivité de la surface, par SECM ou par AFM par exemple. Il demeure également une contribution importante possible de la métallurgie des joints de grain, bien que l'utilisation de cartographies EDX n'ait permis de déceler aucune hétérogénéité chimique au niveau de ces joints de grain.

Ainsi, si ce travail devait être poursuivi, il serait judicieux de tenter de répondre aux questions suivantes : comment la couche passive de l'acier Uranus S1N interagit-elle avec d'autres espèces oxydantes, en particulier pour des couples redox plus nobles que l'acier dont l'espèce réduite est stable en solution, ou des couples redox interagissant avec le milieu nitrique lui-même ? Quelles sont les propriétés vis-à-vis de l'adsorption des espèces nitreuses du Si par rapport au Cr ? Quelle est la composition de l'interface in situ lors de la dissolution transpassive de l'acier Uranus S1N ? Quelles sont les propriétés diélectriques de cette couche passive qui permettraient de réaliser une modélisation fidèle (impédance électrochimique) du système Uranus S1N – acide nitrique en corrosion ?

Enfin, notons que la technique AESEC a permis de soulever un grand nombre de questions plus générales concernant la couche passive des aciers inoxydables, qui pourraient être explorées à travers différentes expériences. Par exemple, la faible épaisseur équivalente de ces couches calculées au cours des cycles actif-passif semble indiquer que les mécanismes de formation et de dissolution de ces couches d'oxydes ne sont pas entièrement élucidés. Leur exploration permettrait sans doute d'expliquer également l'origine de l'absence de dissolution sélective en acide nitrique. Plus généralement, toutes les expériences pouvant être imaginées autour des phénomènes transitoires (changement d'état électrochimique de l'acier, modification de son potentiel, etc.) pourraient livrer de nombreuses informations au sujet des mécanismes impliqués dans la formation et la dissolution de la couche d'oxyde des alliages en milieux très acides. Enfin, il pourrait être imaginé de réaliser l'ensemble des expériences du présent travail de thèse à des températures plus élevées, ce qui présenterait un intérêt industriel certain, mais nécessiterait des ajustements techniques de l'appareil plus poussés.

## LIST OF SYMBOLS

Symbol	Typical unit	Name
$f$	$\text{mL min}^{-1}$	Flow rate
$C_{3\sigma, M}$	$\mu\text{g dm}^{-3}$	Three times the standard deviation measured for M divided by the sensitivity factor of the element. Can be considered as a detection limit.
$C_M$	$\mu\text{g mL}^{-1}$	Concentration of M
$X_M$	wt.% - % m.	Mass fraction of M in the alloy
$M_M$	$\text{g dm}^{-3}$	Molar mass of M
$n_M$	at. % - % at.	Molar fraction of M
$v_M$	$\mu\text{g s}^{-1} \text{cm}^{-2}$	Dissolution rate of M
$v_\Sigma$	$\mu\text{g s}^{-1} \text{cm}^{-2}$	Total dissolution rate (usually comprising dissolution rates of Fe, Cr, Ni, Si, Mn, Cu)
$v_{\Sigma\text{max}}$	$\mu\text{g s}^{-1} \text{cm}^{-2}$	Averaged value of maximum total dissolution rate of M
$v'_M$	$\mu\text{g s}^{-1} \text{cm}^{-2}$	Excess dissolution of M
$v^\circ_M$	$\mu\text{g s}^{-1} \text{cm}^{-2}$	Dissolution rate M normalized by its ratio on Fe in the alloy
$Q_M$	$\mu\text{g cm}^{-2}$	Enrichment of M
$j_M$	$\text{A cm}^{-2}$	Dissolution current of M
$j_\Sigma$	$\text{A cm}^{-2}$	Total dissolution current
$j_e$	$\text{A cm}^{-2}$	External current
$j_e^*$	$\text{A cm}^{-2}$	Convolutated external current
$j_{\text{corr}}^*$	$\text{A cm}^{-2}$	Approximated corrosion current
$E_a$	V vs. Ref	Activation potential, corresponding to a passive-active transition potential
$E_{\text{tp}}$	V vs. Ref	Passive-transpassive transition potential
$E_{\text{corr}}$	V vs. Ref	Corrosion potential
$n_{eM}$	-	Number of electrons exchanged during the oxidation/reduction of M
$\Delta n_{\text{elCP}}$	mol	Total amount of electrons exchanged calculated from dissolution rates
$\Delta n_{\text{ext}}$	mol	Total amount of electrons exchanged calculated from external current

## REFERENCES

### 1. Introduction, state of the art, experimentals, results (except publications)

1. B. Baroux, La corrosion des métaux: Passivité et corrosion localisée, Dunod (2014).
2. P. Fauvet, Nuclear corrosion science and engineering, 679, Woodhead Publishing, Cambridge (2012).
3. A. Desestret, in *Matériaux et Techniques*, S. I. R. P. E. Editeur (1977).
4. J.S. Armijo, B.E. Wilde, *Corrosion Science*, 8, 649-664 (1968).
5. A. Camus, A. Desestret, M. Froment and P. Guiraldenq, *Comptes Rendus Hebdomadaires Des Seances De l'Academie Des Sciences Serie C*, 264, 425 (1967).
6. R. Robin, F. Miserque, V. Spagnol, *Journal of Nuclear Materials*, 375, 65-71 (2008).
7. A.R. Perrin, K.T. Aust, *Materials Science And Engineering*, 51, 165-174 (1981).
8. B.E. Wilde, *Corrosion*, 44, 699-704 (1988).
9. Y. Kuriki, M. Tamura, N. Yamanouchi, K. Kiuchi, *Third International Conference on Nuclear Fuel Reprocessing and Waste Management*. 1049-1053 (1991).
10. T. Honda, T. Yokosuka, Y. Arai, *Corrosion* 97, NACE, (1997).
11. R.R. Kirchheiner, F. Hofmann, T. Hoffmann, G. Rudolph, *Materials Performance*, 26, 49-56 (1987).
12. B. Ghiban, G. Cosmeleata, *European stainless steel conference*, 183-188 (1993).
13. B. Ghiban, S. Ciuca, I. Carceanu, N. Ghiban, I. Nedelcu, *Metalurgia Internaional*, 13, 39-42 (2008).
14. Vaudano, A., *Le traitement recyclage du combustible utilisé*. CEA 2008.
15. A. Desestret, *Corrosion Science*, 8, 225-234 (1968).
16. M. Holtzer, *Werkstoffe Und Korrosion-Materials And Corrosion*, 41, 25-29 (1990).
17. A. Desestret, G. Gay, and P. Soullignac, *Colloque de métallurgie de Saclay* (1982).
18. S. Hervé, *Techniques de l'ingénieur - Traitements thermiques des aciers, des alliages et des fontes*, TIB364DUO, m1155(1997).
19. S. Konosu, *Scripta Metallurgica et Materialia*, 26, 1631-1636 (1992).
20. G. Plante and G. Chaudron, *C.R. Acad. Sc. Paris*, 261, 994-996 (1965).
21. J. Bachelay, *Rappel sur l'évolution des Uranus S Note technique*, (1989).
22. D. D. Macdonald, *Pure Applied Chemistry*, 71, 951 (1999).
23. M. Benoit, C. Bataillon, B. Gwinner, F. Miserque, M. E. Orazem, C. M. Sánchez-Sánchez, B. Tribollet and V. Vivier, *Electrochimica Acta*, 201, 340 (2016).
24. H.-H. Strehblow, *Electrochimica Acta*, 212, 630 (2016).
25. J. E. Castle and C. R. Clayton, *Corrosion Science*, 17, 7 (1977).



26. N. B. Hakiki, S. Boudin, B. Rondot and M. Da Cunha Belo, *Corrosion Science*, 37, 1809 (1995).
27. E. J. W. Verwey, *Physica*, 2, 1059 (1935).
28. N. Cabrera and N. F. Mott, *Reports on Progress in Physics*, 12, 163 (1949).
29. K. J. Vetter and F. Gorn, *Electrochimica Acta*, 18, 321 (1973).
30. N. Sato and M. Cohen, *Journal of The Electrochemical Society*, 111, 512 (1964).
31. A. R. Brooks, C. R. Clayton, K. Doss and Y. C. Lu, *Journal of The Electrochemical Society*, 133, 2459 (1986).
32. M. Legrand, B. Diawara, J. J. Legendre and P. Marcus, *Corrosion Science*, 44, 773 (2002).
33. R. Kirchheim, B. Heine, S. Hofmann and H. Hofsäss, *Corrosion Science*, 31, 573 (1990).
34. J. E. Castle and J. H. Qiu, *Journal of The Electrochemical Society*, 137, 2031 (1990).
35. F. Balbaud, *European Journal of Inorganic Chemistry*, 665 (2000).
36. D. Sicsic, *Modélisation thermodynamique et cinétique de la réduction de l'acide nitrique concentré*, Université Pierre et Marie Curie (2011).
37. R. Lange, *Phénomènes de couplages acier 304L - platinoïdes dans les milieux de dissolution des combustibles usés*, Université Pierre et Marie Curie (2012).
38. J. P. Schosger, *Contribution à la connaissance du comportement de l'acier Z3 CN 18-10 dans l'Acide Nitrique concentré, chaud et confiné*, Institut National Polytechnique de Toulouse (1996).
39. M. Benoit, *Modélisation de la cinétique de réduction de l'acide nitrique concentré sur acier inoxydable 304L*, Université Pierre et Marie Curie (2016).
40. V. P. Razygraev, M. V. Lebedeva, S. A. Kabakchi, E. Y. B. Ponomareva, R. S. and L. P. Lobanova, *Journal of Applied Chemistry USSR*, 61 (1988).
41. E. Tcharkhtchi-Gillard, M. Benoit, P. Clavier, B. Gwinner, F. Miserque and V. Vivier, *Corrosion Science*, 107, 182 (2016).
42. G. Suresh, V. R. Raju, U. Kamachi Mudali and R. K. Dayal, *Corrosion Engineering, Science and Technology*, 38, 309 (2003).
43. B. Raj and U. K. Mudali, *Progress in Nuclear Energy*, 48, 283 (2006).
44. S. D. Phanindra and A. H. S. Reddy, *Electrochemical analysis of austenitic stainless steel of type 304L SS in nitric acid medium*, National Institute of Technology Rourkela (2013).
45. M. Pourbaix, *Atlas of electrochemical equilibria in aqueous solutions*, Pergamon Press (1966).
46. K. Ogle and S. Weber, *Journal of The Electrochemical Society*, 147, 1770 (2000).
47. K. Ogle, P. Lodi and A. Storhay, *Methode d'analyse d'un echantillon metallique par dissolution de sa surface, et dispositif pour sa mise en oeuvre*, Google Patents (1993).
48. G. Plante, *Contributions à l'étude de la passivité d'aciers inoxydables en milieu nitrique bouillant*, Université de Paris (1969).
49. G. Plante, *Comptes-rendus des séances de l'Académie des Sciences* (1967).
50. G. Schmid and G. Krichel, *Berichte der Bunsengesellschaft für physikalische Chemie*, 68, 677 (1964).
51. E. Irisawa, M. Seki, F. Ueno, C. Kato, T. Motooka and H. Abe, in *Global 2015*, Paris (2015).
52. A. Desestret, M. Froment and P. Guiraldenq, *Mémoires Scientifiques de la Revue de Métallurgie*, 66, 389 (1969).
53. Rocha H-J. and L. G., *Archiv für den Eisenhüttenwesen*, 117 (1955).

54. H. H. Uhlig, Zeitschrift für Elektrochemie, Berichte der Bunsengesellschaft für physikalische Chemie, 62, 626 (1958).
55. H. H. Uhlig and P. F. King, Journal of The Electrochemical Society, 106, 1 (1959).
56. H. G. Feller and H. H. Uhlig, Journal of The Electrochemical Society, 107, 864 (1960).
57. P. Lorbeer and W. J. Lorenz, Corrosion Science, 21, 79 (1981).
58. A. R. Moshaweh and G. T. Burstein, Corrosion Science, 113, 126 (2016).
59. F. Flade, Zeitschrift für Physikalische Chemie, LXXVI, 513 (1911).
60. K.J. Vetter, Electrochemical Kinetics, 753, Academic Press, New York (1967)
61. P. F. King and H. H. Uhlig, The Journal of Physical Chemistry, 63, 2026 (1959).
62. D. G. Kolman, D. K. Ford, D. P. Butt and T. O. Nelson, Corrosion Science, 39, 2067 (1997).
63. K. Ogle, M. Mokaddem and P. Volovitch, Electrochimica Acta, 55, 913 (2010).
64. V. Shkirskiy, P. Keil, H. Hintze-Bruening, F. Leroux, P. Volovitch and K. Ogle, Electrochimica Acta, 184, 203 (2015).
65. V. Shkirskiy, P. Maciel, J. Deconinck and K. Ogle, Journal of The Electrochemical Society, 163, C37 (2016).
66. A. Fallet, Influence des ions oxydants issus de la dissolution du combustible nucléaire usé sur le comportement des matériaux de structures, Université de Montpellier (2016).
67. A. E. Hughes, Corrosion Science, 22, 103 (1982).
68. R. P. Frankenthal, Journal of The Electrochemical Society, 114, 542 (1967).
69. C. O. A. Olsson and D. Landolt, Electrochimica Acta, 48, 1093 (2003).
70. S. Haupt and H. H. Strehblow, Corrosion Science, 37, 43 (1995).
71. Novak G.A. and G. G.V., The american mineralogist, 56, 791 (1971).
72. Y. Lee, A. J. Bevolo and D. W. Lynch, Surface Science, 188, 267 (1987).
73. P. T. Moseley, G. Tappin and J. C. Rivière, Corrosion Science, 22, 69 (1982).
74. A. Atkinson, Corrosion Science, 22, 87 (1982).
75. M. J. Guittet, J. P. Crocombette and M. Gautier-Soyer, Physical Review B, 63, 125117 (2001).
76. P. Marcus and J. M. Grimal, Corrosion Science, 33, 805 (1992).
77. V. Maurice, W. P. Yang and P. Marcus, Journal of The Electrochemical Society, 145, 909 (1998).
78. B. Gwinner, M. Auroy, F. Balbaud-Célérrier, P. Fauvet, N. Larabi-Gruet, P. Laghoutaris and R. Robin, Corrosion Science, 107, 60 (2016).
79. M. Froment, Journal de Physique Colloques, 36, C4 (1975).
80. B. Beverskog and I. Puigdomenech, Corrosion Science, 39, 43 (1997).
81. K. Osozawa and H. J. Engell, Corrosion Science, 6, 389 (1966).
82. P. Schmuki, S. Virtanen, H. S. Isaacs, M. P. Ryan, A. J. Davenport, H. Böhm and T. Stenberg, Journal of The Electrochemical Society, 145, 791 (1998).
83. M. Bojinov, G. Fabricius, T. Laitinen and T. Saario, Electrochimica Acta, 44, 4331 (1999)

## 2. Publications

### 2.1. Silicon enrichment of an austenitic stainless steel – impact on electrochemical behavior in concentrated nitric acid with oxidizing ions

1. P. Fauvet, Nuclear corrosion science and engineering, 679, Woodhead Publishing, Cambridge (2012).

2. B. Gwinner, M. Auroy, F. Balbaud-Célérier, P. Fauvet, N. Larabi-Gruet, P. Laghoutaris and R. Robin, *Corrosion Science*, 107, 60 (2016).
3. V. Bague, S. Chachoua, Q. T. Tran and P. Fauvet, *Journal of Nuclear Materials*, 392, 396 (2009).
4. T. Honda, T. Yokosuka and Y. Arai, *Corrosion* 97 (1997).
5. Y. Kuriki, M. Tamura, N. Yamanouchi and K. Kiuchi, *Third International Conference on Nuclear Fuel Reprocessing and Waste Management. RECOD '91 Proceedings*, 1049 (1991).
6. S. Kass, J. D. Grozier and F. L. Shubert, *Transactions ASM*, 69 (1963).
7. B. E. Wilde, *Corrosion*, 44, 699 (1988).
8. O. V. Kasparova and Y. V. Baldokhin, 60 (2011).
9. R. R. Kirchheiner, F. Hofmann, T. H. Hofmann and G. Rudolph, *Corrosion* 86, 120 (1986).
10. A. Desestret, *Matériaux et Techniques*, S. I. R. P. E. (1977).
11. G. Plante and G. Chaudron, *C.R. Acad. Sc. Paris*, 261, 994 (1965).
12. A. Camus, A. Desestret, M. Froment and P. Guiraldenq, *Comptes Rendus Hebdomadaires Des Seances De l'Academie Des Sciences Serie C*, 264, 425 (1967).
13. J. S. Armijo and B. E. Wilde, *Corrosion Science*, 8, 649 (1968).
14. R. Robin, F. Miserque, *Journal of Nuclear Materials*, 375, 65-71 (2008).
15. A. R. Perrin and K. T. Aust, *Materials Science and Engineering*, 51, 165 (1981).
16. O. V. Kasparova, V. Cihal, V. M. Milman, I. Kasova, S. D. Bogolyubskii and N. M. Ostrikova, *Protection of Metals*, 27, 5, 554-562 (1991).
17. G. Plante, *Contributions à l'étude de la passivité d'aciers inoxydables en milieu nitrique bouillant*, Université de Paris (1969).
18. N. Hiroo, K. Haruhiko and U. Noriaki, *Center for Cooperative Research Gifu University*, research report, 28 (1998).
19. D. Landolt, *Corrosion et chimie de surfaces des métaux*, Presses polytechniques et universitaires romandes (1997).
20. V. Maurice and P. Marcus, *Electrochimica Acta*, 84, 129 (2012).
21. C. A. Della Rovere, J. H. Alano, R. Silva, P. A. P. Nascente, J. Otubo and S. E. Kuri, *Materials Chemistry and Physics*, 133, 668 (2012).
22. P. Fauvet, F. Balbaud, R. Robin, Q. T. Tran, A. Mugnier and D. Espinoux, *Journal of Nuclear Materials*, 375, 52 (2008).
23. F. Balbaud, *Mécanisme de corrosion de l'acier inoxydable Z3 CN 18.10 en présence de condensats nitriques*, Université Pierre et Marie Curie (1998).
24. D. Sicsic, F. Balbaud-Celerier and B. Tribollet, *European Journal of Inorganic Chemistry*, 6174 (2014).

25. R. Lange, E. Maisonhaute, R. Robin and V. Vivier, *Electrochemistry Communications*, 29, 25 (2013).
26. M. Benoit, *Modélisation de la cinétique de réduction de l'acide nitrique concentré sur acier inoxydable 304L*, Université Pierre et Marie Curie (2016).
27. V. P. Razygraev, M. V. Lebedeva, S. A. Kabakchi, E. Y. B. Ponomareva, R. S. and L. P. Lobanova, *Journal of Applied Chemistry USSR*, 61 (1988).
28. P. Schmuki, S. Virtanen, H. S. Isaacs, M. P. Ryan, A. J. Davenport, H. Böhm and T. Stenberg, *Journal of The Electrochemical Society*, 145, 791 (1998).
29. M. Bojinov, G. Fabricius, T. Laitinen and T. Saario, *Electrochimica Acta*, 44, 4331 (1999).
30. T. Motooka, C. Kato and M. Yamamoto, *Zairyo-to-Kankyo*, 59, 18 (2010).
31. P. Martin and P. Alena, *IOP Conference Series: Materials Science and Engineering*, 9, 012074 (2010).
32. M. Pourbaix, *Atlas of electrochemical equilibria in aqueous solutions*, Pergamon Press (1966).
33. E. Irisawa, M. Seki, F. Ueno, C. Kato, T. Motooka and H. Abe, *Global 2015*, Paris (2015).
34. D.-Y. Lin and T.-C. Chang, *Materials Science and Engineering: A*, 359, 396 (2003).
35. J. Stolarz, J. Le Coze and A. Desestret, *Colloque de Physique*, 51, 1641-1645 (1990).
36. B. Beverskog and I. Puigdomenech, *Corrosion Science*, 39, 43 (1997).

### **2.2.A direct measurement of the activation potential of stainless steels in nitric acid**

1. P. Fauvet, *Nuclear corrosion science and engineering*, 679, Woodhead Publishing, Cambridge (2012).
2. A. Desestret, *Materiaux et Techniques*, S. I. R. P. E. (1977).
3. E. Tcharkhtchi-Gillard, M. Benoit, P. Clavier, B. Gwinner, F. Miserque and V. Vivier, *Corrosion Science*, 107, 182 (2016).
4. M. Ozawa, O. Yamamura and K. Gonda, *Journal of Nuclear Science and Technology*, 22, 68 (2012).
5. B. Raj and U. K. Mudali, *Progress in Nuclear Energy*, 48, 283 (2006).
6. F. Balbaud, *European Journal of Inorganic Chemistry*, 665 (2000).
7. D. Sicsic, F. Balbaud-Celerier and B. Tribollet, *European Journal of Inorganic Chemistry*, 6174 (2014).
8. K. J. Vetter, *Zeitschrift für Elektrochemie, Berichte der Bunsengesellschaft für physikalische Chemie*, 63, 1189 (1959).
9. G. Schmid and G. Krichel, *Berichte der Bunsengesellschaft für physikalische Chemie*, 68, 677 (1964).

10. P. Fauvet, F. Balbaud, R. Robin, Q. T. Tran, A. Mugnier and D. Espinoux, *Journal of Nuclear Materials*, 375, 52 (2008).
11. M. Benoit, *Modélisation de la cinétique de réduction de l'acide nitrique concentré sur acier inoxydable 304L*, Université Pierre et Marie Curie (2016).
12. P. Lorbeer and W. J. Lorenz, *Corrosion Science*, 21, 79 (1981).
13. H. H. Uhlig and P. F. King, *Journal of the Electrochemical Society*, 106, 1 (1959).
14. Rocha H-J. and L. G., *Archiv für den Eisenhüttenwesen*, 117 (1955).
15. P. F. King and H. H. Uhlig, *The Journal of Physical Chemistry*, 63, 2026 (1959).
16. H. G. Feller and H. H. Uhlig, *Journal of The Electrochemical Society*, 107, 864 (1960).
17. W. S. Hwang, Lee J. J. Yang W. S. and N. S. C., *Materials Science Forum*, 544-545, 423 (2007).
18. R. P. Frankenthal, *Journal of the Electrochemical Society*, 114, 542 (1967).
19. F. Flade, *Zeitschrift für Physikalische Chemie* 6, 513 (1911).
20. U. F. Franck, *Zeitschrift für Naturforschung*, 4a, 378 (1949).
21. G. Plante, *Contributions à l'étude de la passivité d'aciers inoxydables en milieu nitrique bouillant*, Université de Paris (1969).
22. K. Ogle and S. Weber, *Journal of the Electrochemical Society*, 147, 1770 (2000).
23. D.G. Kolman, D.K. Ford, D. P. Butt and T. O. Nelson, *Corrosion Science*, 39, 2067-2093 (1997)
24. K. Ogle, J. Baeyens, J. Swiatowska and P. Volovitch, *Electrochimica Acta*, 54, 5163 (2009).
25. K. Ogle, M. Mokaddem and P. Volovitch, *Electrochimica Acta*, 55, 913 (2010).
26. K. Ogle, A. Tomandl and N. Meddahi, *Innovative Pre-Treatment Techniques to Prevent Corrosion of Metallic Surfaces*, 158, Woodhead Publishing, Washington (2007).
27. V. Shkirskiy, P. Keil, H. Hintze-Bruening, F. Leroux, P. Volovitch and K. Ogle, *Electrochimica Acta*, 184, 203 (2015).
28. T. Shinagawa, A. T. Garcia-Esparza and K. Takanabe, *Scientific Reports*, 5, 13801 (2015).
29. H. H. Uhlig, *Zeitschrift für Elektrochemie, Berichte der Bunsengesellschaft für physikalische Chemie*, 62, 626 (1958).
30. A. Fallet, *Influence des ions oxydants issus de la dissolution du combustible nucléaire usé sur le comportement des matériaux de structures*, Université de Montpellier (2016).
31. J. Stolarz, J. Le Coze and A. Desestret, *Colloque de Physique*, 51 (1990).
32. R. Robin, F. Miserque and V. Spagnol, *Journal of Nuclear Materials*, 375, 65 (2008).
33. A.R. Moshaweh and R. Burstein, *Corrosion Science*, 113, 126-132 (2016)

34. I. Olefjord and B-O. Elfstorm, Corrosion, 39, 46-52 (1982)
35. K.J. Vetter, Electrochemical Kinetics, 753, Academic Press, New York (1967)
36. M. Pourbaix, Atlas of electrochemical equilibria in aqueous solutions. Pergamon Press (1966).
37. B. Beverskog and I. Puigdomenech, Corrosion Science, 39(1), 43-57 (1997)

### **2.3.Dissolution and passivation of a silicon-rich austenitic stainless steel during active-passive cycles in sulfuric and nitric acid**

1. J. Keir, Philosophical Transactions of the Royal Society of London, 80, 359-384 (1790).
2. W. Hisinger, J. J. Berzelius, Gilberts Annalen, 27, 275 (1807).
3. Ch. F. Schönbein, M. Faraday, Philosophical Magazine, 9, 53 (1836).
4. M. Faraday, Experimental Researches in Electricity, 2, Dover, New York (1965).
5. C. L. McBee, J. Kruger, Electrochimica Acta, 17, 1337-1341 (1972).
6. C.O.A. Olsson, D. Landolt, Electrochimica Acta, 48, 1093-1104 (2003).
7. P. Fauvet, Nuclear corrosion science and engineering, 679, Woodhead Publishing, Cambridge (2012).
8. H.-H. Strehblow, Electrochimica Acta, 212, 630-648 (2016).
9. D.D. Macdonald, Pure Applied Chemistry, 71, 951-978 (1999).
10. R. Kirchheim, B. Heine, S. Hofmann, H. Hofsäss, Corrosion Science, 31, 573-578 (1990).
11. M. Legrand, B. Diawara, J.J. Legendre, P. Marcus, Corrosion Science, 44, 773-790 (2002).
12. K.J. Vetter, Electrochemische Kinetik, Springer-Verlag, Berlin-Göttingen-Heidelberg, 748-789 (1961).
13. P. Schmuki, S. Virtanen, H.S. Isaacs, M.P. Ryan, A.J. Davenport, H. Böhm, T. Stenberg, Journal of The Electrochemical Society, 145, 791-801 (1998).
14. F. Balbaud, European Journal of Inorganic chemistry, 665-674 (2000).
15. M. Ozawa, O. Yamamura, K. Gonda, Journal of Nuclear Science and Technology, 22, 68-69 (2012).
16. B. Raj, U.K. Mudali, Progress in Nuclear Energy, 48, 283-313 (2006).
17. M. Pourbaix, Atlas of electrochemical equilibria in aqueous solutions, Pergamon Press (1966).
18. A. Desestret, Matériaux et Techniques, S. I. R. P. E. (1977).

19. Y. Kuriki, M. Tamura, N. Yamanouchi, K. Kiuchi, Third International Conference on Nuclear Fuel Reprocessing and Waste Management, xxii 1154, 1049-1053 (1991).
20. O.V. Kasparova, Y.V. Baldokhin, G.A. Kochetov, Protection of Metals, 38, 176 (2002).
21. G. Hochörtler, E.M. Horn, Metallic corrosion, II, 1447-1452 (1981).
22. B. Ghiban, S. Ciuca, I. Carceanu, N. Ghiban, I. Nedelcu, Metalurgia International, 13, 39-42 (2008).
23. L.Y. Gurvich, A.D. Zhirnov, Protection of metals, 31, 231-235 (1995).
24. T. Honda, T. Yokosuka, Y. Arai, Corrosion 97, NACE (1997).
25. B. Laurent, N. Gruet, B. Gwinner, F. Miserque, M. Tabarant, K. Ogle, Journal of the Electrochemical Society, 164, 9, C481-C487 (2017).
26. S. Haupt, H.H. Strehblow, Journal of Electroanalytical Chemistry, 228, 365 (1987).
27. V. Maurice, P. Marcus, Electrochimica Acta, 84, 129-138 (2012).
28. K. Ogle, M. Mokaddem, P. Volovitch, Electrochimica Acta, 55, 913-921 (2010).
29. V.P. Razygraev, M.V. Lebedeva, S.A. Kabakchi, E.Y.B. Ponomareva, R. S., L.P. Lobanova, Journal of Applied Chemistry USSR, 61 (1988).
30. D.G. Kolman, D.K. Ford, D.P. Butt, T.O. Nelson, Corrosion Science, 39, 2067-2093 (1997).
31. K. Ogle, S. Weber, Journal of the Electrochemical Society, 147, 1770-1780 (2000).
32. V. Shkirskiy, P. Keil, H. Hintze-Bruening, F. Leroux, P. Volovitch, K. Ogle, Electrochimica Acta, 184, 203-213 (2015).
33. P. Lorbeer, W. J. Lorenz, Corrosion Science, 21, 79-86 (1981).
34. K. Ogle, J. Baeyens, J. Swiatowska, P. Volovitch, Electrochimica Acta, 54, 5163-5170 (2010).
35. F. Ruel, P. Volovitch, L. Peguet, A. Gaugain, K. Ogle, Corrosion, 69, 536-542 (2013).
36. R. Robin, F. Miserque, V. Spagnol, Journal of Nuclear Materials, 375, 65-71 (2008).
37. A.A. Hermas, K. Ogura, T. Adachi, Electrochimica Acta, 40, 837-844 (1995).
38. J.S. Armijo, B.E. Wilde, Corrosion Science, 8, 649-664 (1968).
39. B.E. Wilde, Corrosion, 44, 699-704 (1988).
40. B. Ghiban, G. Cosmeleata, Innovation stainless steel, European stainless steel conference 183-188 (1993).
41. B. Ghiban, N. Ghiban, Scientific Bulletin Series B: Chemistry and Materials Science, 62, 79-86 (2000).
42. B. Baroux, Passivity of Metals and Semiconductors, Elsevier, Bombannes, France (1983) 531-545.

43. E. Tcharkhtchi-Gillard, M. Benoit, P. Clavier, B. Gwinner, F. Miserque, V. Vivier, *Corrosion Science*, 107, 182-192 (2016).
44. L. Marchetti, F. Miserque, S. Perrin, M. Pijolat, *Surface and Interface Analysis*, 47, 632-642 (2015).
45. H.S. Nalwa, *Handbook of Surfaces and Interfaces of Materials* (2001).
46. Y. Lee, A.J. Bevolo, D.W. Lynch, *Surface Science*, 188, 267-286 (1987).
47. M. J. Guittet, J.P. Crocombette, M. Gautier-Soyer, *Physical Review B*, 63, 125117 (2001).
48. V. Maurice, W.P. Yang, P. Marcus, *Journal of the Electrochemical Society*, 143 (3), 1182-1200 (1996).
49. N. B. Hakiki, S. Boudin, B. Rondot, M. Da Cunha Belo, *Corrosion Science*, 37 (11), 1809-1822 (1995).
50. W.P. Yang, D. Costa, P. Marcus, *Journal of the Electrochemical Society*, 141 (1), 111-116 (1994).
51. P. Marcus and J. M. Grimal, *Corrosion Science*, 33, 805 (1992).
52. V. Maurice, W. P. Yang and P. Marcus, *Journal of the Electrochemical Society*, 145, 909 (1998).

#### **2.4.The kinetics of transpassive dissolution chemistry of stainless steels in nitric acid: The impact of Si**

1. B. Laurent, N. Gruet, B. Gwinner, F. Miserque, M. Tabarant, K. Ogle, *J. Electrochem. Soc.* 164 (13) (2017) C892eC900.
2. B. Laurent, N. Gruet, B. Gwinner, F. Miserque, M. Tabarant, K. Ogle, *J. Electrochem. Soc.* 164 (9) (2017) C481eC487.
3. P. Fauvet, *Nuclear Corrosion Science and Engineering*, 679, Woodhead Publishing, Cambridge, 2012.
4. J. Stolarz, J. Le Coze, A. Desestret, in: *9th European Congress on Corrosion*, Utrecht, 1, 1989.
5. A. Desestret, J. Ferriol, G. Vallier, *Materiaux Tech.* 9 (1977) 621e636.
6. B. Ghiban, S. Ciuca, I. Carceanu, N. Ghiban, I. Nedelcu, *Metal. Int.* 13 (2008) 39.
7. L. Vehovar, *Kovine Zlitine Tehnol.* 30 (1996) 245.
8. T. Honda, T. Yokosuka, Y. Arai, *Corrosion* 97 (1997).
9. B.E. Wilde, *Corrosion* 44 (1988) 699.
10. B. Ghiban, G. Cosmeleata, in: *Innovation Stainless Steel, European Stainless Steel Conference*, 1993.



11. B. Ghiban, N. Ghiban, Univ. "Politehnica" Buchar. Sci. Bull. Ser. B Chem. Mater. Sci. 62 (2000) 79.
12. R.R. Kirchheiner, F. Hofmann, T. Hoffmann, G. Rudolph, Mater. Perform. 26 (1987) 49.
13. J.S. Armijo, B.E. Wilde, Corros. Sci. 8 (1968) 649.
14. O. V. Kasparova and Y. V. Baldokhin, 60 (2011).
15. O.V. Kasparova, V. Cihal, V.M. Milman, I. Kasova, S.D. Bogolyubskii, N.M. Ostrikova, Prot. Met. 27 (1991) 554.
16. J. Stolarz, J. Le Coze, Colloq. Phys. C1 (1990) 1641.
17. A. Camus, A. Desestret, M. Froment, P. Guiraldenq, Comptes Rendus Hebd. Des. Seances De. l'Academie Des. Sci. Ser. C 264 (1967) 425.
18. N. Hiroo, K. Haruhiko, U. Noriaki, Cent. Coop. Res. Gifu Univ. 28 (1998).
19. A. Desestret, M. Froment, P. Guiraldenq, Memoires Sci. Rev. metallurgie 66 (1969) 389.
20. J.R. Myers, F.H. Beck, M.G. Fontana, Corrosion 9 (21) (1965) 277e287.
21. K. Ogle, S. Weber, J. Electrochem. Soc. 147 (2000) 1770.
22. V. Shkirskiy, P. Maciel, J. Deconinck, K. Ogle, J. Electrochem. Soc. 163 (2016) C37.
23. K.J. Vetter, in: Electrochemische Kinetik, vol. 748, Springer-Verlag, Berlin-Gottingen-Heidelberg, 1961.
24. M. Bojinov, G. Fabricius, T. Laitinen, T. Saario, Electrochem. Acta 44 (1999) 4331.
25. B. Beverskog, I. Puigdomenech, Corros. Sci. 39 (1997) 43.
26. D. Hamm, K. Ogle, C.-O.A. Olsson, S. Weber, D. Landolt, Corros. Sci. 44 (2002) 7.
27. P. Schmuki, S. Virtanen, H.S. Isaacs, M.P. Ryan, A.J. Davenport, H. B€ohm, T. Stenberg, J. Electrochem. Soc. 145 (1998) 791.
28. H. Coriou, J. Hure, G. Plante, Electrochim. Acta 5 (1961) 105.
29. A.R. Perrin, K.T. Aust, Mater. Sci. Eng. 51 (1981) 165.
30. I. Olefjord, B.-O. Elfstrom, Corrosion 38 (1982) 46.
31. M. Pourbaix, Atlas of Electrochemical Equilibria in Aqueous Solutions, Pergamon Press, Oxford (, 1966.
32. R. Robin, F. Miserque, V. Spagnol, J. Nucl. Mater. 375 (2008) 65.
33. M. Froment, J. de Physique Colloques 36 (1975) C4.
34. H.-H. Strehblow, Electrochim. Acta 212 (2016) 630.

# UNACHIEVED EXPERIMENTS

Science! True daughter of Old Time thou art!  
Who alterest all things with thy peering eyes.  
Why preyest thou thus upon the poet's heart,  
Vulture, whose wings are dull realities?

**Edgar Allan Poe**

Dante écrit deux vers, puis il sort ; et les deux vers  
Se parlent. Le premier dit : - Les cieux sont ouverts.  
Cieux ! Je suis immortel. - Moi, je suis périssable.  
Dit l'autre. - Je suis l'astre. - Et moi le grain de sable.  
- Quoi ! Tu doutes étant fils d'un enfant du ciel !  
- Je me sens mort. - Et moi, je me sens éternel.  
Quelqu'un rentre et relit ces vers, Dante lui-même:  
Il garde le premier et barre le deuxième.  
La rature est la haute et fatale cloison.  
L'un meurt, et l'autre vit. Tous deux avaient raison.

**Victor Hugo**



# UNACHIEVED EXPERIMENTS

This complementary chapter aims at presenting few unachieved experiments that were found of interest for the present work.

## 1. Impact of an argon flow in the electrolyte on the corrosion potential of the 304L and the Uranus S1N SS

### 1.1. Experimentals

The open circuit potentials of both SS and platinum electrode were measured over time in a 4 mol dm<sup>-3</sup> HNO<sub>3</sub> at 100°C. The 0.2 dm<sup>-3</sup> reactor is equipped with a bubbling system providing a constant flow of Ar (Air products, 99.9992%). It was shown by Sicsic et al. [1] that a bubbling of inert gas limited the concentration of several gaseous nitrous species in the solution and above. The quantification of this limitation and the exact identification of which species are actually removed remain unclear.

### 1.2. Results and discussion

Pt and SS OCP recorded over 2 hours (304L SS) and 6 hours (Uranus S1N) are displayed on Fig. 1. During this period, Ar is intermittently supplied through the electrolyte.

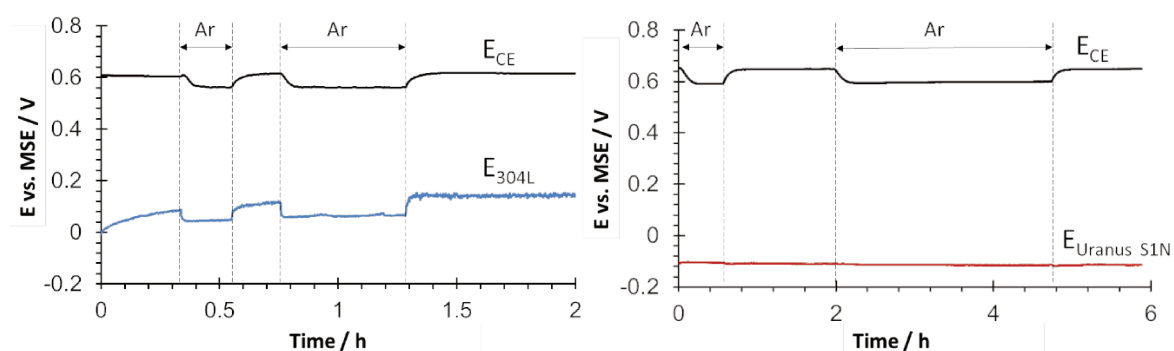


Fig. 1. OCP measured for the 304L SS (blue), Uranus S1N (red) and Pt (black) depending on Ar bubbling in the electrolyte (4 mol dm<sup>-3</sup> HNO<sub>3</sub> at 100°C)

Pt potential, which directly relies on the equilibrium potential of the electrolyte, decreases of 50 mV with bubbling Ar, indicating that the removed species are likely to be associated to high oxidation states [2, 3]. The 304L SS behaves very similar to Pt, showing a

decrease of the same amplitude when Ar is introduced. This is consistent with the idea that if the electrolyte becomes less oxidizing, the reduction reaction kinetics will be lowered and the corrosion potential of the material will lower as well.

On the other hand, the corrosion potential of the Uranus S1N SS does not react to the Ar bubbling. It could be thought that there is an effect of the slope  $j$  vs.  $E$  that is higher for the Uranus S1N than for the 304 L SS [4]. Thus, a small variation of the reduction reaction intensity would impact more visibly a material that presents a small  $\frac{\Delta j}{\Delta E}$  such as the 304L SS. Another hypothesis would be associated to the mechanisms of the reduction reaction. For example, if the removed nitrous species are not involved in the reduction reaction happening at the Si-rich surface, then the OCP of the Uranus S1N would not vary with their removal. Regarding the conclusions of “Si enrichment of an austenitic stainless steel – impact on the electrochemical behavior in concentrated nitric acid with oxidizing ions”, this experiment shows at least once again the lowering of the reduction reaction kinetics by Si, that leads to a limited impact of nitrous species equilibria modifications in the electrolyte on the open circuit potential of the Uranus S1N SS.

### **1.3. Perspectives**

In his thesis work, Lange [5] tried to set up a protocol for identifying the reduction reaction products in  $\text{HNO}_3$  using a Pt micro-electrode (generator-collector SECM mode). If close enough to the surface, it is theoretically possible to identify species generated during the reduction reaction by reoxidizing them at specific potential applied on the micro-electrode. By using this technique under an intermittent Ar bubbling could possibly discriminate the involvement of one or several species in the reduction reaction occurring for the two SS.

## 2. Ratio of the reduction current density between the two SS in 4 mol dm<sup>-3</sup> HNO<sub>3</sub> at 100°C

### 2.1. Experimental

In the context of the first chapter of this thesis work, density currents for the reduction reaction of 4 mol dm<sup>-3</sup> HNO<sub>3</sub> at 100°C for the 304L ( $j_{c_{304L}}$ ) and Uranus S1N ( $j_{c_{US1N}}$ ) were measured and compared between  $E_{corr}$  and -0.47 V vs. MSE.  $\frac{j_{c_{304L}}}{j_{c_{US1N}}}$  is plotted as a function of potential.

### 2.2. Results and discussion

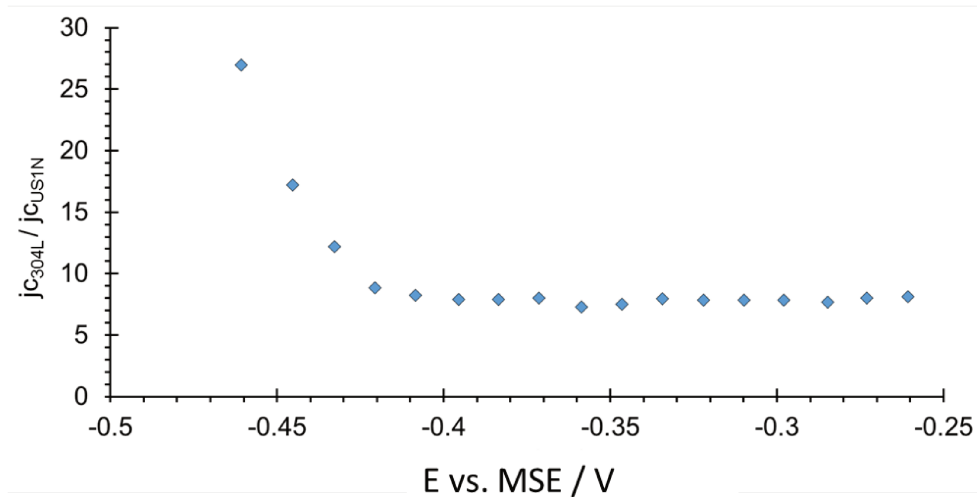


Fig. 2. Ratio  $\frac{j_{c_{304L}}}{j_{c_{US1N}}}$  as a function of potential in 4 mol dm<sup>-3</sup> HNO<sub>3</sub> at 100°C (current density values determined over a linear polarization curve at 0.2 mV s<sup>-1</sup>, cathodic sweep)

It is shown on Fig. 2 that the ratio  $\frac{j_{c_{304L}}}{j_{c_{US1N}}}$  varies differently depending on the potential. Between -0.25 V vs. MSE and -0.40 V vs. MSE, the reduction current densities are proportional. Between -0.40 and -0.47 V vs. MSE the ratio increases with E diminishing.

Under the hypothesis of a charge transfer limited mechanism, it is possible to express these cathodics current according to Butler-Volmer's equation [6, 7] :

$$j_{c_{304L}} = -n_{e_{304L}} F k^{\circ}_{304L} COx^*_{304L} \exp\left(\frac{-\alpha_{c_{304L}} n_{e_{304L}} F}{RT} (E - E^{\circ}_{304L})\right) \quad (1)$$

$$j_{c_{US1N}} = -n_{e_{US1N}} F k^{\circ}_{US1N} COx^*_{US1N} \exp\left(\frac{-\alpha_{c_{US1N}} n_{e_{US1N}} F}{RT} (E - E^{\circ}_{US1N})\right) \quad (2)$$

With  $n_{e_M}$  number of electrons exchanged during the reduction reaction,  $k^{\circ}_M$  standard rate constant,  $COx^*_M$  Ox volumic concentration in the electrolyte,  $\alpha_{c_M}$  charge transfer coefficient for the reduction reaction.

The ratio is:

$$\frac{j_{c_{304L}}}{j_{c_{US1N}}} = K \exp(AE + B) \quad (3)$$

With:

$$K = \frac{n_{e_{304L}} k^{\circ}_{304L} COx^*_{304L}}{n_{e_{US1N}} k^{\circ}_{US1N} COx^*_{US1N}} \quad (4)$$

$$A = \frac{F}{RT} (\alpha_{c_{US1N}} n_{e_{US1N}} - \alpha_{c_{304L}} n_{e_{304L}}) \quad (5)$$

$$B = \frac{F}{RT} (E^{\circ}_{304L} \alpha_{c_{304L}} n_{e_{304L}} - E^{\circ}_{US1N} \alpha_{c_{US1N}} n_{e_{US1N}}) \quad (6)$$

$\frac{j_{c_{304L}}}{j_{c_{US1N}}}$  is then constant with E only if A = 0 which implies  $\alpha_{c_{US1N}} n_{e_{US1N}} = \alpha_{c_{304L}} n_{e_{304L}}$ .

Otherwise it varies exponentially, which seems to correspond to what is shown on Fig. 2 between -0.40 and -0.47 V vs. MSE.

### 2.3. Perspectives

The condition  $\alpha_{c_{US1N}} n_{e_{US1N}} = \alpha_{c_{304L}} n_{e_{304L}}$  in the present case cannot be elucidated. A better identification of the nitrous species reduced would highly facilitate the comprehension of what is observed in this case. As said previously, the use of SECM could help determining  $\alpha_{c_{US1N}}, n_{e_{US1N}}, \alpha_{c_{304L}}, n_{e_{304L}}$ . It also felt that between -0.25 V vs. MSE and –

0.40 V vs. MSE where the ratio is constant, an effect of a limitation by the adsorption of species could be involved. If so, the value of the ratio could simply rely on the ratio of adsorption sites densities between the 304L and the Uranus S1N passive layers. In this case, techniques such as atomic force microscopy and/or in situ Raman spectroscopy could help visualizing preferential adsorption sites at these two different interfaces.

### **3. Electrochemical microscopy : determining the reduction mechanisms and characterization of the passive layer's conductivity**

The use of ultra-micro-electrodes (UME), whose dimension do not exceed 25  $\mu\text{m}$  (diameter), enabled by the beginning of the 80s [8] to perform electrochemical measurements close to the reactive interfaces in solution, without being biased by diffusional limitations. Indeed, while classical electrodes present linear diffusion regime, UME are associated with semi-spherical diffusion regime, and allow a greater current density than for unidimensional diffusion.

In the 90s, Bard et al. [9] developed the scanning electrochemical microscopy (SECM), using the UME as a probe whose position and current/potential can be controlled. The spatial resolution of the SECM is directly related to the size of the probe, since the interpenetration of the diffusion gradients (between surface and solution) depend on its diameter. The communication between the substrate (surface analyzed) and the probe is enabled by the electrolyte.

The SECM is usually associated with two functions: the feedback mode, for which is used a redox mediator in the solution. This mode gives access to conduction characteristics of the substrate. The second mode is called generator-collector, in which



the UME is used as a detector to identify electroactive species produced nearby the substrate.

In the present work, a SECM device was set up in the laboratory in order to briefly explore the possibilities of this technique regarding the issues of the thesis. The feedback mode would be of interest to identify differences of conductivities in the passive layers of the 304L and the Uranus S1N SS, while the generator-collector mode would have preferentially been used to detect nitrous species reducing or their reduced form produced at the interface.

### **3.1. Feedback mode**

For this experiment, the electrolyte is a 10 mM  $\text{K}_3\text{Fe}(\text{CN})_6$  + 0.5 M  $\text{K}_2\text{SO}_4$  at 25 °C. The substrate is a Uranus S1N polished electrode (diamond finished, as described in the experimental parts of the four main chapters) and the probe is a gold UME (10  $\mu\text{m}$  diameter). The redox couple  $\text{Fe}(\text{III})/\text{Fe}(\text{II})$  is used, and the electrolyte originally contains  $\text{Fe}(\text{III})$ . The probe is polarized at -0.5 V vs. MSE which enables the  $\text{Fe}^{3+}$  ions to reduce and a negative stationary current  $i_{\text{lim}}$  of about 10 nA was measured when the probe was in the electrolyte away from the substrate. In the same time, the substrate is polarized at different potentials from 0 to 0.3 V vs. MSE which enable  $\text{Fe}^{2+}$  to oxidize back into  $\text{Fe}^{3+}$ .

As the probe is approached to the substrate, two phenomena can be observed.

- If the substrate is a good conductor,  $\text{Fe}^{2+}$  ions produced at the probe will be reoxidized and the probe current absolute value will elevate, which is called « positive feedback » because the ratio  $i/i_{\text{lim}}$  increases.

- If the substrate is an insulator, the  $\text{Fe}^{3+}$  ions will not be provided to the probe anymore because of the limited space separating the substrate and the probe. The probe current will decrease and this behavior will be called a « negative feedback ».

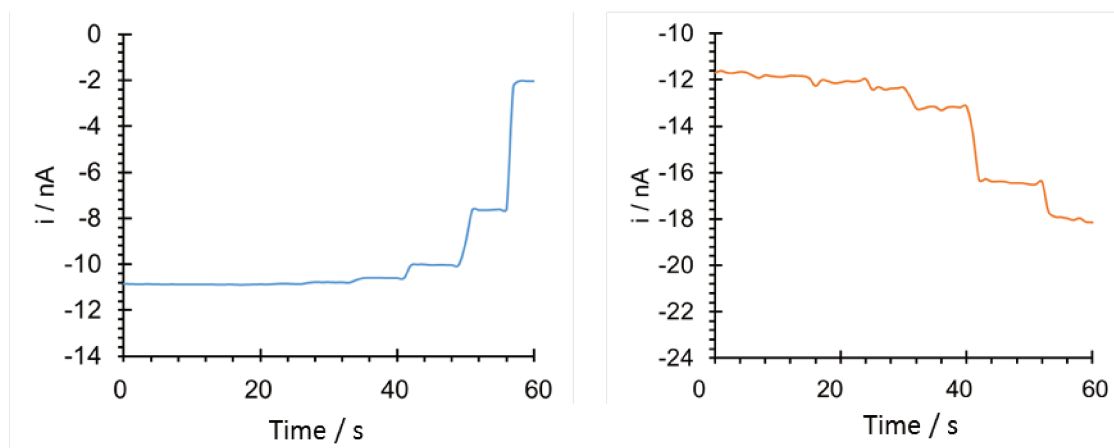


Fig. 3. Measurements of probe current (gold UME 10 $\mu\text{m}$ ) for substrate polarization at 0.1 V vs. MSE (blue) and 0.3 V vs. MSE (orange) when the probe (polarized at -0.5 V vs. MSE) approaches the Uranus S1N substrate in 10 mM  $\text{K}_3\text{Fe}(\text{CN})_6$  + 0.5 M  $\text{K}_2\text{SO}_4$  at 25 °C

Fig. 3 illustrates both cases described: negative feedback at 0.1 V vs. MSE, positive at 0.3 V vs. MSE. A third measurement was also performed at 0 V vs. MSE.  $i/i_{\text{lim}}$  is plotted in Fig. 4 as a function of the dimensionless  $d/a$  ratio (distance between probe and substrate on probe diameter).

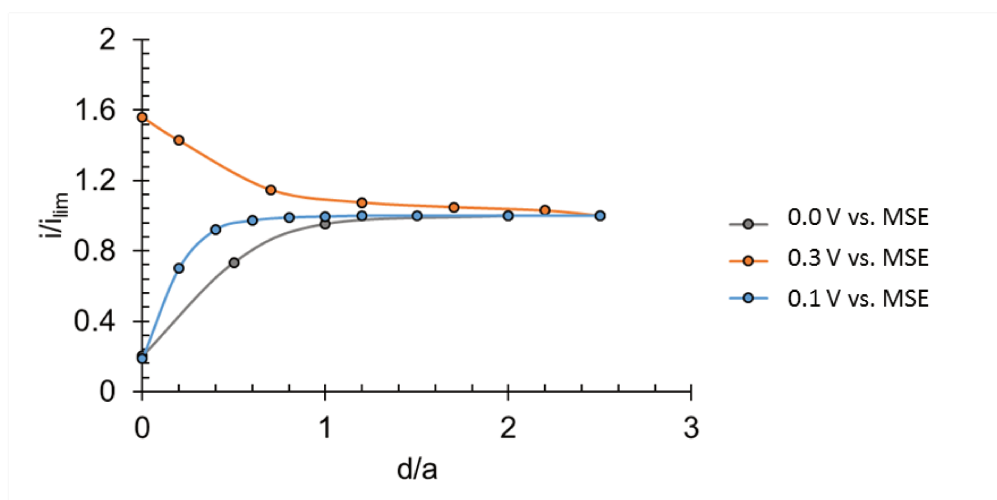


Fig. 4. Approach curves on Uranus S1N substrate polarized between 0 and 0.3 V vs. MSE in 10 mM  $\text{K}_3\text{Fe}(\text{CN})_6$  + 0.5 M  $\text{K}_2\text{SO}_4$  at 25 °C with a 10  $\mu\text{m}$  gold UME polarized at -0.5 V vs. MSE

These measurements show that it does exist a potential from which the Uranus S1N becomes a conductor. Although it can be mentioned that the SS will probably produce  $\text{Fe}^{3+}$  from its own oxidation reaction, which could participate in the positive feedback observed, previous similar work on 304L SS [10] did not mention any positive feedback for this SS. To ensure this result, another redox mediator such as Ru(III) could be used for example. Another possibility offered by the SECM, not available for this device at the time of the experiment, is to perform a map scan of the surface, realizing several approaching curves at different locations of the substrate. This would probably give interesting information of the reproducibility of this result.

### 3.2. Generator-collector mode

This part is directly inspired from Lange et al. [5] who attempted to realize a nitrous species detector at the 304L SS surface in  $\text{HNO}_3$ . The substrate could be immersed into a 4  $\text{mol dm}^{-3}$   $\text{HNO}_3$  that would be polarized at low potentials to reduce nitrous species. At different distances from the substrate, the probe could perform cyclic voltammetries on a

large scale of potentials to identify possible produced species and their diffusion gradients in the solution. Several experiments were conducted in order to set an electrochemical detector to  $\text{Fe}^{3+}$  ions as first step, but couldn't achieve a fully operative nitrous species detector.

We are grateful to Renaud Cornut<sup>1</sup> who spent a tremendous amount of time helping us fixing the SECM.

#### **4. Why is the selective dissolution invisible during active-passive cycles in $\text{HNO}_3$ ?**

##### **4.1. A quick reminder of the results**

In the third publishing project « Dissolution and passivation of a silicon-rich austenitic stainless steel during active-passive cycles in sulfuric and nitric acid », it is said that the enrichment in Cr and Si was not measurable during active-passive cycles in  $4 \text{ mol dm}^{-3} \text{HNO}_3$  at  $25^\circ\text{C}$ . Actually, not mentioned in the text, an opposite excess dissolution was measured for Cr and Si.

##### **4.2. Is the AESEC technique sensitive enough?**

In first approach, the idea that the dissolution rate in the active domain was too high in  $\text{HNO}_3$  was enunciated as a hypothesis to explain the absence of clear selective dissolution of Cr and Si during passivation and activation transients. However, the  $-0.8 \text{ V vs. MSE}$  activation gave a lower dissolution rate in the active domain and the same result was found (Fig. 5). A slight negative excess of Cr and Si is found during activation and positive excess during passivation, which is the opposite of what was expected and what is observed in  $\text{H}_2\text{SO}_4$ .

---

<sup>1</sup> CEA / IRAMIS / Nanosciences et Innovation pour les Matériaux, la Biomédecine et l'Energie / Laboratoire Innovation, Chimie des Surfaces et Nanosciences, [renaud.cornut@cea.fr](mailto:renaud.cornut@cea.fr)

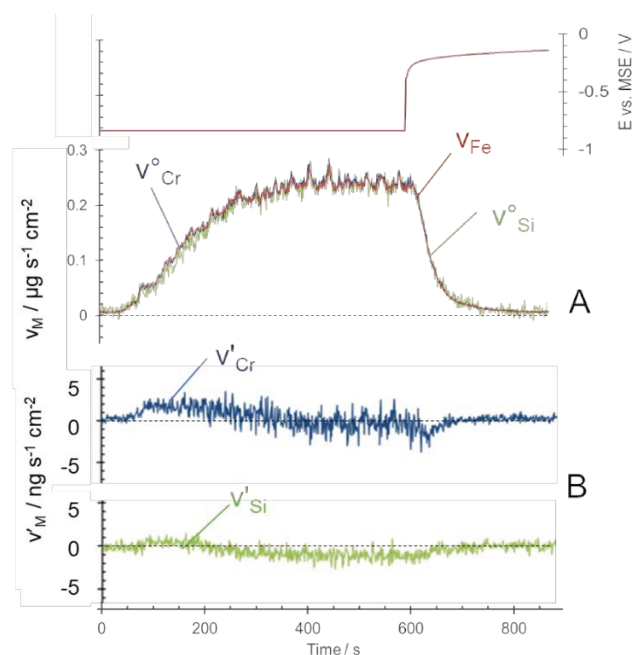


Fig. 5. Uranus S1N active passive cycle in 4 mol dm<sup>-3</sup> HNO<sub>3</sub> at 25°C, A/  $v_{Fe}$ ,  $v_{Cr}^{\circ}$  and  $v_{Si}^{\circ}$  vs. time. B/  $v'_{Cr}$  and  $v'_{Si}$  vs. time

Moreover, in the fourth publishing project « Impact of silicon enrichment on the transpassive dissolution chemistry of stainless steels in nitric acid », a selective dissolution of Cr is recorded in the passive-transpassive transition and the maximum dissolution rate is of the same order of magnitude than for passive-active transition shown in Fig. 6 (approximately 400 ng s<sup>-1</sup> cm<sup>-2</sup>). This result proves that the AESEC can detect an enrichment of 50 ng in Cr, that would correspond to a theoretical 0.1 nm thick passive layer (using an oxide density of 5.22 g cm<sup>-3</sup>).

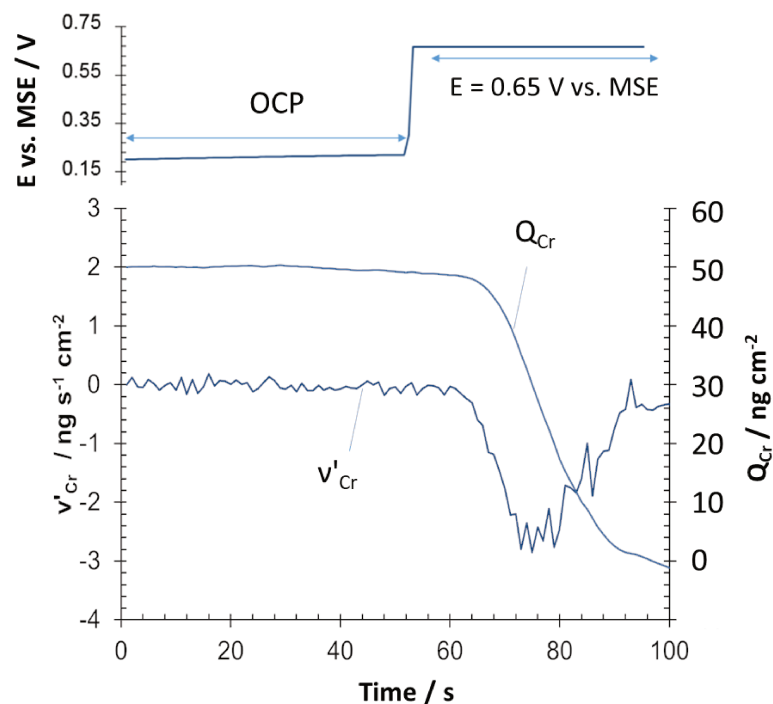


Fig. 6.  $Q_{Cr}$  and  $v'_{Cr}$  over first 100 seconds of passive-transpassive transition in  $4 \text{ mol dm}^{-3}$   $\text{HNO}_3$  at  $40^\circ \text{C}$ .

It is still unclear why the selective dissolution is invisible during active-passive cycles, but it is not related to the technique itself.

### 4.3. Perspectives

Firstly, it is still delicate to compare  $\text{H}_2\text{SO}_4$  and  $\text{HNO}_3$ , since even the measurement has to be different in  $\text{HNO}_3$  (the polarization in the active domain has to be maintained during the experiment in  $\text{HNO}_3$ ). It is also possible that the dissolution of the passive layer during the passive-active transition for example is immediately compensated by the formation of a new passive layer, which is less protective since the active dissolution is visible, but does not allow to visualize the selective dissolution during this transient period.

## 5. AESEC transpassive measurements versus SCIANS model

### 5.1. State of the art

The SCIANS model (intergranular corrosion modelling for non-sensitized steels) was developed [11] to model geometrical evolution of the intergranular attack that was observed on certain SS such as 304L. The model relies on the following hypothesis that were experimentally verified:

- Intergranular attack is characterized by triangular grooves at grain boundaries forming an angle referred to as  $\alpha$  (Fig. 7)
- Grooves are symmetrical with respect to the grain boundary
- It is considered that the groove angles have almost the same value all over the surface and remain constant with time

Average size of grains  $D$  must be known, along with two dissolution rates (Fig. 7):

- $V_s$ , which is the dissolution rate on the grain surface
- $V_j$ , which corresponds to the local dissolution rate at grain boundaries

Under the hypothesis of a preferential attack at grain boundaries,  $V_j > V_s$ , and these

dissolution rates are relative to the  $\alpha$  groove angle according to  $\frac{V_j}{V_s} = \frac{1}{\sin \frac{\alpha}{2}}$ .

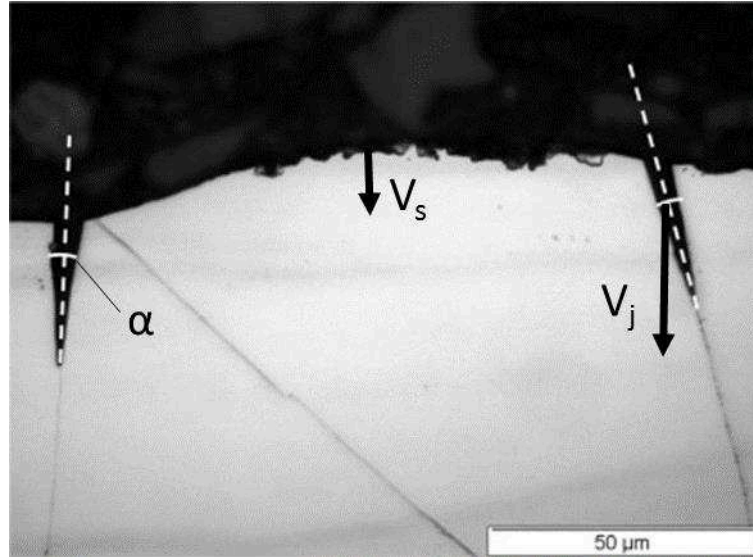


Fig. 7. Cross section of a 310L SS sample after 160h immersion in boiling 8 mol dm<sup>-3</sup> HNO<sub>3</sub> containing 357 mg dm<sup>-3</sup> of V<sub>2</sub>O<sub>5</sub> [11]

$V_j$  and  $V_s$  can be determined from morphological consideration of the grooves after a few hours experiments using  $V_j = \frac{H}{(1-\sin \frac{\alpha}{2})t}$  with  $H$  being the depth of the groove and  $t$  the time of immersion. The model may enable the prediction of the surface increasing with time and total mass loss regarding this particular type of corrosion behavior.

In the fourth publishing project, polarizations in the transpassive domain of the 304L SS were performed in 4 mol dm<sup>-3</sup> HNO<sub>3</sub> at 40 °C and an attempt to apply the SCIANS model on these experiments is presented. It is proposed to verify whether the SCIANS model can be applied in the conditions of the AESEC (limited electrolyte volume, constant flow rate, moderate temperature). The samples studied were, after AESEC treatment, cut, coated and their cross sections were observed using SEM and optical microscopy.

## 5.2. Results

Firstly, the 304L SS sample was polarized at 0.65 V vs. MSE (transpassive domain of the SS) for 20 mins. During this polarization,  $j_e^*$  was recorded along with  $j_\Sigma$  which results from  $j_M$  for  $M = \text{Fe, Cr, Ni}$  using respective valence states of II, VI and IV in accordance to what is



described in this publishing project. It can be seen that both  $j_e^*$  and  $j_\Sigma$  lightly increase over this period (Fig. 8) of about + 10 % at the end of the experiment (from about  $2.9 \text{ mA cm}^{-2}$  to  $3.2 \text{ mA cm}^{-2}$ ).

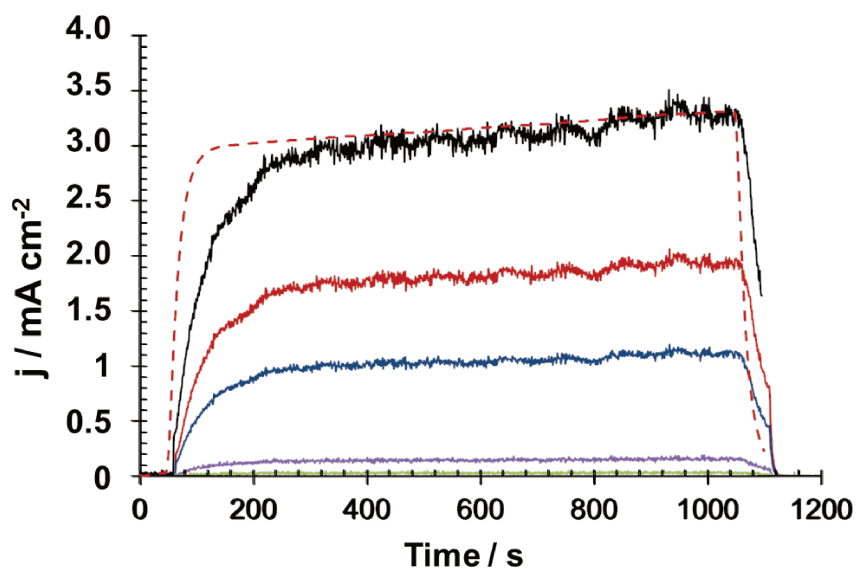


Fig. 8. Potentiostatic polarization ( $E = 0.65 \text{ V vs. MSE}$ ) for the 304L SS in  $4 \text{ mol dm}^{-3} \text{ HNO}_3$  at  $40^\circ\text{C}$ .

$j_{\text{Fe}}$  (red),  $j_{\text{Cr}}$  (blue),  $j_{\text{Ni}}$  (purple),  $j_\Sigma$  (black) et  $j_e^*$  (red dashed line)

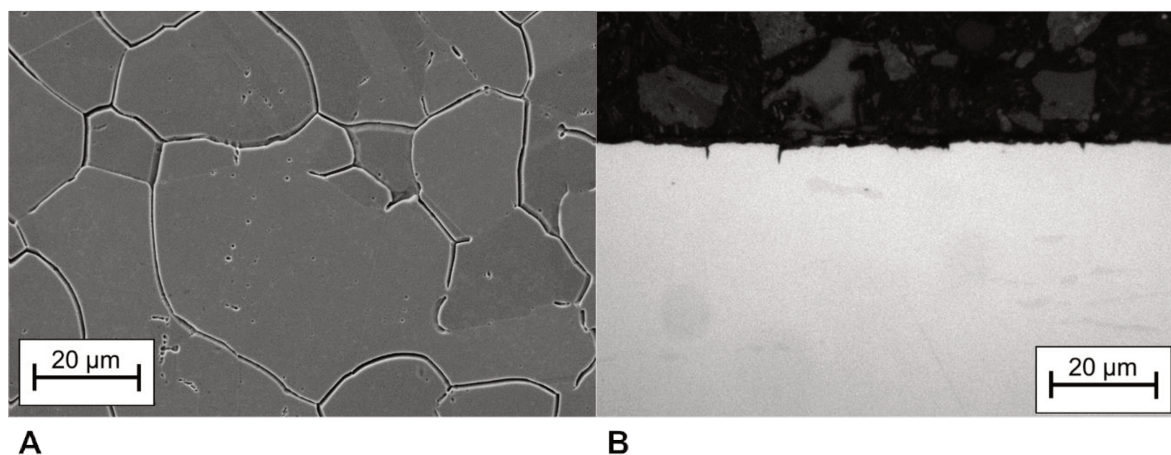


Fig. 9. Top view (A) and cross section (B) of a 304L SS sample after 20 min polarization at  $0.65 \text{ V vs. MSE}$  in  $4 \text{ mol dm}^{-3} \text{ HNO}_3$  at  $40^\circ\text{C}$

On Fig. 9B can be measured an averaged groove depth of  $2.3 \pm 0.9 \mu\text{m}$  and groove angle of  $20.9 \pm 3.2^\circ$ . This leads to  $V_j = 206 \mu\text{m d}^{-1}$  and  $V_s = 39 \mu\text{m d}^{-1}$ .

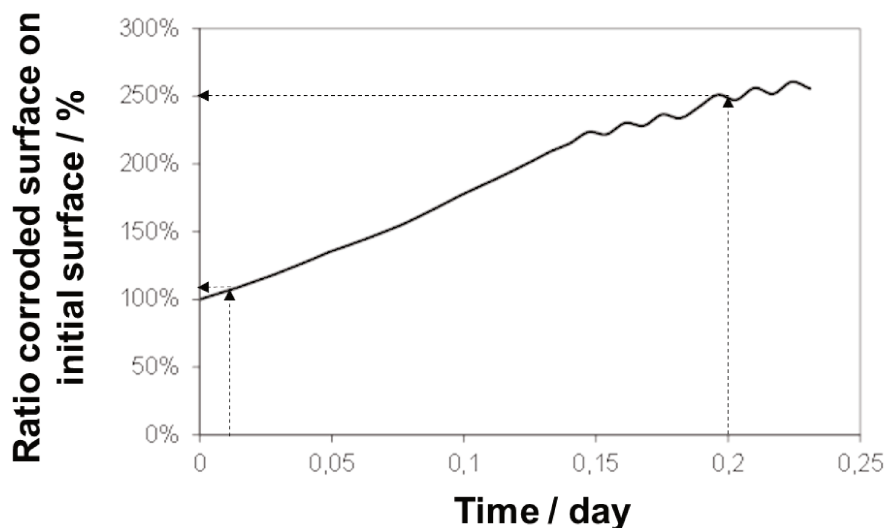


Fig. 10. SCIANS estimation of surface increasing over time in the present conditions

The calculation leads to an increasing of 9% after 20 mins (Fig. 10), which is consistent with the experiment.

To go further, a similar sample is then polarized in the same conditions (E, flow rate, temperature) for a longer time (5 hours). For technical reasons, the ICP-AES is performed twice for 20 mins each, at the beginning and at the end of the experiment. Fig. 10 expects an increasing of the surface of 250%, and Fig. 11 reveals a highly attacked surface with visible grains removal.

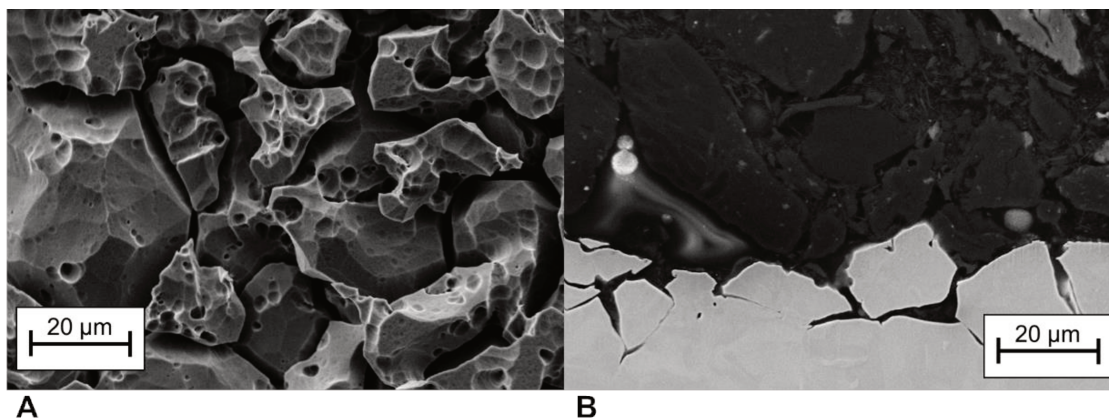


Fig. 11. Top view (A) and cross view (B) of a 304L SS sample after 5 h polarization in  $4 \text{ mol dm}^{-3} \text{ HNO}_3$  at  $40^\circ \text{C}$  ( $E = 0.65 \text{ V vs. MSE}$ )

But the measurement on Fig. 11B leads to an increase of the surface between 114 and 137 %. Although this value is lower than what was expected through the SCIANS model, it is more consistent with the increase of external current recorded by the potentiostat,  $3.5 \text{ mA cm}^{-2}$  at the end of the experiment, which corresponds to + 20% of the initial value. One surprising result that is displayed on Fig. 12 is that  $j_{\Sigma}$  is no longer consistent with  $j_e^*$  at the end of the experiment, although the exact same parameters were used for the calculation. The dissolution observed on Fig. 12 is also non selective for all elements measured.

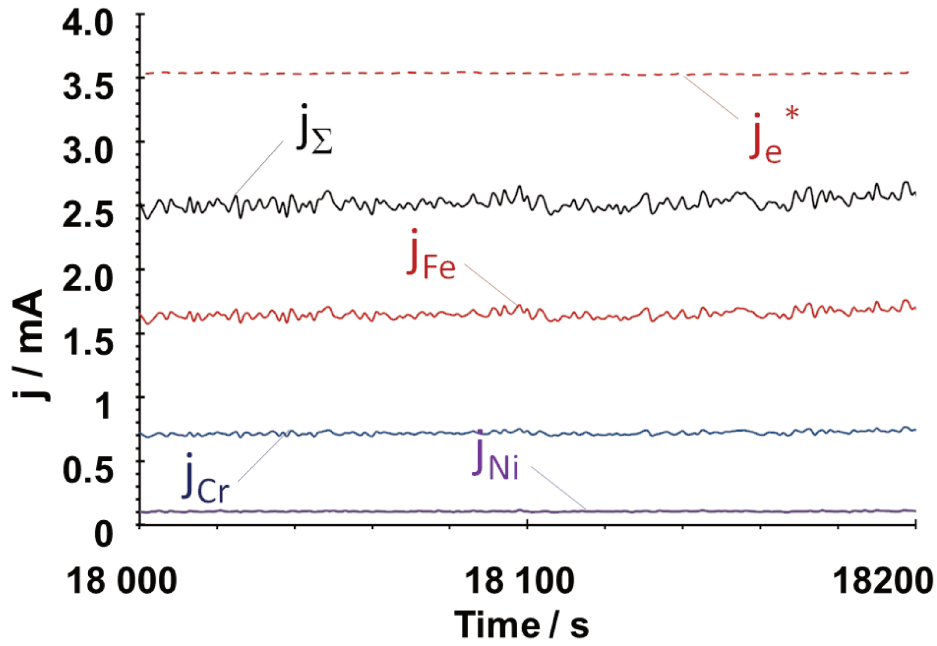


Fig. 12. Potentiostatic polarization ( $E = 0.65$  V vs. MSE) for the 304L SS in  $4 \text{ mol dm}^{-3} \text{ HNO}_3$  at  $40^\circ\text{C}$  after 5 hours polarization.

$j_{\text{Fe}}$  (red),  $j_{\text{Cr}}$  (blue),  $j_{\text{Ni}}$  (purple),  $j_{\Sigma}$  (black) et  $j_e^*$  (red dashed line))

The exact origin of this difference couldn't be explained by this single measurement. The difference between  $j_{\Sigma}$  and  $j_e^*$  could be for example explained if an oxide film was forming, but this would not be expected in the case of transpassive dissolution without any selective behavior identified.

### 5.3. Conclusions

In the case of intergranular corrosion, a certain consistence between experiments lead in the AESEC device and what the SCIANS model calculates was shown. The results are congruent for a short period of time (20 mins).

For longer periods, two main divergences appeared:

- the SCIANS model expected a higher surface increasing than what was experimentally observed

- $j_\Sigma$  and  $j_e^*$  are no longer superimposable

With the given amount of experiments, it was not possible to determine the origin of these divergences. It should be of interest to perform a continue measurement with the AESEC and repeat the experiment.

## REFERENCES – UNACHIEVED EXPERIMENTS

1. D. Sicsic, Modélisation thermodynamique et cinétique de la réduction de l'acide nitrique concentré, Université Pierre et Marie Curie (2011).
2. F. Balbaud, European Journal of Inorganic Chemistry, 665 (2000).
3. N. Larabi-Gruet, E. Buravand, B. Gwinner, R. Robin and P. Fauvet, ECS Transactions, **41**, 57 (2012).
4. R. Robin, F. Miserque and V. Spagnol, Journal of Nuclear Materials, **375**, 65 (2008).
5. R. Lange, Phénomènes de couplages acier 304L - platinoïdes dans les milieux de dissolution des combustibles usés, Université Pierre et Marie Curie (2012).
6. J. A. V. Butler, Transactions of the Faraday Society, **19**, 729 (1924).
7. T. Erdey-Grúz and M. Volmer, Zur Theorie der Wasserstoff Überspannung, in Zeitschrift für Physikalische Chemie, 203 (1930).
8. R. M. Wightman, Analytical Chemistry, **53**, 1125A (1981).
9. A. J. Bard, F. R. F. Fan, J. Kwak and O. Lev, Analytical Chemistry, **61**, 132 (1989).
10. D. Sidane, Etude par microscopie électrochimique (SECM) de la réactivité d'une surface métallique hétérogène passivée : effet de la contrainte mécanique et thermomécanique, Université de Bordeaux 1 (2012).
11. B. Gwinner, M. Auroy, F. Balbaud-Célérrier, P. Fauvet, N. Larabi-Gruet, P. Laghoutaris and R. Robin, Corrosion Science, **107**, 60 (2016).



### About the Author



*After mathematics and physics “Classes préparatoires aux grandes écoles” in Marseille, I passed the national competition exam and integrated Grenoble INP- Physics, Electronics and Materials (PHELMMA) engineering school. I graduated in 2014 with a Master degree in Electrochemistry.*

In a first internship during the second academic year, I discovered the Research community through the study of molten salts electrochemistry for 4<sup>th</sup> generation nuclear waste recycling process.

The second internship undergone was more industrially-orientated, as I participated to the development of a thin coating for galvanized steels designed for the automotive industry.

Then I brought together both the nuclear field I enjoyed working for and the corrosion knowledge base I had and prepared the present work, exclusively based on the *Electrochemistry I've always enjoyed.*



## Résumé

L'objectif de ces travaux est de mieux comprendre le comportement en corrosion de l'acier Uranus S1N en milieu acide nitrique chaud et concentré et en présence d'espèces oxydantes. La littérature montre que les aciers 304L et Uranus S1N, qui ont une composition chimique similaire à l'exception du silicium (moins de 1 %m. pour le 304L et 4 %m. pour l'Uranus S1N) se comportent de façon différente dans ces milieux. En milieu acide nitrique seul, l'acier 304L présente une vitesse de corrosion plus faible que celle de l'acier Uranus S1N. Cette tendance s'inverse lorsque l'on ajoute des ions oxydants au milieu. Les mécanismes physico-chimiques en jeu ne semblent pas clairement établis. On souhaite comprendre quel est l'effet de l'enrichissement en silicium conduisant à cette différence de comportement. Les phénomènes de réduction et d'oxydation sont comparés entre les deux aciers pour différentes conditions : acide nitrique pur, présence de vanadium pentavalent, présence de chrome hexavalent. On montre que la présence de Si diminue les cinétiques de réduction et donc empêche l'acier Uranus S1N de se trouver dans son domaine transpassif même en conditions très oxydantes. Puis la couche passive de l'acier Uranus S1N est étudiée à travers trois jeux d'expériences. D'une part ses caractéristiques thermodynamiques sont étudiées par la mesure du potentiel d'activation de l'acier. D'autre part, sa composition chimique, sa morphologie et sa structure sont mis en lumière par la corrélation de différentes techniques in-situ et ex-situ cohérentes. Enfin, la rupture de passivité à haut potentiel est observée car le Si est suspecté responsable de la disparition de l'attaque intergranulaire. Ces trois axes d'études de l'oxyde protecteur de l'acier Uranus S1N font appel à des techniques in-situ originales comme l'Atomic emission spectro electrochemistry permettant de coupler la mesure électrochimique à l'analyse élémentaire en ligne, mais également à des techniques d'analyses ex-situ telles que la spectroscopie à photoélectrons X ou la spectroscopie d'énergie dispersive sur lame mince.

**Mots clés :** Corrosion, Electrochimie, Acier inoxydable, Acide nitrique, Passivité

## Abstract

This work aims at understanding the corrosion behavior of the Uranus S1N stainless steel (SS) in hot and concentrated nitric acid. The Uranus S1N SS is a 304L type SS (18Cr-15Ni) added by 4 wt. % of Si. In pure nitric acid, the 304L SS dissolves slower. In other words, Si enhances the corrosion rate of the SS. But when oxidizing species are added, the 304L dissolves at a much higher rate than the Uranus S1N. Mechanisms involving Si that bring to this phenomenon are not clearly established. The purpose of this thesis project is to elucidate the role of Si in the spontaneous corrosion of the SS in pure nitric acid and in presence of oxidizing species. Reduction and oxidation phenomena are compared, through I-V curves measurements, between both steels, for different conditions: pure nitric acid, presence of pentavalent vanadium, hexavalent chromium. It was shown that Si diminishes the reduction kinetics and prevents the Uranus S1N SS to be shifted to its transpassive domain even when conditions are largely oxidizing. Then the oxide layer was investigated through three sets of experiments. Firstly, thermodynamics of the oxides were characterized by measuring the activation potential of the SS. Secondly, their chemical composition, thickness and structure were investigated coupling congruent in-situ and ex-situ measurements. Eventually, high potential passivity breakdown was investigated to understand why Si inhibits the intergranular attack at the surface.

These three investigations rely on coupling original in-situ techniques as the atomic emission spectro electrochemistry (electrochemical measurements coupled to elemental on line analysis) and ex-situ surface analysis as X-Ray photoelectron spectroscopy or Energy dispersive X-ray spectroscopy on cross-section thin blades.

**Key words:** Corrosion, Electrochemistry, Stainless Steel, Nitric acid, Passivity